EXPERIMENTAL INVESTIGATION AND 3D CYCLIC FINITE ELEMENT SIMULATION OF R/C EXTERIOR BEAM-COLUMN JOINTS RETROFITTED WITH CFRP COMPOSITE MATERIALS

by

Selçuk Altay

B.S. in Civil Engineering, Yıldız Technical University, 2000

M.Sc. in Civil Engineering, Boğaziçi University, 2003

Submitted to the Institute for Graduate Studies in

Science and Engineering in partial fulfillment of

the requirements for the degree of

Doctor of Philosophy

Graduate Program in Civil Engineering

Boğaziçi University

2010

EXPERIMENTAL INVESTIGATION AND 3D CYCLIC FINITE ELEMENT SIMULATION OF R/C EXTERIOR BEAM-COLUMN JOINTS RETROFITTED WITH CFRP COMPOSITE MATERIALS

APPROVED BY:

Assoc. Prof. Cem Yalçın (Thesis Supervisor)	.....
Assist. Prof. Sami And Kılıç (Thesis Co-Supervisor)	.....
Prof. Cengiz Karakoç	.....
Prof. Fazıl Önder Sönmez	.....
Assoc. Prof. Şevket Özden	.....

DATE OF APPROVAL: .....

Dedicated to my grandfather Mürvet Özgür, my mother Gönül Altay
and my wife Begüm Altay

SPECIAL ACKNOWLEDGEMENTS

The author wishes to express his gratitude to Associate Professor Azadeh Parvin from the University of Toledo for her invaluable co-advising role, motivation and assistance in the numerical and experimental phases of this study. Her guidance in the preparation of this thesis is deeply appreciated.

This thesis work, entitled "*Experimental Investigation and 3D Cyclic Finite Element Simulation of R/C Exterior Beam-Column Joints Retrofitted with CFRP Composite Materials*" was accomplished by a collaborative program of NSF (OISE-0352947) and TUBITAK (İCTAG I 597 NSF 103I026) and co-directed by Dr. Azadeh Parvin and Dr. Cem Yalçın.

ACKNOWLEDGEMENTS

I am deeply grateful to my thesis supervisor Assoc. Prof. Cem Yalçın, Assist. Prof. Sami And Kılıç and Assoc. Prof. Azadeh Parvin for their guidance and encouragement throughout the course of this study. I am profoundly indebted for their deep commitment to excellence and it was pleasure for me to work with them.

I would like to thank my dissertation examining committee members Prof. Cengiz Karakoç, Assoc. Prof. Şevket Özden and Prof. Fazıl Önder Sönmez for their time, comments and recommendations.

I wish to express my further gratitude to Dr. Sami And Kılıç for providing me the background information on parallel computing and the facility of Compute Cluster System for the finite element simulations. Without his assistance and support this dissertation could not be accomplished.

I am very thankful to my friend and colleague Osman Kaya for his personal support and friendly advice over the years. His assistance in the lab and his willingness to frequently discuss important aspects of our work is appreciated. Many thanks go to my friends at Structures Laboratory, Onur Ertaş, Erdal Gökgöz, İbrahim Topçu, Serap Kaya, Tevfik Terzioğlu and Hasan Altun for their personal and professional help. Much of the work described in this report (particularly the experimental investigation) would not have been possible without the able assistance of the lab technicians, Hasan Şenel, Hamdi Ayar, Ümit Melep and Mesut Kardaş. I appreciate my close friends, Mustafa and Başak Piliç, Burak Tekelioğlu, Selin Kekevi, Nilay Kurtuluş and Serkan Sağıroğlu for their patience during my PhD study and for making my life more enjoyable.

I am deeply grateful to my mother Gönül Altay, for her continuous and unconditional encouragement, support and love for all these years during the pursuit of my life.

I would like to express my special gratitude to my lovely wife, Begüm, for her support, patience, faithful companionship and the endless love.

This research has been financially supported by the U.S. National Science Foundation (NSF) through grant OISE-0352947; the Scientific and Technological Research Council of Turkey (TUBITAK) through grant ICTAG-I597-NSF (103I026) and Boğaziçi University Scientific Research Project, under Grant No. 05A401. I would also like to acknowledge the BASF-YKS Construction Chemicals, for providing support in material supply.

ABSTRACT

EXPERIMENTAL INVESTIGATION AND 3D CYCLIC FINITE ELEMENT SIMULATION OF R/C EXTERIOR BEAM-COLUMN JOINTS RETROFITTED WITH CFRP COMPOSITE MATERIALS

The research presented attempts to develop carbon fiber reinforced polymer (CFRP) retrofitting techniques for improving existing reinforced concrete (R/C) beam-column joints designed for gravity loads only including common pre-1970's seismically deficient steel reinforcement details. Full-scale experimental as well as numerical investigations are conducted to achieve the objectives of the research. The experimental study consisted of testing of twelve T-shaped beam-column joints including as-built, CFRP retrofitted and repaired and then CFRP retrofitted under constant column axial load and cyclic lateral loading reversals simulating an earthquake motion. The numerical investigation involved 3-D finite element (FE) simulations of as-built and CFRP retrofitted reinforced concrete beam-column joints under the similar loading and boundary conditions using explicit dynamic software, LS-Dyna. Effects of concrete cracking, shear transfer due to aggregate interlocking, three axial state of stress, complex behavior due to orthotropic property of the CFRP, asymmetric stress-strain relationships for tensile and compressive deformations of concrete and CFRP materials, concrete crushing, and CFRP rapture are included in the FE analyses.

In the experimental study, as-built beam-column joint specimens failed due to excessive shear damage at the joint core and/or slippage of the shortly embedded beam bottom longitudinal reinforcement. Accordingly, three different CFRP retrofitting schemes were developed. The damage at the joint core and the slippage of shortly embedded beam positive reinforcement was substantially controlled due to the developed CFRP retrofitting.

Finite Element (FE) simulation results were verified with the experimental findings. This provided additional understanding on the behavior and also proved that the explicit

FE could be used as a tool for predicting the response of 3-D R/C beam-column joints under cyclic loadings.

ÖZET

CFRP KOMPOZİT MALZEMELER İLE GÜÇLENDİRİLMİŞ BETONARME DIŞ KOLON-KİRİŞ BİRLEŞİMLERİNİN DENEYSEL İNCELEMESİ VE 3 BOYUTLU TEKRARLI SONLU ELEMANLAR SİMÜLASYONU

Bu çalışma, 1970 öncesinde, sadece düşey yüklere göre tasarlanmış ve depreme karşı yetersiz donatı detayına sahip mevcut betonarme kolon-kiriş birleşim bölgelerinin karbon fiber polimer güçlendirme tekniği ile iyileştirmesini amaçlamaktadır. Araştırma hedefine ulaşmak için, tam ölçekli deneysel ve nümerik çalışma yürütülmüştür. Deneysel araştırma, sabit kolon eksenel ve deprem hareketini simüle eden, tekrarlı yatay yüklere maruz kalmış, "T" şeklindeki kolon-kiriş birleşim bölgelerinin, inşaa edildiği haliyle, karbon fiber polimer ile güçlendirilmiş ve tamir edildikten sonra karbon fiber polimer ile güçlendirilmiş halde olmak üzere toplam oniki adet numunenin testini içermektedir. Nümerik çalışma, benzer yük ve sınır şartları altında, inşaa edilmiş haliyle ve karbon fiber polimer ile güçlendirilmiş haliyle oluşturulmuş betonarme kolon-kiriş birleşim bölgelerinin, LS-Dyna açık dinamik yazılım programı kullanılarak yapılmış, üç boyutlu sonlu elemanlar simulasyonlarından oluşmaktadır. Sonlu elemanlar analizleri, betonda çatlama, agrega etkileşimine bağlı kesme kuvveti transferi, üç eksenli gerilme, karbon fiber polimerin ortotropik özellikli kompleks davranışı, beton ve karbon fiber polimerin çekme ve basınç dayanım farklılıkları, beton ezilmesi ve karbon fiber polimerin yırtılması etkilerini dikkate almaktadır.

Deneysel çalışmada, inşa edilmiş halindeki kolon-kiriş birleşim bölgelerinin numuneleri, birleşim bölgesinde kesme kuvvetinden kaynaklanan aşırı hasar ve/veya kiriş alt boyuna donatısının sıyrılması sebebiyle göçmüştür. Buna bağlı olarak üç farklı karbon fiber polimer ile güçlendirme tasarısı geliştirlmiştir. Birleşim bölgesindeki hasar ve kiriş alt boyuna donatısındaki sıyrılma, karbon fiber polimer güçlendirme tasarımları vasıtasıyla önemli ölçüde kontrol altına alınmıştır.

Sonlu elemanlar simülasyonu ile elde edilmiş sonuçlar deneysel bulgularla doğrulanmıştır. Bu simülasyonlar, davranışı daha iyi anlamayı sağlamış ve üç boyutlu betonarme kolon-kiriş birleşimlerinin, tekrarlı yüklere verdiği tepkiyi tahmin etmede, açık sonlu elemanlar metodunun uygun bir araç olduğunu kanıtlamıştır.

TABLE OF CONTENTS

ACKNOWLEDGEMENTS v

ABSTRACT vii

ÖZET ix

LIST OF FIGURES xv

LIST OF TABLES xxvii

LIST OF SYMBOLS / ABBREVIATIONS xxix

1. INTRODUCTION 1

1.1. Problem Statement 1

1.2. Objectives and Scope 3

1.2.1. Objectives 3

1.2.2. Scope & Methodology 3

1.3. Research Significance 4

1.4. Report Outline 4

2. REVIEW OF PREVIOUS RESEARCH 5

2.1. Experimental Background Information 5

2.1.1. Experiments Conducted on as Built Beam-Column Joints 5

2.1.2. Repaired and / or Retrofitted Beam-Column Joints 8

2.1.3. Previous Work on FRP Strengthening of Beam-Column Joints 10

2.2. Existing Studies on Finite Element and Analytical Modeling of R/C Beam-Column Joints 12

3. EXPERIMENTAL INVESTIGATION 14

3.1. Description of the Testing Program 14

3.2. Design and Construction of the Test Specimens 17
3.3. Material Properties 20
3.4. Geometry and Reinforcement Detailing of the Subassemblies 24
3.4.1. US1 Specimens 25
3.4.2. US2 Specimens 26
3.4.3. US3 and US4 Specimens 28
3.5. CFRP Retrofitting and Wrapping Configurations 29
3.5.1. FRP1 Wrapping Configuration 31
3.5.2. FRP2 Wrapping Configuration 34
3.5.3. FRP3 Wrapping Configuration 39
3.6. Repairing Technique 44
3.7. Test Setup and Loading 45
3.8. Instrumentation 49
4. EXPERIMENTAL OBSERVATIONS AND RESULTS 57
4.1. General 57
4.2. Overall Behavior and Load vs. Top Displacement Responses 57
4.2.1. Specimen US1 57
4.2.2. Specimen US2 62
4.2.3. Specimen US3 68
4.2.4. Specimen US4 73
4.2.5. Specimen US1-FRP1 80
4.2.6. Specimen US2-FRP2 85
4.2.7. Specimen US3-FRP3 89
4.2.8. Specimen US4-FRP3 95
4.2.9. Specimen US1-R-FRP1 100

4.2.10. Specimen US2-R-FRP2 102
4.2.11. Specimen US3-R-FRP3 106
4.2.12. Specimen US4-R-FRP3 110
4.3. Shear Deformation of the Joints 115
4.4. Stiffness Degradations of the Subassemblies 119
4.5. Energy Dissipation of the Beam-Column Joints 123
5. FINITE ELEMENT MODELING OF THE BEAM-COLUMN JOINTS 126
5.1. Introduction 126
5.2. Solution Procedures 126
5.3. Concrete Model 127
5.3.1. Ottosen Failure Surface 127
5.3.2. Behavior of the Concrete Model in Tension 130
5.3.3. Concrete in Compression 131
5.3.4. Shear Transfer across Crack Face 132
5.4. Model for the Steel Reinforcement 133
5.4.1. Treatment of the Rebar Slip 135
5.5. FRP Material Model 135
5.6. Mesh Generation 136
5.7. Boundary and Loading Conditions 142
5.8. Run Time of the Simulations 144
5.9. Verification of the Finite Element Models with Experimental Results 145
5.9.1. Specimen US1 145
5.9.2. Specimen US1FRP1 150
5.9.3. Specimens US2 and US3 155
5.9.4. Specimen US2FRP2 157

5.9.5. Specimen US3FRP3 158

5.9.6. Specimen US4..... 159

5.9.7. Specimen US4FRP3 161

6. SUMMARY, CONCLUSIONS AND RECOMMENDATIONS 162

APPENDIX A. MOMENT CURVATURE RELATIONSHIPS..... 166

APPENDIX B. BEAM LONGITUDINAL REINFORCEMENT STRAINS 170

REFERENCES 174

LIST OF FIGURES

Figure 1.1.	Beam-column joint failure	2
Figure 2.1.	Elevation view of an exterior beam-column connection region	8
Figure 3.1.	Sketch of reinforcement detailing	17
Figure 3.2.	Construction of the specimens	19
Figure 3.3.	Use of immerse vibrator	19
Figure 3.4.	Formation of the construction joints	20
Figure 3.5.	Stress-strain relationship for steel	21
Figure 3.6.	Stress-strain relationship for CFRP material	22
Figure 3.7.	Dimensions of the beam-column joint subassemblies	24
Figure 3.8.	Steel reinforcement detailing of US1, US1-FRP1 and US1-R-FRP1	26
Figure 3.9.	Steel reinforcement detailing of US2, US2-FRP2 and US2-R-FRP2	27
Figure 3.10.	Steel reinforcement detailing of US3, US4, US3-FRP, US4-FRP, US3-R-FRP3 and US4-R-FRP3	29
Figure 3.11.	Diagonal CFRP sheet application, step (i)	32
Figure 3.12.	U–shaped CFRP sheet application, step (ii)	33
Figure 3.13.	L–shaped CFRP sheet application, step (iii)	33
Figure 3.14.	Column CFRP wraps, step (iv)	34
Figure 3.15.	Beam CFRP wrap, step (v)	34
Figure 3.16.	Location of the anchorage holes, step (i)	37
Figure 3.17.	CFRP sheets used as a column flexural reinforcement, step (ii)	37
Figure 3.18.	U-shaped CFRP applied to the top portion of the joint, step (iii)	38
Figure 3.19.	U-shaped CFRP applied to the bottom portion of the joint, step (iv)	38

Figure 3.20. Additional column confinement wraps, step (v) 39
Figure 3.21. Application of CFRP strips, step (vi) 39
Figure 3.22. Location of the anchorage holes, step (i) 42
Figure 3.23. CFRP sheets used as a column flexural reinforcement, step (ii) 42
Figure 3.24. Column confinement wraps, step (iii) 43
Figure 3.25. U-shaped CFRP application, step (iv) 43
Figure 3.26. Application of CFRP strips, step (v) 44
Figure 3.27. Repairing procedure 45
Figure 3.28. Free body diagram of the test setup 46
Figure 3.29. General view of the test setup 47
Figure 3.30. Sketch of the test setup 47
Figure 3.31. Lateral loading pattern 49
Figure 3.32. LVDT locations for measurement of top displacement 50
Figure 3.33. LVDT locations for measurement of joint shear deformation 51
Figure 3.34. LVDT locations used as a curvature measurement 53
Figure 3.35. Measurement of slippage 54
Figure 3.36. Typical strain gauge placement for steel reinforcement 55
Figure 3.37. Typical strain gauge placement for CFRP sheet reinforcement 56
Figure 4.1. Lateral load vs. top displacement, specimen US1 58
Figure 4.2. Slip vs. drift relationship of the beam positive reinforcement, US2 63
Figure 4.3. Failure modes; (a) pull, (b) push direction of loading 66
Figure 4.4. Lateral load vs. top displacement, US2 67
Figure 4.5. Crack pattern and internal forces; (a) pull, (b) push loading direction 67
Figure 4.6. Slip vs. drift relationship of the beam positive reinforcement, US3 72
Figure 4.7. Lateral load vs. top displacement, US3 73

Figure 4.8. Slip vs. drift relationship of the beam positive reinforcement, US4 74

Figure 4.9. Crack pattern at the end of test US4 79

Figure 4.10. Lateral load vs. top displacement, US4 79

Figure 4.11. Lateral load vs. top displacement, US1-FRP1 81

Figure 4.12. Drift vs. strain at beam negative reinforcement, US1-FRP1 85

Figure 4.13. Lateral load vs. top displacement, US2-FRP2 86

Figure 4.14. Lateral load vs. top displacement, US3-FRP3 94

Figure 4.15. Damage at the joint region after removal of the CFRP sheets 94

Figure 4.16. Stress distribution due to U-shaped CFRP 99

Figure 4.17. Slippage of the beam positive reinforcement, US4-FRP3 100

Figure 4.18. Lateral load vs. top displacement, US4-FRP3 100

Figure 4.19. Lateral load vs. top displacement, US1-R-FRP1 101

Figure 4.20. Lateral load vs. top displacement, US1-R-FRP1 101

Figure 4.21. Lateral load vs. top displacement, US2-R-FRP2 102

Figure 4.22. Lateral load vs. top displacement, US3-R-FRP3 107

Figure 4.23. Lateral load vs. top displacement, US4-R-FRP3 115

Figure 4.24. Joint panel shear deformation 116

Figure 4.25. Shear deformation vs. load, US1, US1-FRP1 and US1-R-FRP1 117

Figure 4.26. Shear deformation vs. load, US2, US2-FRP2 and US2-R-FRP2 117

Figure 4.27. Shear deformation vs. load, US3, US3-FRP3 and US3-R-FRP3 118

Figure 4.28. Shear deformation vs. load, US4, US4-FRP3 and US4-R-FRP3 118

Figure 4.29. Secant stiffness 120

Figure 4.30. Stiffness degradation, US1, US1-FRP1 and US1-R-FRP1 121

Figure 4.31. Stiffness degradation, US2, US2-FRP2 and US2-R-FRP2 121

Figure 4.32. Stiffness degradation, US3, US2-FRP3 and US3-R-FRP3 122

Figure 4.33. Stiffness degradation, US4, US4-FRP3 and US4-R-FRP3 122
Figure 4.34. Energy dissipation per cycle 123
Figure 4.35. Energy dissipation, US1, US1-FRP1, US1-R-FRP1 124
Figure 4.36. Energy dissipation, US2, US2-FRP2, US2-R-FRP2 124
Figure 4.37. Energy dissipation, US3, US3-FRP3, US3-R-FRP3 125
Figure 4.38. Energy dissipation, US4, US4-FRP3, US4-R-FRP3 125
Figure 5.1. Views of the Ottosen failure surface 129
Figure 5.2. Crack width-tensile stress 130
Figure 5.3. Constitutive model for concrete under compression 131
Figure 5.4. Shear stress modification function 132
Figure 5.5. Stress-strain model for steel under cyclic loading 134
Figure 5.6. Deviatoric section of the yield surface for steel 134
Figure 5.7. Finite element components 136
Figure 5.8. Mesh for concrete and supports 138
Figure 5.9. Steel reinforcement mesh for US1 and US1FRP1 139
Figure 5.10. Steel reinforcement mesh for US2-US4, US2FRP2, US3FRP3 and US4FRP3 139
Figure 5.11. CFRP mesh components for US1FRP1 140
Figure 5.12. CFRP mesh for US1FRP1 140
Figure 5.13. CFRP mesh components for US2FRP2 141
Figure 5.14. CFRP mesh for US2FRP2 141
Figure 5.15. CFRP mesh components for US3FRP3 and US4FRP3 142
Figure 5.16. CFRP mesh for US3FRP3 and US4FRP3 142
Figure 5.17. Boundary conditions 143
Figure 5.18. Applied loading 144

Figure 5.19. Energy vs. time, output from LS-Dyna [72], US1 146
Figure 5.20. Lateral load vs. top displacement comparison, US1 147
Figure 5.21. Shear failure at the joint; (a) push, (b) pull direction of loading..... 147
Figure 5.22. Shear failure at the joint core 148
Figure 5.23. Flexural cracks at the beam; (a) push, (b) pull direction of loading 148
Figure 5.24. Flexural cracks at the beam..... 149
Figure 5.25. Joint shear deformation vs. lateral load..... 150
Figure 5.26. Energy vs. time, output from LS-Dyna [72], US1FRP1 151
Figure 5.27. Lateral load vs. top displacement comparison, US1FRP1 152
Figure 5.28. Plastic hinge at the beam..... 153
Figure 5.29. Maximum principal strain contours showing the plastic hinging at the beam; (a) push, (b) pull direction of loading..... 153
Figure 5.30. Stress at the steel reinforcements showing yielding of the beam longitudinal reinforcements; (a) push, (b) pull direction of loading..... 154
Figure 5.31. Strain readings of beam top longitudinal, US1FRP1 154
Figure 5.32. Joint shear deformation vs. lateral load..... 155
Figure 5.33. Lateral load vs. top displacement comparison, US2 and US3 156
Figure 5.34. Maximum principal strain contours and crack pattern; (a) push, (b) pull direction of loading 156
Figure 5.35. Observed damage at the end of the experiment of US2..... 157
Figure 5.36. Lateral load vs. top displacement comparison, US2FRP..... 158
Figure 5.37. Lateral load vs. top displacement comparison, US3FRP3..... 159
Figure 5.38. Lateral load vs. top displacement comparison, US4..... 160
Figure 5.39. Crack pattern; (a) push, (b) pull direction of loading..... 160
Figure 5.40. Lateral load vs. top displacement comparison, US4FRP3..... 161

Figure A.1. Beam moment curvature for US1 166
Figure A.2. Beam moment curvature for US1FRP1 166
Figure A.3. Beam moment curvature for US1RFRP1 166
Figure A.4. Beam moment curvature for US2 167
Figure A.5. Beam moment curvature for US2FRP2 167
Figure A.6. Beam moment curvature for US2RFRP2 167
Figure A.7. Beam moment curvature for US3 168
Figure A.8. Beam moment curvature for US3FRP3 168
Figure A.9. Beam moment curvature for US3RFRP3 168
Figure A.10. Beam moment curvature for US4 169
Figure A.11. Beam moment curvature for US4FRP3 169
Figure A.12. Beam moment curvature for US4RFRP3 169
Figure B.1. US1 ;(a) bottom (b) top longitudinal reinforcement 170
Figure B.2. US1FRP1 ;(a) bottom (b) top longitudinal reinforcement 170
Figure B.3. US1RFRP1 ;(a) bottom (b) top longitudinal reinforcement 170
Figure B.4. US2 ;(a) bottom (b) top longitudinal reinforcement 171
Figure B.5. US2RFRP2 ;(a) bottom (b) top longitudinal reinforcement 171
Figure B.6. US2RFRP2 ;(a) bottom (b) top longitudinal reinforcement 171
Figure B.7. US3 ;(a) bottom (b) top longitudinal reinforcement 172
Figure B.8. US3RFRP3 ;(a) bottom (b) top longitudinal reinforcement 172
Figure B.9. US3RFRP3 ;(a) bottom (b) top longitudinal reinforcement 172
Figure B.10. US4 ;(a) bottom (b) top longitudinal reinforcement 173
Figure B.11. US4FRP3 ;(a) bottom (b) top longitudinal reinforcement 173
Figure B.12. US4RFRP3 ;(a) bottom (b) top longitudinal reinforcement 173

LIST OF TABLES

Table 3.1. Specimens and test parameters 16

Table 3.2. Flexural capacities of the members 18

Table 3.3. Mechanical properties of CFRP 21

Table 3.4. Mechanical properties of *Concresive 1406* 23

Table 3.7. LVDT locations for measurement of joint shear deformation 51

Table 4.1. Observations on specimen US1 59

Table 4.2. Observations on specimen US1 (continued) 60

Table 4.3. Observations on specimen US1 (continued) 61

Table 4.4. Observations on specimen US1 (continued) 62

Table 4.5. Observations on specimen US2 64

Table 4.6. Observations on specimen US2 (continued) 65

Table 4.7. Observations on specimen US2 (continued) 66

Table 4.8. Observations on specimen US3 69

Table 4.9. Observations on specimen US3 (continued) 70

Table 4.10. Observations on specimen US3 (continued) 71

Table 4.11. Observations on specimen US3 (continued) 72

Table 4.12. Observations on specimen US4 75

Table 4.13. Observations on specimen US4 (continued) 76

Table 4.14. Observations on specimen US4 (continued) 77

Table 4.15. Observations on specimen US4 (continued) 78

Table 4.16. Observations on specimen US1-FRP1 82

Table 4.17. Observations on specimen US1-FRP1 (continued) 83

Table 4.18. Observations on specimen US1-FRP1 (continued) 84

Table 4.19. Observations on specimen US2-FRP2..... 87

Table 4.20. Observations on specimen US2-FRP2 (continued) 88

Table 4.21. Observations on specimen US3-FRP3..... 90

Table 4.22. Observations on specimen US3-FRP3 (continued) 91

Table 4.23. Observations on specimen US3-FRP3 (continued) 92

Table 4.24. Observations on specimen US3-FRP3 (continued) 93

Table 4.25. Observations on specimen US4-FRP3..... 97

Table 4.26. Observations on specimen US4-FRP3 (continued) 98

Table 4.27. Observations on specimen US4-FRP3 (continued) 99

Table 4.28. Observations on specimen US2-R-FRP2..... 103

Table 4.29. Observations on specimen US2-R-FRP2 (continued) 104

Table 4.30. Observations on specimen US2-R-FRP2 (continued) 105

Table 4.31. Observations on specimen US2-R-FRP2 (continued) 106

Table 4.32. Observations on specimen US3-R-FRP3..... 108

Table 4.33. Observations on specimen US3-R-FRP3 (continued) 109

Table 4.34. Observations on specimen US4-R-FRP3..... 111

Table 4.35. Observations on specimen US4-R-FRP3 (continued) 112

Table 4.36. Observations on specimen US4-R-FRP3 (continued) 113

Table 4.37. Observations on specimen US4-R-FRP3 (continued) 114

Table 5.1. Ottosen failure surface parameters 128

LIST OF SYMBOLS / ABBREVIATIONS

a	Aggregate diameter
A, B, K_1, K_2	Ottosen failure surface constants
CR#	Crack number
d_1', d_2'	Diagonal distances of deformed shape of the joint shear panel
EA	Young's modulus of CFRP in longitudinal direction
EB	Young's modulus of CFRP in transverse direction
E_c	Elasticity modulus of steel
E_s	Young's modulus of steel
E_t	Tangent modulus of steel
f_c	Uniaxial compressive strength of concrete
f_t	Uniaxial tensile strength of concrete
F	Force
h	Height of the joint shear panel
H	Lateral load
I_1	First stress invariant
J_2	Second deviatoric stress invariant
K	Secant stiffness
n	Number of response cycles
N	Beam end vertical reaction
P	Axial load
w_c	Column width
XC	Compressive strength of CFRP in longitudinal direction
XT	Tensile strength of CFRP in longitudinal direction
YC	Compressive strength of CFRP in transverse direction
YT	Tensile strength of CFRP in transverse direction
Δ	Column top displacement
Δ/H	Drift ratio

ε	Strain
Ø	Reinforcement diameter
φ	Curvature
γ	Shear deformation
η	Poison ratio
σ_y	Yield stress
$\sigma_1, \sigma_2, \sigma_3$	Principal stresses
θ	Lode angle

ACI	American Concrete Institute
ASTM	American society for testing and materials
CDE	Cumulative dissipated energy
CFRP	Carbon fiber reinforced polymer
R/C	Reinforced concrete
FE	Finite element
FRP	Fiber reinforced polymer
GFRP	Glass fiber reinforced polymer
LVDT	Linear variable differential transformer
SSC	Shear stress reduction coefficient
3 - D	Three dimensional

1. INTRODUCTION

1.1. Problem Statement

There are many existing reinforced concrete (R/C) buildings in urban areas that are built according to the pre-70s codes, which consider only the gravity loads or without considering lateral loads such as earthquake or wind loads. This type of structures suffered from earthquakes with severe damage or total collapse as shown in Figure 1.1. Under seismic actions one of the most critical structural subassemblage, which transfer the forces from the beams to the columns or vice versa, is the beam-column joint. In order to have a continuous force transfer between beams and columns, the connection region must have sufficient shear strength. Joints designed for gravity loads only do not posses that strength [1-4].

Post earthquakes and related studies have revealed the importance of beam-column joints and the need for retrofitting the existing beam to column connections emerged. Methods for improvement of joints such as steel jacketing, reinforced concrete jacketing, or epoxy injection have been investigated by many researchers and their positive effects were emphasized [1-2, 5-7].

One of the upgrade methods studied in recent decades is the application of Fiber-Reinforced Polymer (FRP) materials. These materials have many advantages compared to the conventional steel or reinforced concrete jacketing. These favorable characteristics are resistance to corrosion, high strength, ease of application, being very light, which are desired property for seismic actions due to inertia forces produced by the mass of the structure. Today, FRP materials are available in the form of bars, strips and sheets. In this research it is intended to examine the application of FRP sheets only.

Although there are limited recommendations on FRP design and applications in the literature [1], there is need of an explicit design and application guideline of FRP's which is the primary motivation of this research.



Izmit, Turkey earthquake, Aug. 17, 1999. Photo by Sezen, Halil



Chi-Chi, Taiwan earthquake, Sept. 21, 1999. Photo by Mahin, Stephen A.



Caracas, Venezuela earthquake, July 29, 1967. Photo by Steinbrugge, Karl V.



Izmit, Turkey earthquake, Aug. 17, 1999. Photo by Whittaker, Andrew S.



Izmit, Turkey earthquake, Aug. 17, 1999. Photo by Sezen, Halil



Izmit, Turkey earthquake, Aug. 17, 1999. Photo by Sezen, Halil

Figure 1.1. Beam-column joint failure

1.2. Objectives and Scope

1.2.1. Objectives

The objectives of this research are: (1) to identify the effects of reinforcement detailing deficiencies and different CFRP orientations on exterior beam-column joint behavior; (2) to develop a CFRP retrofitting strategy for an existing beam-column joints with certain deficiencies trough full-scale experimental investigation; (3) to construct a 3-D nonlinear finite element, FE, model that can simulate the structural behavior under cyclic loading of as-built and CFRP retrofitted beam column joints; (4) to verify that explicit FE analysis could be used as a design tool of R/C and CFRP retrofitted R/C beam column joints.

1.2.2. Scope & Methodology

Identification of seismically critical joints is the first step of this research. Subsequently, an experimental program is conducted on full scale 3-D T-shaped test specimens, which represent an exterior R/C beam-column joint of a structure, deficiently designed to resist the seismic actions. The effects of slab and transverse beams are not included in the experimental program. Furthermore, an experimental study on CFRP retrofitted and both repaired and CFRP retrofitted specimens are conducted. From the results of the experiments, adequate information to understand the behavior of as-built and CFRP retrofitted beam to column joints is obtained. These results then provide guidance for the implementation of nonlinear finite element modeling of the tested specimens, which is the next step of this study. A nonlinear quasi-static analysis is performed on the finite element models, which include the effects of bar slippage and crack propagation scheme. Each experimentally tested specimen is modeled with an advanced nonlinear explicit dynamic finite element program, LS-Dyna. Then, the finite element results are verified with the test results obtained from the experiments.

1.3. Research Significance

Current seismic design codes and guidelines provide partial or some general procedures for designing or upgrading for shear of reinforced concrete members with externally bonded FRP systems. These guidelines are more related to beams and columns but not specifically for beam-to-column joints. Even in the recent literature survey there is very limited range of applicability and lack of knowledge on the design and retrofit procedures for shear resistance of reinforced concrete beam-to-column connections with externally bonded FRP [1, 8]. The current research presents full-scale experimental and finite element analysis investigation on the behavior of as-built and CFRP retrofitted external beam-column joints under constant axial and cyclic lateral loads and it attempts to provide further understanding for the design approach for shear strengthening of an exterior reinforced concrete beam-column joint with externally bonded CFRP materials. The presented FE analyses, which include the effects of concrete cracking, tri-axial state of stress and CFRP rupture, are unique in terms of simulation the cyclic behavior of a 3-D R/C and CFRP retrofitted R/C beam column joints.

1.4. Report Outline

This report presents full-experimental investigation and nonlinear finite element modeling of R/C exterior beam-column joints retrofitted with externally bonded CFRP sheets. Chapter 1 provides the introductory material and research significance. Chapter 2 summarizes previous research conducted on beam-column joints. A detailed description on the current experimental study is presented in Chapter 3. Chapter 4 contains complete information of the test results and observations. Nonlinear finite element modeling of R/C and CFRP retrofitted R/C beam-column joints is described in Chapter 5. Calibration of the numerical models and verification of the results are also provided in the same chapter. Finally, Chapter 6 summarizes the research program and presents the conclusions and recommendations for future investigations.

All figures and tables are included within the text and a complete listing of the cited studies is presented at the end of the report.

2. REVIEW OF PREVIOUS RESEARCH

In this chapter, firstly, literature review on experimental and numerical (finite element modeling) studies conducted on R/C beam-column joints is provided and then seismically critical joint details used in pre-1970's are revealed.

2.1. Experimental Background Information

Previous experimental researches on R/C beam-column joints are classified into three main groups: (1) Experiments performed only to understand the behavior of as-built beam to column joints; (2) Studies conducted on retrofitting and repair strategies applied to beam-column connections; (3) Experiments conducted on beam-column joints with externally bonded FRP materials.

2.1.1. Experiments Conducted on as Built Beam-Column Joints

The first beam-column joint studies, which were performed by Hanson and Conner [9, 10] in 1967, demonstrated that the behavior of joints is governed by shear. Also, it was pointed out that the transverse reinforcement within the joint plays a significant role in shear resistance of the joint. These initial experiments conducted by Hanson and Conner constructed a base to the joint design recommendations of the 1971 ACI code [11].

One of the most comprehensive descriptions of the behavior of reinforced concrete beam-column joints was presented by Park and Paulay [3] and three years after by Paulay, Park, and Priestley [12]. The investigations were based on experiments, which were carried out at the University of Canterbury in New Zealand. The results of the tests provide a broad explanation on the force transfer within the joint, including the two now well known compression and truss mechanism.

Ehsani and Wight conducted tests to investigate the effects of several parameters on the behavior of exterior R/C joints. The primary variables were the ratio of the column-to-beam flexural capacity, the joint shear stress, and the transverse reinforcement

in the joint. They concluded that to avoid formation of plastic hinges the flexural strength ratio of the column to beam should not be less than 1.4, and the shear stress should be limited to $\sqrt{f_c'}$ [13].

Popov, Bertero and Viwathanatepa investigated the influence of cyclic loading pattern on the interior joint behavior by applying two different loadings. The results showed that the maximum strength of the subassemblages was affected very little by the loading sequence. Larger displacement ductility, while maintaining the high lateral load, was observed for the monotonically loaded specimen than for the one loaded cyclically. Another important issue that they pointed out was the severe degrading of the hysteretic loops was caused by the damage in the joint which was principally by the loss of bond and pull out action of the lower longitudinal reinforcement [14].

Üzümeri and Seçkin conducted experimental study of the behavior of cast-in-place reinforced concrete beam-column joints subjected to slow load reversals simulating seismic loading. Their investigation exhibited the indispensable role of the stirrups to provide confinement and shear resistance to the joint and to increase the ability of the connection to provide continued anchorage to beam reinforcement. They recommended that the primary aim of the designer should be to prevent the yielding of the joint steel, since the ductility in the joint must be avoided. As suggested by Üzümeri and Seçkin, this could be achieved by not using steel with stress-strain characteristics that exhibit a flat yield plateau as joint confinement reinforcement [15].

Another experimental study on the factors influencing the shear strength of beam-column joints was conducted by Meinheit and Jirsa and Jirsa et al. Main parameters were the longitudinal column reinforcement ratio, column axial load and depth of the column. The purpose of this investigation was to examine experimentally the significance of above mentioned parameters and as a result of their study mainly the following conclusions were derived: (1) column axial load appeared to influence the shear at which the first crack occurred but had little influence on the ultimate shear strength of the joint; (2) percentage of the column longitudinal reinforcement and column orientation did not substantially influence the strength of the joint [16-17].

A comprehensive experimental research on both interior and exterior beam-column joints, designed primarily for gravity induced loads, was conducted at Cornell University. In this research attention was focused on beam-column connections that are typically the weakest link in the lateral load resistance. The experimental program consisted of tests on full scale beam-column joint region specimens and on small scale model buildings, with details reflecting the distinctive features of the past design and construction practice. Results of this experimental program were used to improve the inelastic dynamic analysis software, IDARC, and to provide a background for devising repair and retrofit strategies [4, 7, 18-21]. Through their reviews of detailing manuals and design codes from the past five decades and their consultation with practicing engineers, Beres et al. identified seven details, shown in Figure 2.1, as typical and potentially critical to the safety of the gravity load designed structures in an earthquake [22]. These seismically critical details are;

- Longitudinal reinforcement in the columns not exceeding 2%.
- Lapped splices of column reinforcement at the maximum moment region just above the construction joint at the floor level.
- Widely spaced column ties that provide little confinement to the concrete.
- Little or no transverse reinforcement within the joint region.
- Discontinuous positive beam reinforcement with a short embedment length into the column.
- Construction joints below and above the beam-column joint.
- Columns having bending moment capacity less than those of the beams.

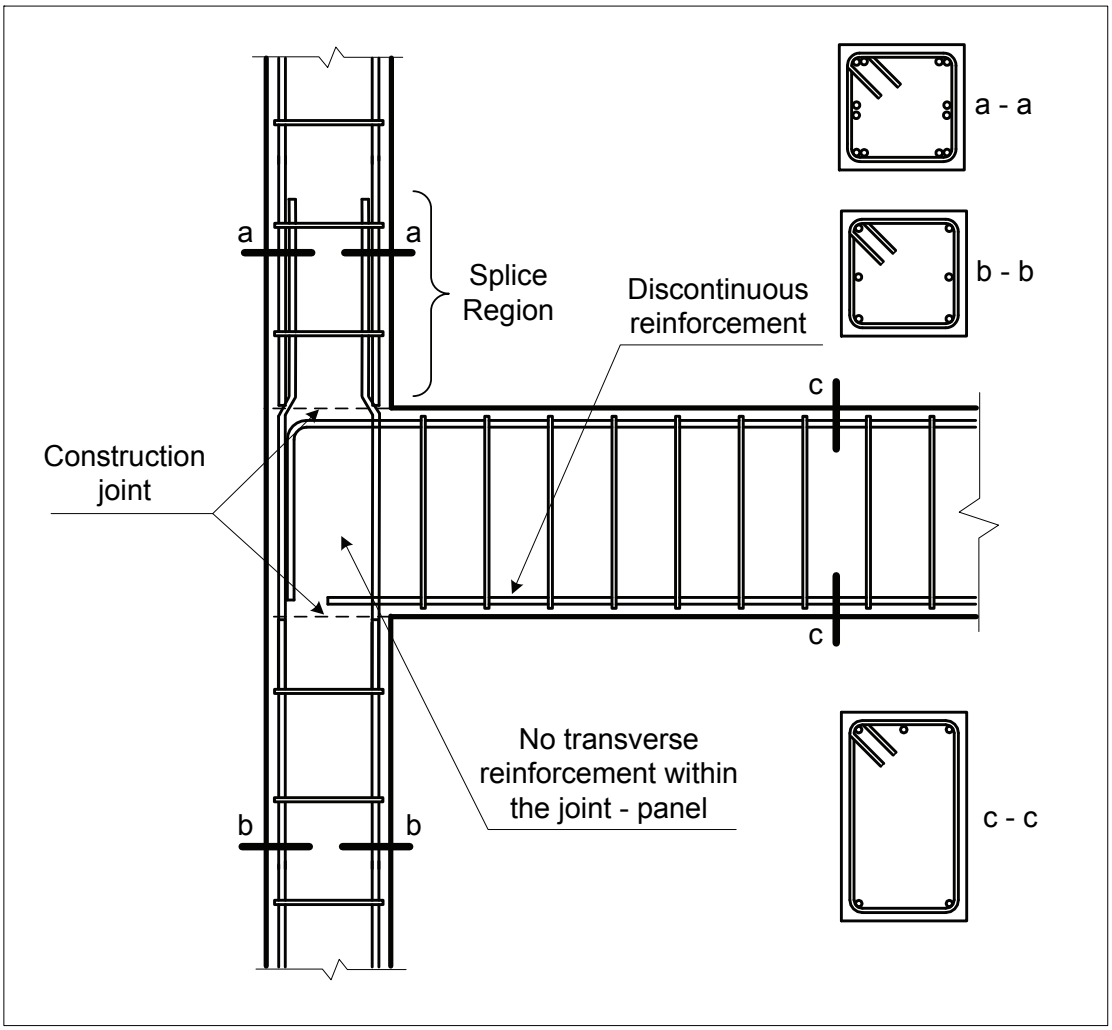


Figure 2.1. Elevation view of an exterior beam-column connection region [22]

2.1.2. Repaired and / or Retrofitted Beam-Column Joints

One of the first investigations on the repair and retest of R/C exterior beam-column subassemblages is presented by Lee, Wight and Hanson. The specimens were designed according to the 1971 ACI code [11] for both seismic and non-seismic areas and then were subjected to moderate or severe lateral loading to obtain different degrees of damage. Epoxy injection and different removal and replacement techniques were used to repair specimens and it was concluded that epoxy injection, and removal and replacement methods can restore structural integrity [23].

Adin, Yankelevsky, and Farhey conducted experiments on four reinforced concrete beam-column joints which were first damaged to a certain level and subsequently were

epoxy injected and steel jacketed and eventually were retested. Comparison between before and after repair indicated considerable increase in initial stiffness, yield resistance, envelope stiffness, and ultimate resistance with energy-dissipation capacity. The repair technique was found to be efficient for mass repair or upgrading of structures not suitably designed to withstand seismic actions [24].

Another experimental program on the implementation to assess the effectiveness of jacketing of R/C frame connections was conducted by Alcocer and Jirsa. The specimens were interior joints and constructed with the inclusion of slab and the transverse beams. Four large-scale beam-column connections were rehabilitated and then tested under bidirectional cyclic loading and it was aimed at studying the shear strength performance of jacketed joints. Results showed that the shear strength of jacketed joints can be estimated using current recommendations for design of beam-column joints in new construction. Test results also indicated that the criterion on bar development of current recommendations should be fulfilled by longitudinal reinforcement in the jacket [25-28]. However, in this study it was also accepted by the author that beam jacketing required large and heavy forms as well as artful detailing during construction that might be uneconomical for practice.

Ghobarah, Aziz and Biddah performed experimental study on reinforced concrete beam-column frame connections which were jacketed with corrugated steel plates. The investigated test parameters include the amount of joint and column transverse reinforcement, corrugated steel sheet thickness, and jacketing of column only or both column and beam. It is stated by the authors that the corrugated steel jacket is an effective system of upgrading and a method for the design of the steel thickness and depth of corrugation is formulated [29-30].

Experimental studies were conducted to two exterior reinforced concrete subassemblages subjected to severe earthquake loading. The specimens first were damaged and then were repaired according to the United Nations Industrial Development Organization Manual guidelines. Repair and strengthened specimens exhibited higher strength, greater stiffness, and better energy dissipation capacity than the original specimens [32].

Beres, El-Borgi, White and Gergely performed an experimental investigation on the repair and retrofit of both interior and exterior, existing R/C beam-column joints. One of the major problem of the existing pre 1970's designed connection is the short development length of the positive beam reinforcement. This short development length is inadequate to provide anchorage to the bottom beam reinforcement and this positive beam reinforcement pulls out when the structure is subjected to lateral loading. Low cost retrofit method (a different application of steel plates) was used to eliminate the pullout effect which is the critical mechanism controlling joint region capacity. Pullout was stopped when an interior joint is in concern but for the exterior joints it was not able to stop that action. But in overall, both interior and exterior joint retrofitting strategies had some positive effects on the behavior [7].

2.1.3. Previous Work on FRP Strengthening of Beam-Column Joints

Externally bonded FRP strengthening is an alternative strategy to steel and reinforced concrete jacketing. It has many attractive advantages when compared to the previous conventional retrofitting methods. Main advantages are ease of application, very high strength, non-corrosive characteristic and light weighted property.

One of the most important features of the material is being light weight. This is an important property, since the lateral load caused by an earthquake is proportional to the weight of the structure. In recent researches, these features make FRP as one of the favorable material to be studied for seismic strengthening of structures. However investigations on retrofitting of beam-column joints with externally bonded FRP is still in the early stages and the knowledge of its behavior is very limited. Below is a brief summary of the previous works on FRP applications on beam-column joints.

The application of carbon fiber composite jackets for the three columns and cap beam of an existing concrete bridge bent was performed in 1996 by Gergely, Pantelides, Nuismer, and Reaveley. The objectives of this study were to restore the use of the bridge pier to as close as possible to its original condition by enhancing the shear capacity of the columns, cap beam and cap beam-column joints and to improve the performance of the

bridge pier when subjected to a severe earthquake. It was found that the ductility of the pier and the shear capacity of the cap beam and columns were increased [33]. Another two applications of FRP and then verification of rehabilitation were conducted by the same authors on an existing bridge bents and 1/3-scale beam-column joints. The results were favorable exhibiting ductility and lateral load increase [8, 34]. Recently, a new experimental study on the two column bents retrofitted with FRP was presented by Pulid, Saiidi, Sanderas, Itani and El-Azazy. The beam-column joints were retrofitted for shear with FRP fabrics in the horizontal and vertical direction in the joint region. FRP fabrics enhance the joint shear capacity and allowed easy installation. [35]

Ghobarah and Said conducted an experimental research of exterior reinforced concrete beam-column joints with strong beam and weak columns connected to it to upgrade joint's seismic performance by applying glass fiber reinforced polymer (GFRP). Each specimen had the same reinforcement detailing and member dimensions. Two of them were control specimens and two of them were rehabilitated with different FRP orientation. The tested control specimens were repaired and retested. The results of the experimental program indicated that some of the proposed rehabilitation techniques for beam-column joints delayed the shear mode of failure and some were unsuccessful to eliminate shear failure in the joint. [2]

Another experimental program on Glass Fiber Reinforced Polymers (GFRP) strengthened beam-column joints was performed by El-Amoury and Ghobarah. A total of three specimens were built in accordance to pre-1970's codes. One of the main problems, which is the short extension of the bottom beam reinforcement within the joint was attempted to be solved by applying L-shaped FRP on the bottom face of the beam and anchoring it to the column with steel angles and bolts. These experiments were unsuccessful in representing the existing structures designed in pre-1970's, since the average of the concrete compressive strength was 37.9 MPa. Also the control specimen had a lower compressive strength of 23%-30% when compared to the other two rehabilitated specimens. Still these experiments show the positive effect of FRP in delaying the failure. [1]

Another positive effect of FRP, which is externally bonded on beam-column joint, is seen from the study of Granata and Parvin. Six scaled down exterior beam-column connections were tested to specifically evaluate the moment capacity of a joint wrapped with Kevlar FRP fabrics. The results showed 60% increase in the moment capacity of the beam-column connections [36].

A comprehensive experimental and analytical research on beam-column joints was conducted by Antonopoulos and Triantafillou. A total of 18, 2/3-scaled, reinforced concrete joints were tested with different orientation of FRP. The tests performed in this study demonstrated that externally bonded FRP reinforcement is a viable solution towards enhancing the strength, energy dissipation, and stiffness characteristics of poorly detailed (in shear) R/C joints subjected to simulated seismic loads. Relatively low FRP area fractions increased both the strength (peak lateral load capacity) and the cumulative dissipated energy up to about 70-80%. The increase in stiffness varied with the imposed displacement level and reached values in the order of 100% [39-40].

The combination of externally bonded FRP laminates and near surface mounted FRP bars was experimentally validated for the seismic upgrade of 11 under-designed beam-column connections by Prota, Nanni, Manfredi, and Cosenza. The experiments pointed out with a certain amount and location of FRP, axial load and material properties can play an important role on the performance of retrofitted joints. Also it was stated that the effects of axial load and concrete strength could represent a crucial step towards upgrade of an existing structure [41].

2.2. Existing Studies on Finite Element and Analytical Modeling of R/C Beam-Column Joints

It is a challenging task to model a 3-D reinforced concrete member when both material and geometric nonlinearity is to be considered. It becomes more complex, especially when the member is subjected to different loadings at the same time; the materials have a softening property, and cracking and bond problems are to be included in the model.

The finite element technique has the potential to play an increasingly important role in all areas of reinforced concrete research, design and analysis. Despite the power of the technique, its applicability to general reinforced concrete structures is limited to some extend by the inadequacy of available cracking and constitutive models. Because of this reason some constitutive and cracking models were developed to be used in finite element procedures [42-49].

Based on experimental and analytical results, many attempts were conducted on modeling of reinforced concrete members [42-50]. However, there are limited attempts on nonlinear finite element modeling of R/C beam-column joints [51-54] and very few modeling attempts on FRP strengthened joints were performed [53-54]. None of the existing FE studies of R/C structures retrofitted with CFRP incorporate the three axial state of stress, the cracking of the concrete medium and shear transfer due to aggregate interlocking phenomena under cyclic loading. Many of the studies are limited on 2-D analyses and few of them are analyzing 3-D reinforced concrete beam column joint members [55-57].

3. EXPERIMENTAL INVESTIGATION

3.1. Description of the Testing Program

The experimental study aims to investigate the effect of seismically critical details of reinforced concrete exterior beam-column joints as mentioned in Section 2.1.1. The applicability and effectiveness of the herein developed carbon fiber reinforced polymers (CFRP) strengthening techniques on beam column joints was also studied. The behavior of the test specimens were investigated by measuring the member deformations, strains on the reinforcing steel and CFRP sheets and by observations of the cracking patterns on the beam column subassemblages.

Totally 12 full scale tests on the beam column joint specimens were conducted. The experimental investigation was divided into three main testing groups; testing of as-built specimens (4 tests), testing of undamaged and CFRP retrofitted specimens (4 tests), and testing of damaged and CFRP retrofitted specimens (4 tests). The first group of tests was conducted to investigate the behavior of as-built exterior beam column joints. The experimental results of the first group were used as control data for the second and third group of specimens. The specimens of the second group were designed identically to those in the first group and then were retrofitted with CFRP sheets. The objective of the second group of tests was to investigate the effectiveness and applicability of CFRP retrofitting. At the end of the first group of tests, the damaged control specimens were repaired and then CFRP retrofitted. These firstly damaged and then repaired and CFRP retrofitted specimens constitute the last group of tests. The goal of the last group of tests was to examine the scenario of what if a damaged beam column joint is repaired and retrofitted.

Discontinuous beam longitudinal reinforcement, column lap splicing region just above the joint, inadequate or no shear reinforcement in the joint shear panel, construction joints just above or below the joint and widely spaced shear reinforcements in the beams and columns were identified as seismically critical details in the testing program. The first two details were taken as testing parameters in the experimental investigation. The other details were built-in all specimens to reflect the actual application in pre-1970's.

Magnitude of column axial load was another parameter that was studied. Table 3.1 summarizes the specimens' parameters and Figure 3.1 illustrates sketches of the reinforcement detailing.

Three different CFRP wrapping configurations were developed and applied to the specimens of the last two groups. Failures modes of the control specimens provided guidance to the orientations of the CFRP sheets applied to the retrofitted beam column joints. In general, orientations of the CFRP sheets were applied perpendicularly to the observed cracking pattern of the control specimens.

In this study, specimen name designation was made such that "US#" indicates the type of steel reinforcement detailing, "FRP#" designates the CFRP wrapping configuration type and "R" denotes that the specimen is repaired. For instance, US4-R-FRP3 can be identified as; it is a beam column joint designed with the reinforcement detailing US4, which is provided in Section 3.4; the specimen is repaired as described in Section 3.6; and the specimen is retrofitted with FRP3 wrapping configuration which is described in Section 3.5.

Table 3.1. Specimens and test parameters

Test Group	Test #	Specimen Name	Lap Splicing Length (mm)	Short Embedment Length (mm)	Column Axial Load (kN)	CFRP Wrapping Configuratio
Control Specimens	1	US1	—	—	700	—
	2	US2	500	—	700	—
	3	US3	500	150	700	—
	4	US4	500	150	350	—
FRP Retrofitted Specimens	5	US1FRP1	—	—	700	FRP1
	6	US2FRP2	500	—	700	FRP2
	7	US3FRP3	500	150	700	FRP3
	8	US4FRP3	500	150	350	FRP3
Repaired and FRP Retrofitted Specimens	9	US1RFRP1	—	—	700	FRP1
	10	US2RFRP2	500	—	700	FRP2
	11	US3RFRP3	500	150	700	FRP3
	12	US4RFRP3	500	150	350	FRP3

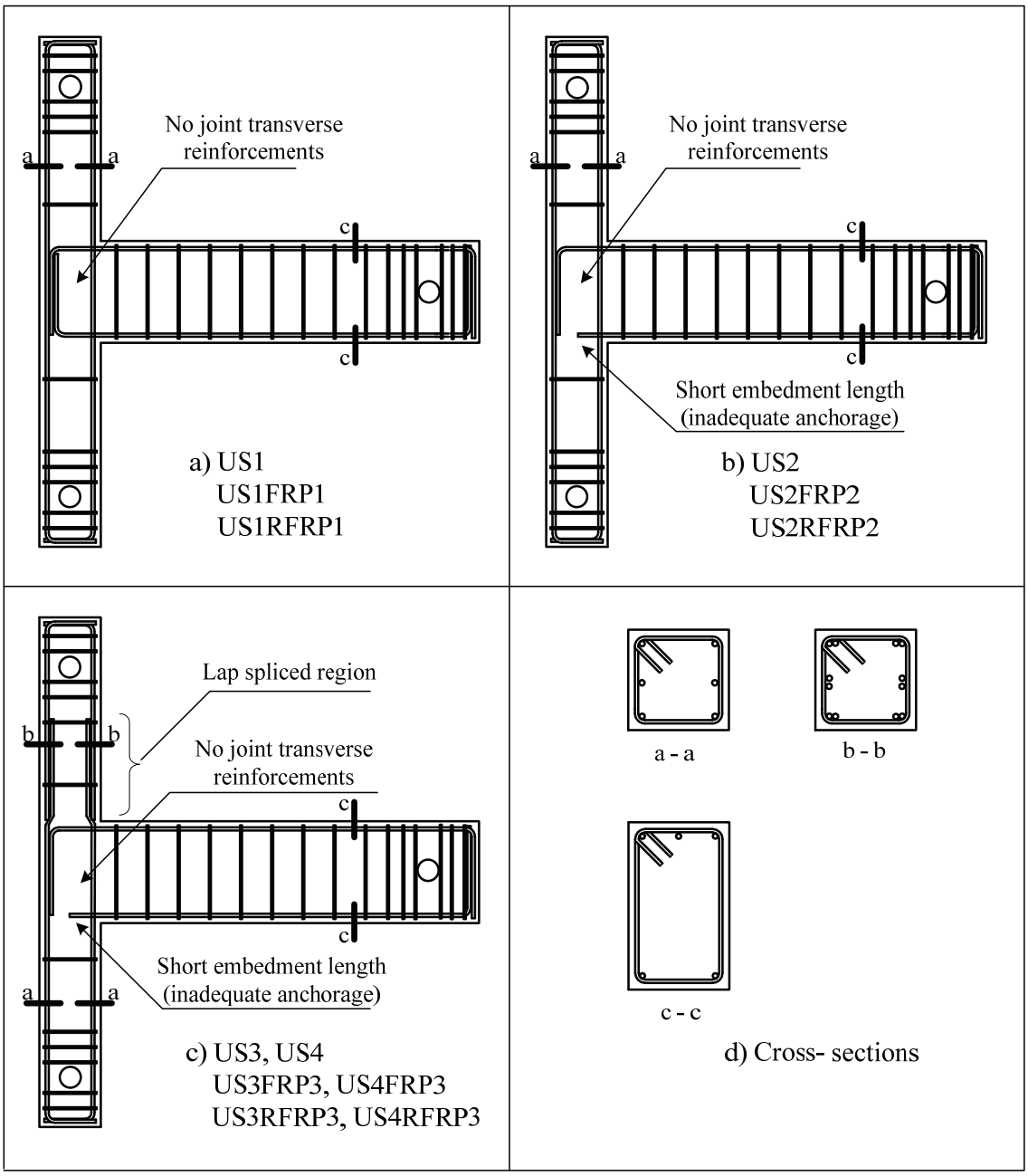


Figure 3.1. Sketch of reinforcement detailing

3.2. Design and Construction of the Test Specimens

The test specimens can be considered as beam to column joints of a multi-story structure with certain detailing deficiencies to resist seismic actions. These beam-column joint subassemblies were designed according to the pre 1970's codes for gravity loading only and can be considered as exterior joints of a building with a regular load carrying frame.

To be consistent, all specimens were produced with exactly the same dimensions. Column dimensions were 300 x 300 mm and beam dimensions were 300 x 500 mm. Each specimen had a column reinforcement ratio of 0.01 while top and bottom reinforcements are considered separately. Beam reinforcement ratio was 0.006 and 0.004 for the top and bottom of the cross-section, respectively. Widely spaced transverse reinforcement was used for the columns and the beam. Transverse reinforcement for the top and bottom columns was symmetrical with respect to the longitudinal axis of the beam. An extra reinforcement was used at the support regions of the columns and the beam to prevent any undesirable local support failure. Table 3.2 provides flexural capacities of the columns and the beam of the test specimens. Ultimate moments were calculated through a sectional analysis considering an unconfined concrete behavior. For US4 set of specimens, flexural ratio of the columns to the beam is approximately 1.10 and for the rest of the specimens this is value is approximately 1.30.

Table 3.2. Flexural capacities of the members

Member	f_c' (MPa)	f_y (MPa)	Section Width / Height (mm)	Reinforcement top / bottom	Axial Load (kN)	Ultimate Moment (kNm)
Beam	24	450	300 / 500	3Ø20 / 2Ø20	0	220*
					0	155**
Column	26		300 / 300	3Ø20 / 3Ø20	700	145
					350	125

* top reinforcement in tension

** bottom reinforcement in tension

The beam column joint specimens were produced at the construction side in a horizontal position as shown in Figure 3.2. Reinforcement and formworks were prepared by actual construction workers. First, formworks were erected and then reinforcing cages were placed inside the formworks. Strain gauges were mounted on desired locations of the reinforcing steel. In order to keep away water contact, strain gauges were coated with silicon and wrapped with tape. After that, ready mix concrete was ordered from a local concrete plant. The concrete was cast such that the subassemblies were in a horizontal position. During the casting, concrete samples were taken in 150 x 300 mm cylinder

formworks. As illustrated in Figure 3.3, immerse vibrator was used to prevent air voids inside the concrete. In order to represent an actual construction application, concrete was poured in two different days such that construction joints form between the columns and the beam as shown in Figure 3.4. Since the specimens were under the sun-exposed area, all specimens were covered with burlap and were cured with water spraying. After a week all formworks were removed.



Figure 3.2. Construction of the specimens



Figure 3.3. Use of immerse vibrator

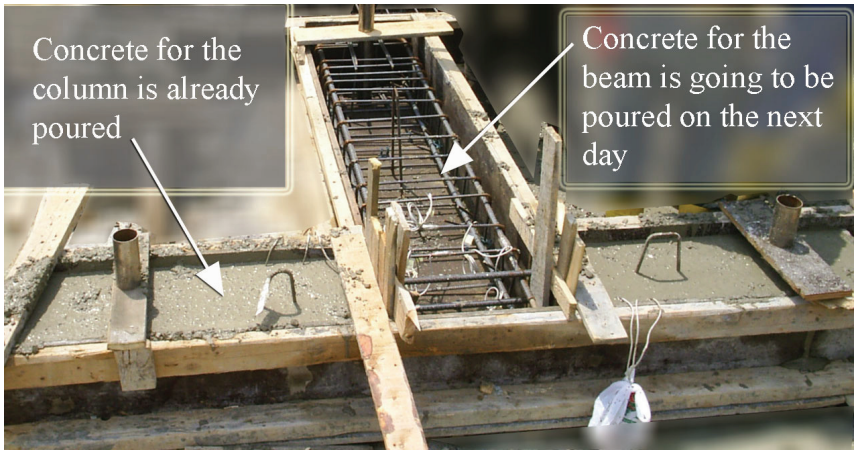


Figure 3.4. Formation of the construction joints

3.3. Material Properties

It was intended to use conventional materials with properties that reflect material properties used in the structures designed and constructed in pre-1970 [4, 9, 13]. Below, the properties of conventional materials (concrete and steel) as well as materials used for retrofitting and repair (CFRP, epoxy based repair material, etc.) are provided.

Concrete: The concrete was ordered from a ready mix concrete company. Construction joint above and below the beam column joint was one criteria to be studied, so pouring of concrete was done in two parts. First, columns were poured and a day after concrete for the beam was poured to complete the specimen. 21 samples of cylinders are taken for columns and beams. Each test day 2-3 cylinder specimens were tested under compression up to failure, according to ASTM C39 standard. Average concrete compressive strength of 24 MPa for the beams and joints, and 26 MPa for the columns were obtained.

Steel: Deformed bars were used as longitudinal and transversal reinforcement for both columns and beams. Steel reinforcements were tested under uniaxial tension until rupture. The stress-strain relationship for longitudinal reinforcement is given in Figure 3.5. The average yield strength of the mild steel used as longitudinal reinforcement was 450 MPa and ultimate tensile strength was 730 MPa. Steel used as transverse reinforcement had average yield strength of 500 MPa and ultimate tensile strength of 559 MPa.

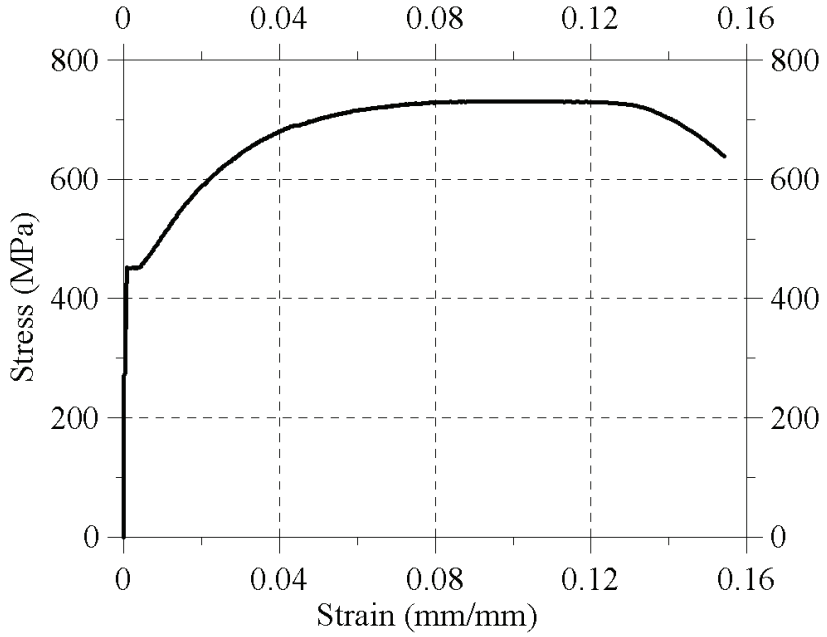


Figure 3.5. Stress-strain relationship for steel

All material properties used as an external reinforcement were provided by BASF Construction Chemicals [58].

CFRP: Unidirectional carbon fiber reinforced polymer sheet, *MBrace Fiber C1-30* produced by BASF, was used as an externally bonded reinforcement for retrofitting of the beam column joints. Mechanical material properties, provided by the manufacturer, are given in Table 3.3 and Figure 3.6. It has very limited compressive strength such that it should be ignored in the design of CFRP retrofitting.

Table 3.3. Mechanical properties of CFRP

Nominal Thickness mm / ply	Ultimate Tensile Strength (0°) (MPa)	Elasticity Modulus (0°) (GPa)	Ultimate Rupture Strain (0°) (mm/mm)
0.176	3800	240	0.0155

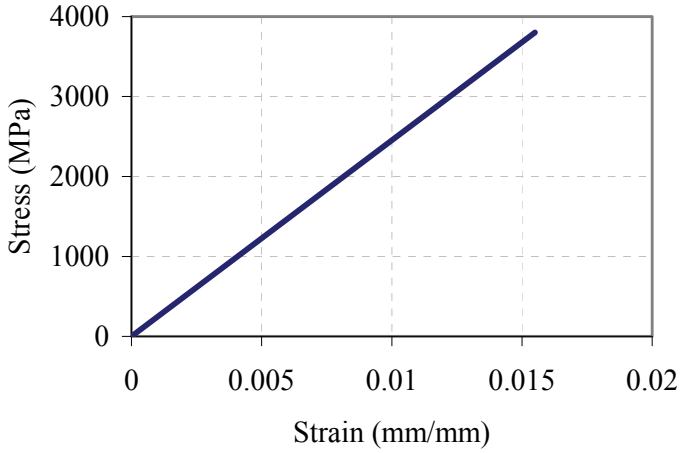


Figure 3.6. Stress-strain relationship for CFRP material

MBT MBrace Pimer: It is a two component, epoxy based material which is produced by BASF Construction Chemicals. Due to its low viscosity feature it can easily penetrate inside the concrete media and thus increase the bond strength between epoxy, CFRP sheets and the concrete.

MBT MBrace Adesivo Saturant: It is a two component; high strength epoxy based material. It is specially developed adhesive for carbon and glass fibers polymer sheets in retrofitting of reinforced concrete structures. According to the manufacturer's data sheet, its bond strength on concrete surface is higher than 3 MPa. Its 7 day compressive and tensile strengths are 60 and 50 MPa, respectively.

Concresive 1495: This type of epoxy based repairing material, produced by BASF, is used for repairing and filling the wide cracks at the damaged region. Compared to the concrete its bond strength is very high.

Concresive 1406: Another type of epoxy based repairing material produced by BASF is used for replacing all loose concrete around the joint region. Before the injection process, joint core is covered with *Concresive 1406*. Mechanical properties of *Concresive 1406* are given in Table 3.4.

Table 3.4. Mechanical properties of *Concresive 1406*

Application Thickness mm	Bending strength 7 days (MPa)	Compressive Strength 7 days (MPa)	Bond Strength Concrete (MPa)	Bond Strength Steel (MPa)
2 – 30	25	75	3.0	3.5

Emaco S88C: Cement based repairing material produced by BASF is used for preparing the surface before the application of injection. Mechanical properties of *Emaco S88C* are given in Table 3.5.

Table 3.5. Mechanical properties of Emaco S88C

Application Thickness (mm)	Tensile Strength (20°) 28 days (MPa)	Compressive Strength (20°) (MPa)	Bond Strength Steel smooth bar (MPa)	Bond Strength Steel ribbed bar (MPa)	Bond Strength Concrete (MPa)	Modulus of Elasticity (0°) (GPa)
min. 10	3.6	70 MPa	14	30	6.5	>28

Concresive 1302: This material is used for repairing up to 1 mm width cracks by injecting into openings. Due to its low viscosity, it can penetrate in to hairline cracks with low pressure. Table 3.6 shows the mechanical properties of *Concresive 1302* produced by BASF.

Table 3.6. Mechanical properties of Concresive 1302

Viscosity (MPa.s)	Tensile Strength 7 days (MPa)	Compressive Strength (20°) 7 days (MPa)	Bond Strength to Steel and Concrete (MPa)	Application Thickness (mm)	Modulus of Elasticity (0°) (GPa)
100 – 350	45	110	3.5 MPa	0.2 – 1.0	3.1 – 3.3

3.4. Geometry and Reinforcement Detailing of the Subassemblies

The geometry of the beam-column joint subassemblies was chosen such that it could be seen in a regular reinforced concrete structure constructed in pre-1970's. The specimens consist of three members; two columns and a beam. Overall dimensions of all specimens are shown in Figure 3.7. It is assumed that under lateral loading applied to a structure, midpoints of the longitudinal axis of the members would act as a point of contra-flexure. Therefore only half lengths of actual members were considered in the design of the test specimens.

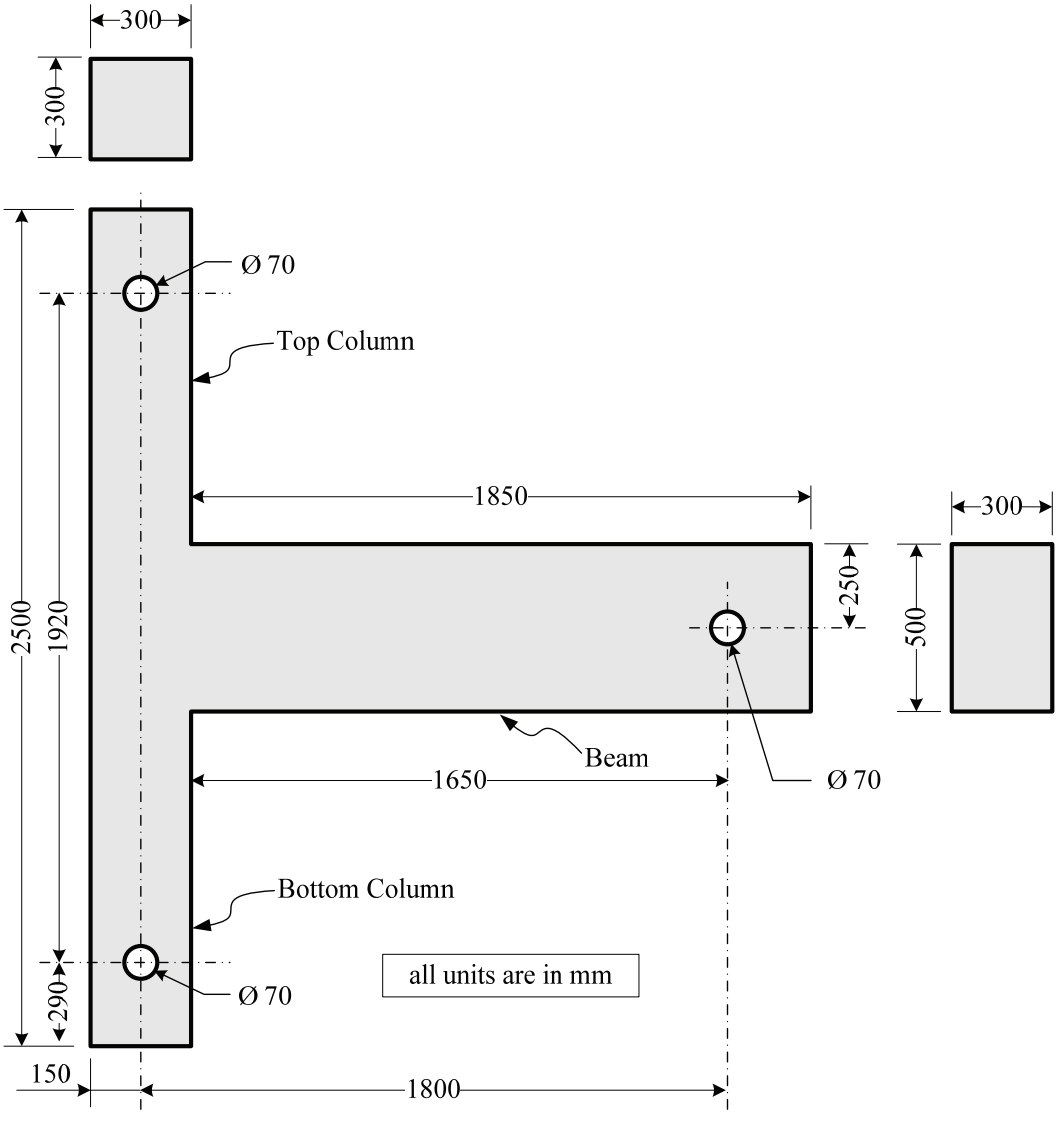


Figure 3.7. Dimensions of the beam-column joint subassemblies

3.4.1. US1 Specimens

In this study, the effect of several steel reinforcement detailing deficiencies, provided in section 3.1, were investigated. Detailing deficiencies incorporated in specimens US1, US1-FRP1 and US1-R-FRP1 are listed below;

- Inadequate transverse reinforcement: both for the beam and the column, this type of detailing deficiency provides little or almost no confinement to the concrete under excessive moments acting at the maximum moment regions of the members. But more critical, it may result in a sudden shear failure and consequently a total collapse of the structure.
- No transverse reinforcement in the joint region: under high lateral loading condition, any transverse reinforcement will cause diagonal shear cracks within the joint shear panel since the effective concrete shear area is inadequate. This may cause an undesirable sudden failure and consequently a total collapse of the structure.

Steel reinforcement configuration of specimens US1, US1-FRP1 and US1-R-FRP1 is illustrated in Figure 3.8.

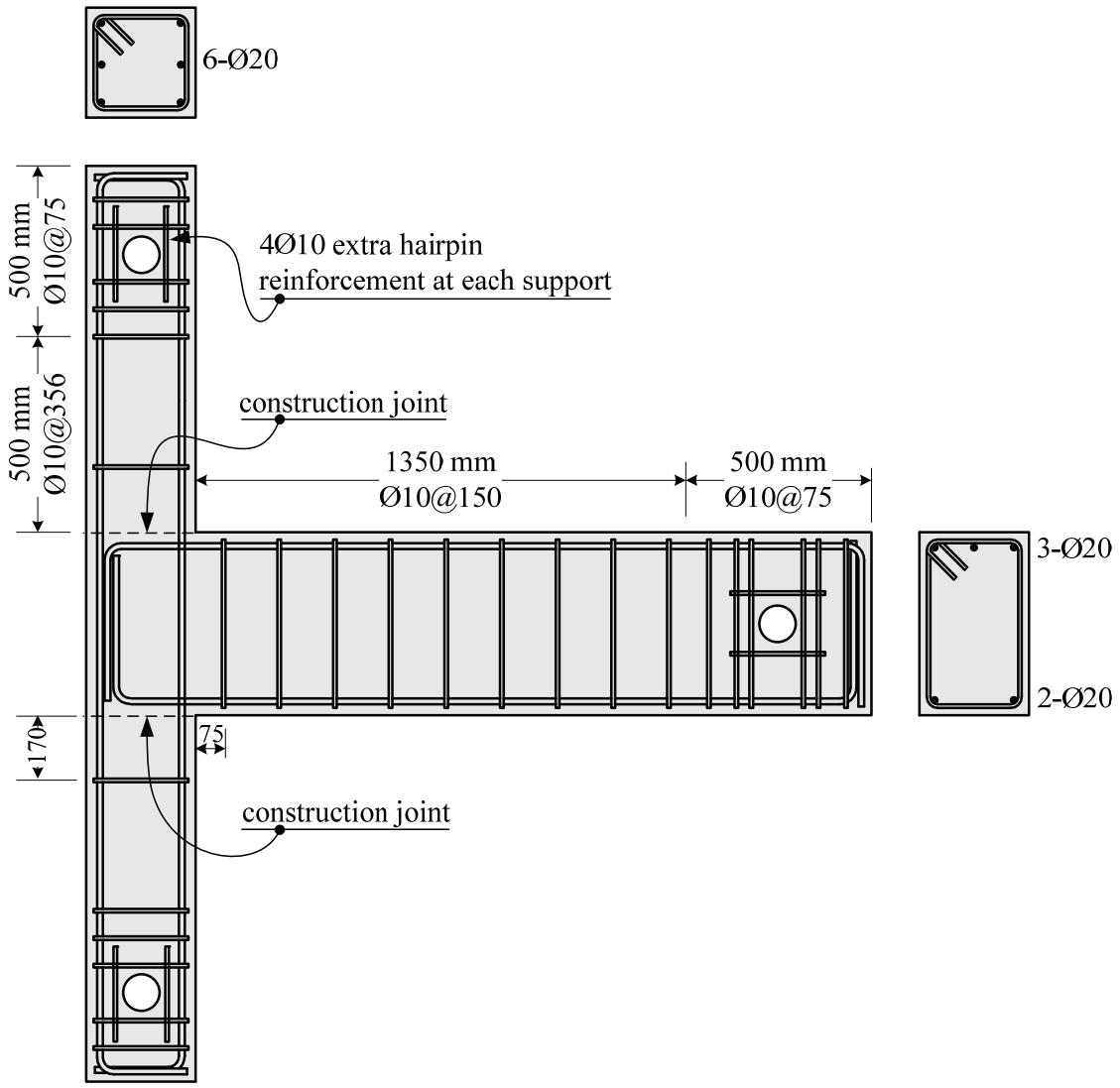


Figure 3.8. Steel reinforcement detailing of US1, US1-FRP1 and US1-R-FRP1

3.4.2. US2 Specimens

Steel reinforcement detailing deficiencies incorporated in specimens US2, US2-FRP2 and US2-R-FRP2 are given below;

- Short embedment length for the beam bottom longitudinal reinforcement: Beam bottom longitudinal reinforcement was embedded 15 cm into the joint. In pre-1970's, beam positive moments at the supports were not considered, since the design was conducted for dead loads only. In such a design 15 cm embedment of beam bottom longitudinal reinforcement is adequate since no tensile forces would be exerted at the end of bottom rebars. However, under cyclic lateral loading condition, both positive

and negative moments at beam ends are observed. According to the current ACI 318-08 code [59], 15 cm of embedment is inadequate when development length is under consideration.

- All other reinforcement detailing deficiencies incorporated in specimen US1.

Steel reinforcement configuration of specimens US2, US2-FRP2 and US2-R-FRP2 is shown in Figure 3.9.

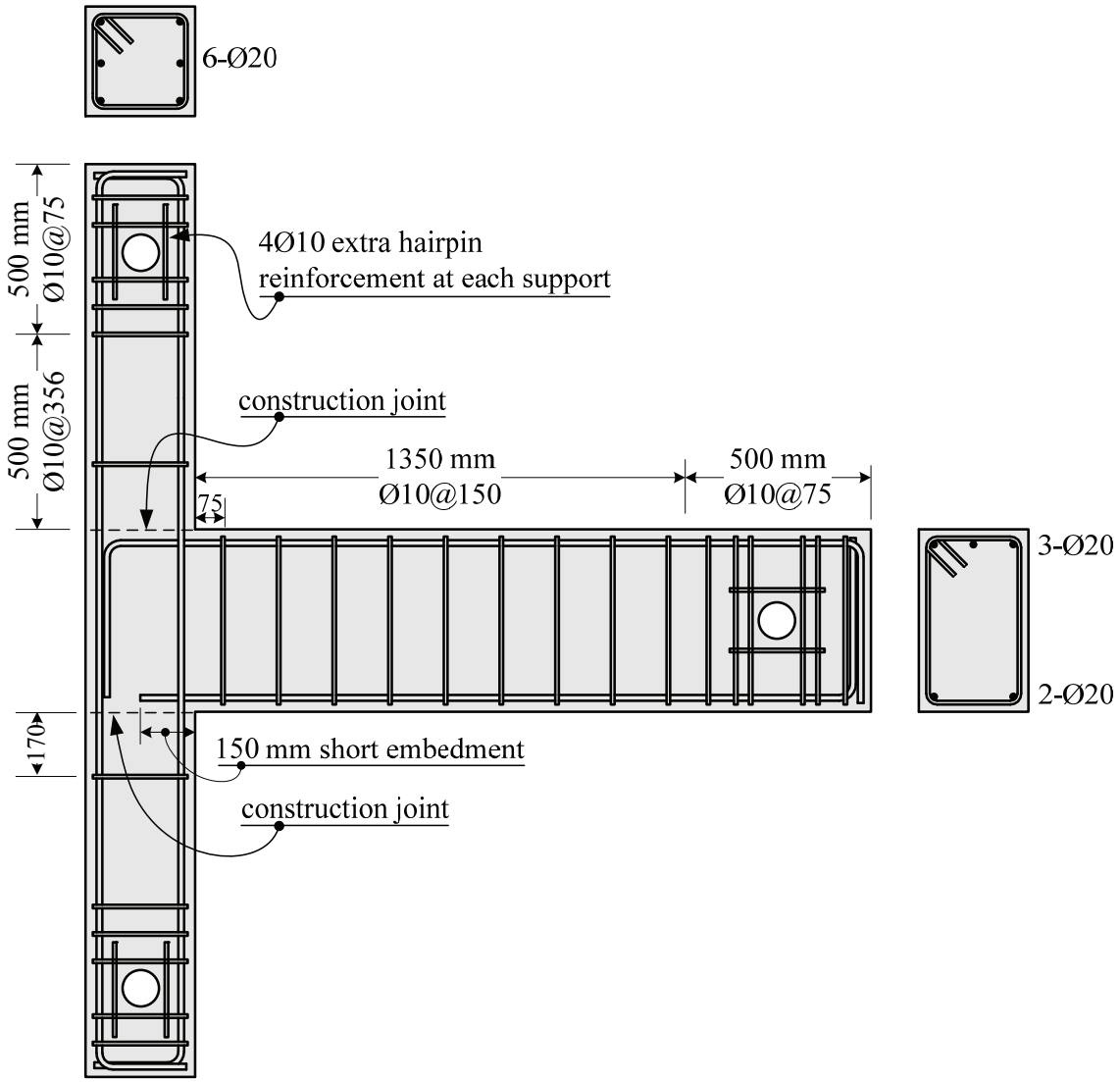


Figure 3.9. Steel reinforcement detailing of US2, US2-FRP2 and US2-R-FRP2

3.4.3. US3 and US4 Specimens

Steel reinforcement detailing deficiencies incorporated in specimens US3, US4, US3-FRP, US4-FRP, US3-R-FRP3 and US4-R-FRP3 are listed below;

- Lap splice just above the joint: Column longitudinal reinforcements are lap spliced 50 cm just above the joint. In seismic regions, current ACI 318-08 [59] code does not allow lap splicing at the maximum moment region of the columns. Moreover 50 cm of splice length is inadequate according to the ACI 318-08. Thus, under high level of lateral loading it is possible to observe slippage of the column longitudinal reinforcements. This deficiency could result in total collapse of an actual structure.
- All other reinforcement detailing deficiencies incorporated in specimen US2.

Steel reinforcement configuration of specimens US3, US4, US3-FRP, US4-FRP, US3-R-FRP3 and US4-R-FRP3 is shown in Figure 3.10.

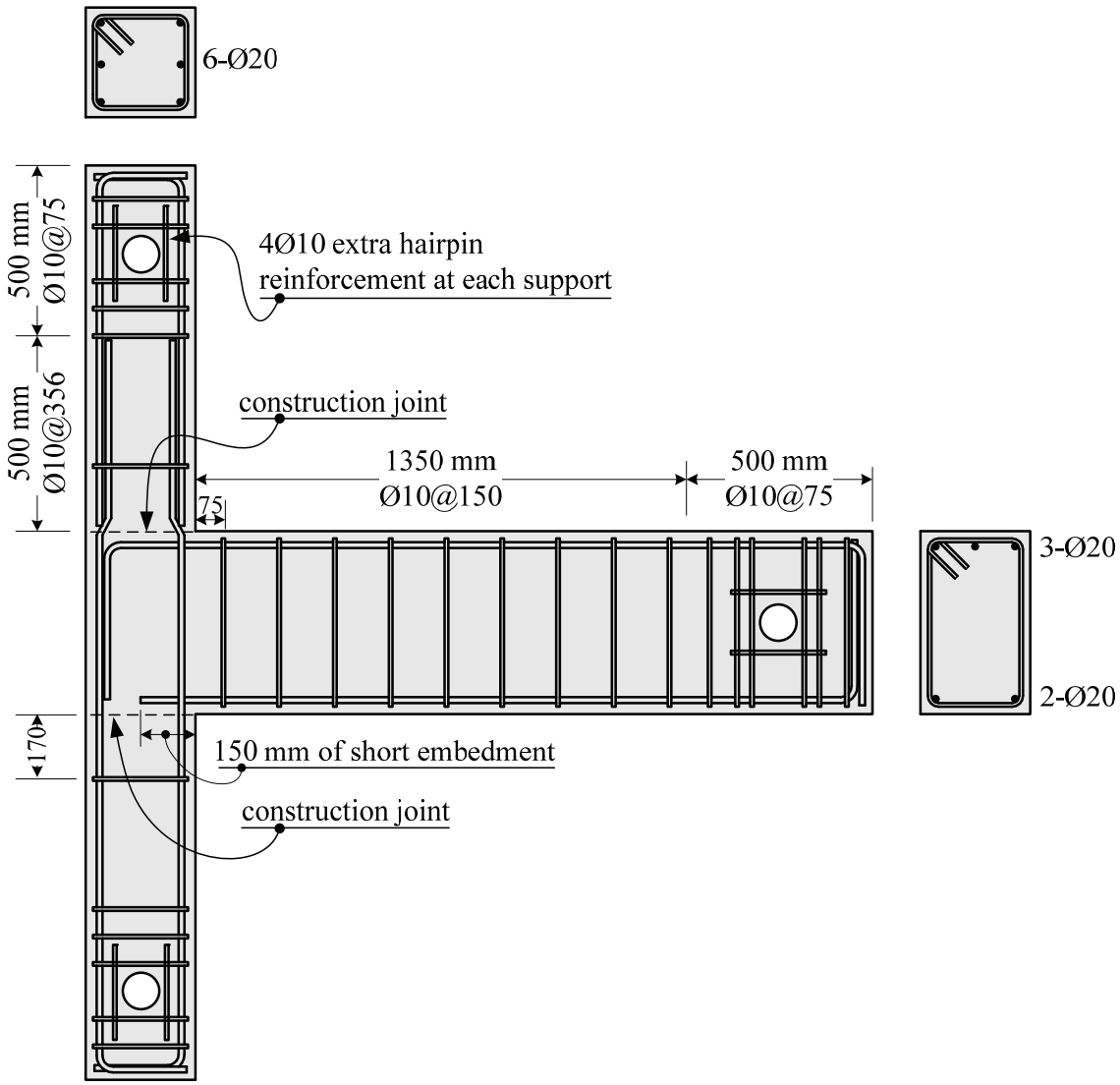


Figure 3.10. Steel reinforcement detailing of US3, US4, US3-FRP, US4-FRP, US3-R-FRP3 and US4-R-FRP3

3.5. CFRP Retrofitting and Wrapping Configurations

Installation of CFRP sheets need special care and only trained technicians can install them. The procedure for installing the CFRP sheets followed in this study is given below:

- Preparing the surface of the specimen: All faces of the beam-column joint subassemblies were first smoothened to increase the effective bond area between the CFRP and the concrete. The corners were rounded with a radius of approximately 20 mm, since increasing the radius will reduce stress concentrations on the edges of the specimens. Large and loose concrete particles were removed from the area where

CFRP was to be applied. All large gaps were filled with putty, Concressive 1406. The specimens were cleaned with a wire brush and then the concrete surface was vacuumed to obtain a clean surface for an increased bond between CFRP sheets and the concrete.

- Application of the primer: A primer, MBrace Pimer, was applied to the cleaned surfaces with a roll brush. Approximately 24 hour curing time was required before the application of CFRP with epoxy. The primer is a low viscosity material and can easily penetrate the concrete media. This characteristic of the primer enhances the bond strength between the epoxy, CFRP sheets and the concrete.
- Application of the CFRP with epoxy: After the primer gets dry, two-component epoxy adhesive for FRP, MBrace Adesivo Saturant, was applied to the surface of the retrofitted area. CFRP fabrics were then installed to the beam column joint region such that no air pockets were left under the CFRP sheets.

In this study, three different CFRP wrapping configurations were developed. In the CFRP application, it is important to apply the CFRP such that fibers' directions are perpendicular to the expected crack path, since CFRP mainly resists on tensile forces. In this sense, the behavior and cracking patterns of the control specimens played an important role in the development of the CFRP wrapping configurations.

3.5.1. FRP1 Wrapping Configuration

FRP1 was the first wrapping configuration developed after the test of the control specimen US1. Governing failure mode of US1 control specimen was shear failure at the beam column connection region which can be observed as diagonal cracks at the joint core. Thus, FRP1 wrapping configuration was developed accordingly. This strengthening technique was used for specimens US1-FRP1 and US1-R-FRP1.

The followings are the steps of FRP1 wrapping configuration:

(i) In the first step, CFRP sheets were placed diagonally at the joint shear panel with +α and -α angles. Here, α is the angle between the horizontal and diagonal of the joint shear panel. This orientation scheme is associated with the damage observed in the control specimen that was caused due to the lack of the shear reinforcement in the joint. Diagonally placed CFRP sheets were wrapped at the north and south face and on both diagonals of the joint shear panel as shown in Figure 3.11. It was aimed that the shear force at the joint core is carried by these CFRP diagonals, serving as conventional stirrups at the joint. Totally four CFRP sheets were used, two at the south face and two at the north face. The length of a single CFRP diagonal sheet was1250 mm and the width was 420 mm.

(ii) A single layer of U-shaped wrapping was applied to the joint and was extended 300 mm on the north and south faces of the beam as shown in Figure 3.12. The purpose of this application was to provide additional confinement to the joint region and consequently to decrease the shear damage in the joint core. One of the main purposes was to plastify the beam and obtain a more ductile behavior. Thus the distance that was extended along the beam should be short enough to satisfy this requirement and at the same time, it should be long enough to provide sufficient anchorage. The total length of this CFRP sheet was 1500 mm (600 + 600 + 300 = 1500 mm) and the width was 500 mm.

(iii) A single layer of L–shaped CFRP sheet was applied to each top and bottom corner of the specimens as shown in Figure 3.13. On the beam and column faces, CFRP wrap was extended 300 mm. Total length of a single L–shaped CFRP sheet was 600 mm

and the width was 300 mm. The use of L–shaped CFRP sheets was to stop crack propagation which starts from the corners.

(iv) In the next step, CFRP wraps were applied around the columns as shown in Figure 3.14. These wraps were expected to serve as anchorage for the L–shaped CFRP sheets and also as confinement reinforcement at the maximum moment region of the columns. This application was associated with the deficiency of widely spaced column ties, in order to increase the ductility. According to the reinforcement details, 500 mm above and below from the beam faces, there was not sufficient stirrups for the confinement of the concrete, so these wraps were extended 500 mm towards column free ends. Total length of a single column wrap, including the overlap shown in Figure 3.14, was 1350 mm.

(v) As illustrated in Figure 3.15, wrapping around the beam is the last step of this CFRP orientation scheme. The purpose of these wraps was to provide anchorage for the L-shaped overlays and U-shaped CFRP sheet and also to increase the shear resistance of the beam. The width of the CFRP sheet was 300 mm and the length was 1750 mm.

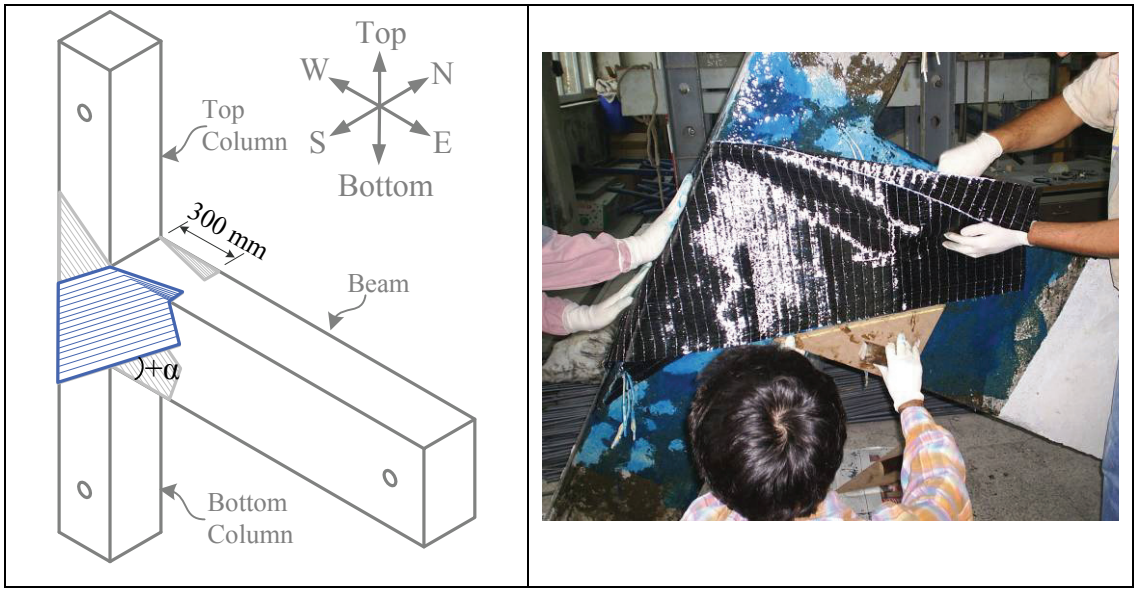


Figure 3.11. Diagonal CFRP sheet application, step (i)

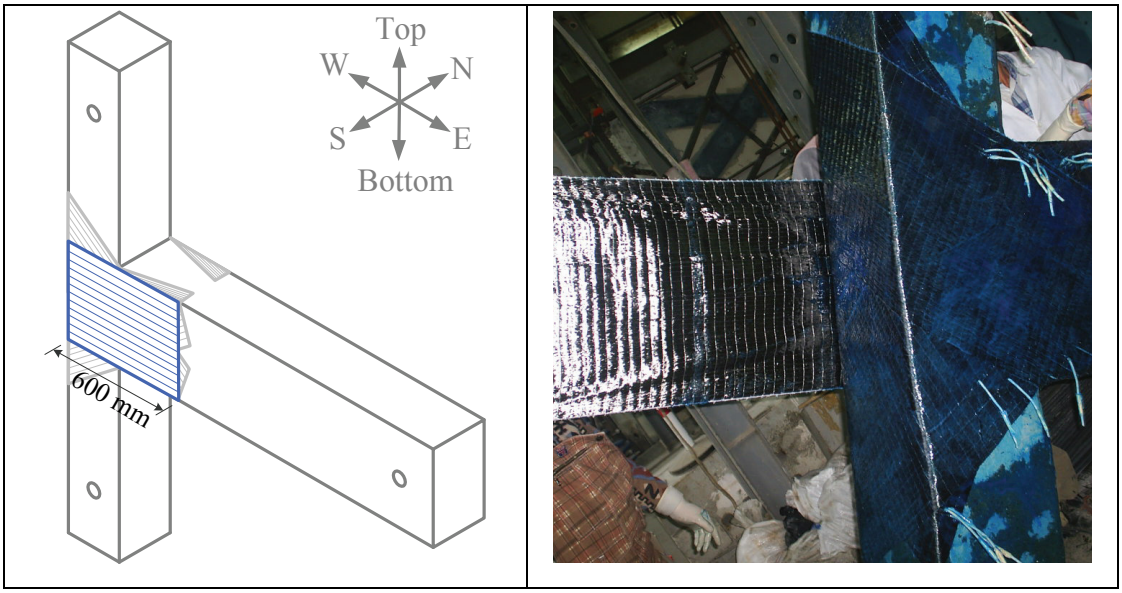


Figure 3.12. U–shaped CFRP sheet application, step (ii)

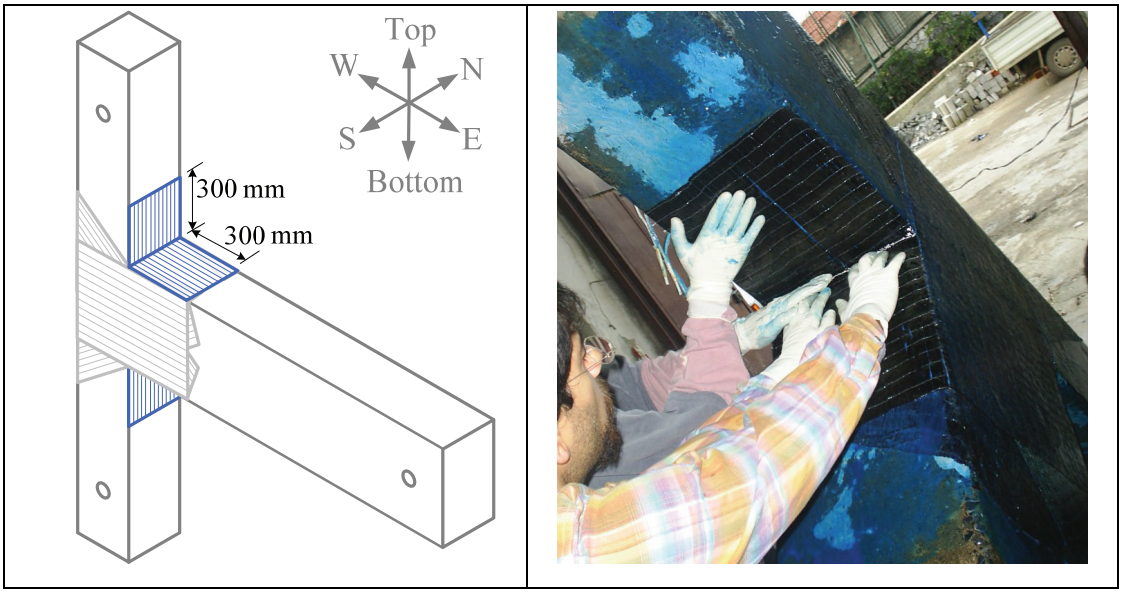


Figure 3.13. L–shaped CFRP sheet application, step (iii)

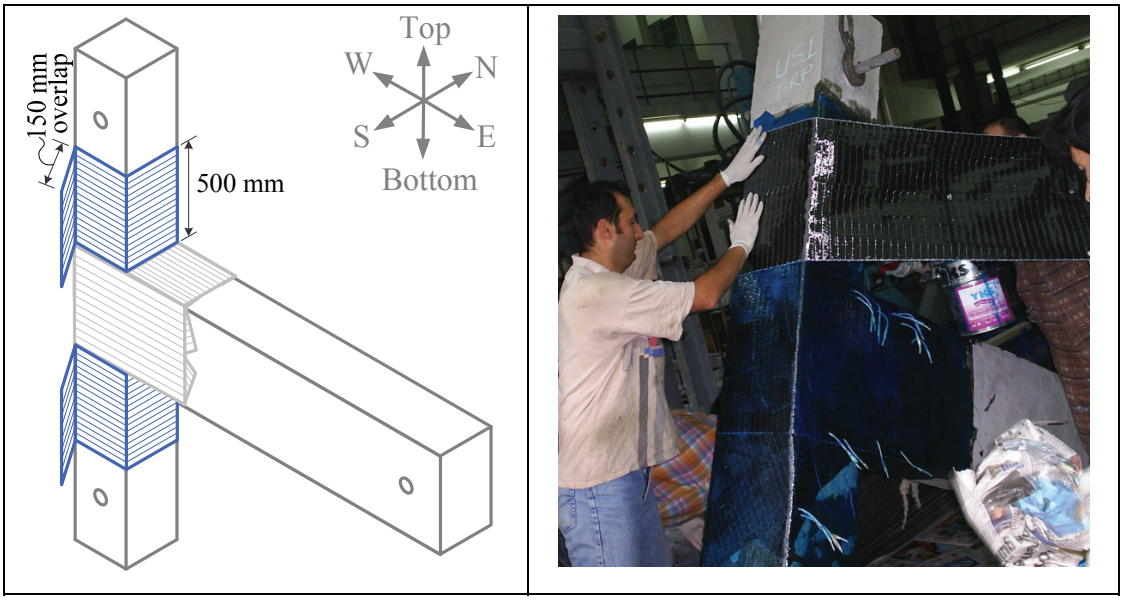


Figure 3.14. Column CFRP wraps, step (iv)

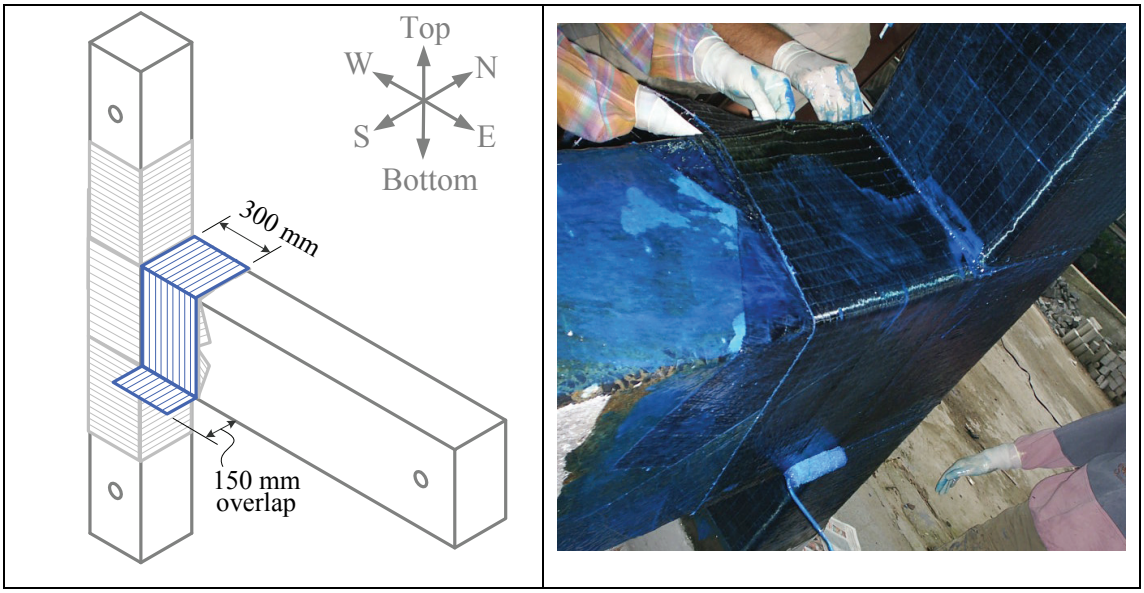


Figure 3.15. Beam CFRP wrap, step (v)

3.5.2. FRP2 Wrapping Configuration

FRP2 was the second wrapping configuration developed after the test of the control specimen US2. This strengthening technique was applied to specimens US2-FRP2 and US2-R-FRP2.

Two different failure modes were observed in the test of control specimen US2 due to the reinforcement detailing asymmetry in the loading directions. Slippage of the beam

bottom longitudinal reinforcement and shear failure at the joint region were the governing modes of failure. Accordingly, FRP2 wrapping configuration was developed such that precaution to these failure types was taken.

Debonding of CFRP sheet from concrete surface was observed during the test of US1-FRP1. This leaded to take precaution to the anchorage problem in the development of FRP2 wrapping configuration.

The followings are the steps of FRP2 wrapping configuration:

(i) In order to fix the anchorage problem observed in US1-FRP1, two holes were drilled starting from the south face and ending at the north face of the beam as shown in Figure 3.16. Locations of these holes were determined considering the reinforcement detailing (both longitudinal and transverse reinforcement of the beam), clear cover distance and adequate anchorage length for the CFRP sheets. Holes were drilled with 25 mm drill that opened holes with approximately 27 mm of diameter. In order to reduce the stress concentrations at the ends of the holes both ends of these holes were beveled with approximate radius of 20 mm. The use of the holes will be explained in step (vi).

(ii) In order to extend the failure away from the joint to the beam, one of the remedies was to increase the flexural capacity ratio of the columns to the beam. As a second step, to increase the column flexural capacity, 2 layers of CFRP sheets were applied on both south and north faces of the column as shown in Figure 3.17. By the application of these layers, it was not only expected to increase the flexural capacity of the column, but also to provide some resistance to shearing forces coming to the joint. Total length of a single CFRP sheet was 1700 mm, 600 mm of which was extended towards each end of columns.

(iii) From the test of US1-FRP1, it was observed that U-shaped CFRP sheet, applied around the joint, improved the shear capacity of the joint. The only observed problem for the U-shaped CFRP was debonding of the CFRP sheets from the beam faces. Therefore, in the current step, a single layer of U-shaped CFRP was applied around the joint and was extended to the beam south and north faces, but in this case the extension was kept longer. As shown Figure 3.18, 200 mm in width portion of this

CFRP sheet, was wrapped around the column to increase the effect of confinement. Total length of the U–shaped CFRP was 2000 mm.

(iv) A single layer CFRP sheet was applied around the joint, south and north faces of the beam and around the column in the same way as explained in step (iii) but in this step the bottom portion of the specimen was retrofitted. Figure 3.19 illustrates the way of the CFRP application.

(v) As a continuation of step (iii) and (iv), additional column wraps were applied around the top and bottom columns as shown in Figure 3.20. The main idea for the application of the column wraps was to increase the confinement effect in the columns, which was associated with the deficiency of widely spaced column ties, in order to increase the ductility. According to the reinforcement details, 500 mm above and below from the beam top and bottom faces, there are not sufficient stirrups for the confinement of the concrete. In addition to the wraps applied to the columns shown in Figure 3.18 and Figure 3.19, towards up and bottom from the beam top and bottom faces additional wraps were extended 300 mm more to cover 500 mm of the column region. In order to avoid any anchorage problem, these wraps were overlapped 150 mm. Total length of a single wrap was 1350 mm.

(vi) Short embedment length of the beam positive longitudinal reinforcement was one of the most critical deficiencies. In the test of US2 control specimen it was observed that the positive longitudinal reinforcement of the beam had slipped even at very small drift level of 0.5%. This slippage was mainly due to the inadequate anchorage length of the reinforcement which caused discontinuity in the force transfer from the reinforcement to its surrounding concrete media. Thus, the last and maybe the most crucial step was the application of the CFRP strips as illustrated in Figure 3.21. Application of strips was expected to augment the above mentioned reinforcement anchorage problem and assists for the force transfer between the beam bottom longitudinal reinforcements and concrete. It was also expected to improve the anchorage capacity of the U-shape FRP.

FRP Strip 1 was inserted through the hole closer to the joint then wrapped around the joint and finally was overlapped with 150 mm on the west side of the joint. The primary expected benefit of this single layer strip was to stop the slippage of the beam bottom longitudinal reinforcement and its secondarily expected benefit was to provide anchorage to the U-shaped FRP.

Strip 2 was inserted to the hole away from the joint and was overlapped over the U-shaped FRP. Strips 3 and 4 were inserted through their respective holes as shown in Figure 3.21, and then wrapped around the beam such that they cover the beam south, north and bottom faces. The main purpose of strips 2, 3 and 4 was to improve the anchorage capacity of the U-shaped CFRP by confining the region that they were applied.

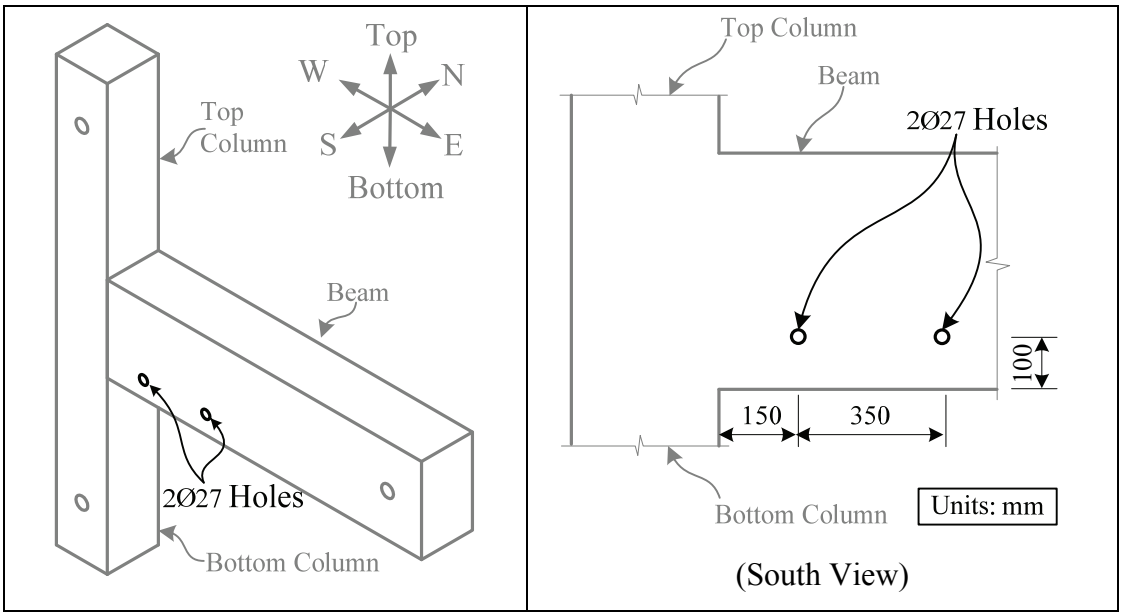


Figure 3.16. Location of the anchorage holes, step (i)

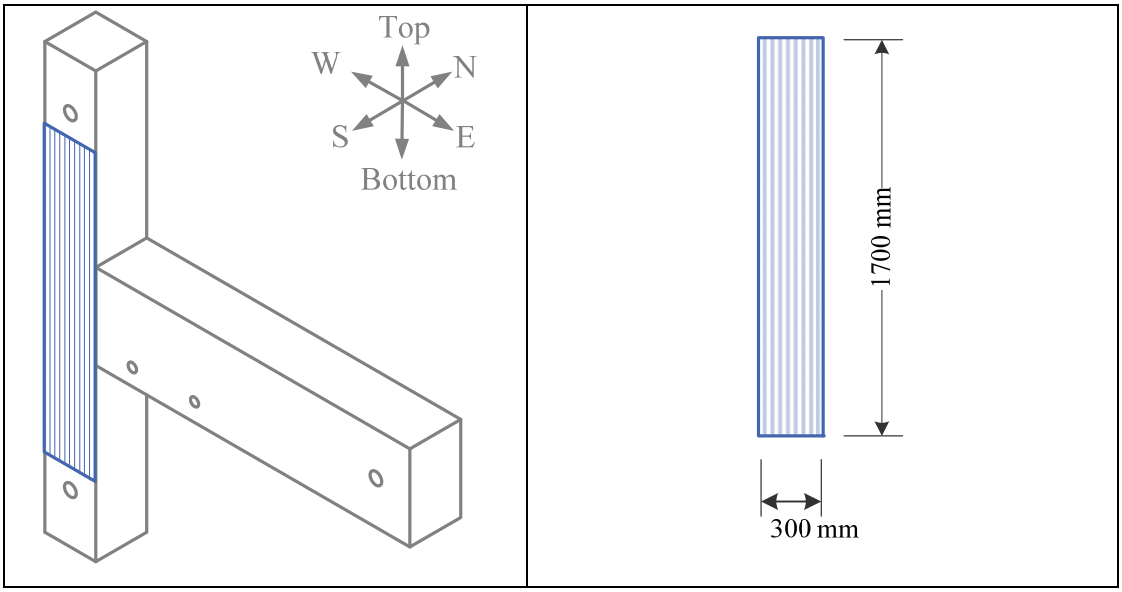


Figure 3.17. CFRP sheets used as a column flexural reinforcement, step (ii)

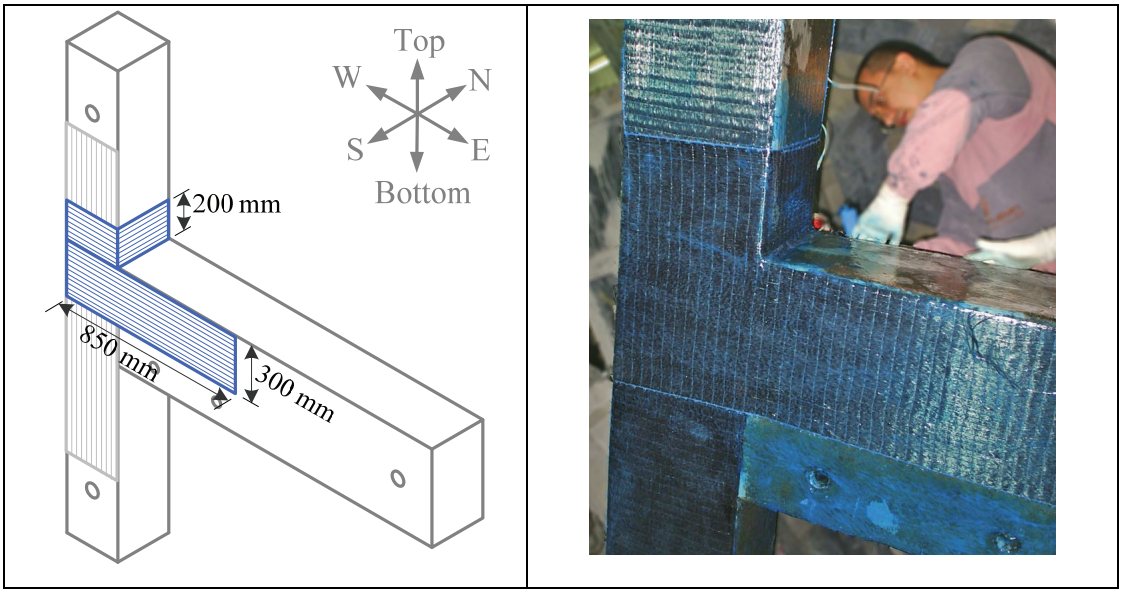


Figure 3.18. U-shaped CFRP applied to the top portion of the joint, step (iii)

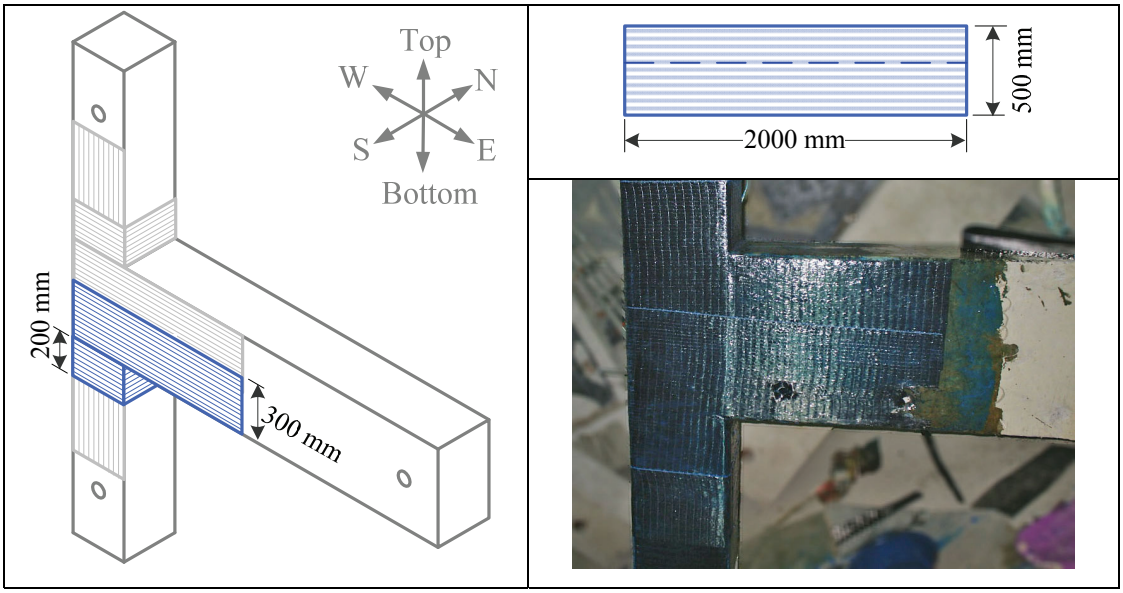


Figure 3.19. U-shaped CFRP applied to the bottom portion of the joint, step (iv)

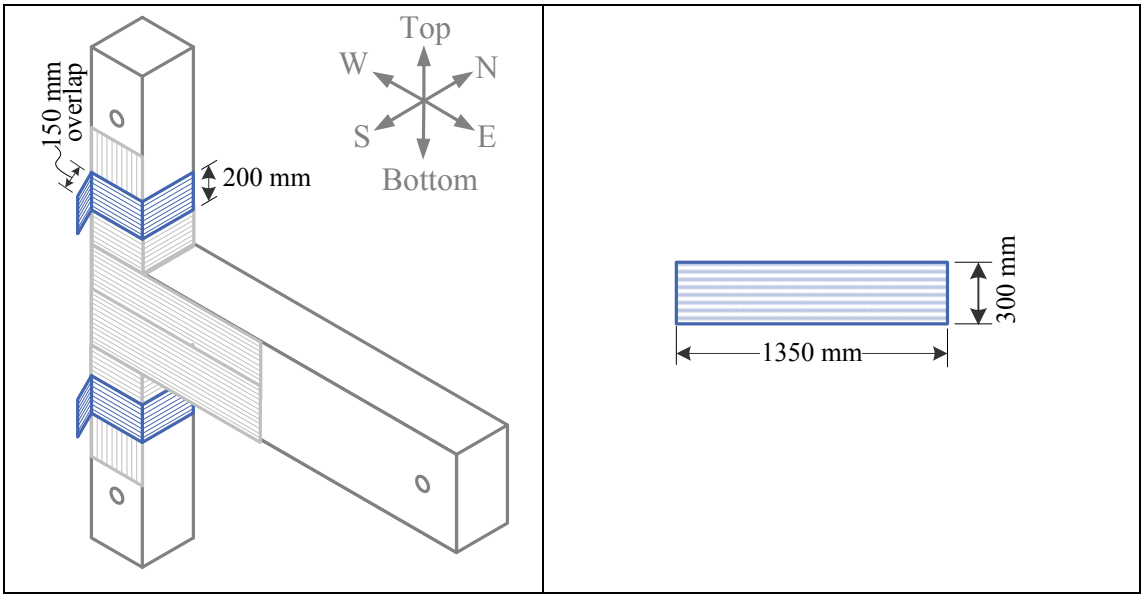


Figure 3.20. Additional column confinement wraps, step (v)

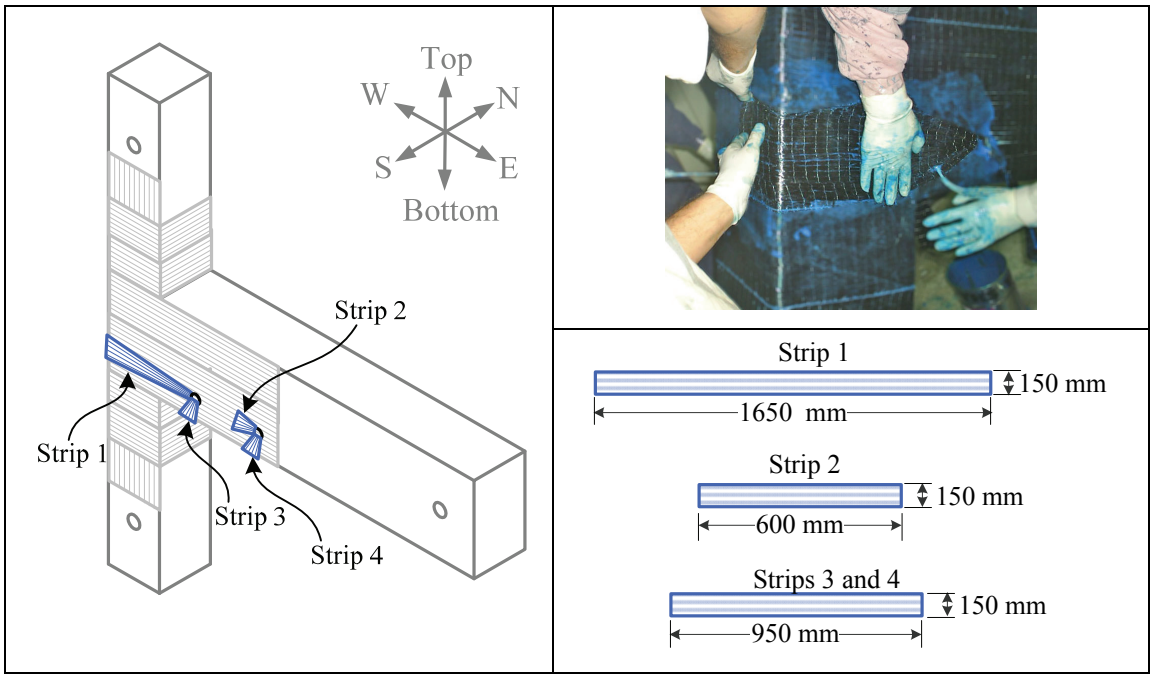


Figure 3.21. Application of CFRP strips, step (vi)

3.5.3. FRP3 Wrapping Configuration

FRP3 was the third wrapping configuration developed after the test of the control specimen US3. Test observations and results of US3, US1-FRP1 and US2-FRP2 were utilized in the development of the current wrapping configuration. This strengthening

technique was applied to specimens US3FRP3, US4-FRP3, US3-R-FRP3 and US4-R-FRP3.

The followings are the steps of FRP3 wrapping configuration with the appropriate reasons of application:

(i) As a first step, four anchorage holes with 20 mm diameter were drilled from the north to south face of the beam as shown in Figure 3.22. In the current strengthening method minimum diameter for the holes was chosen such that 150 mm width CFRP strips can penetrate through these holes. During the test of US2-FRP2, the cracking propagated through the anchorage holes since the effective section height was reduced. To prevent this undesirable result, the diameter of the holes was reduced from 27 mm to 20 mm. Two levels for the holes were considered both in the east–west and top–bottom directions. In the previous test of US2-FRP2, debonding of the top portion of the U-shape CFRP sheet was observed. Thus, top level of holes was considered to provide additional anchorage for a possible debonding. On the other hand, drilling two holes at the same section was avoided.

(ii) As a second step, column flexural CFRP sheets, fibers in the direction of the column longitudinal axis, were installed on the north and south face of the column as shown in Figure 3.23. In the test of US2-FRP2, there was no anchorage problem regarding the flexural CFRP sheets applied to the columns. Thus, the length of the column flexural CFRP sheets was assumed to be adequate, which was 1700 mm. However, CFRP applications that will be described in steps (iv) and (v) were expected to increase the beam capacity so that it may reduce the column to beam flexural ratio. In order to prevent the damage in the column, additional CFRP sheet (additional 1 layer per face) on both north and south faces of the column was applied. Thus, totally 3 layers per face was applied.

(iii) One possible failure could be the slippage of the column longitudinal reinforcement in the lap spliced region, if an adequate shear strengthening of the joint was achieved through the application of FRP. In order to restrict the slippage of the column longitudinal steel reinforcement and provide confinement to the column, wraps were applied around the column in the lap spliced region. 300 mm from the beam top and bottom face, the column is wrapped with CFRP sheets. The lap spliced region was

wrapped with 3 layers and the bottom column was wrapped with 2 layers of CFRP sheet. Figure 3.24 illustrates the application of the column confinement wraps.

(iv) Three layers of U-shape wrapping were applied around the joint and were extended 450 mm on the beam north and south faces. The purpose of this application was to provide additional confinement to the joint region and reduce the shear damage in the joint. Since one of the main purposes was to shift the plastic hinge to the beam, the distance that was extended along the beam should be short enough to satisfy this requirement, and on the other hand it should be long enough to provide sufficient anchorage for the U-shaped CFRP sheet. Sketch of the U-shaped CFRP sheet and a picture of the application are illustrated in Figure 3.25. 500 mm CFRP strip extension, shown on the top right of Figure 3.25, was left deliberately to anchor the U-shape CFRP sheet by inserting this strip through the hole (closer to the beam free end) from the south face of the beam and overlapping it on the north face of the beam with 200 mm lap length. The location of this anchorage strip within the height of the beam was chosen to be at the level where the shortly embedded beam bottom longitudinal reinforcement was located, since maximum stress distribution was expected at this region.

(v) Last step was the application of CFRP strips which were expected to provide adequate anchorage. The CFRP strip 1 was inserted through the first hole and then wrapped around the column and finally was penetrated again from the first hole. It was used to prevent slippage of the shortly embedded beam bottom longitudinal reinforcement. CFRP strips 2 and 3 penetrated from the upper level of holes were used to prevent possible debonding of U-shaped CFRP sheet. These CFRP strips were wrapped around the bottom of the beam like a belt. Sketch of the current step of application is shown on Figure 3.26.

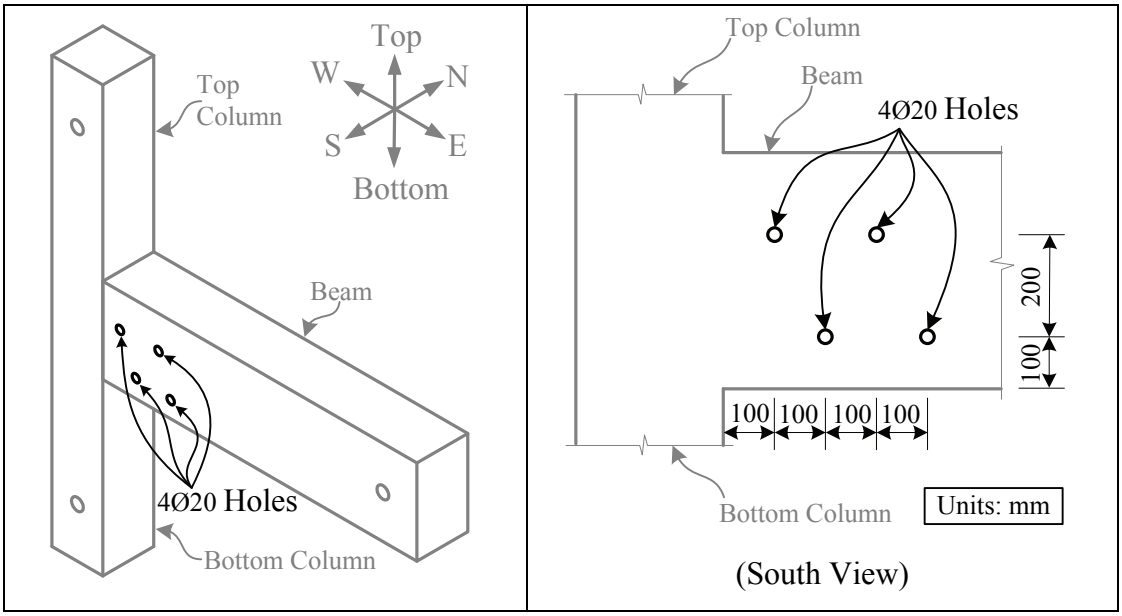


Figure 3.22. Location of the anchorage holes, step (i)

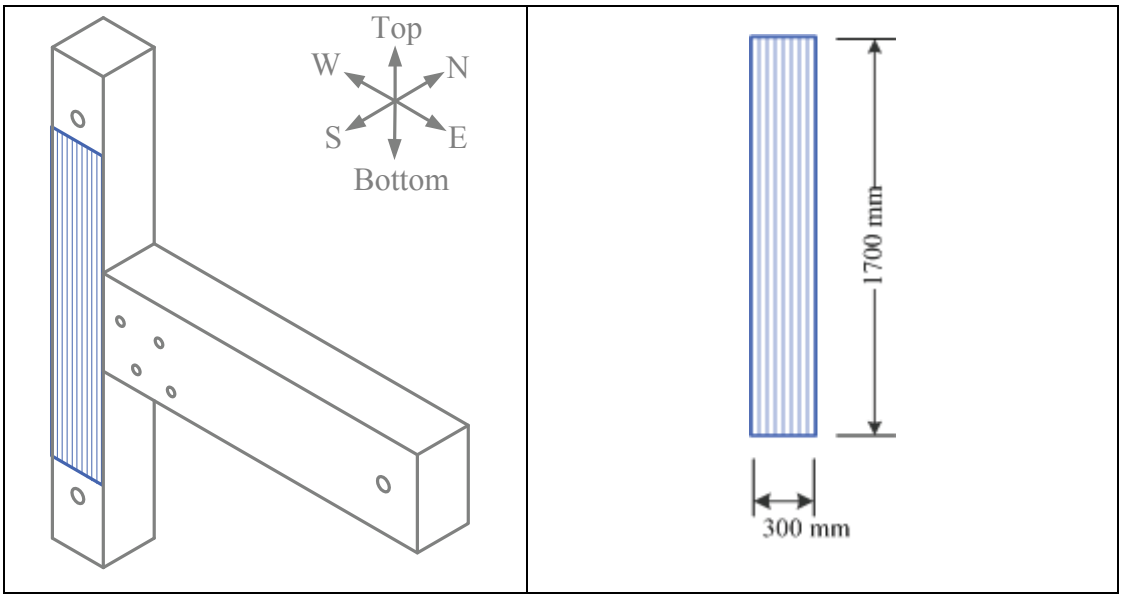


Figure 3.23. CFRP sheets used as a column flexural reinforcement, step (ii)

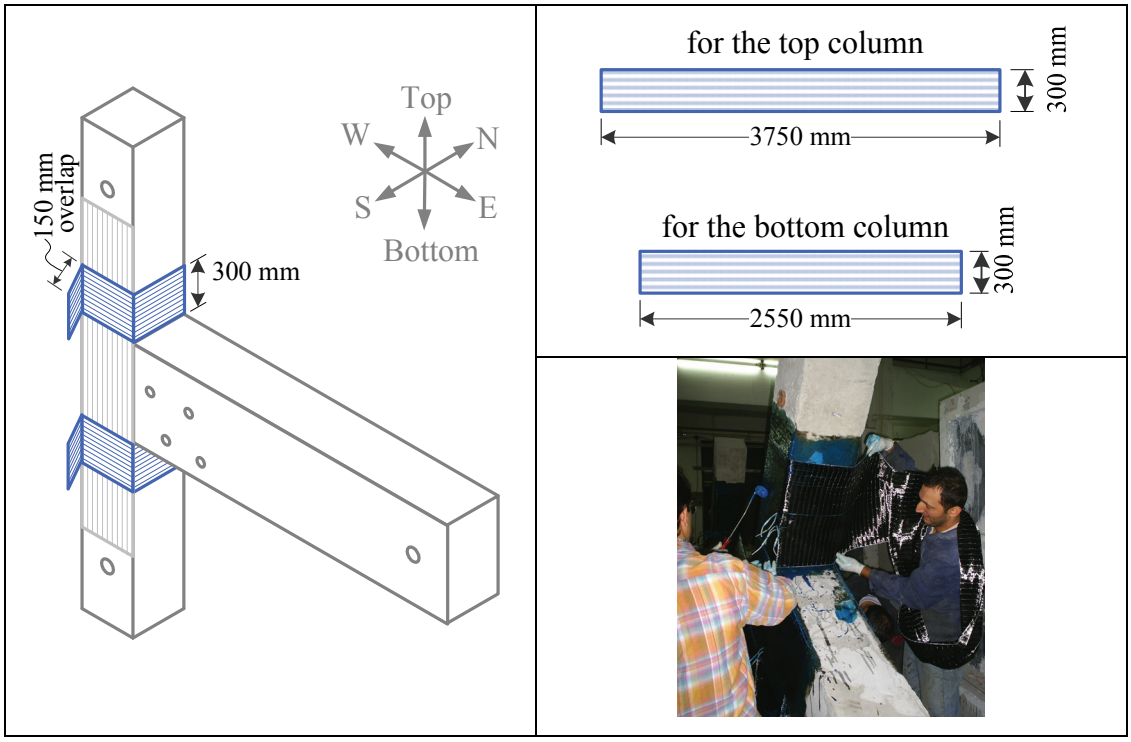


Figure 3.24. Column confinement wraps, step (iii)

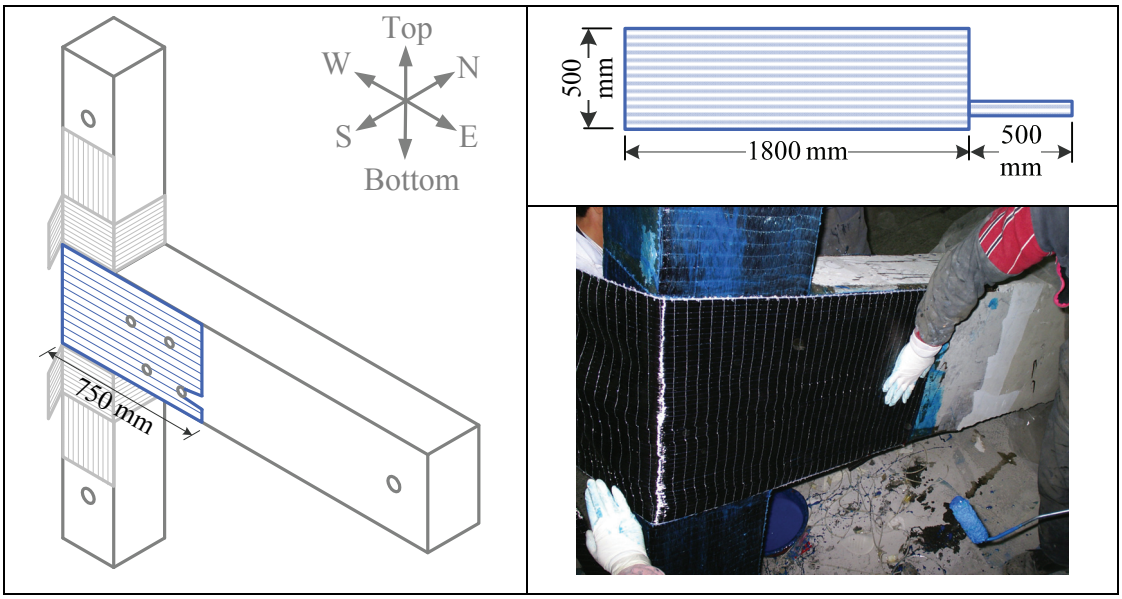


Figure 3.25. U-shaped CFRP application, step (iv)

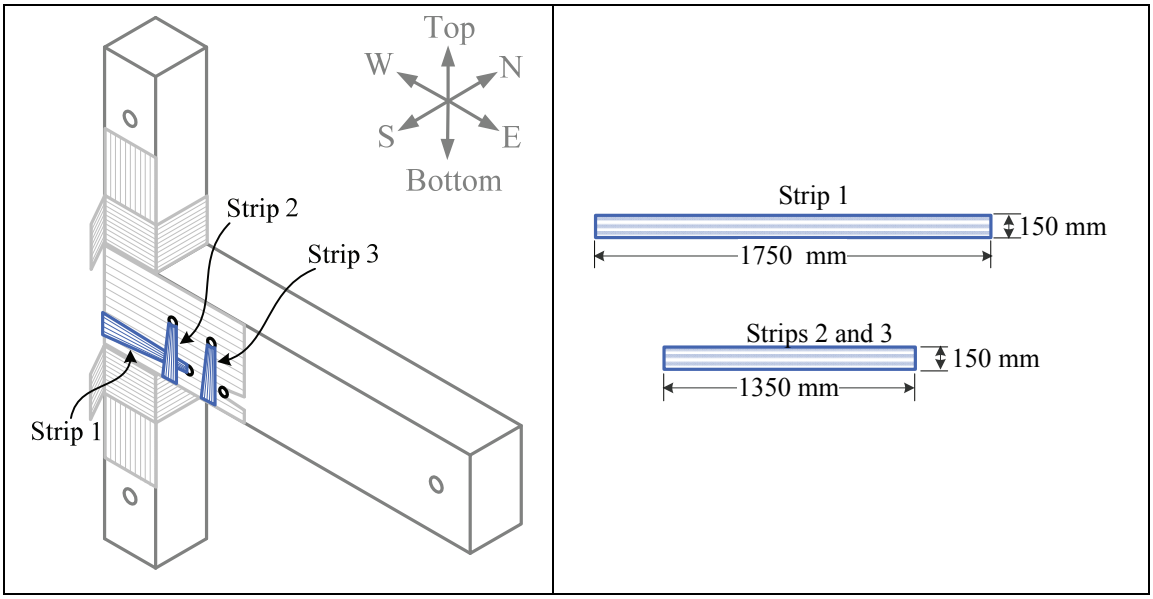


Figure 3.26. Application of CFRP strips, step (v)

3.6. Repairing Technique

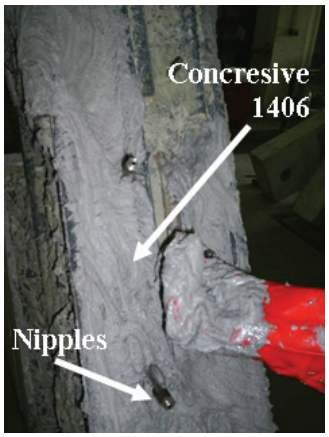
Repair procedure was performed to the already damaged control specimens. Epoxy injection technique was chosen as a repair method. Cement and epoxy based materials were used during the repair process.

The repair procedure started with the removal of the loose concrete from the damaged region of a specimen. The surface and the cracks were cleaned using wire brush. Before the epoxy injection, the damaged area was blown by high–pressure air until it was free from dust particles. Several holes were drilled along the cracks. Then, check valve nipples were placed into the holes. Large cracks were filled with epoxy–based high strength repair material, Concresive 1495. All remaining voids were filled with epoxy based material Concresive 1406. Next, the surface was smoothened with the cement based repairing material Emaco S88C. Then the specimen was left for curing of the materials. After a week low viscosity epoxy, Concresive 1302 was injected with 200–bar pressure through the nipples via special pumps as shown in Figure 3.27. Epoxy injection process was continued until leakage of the epoxy was observed from the nipples placed on the other sides of the specimen.

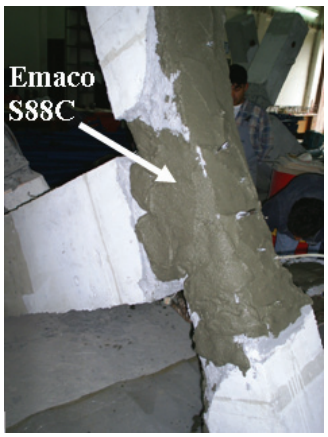
When the injection is completed, the concrete surface is prepared for CFRP wrapping as explained in section 3.5.



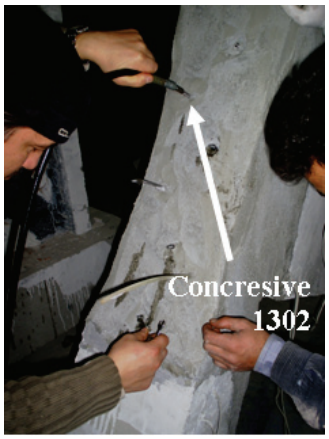
Epoxy injection of large cracks



Replacement of loose concrete voids



Replacement of loose concrete voids



High-pressure epoxy injection

Figure 3.27. Repairing procedure

3.7. Test Setup and Loading

All tests were performed at Structures Laboratory in the Civil Engineering Department of Bogazici University. Simplified free body diagram of the specimens is shown in Figure 3.28. Structural P-Δ effects were neglected in the test setup. The beam-column joint subassemblies and testing method is in accordance with the

specifications recommended by the ACI committee of Acceptance Criteria for Moment Frames Based on Structural Testing, ACI T1.1-01 [60].

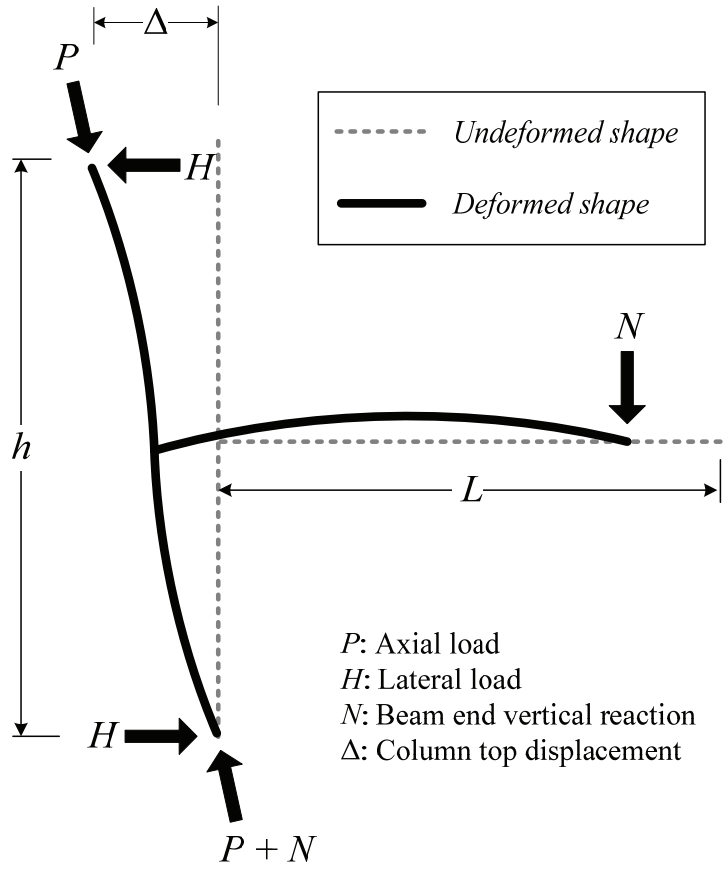


Figure 3.28. Free body diagram of the test setup

A general view of the test setup is shown in Figure 3.29. The specimens were tested in beam horizontal position with a hinge at the end and the columns in vertical position supported by a pin at the bottom end as shown Figure 3.30. The top of the column is free to move and rotate and the hinged end of the beam can easily rotate and translate horizontally. Hence the point of contraflexure for both the beam and the column can be modeled within the loading setup. A constant load is applied through the use of 1000 kN hydraulic cylinder on the axis of the column. In order to restrict any out of plane actions, an out of plane frame was mounted on the two sides of the specimens as seen on the bottom left in Figure 3.29. A closed loop double acting dynamic actuator with a load capacity of 250 kN and 200 mm stroke capacity was used in the testing. The available capacity of the reaction wall was 2000 kN.



Figure 3.29. General view of the test setup

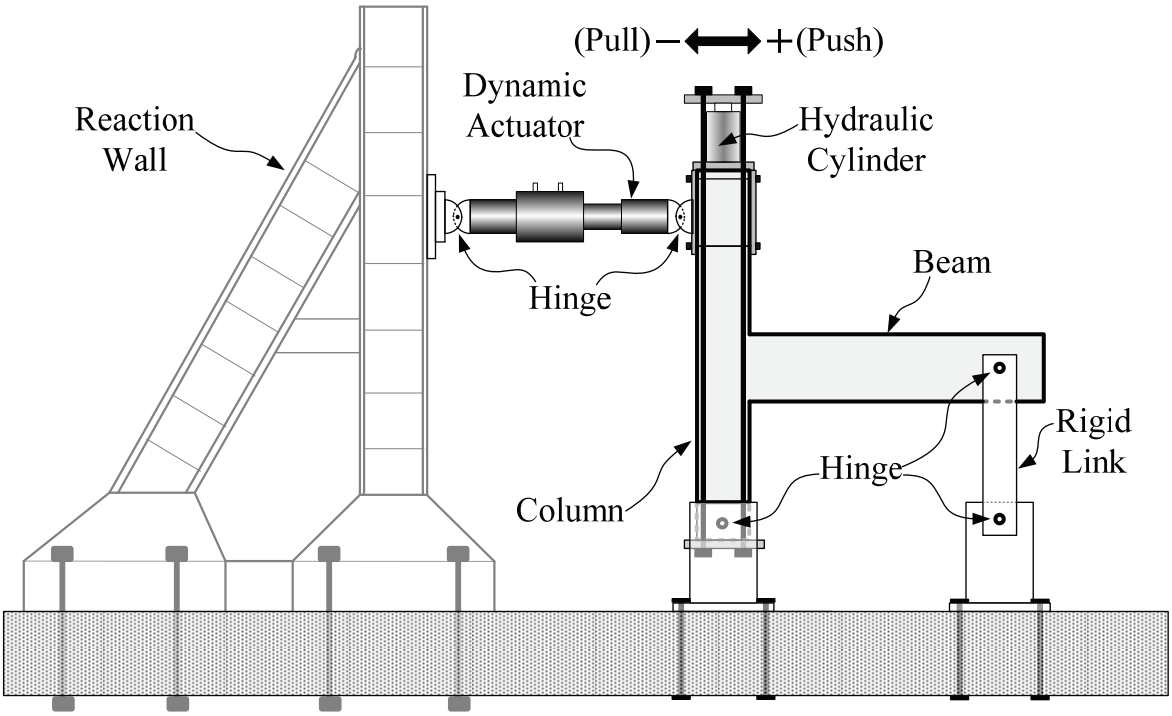


Figure 3.30. Sketch of the test setup

Test was performed according to ACI T1.01 recommendations. Minimum requirements of the test procedure extracted from the ACI T1.01 recommendations are summarized as follows:

- Test modules shall be subjected to a sequence of displacement-controlled cycles representative of the drifts expected under earthquake motions for that portion of the frame represented by the test module. Cycles shall be predetermined drift ratios.
- Three fully reversed cycles shall be applied at each drift ratio.
- The initial drift ratio shall be within the essentially linear elastic response range for the module. Subsequent drift ratios shall be values not less than one and one-quarter times, and not more than one and one-half times the previous drift ratio.
- Testing shall continue with gradually increasing drift ratios until drift ratio equals or exceeds 0.035
- Data shall be recorded from the test such that a quantitative, as opposed to qualitative, interpretation can be made of the performance of the module. As continuous recording shall be made of the test module, drift ratio versus column shear force, and photographs shall be taken that show the condition of the test module at the completion of testing for each sequence of three cycles.

Displacement controlled lateral load was applied based on the above criteria. The loading cycles are shown in Figure 3.31. Cyclic lateral displacement was imposed at the top of the column by considering the inter-story drifts. Three reversed cycles of the same amplitude in story drift were repeated before displacement amplitude was increased. Approximately 35-40 reversed cycles were applied throughout the test. All data were collected with a TML 602 50 Hz. 50 channel data acquisition box.

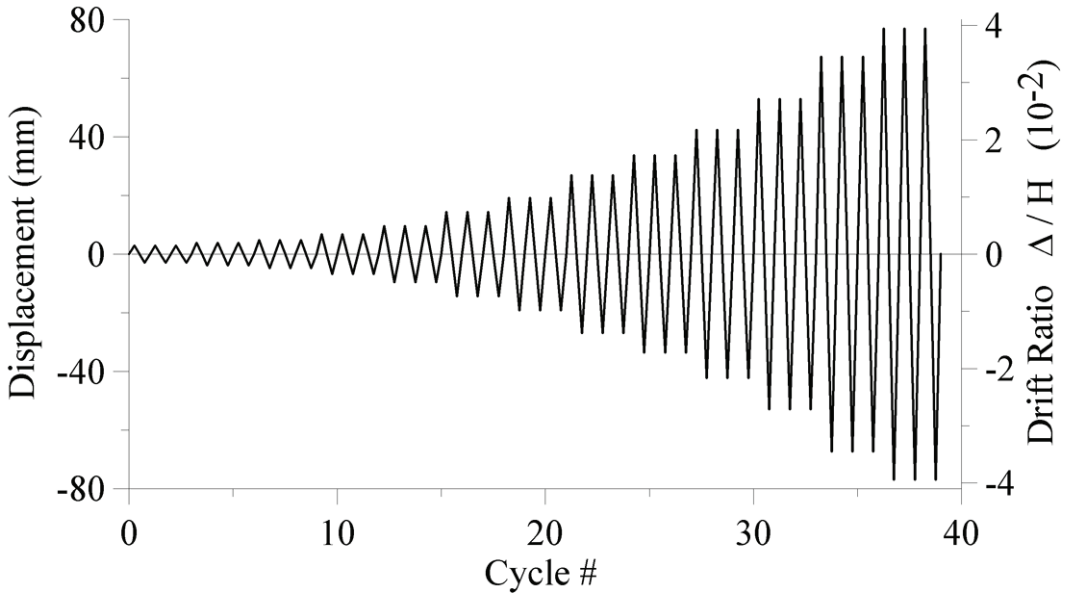


Figure 3.31. Lateral loading pattern

Each specimen was tested under constant column axial load. However the axial load differed from specimen to specimen. Column axial load levels for each test specimen are summarized in Table 3.1. Two different column axial load levels presented in Table 3.1, 350 kN and 700 kN correspond to approximately 12% and 24% of the column axial load capacity, respectively. The axial load, which was constant during the tests, was applied manually through a hydraulic ram. Thus, fluctuation of ±10 kN during the experiment was inevitable especially when sudden deterioration of the joint shear resistance was observed.

3.8. Instrumentation

Several LVDTs, dial gauges and strain gauges were mounted on the test specimens in order to monitor the story drift; joint rotation, crack openings, curvatures of the members, strain levels on the steel and CFRP materials. Cracks, CFRP fractures and debonding and failures were noted in each 3-cycle loading sets. LVDTs used to measure the top displacement of specimens are shown in Figure 3.32. Effect of support movement was incorporated in the measurement of the overall top displacement. Corrected top displacement, Δ was calculated as indicated in Equation 3.1.

$$\Delta = \left(\frac{\Delta_1 + \Delta_2}{2}\right) - \Delta_3 - \left(\frac{1920}{1800}\right)\Delta_4 \qquad (3.1)$$

Subscripts in Equation 3.1 indicate the number of the LVDT. For instance, Δ_3 is the displacement measurement of LVDT 3 shown in Figure 3.32.

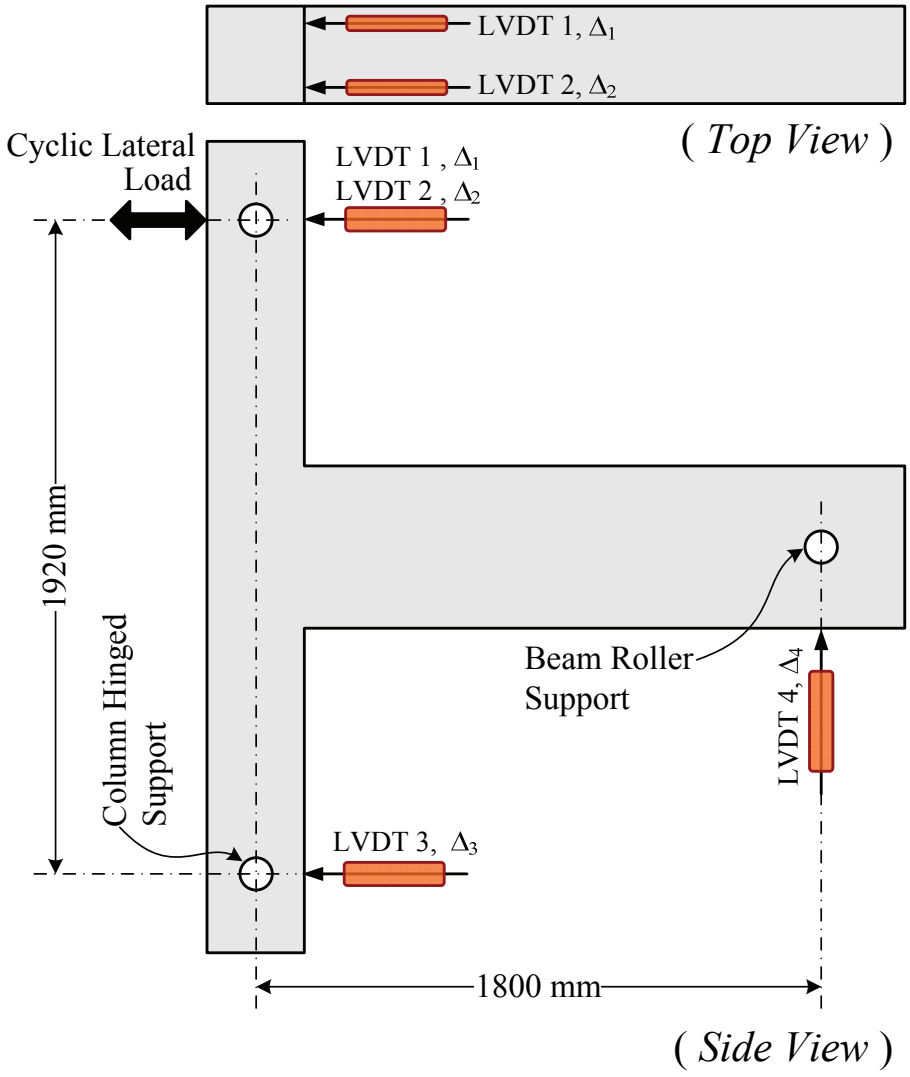


Figure 3.32. LVDT locations for measurement of top displacement

Joint shear deformations were measured through the use of two LVDTs placed diagonally at the joint shear panel as shown in Figure 3.33. The value of each distance is provided in Table 3.7. All designations shown in this figure are the undeformed distances measured just before the tests.

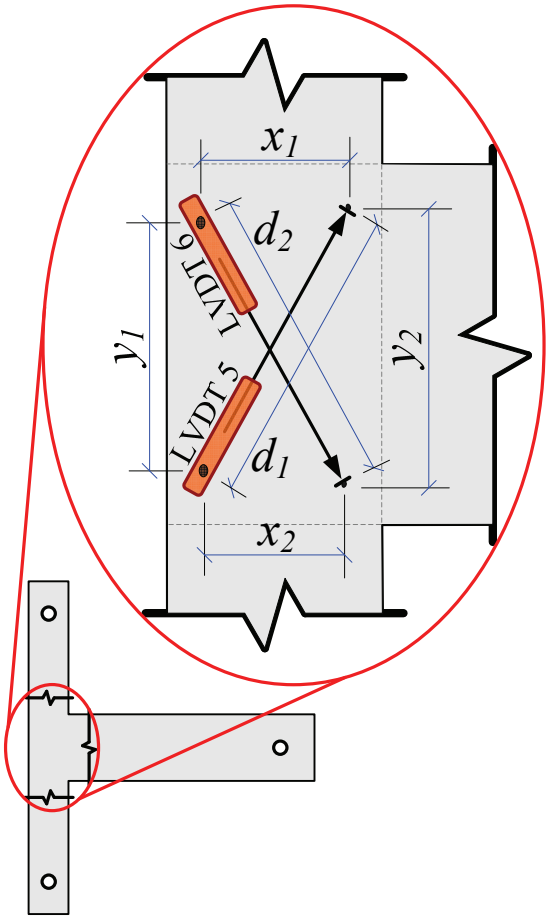


Figure 3.33. LVDT locations for measurement of joint shear deformation

Table 3.7. LVDT locations for measurement of joint shear deformation

Specimen Name	x_1 mm	x_2 mm	y_1 mm	y_2 mm	d_1 mm	d_2 mm
US2	205	220	400	400	458	488
US2-FRP2	190	190	370	380	425	420
US3	215	190	395	405	435	460
US3-FRP3	170	200	310	310	375	345
US4	200	220	400	410	450	465
US4-FRP3	175	158	367	370	404	405

Curvatures of the members were measured through the use of LVDTs shown in Figure 3.34. Below, the top column curvature value is calculated, as an example. All other members' curvature values can be calculated in the same way.

LDVT 11 and LVDT 12 were used to measure the curvature of the top column. Δ_{11} and Δ_{12} are the respective displacement measurements of these LDVTs'. Summation of g_1, g_2 and the column width, w_c, gives the total length between LVDT 11 and LVDT 12. ε_{11} and ε_{12} are the strain values within the length of measurement of LVDT 11 and LVDT 12 and are calculated as follows:

$$\varepsilon_{11} = \frac{\Delta_{11}}{e_1}, \qquad \varepsilon_{12} = \frac{\Delta_{12}}{e_2} \tag{3.6}$$

Thus the top column curvature, φ, is calculated with the following equation:

$$\varphi = \frac{\varepsilon_{11} - \varepsilon_{12}}{g_1 + g_2 + w_c} \tag{3.7}$$

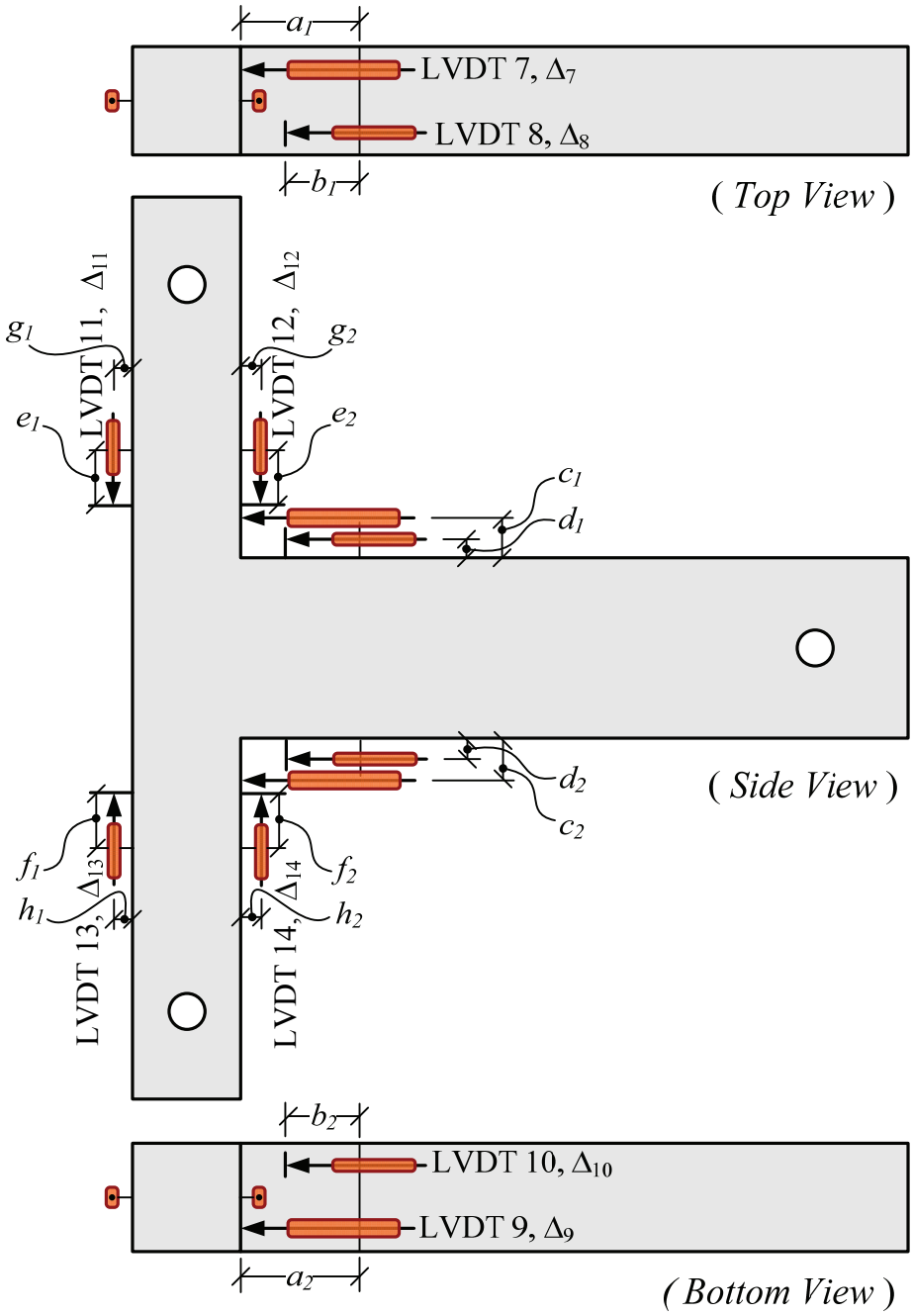


Figure 3.34. LVDT locations used as a curvature measurement

Additional LVDT was used to measure the slippage of the shortly embedded beam bottom longitudinal reinforcement. This was achieved by leaving a 10 mm plastic tube in the concrete during casting. One end of the tube was touching the tip of the shortly embedded reinforcement and the other end was extended through the formworks. After curing of the concrete, a hole was formed such that the tip of the LVDT can penetrate

through the hole. The slippage value was measured with respect to the back face of the column. The measurement procedure is shown in Figure 3.35.

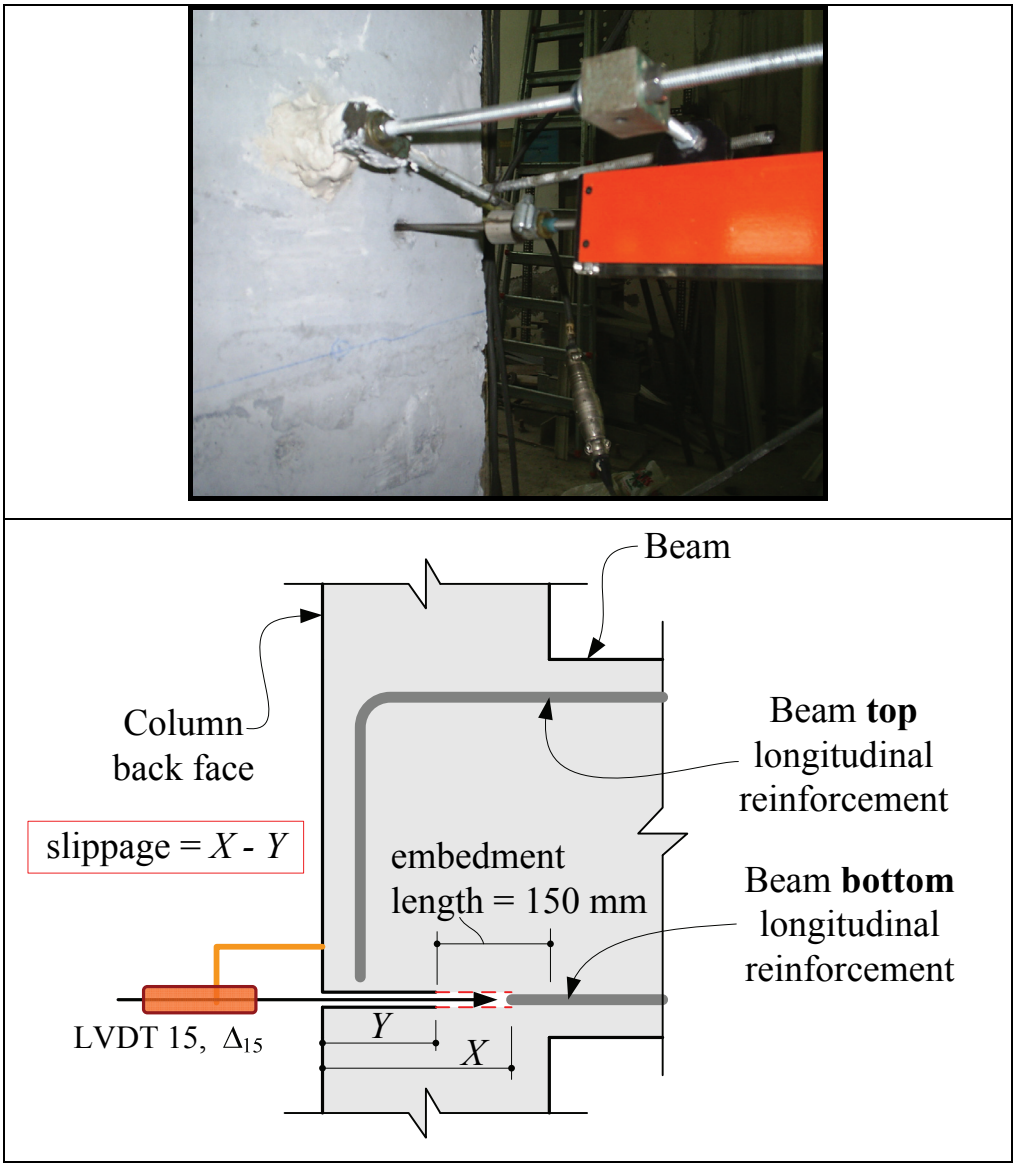


Figure 3.35. Measurement of slippage

Foil type strain gauges were installed on both steel and CFRP sheet reinforcements to determine the strain levels of the steel and CFRP materials throughout the testing. Strain gauges were mounted on the expected maximum stress regions. Typical locations of strain gauges, mounted on steel and CFRP reinforcement, are shown in a sketch in Figure 3.36 and Figure 3.37, respectively. Strain gauges are indicated with short thick red lines in the figures. Two different in length, 20 mm and 40 mm, strain gauges were used for the CFRP sheets.

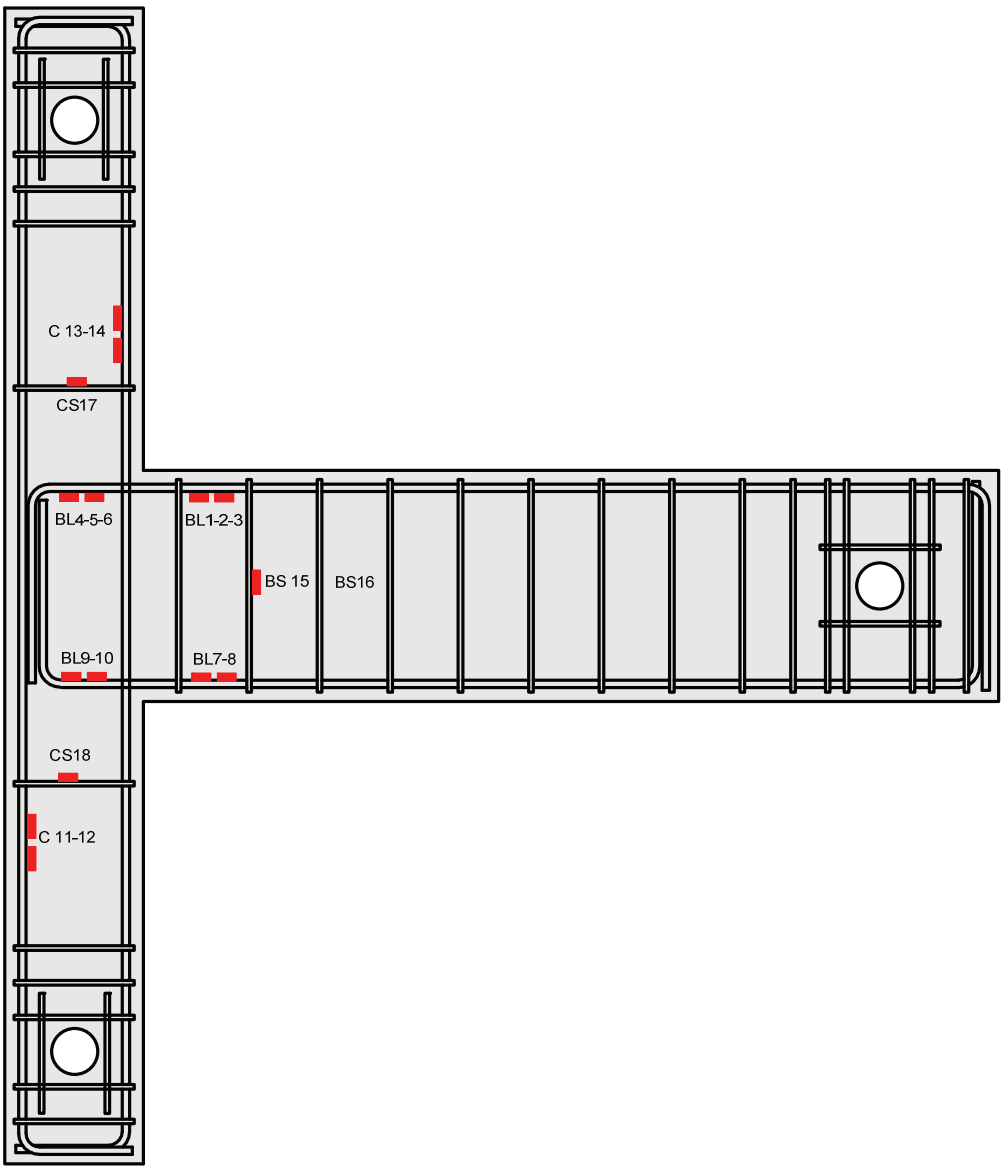
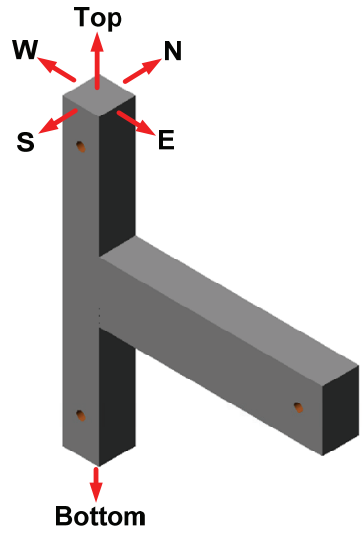
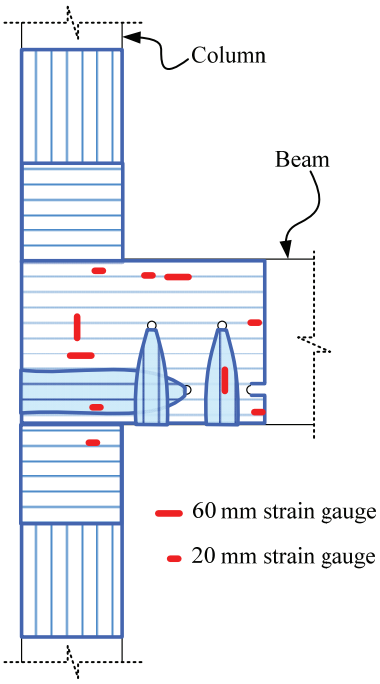


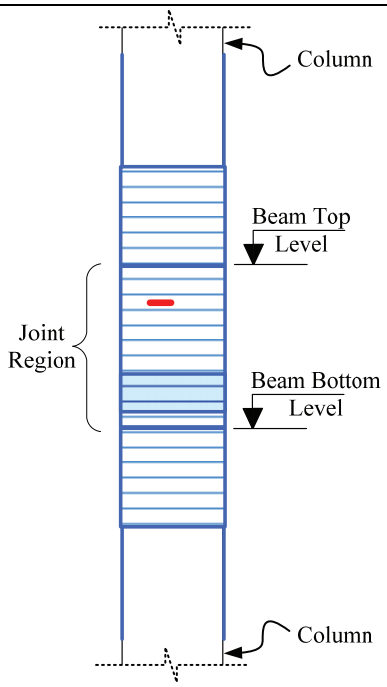
Figure 3.36. Typical strain gauge placement for steel reinforcement



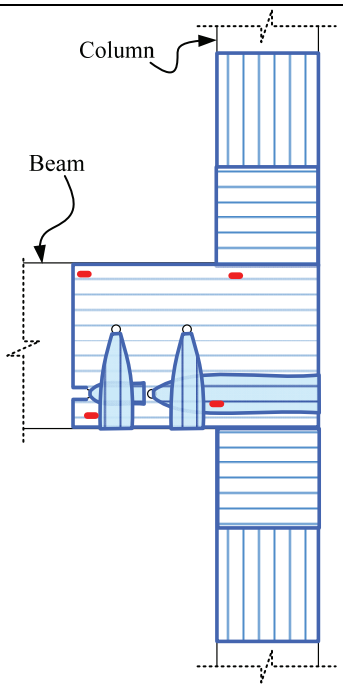
(a) 3D View



(b) South View



(c) West View



(d) North View

Figure 3.37. Typical strain gauge placement for CFRP sheet reinforcement

4. EXPERIMENTAL OBSERVATIONS AND RESULTS

4.1. General

In this chapter, experimental results of twelve full-scale reinforced concrete exterior beam-column joint specimens tested under reversed cyclic lateral loading are presented. Overall behavior of each test specimen is discussed in terms of load-displacement hysteresis response, joint shear deformation, member deformations, crack formation and failure modes. Energy dissipations and stiffness degradations of each specimen are calculated and presented. Monitored strain levels in the main steel reinforcements and CFRP sheets are discussed. Effectiveness of the wrapping configurations is evaluated through a comparison of ultimate drift and lateral load, stiffness degradations and amount of energy dissipations. For specimens with shortly embedded beam bottom longitudinal reinforcement, drift vs. slip and rebar slip vs. rebar strain responses are also presented in this chapter. Moment curvature relationships for the beam of all specimens are presented in the Appendix A and the strain levels developed on the beam longitudinal reinforcement are presented in Appendix B.

4.2. Overall Behavior and Load vs. Top Displacement Responses

In this section overall behavior of the test specimens is described. Mainly lateral load vs. top displacement responses and observation during testing are provided and modes of failure are discussed.

4.2.1. Specimen US1

General dimensions and reinforcement detailing of the control specimen US-1 is given in Section 3.4. Widely spaced transverse reinforcements and no shear reinforcement within the joint region were the main detailing deficiencies. The overall performance of the specimen during testing is described in the following.

Cracks of flexural nature were observed first at 0.20 % drift level along the beam and about 8 cm away from the column face. Observation of flexural cracks on the beam continued until 0.75 % drift level. Shear cracks at corners of the joint panel and some hairline cracks inside the joint core appeared at 0.75 % drift level, and later, expanded diagonally throughout the joint panel. The observed crack formation history is shown in Table 4.1. As seen in Figure 4.1, the lateral load levels reached a maximum of 62 kN and 76 kN at a level of 1.0 % of drift for push and pull direction of loading, respectively. After that drift level, strength degradation was observed due to excessive shear cracks at the joint region. At 1.75 % drift the test was aborted when the applied lateral load decreased to the 20 % of the maximum lateral load. Both in push and pull direction of loading the governing mode of failure was shear damage at the joint core. Therefore applied lateral load versus top displacement relationship is similar in shape for both directions of loadings. Pinched shape of the load-drift response is due to the closing and opening of the shear cracks at the joint region.

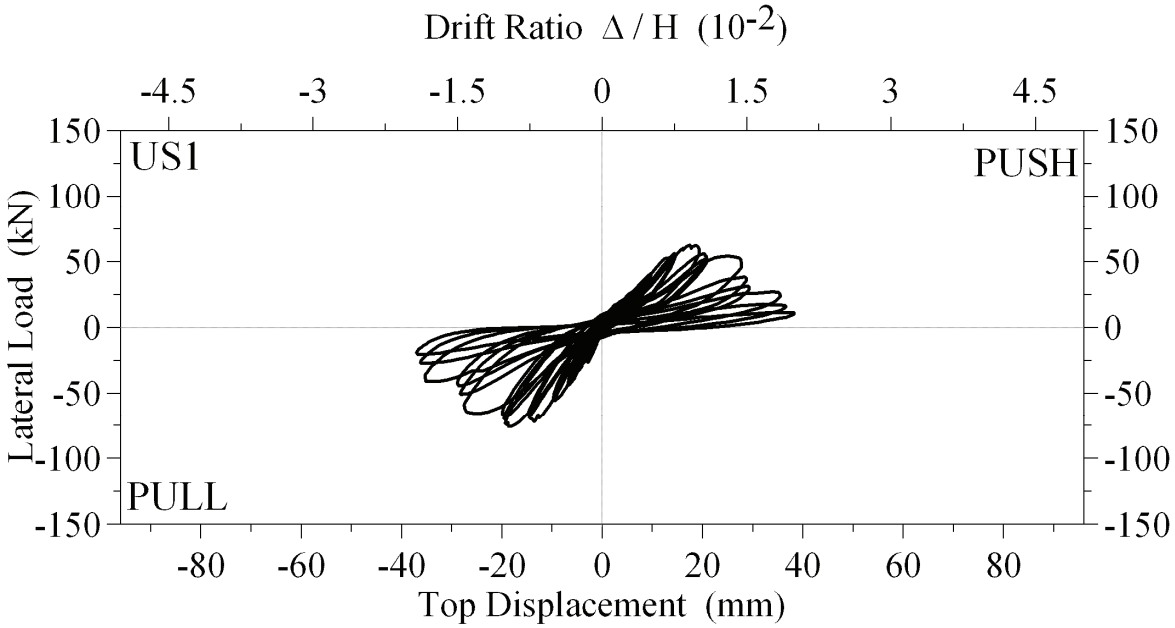


Figure 4.1. Lateral load vs. top displacement, US1

Table 4.1. Observations on specimen US1

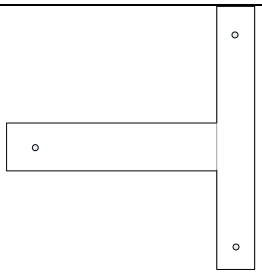
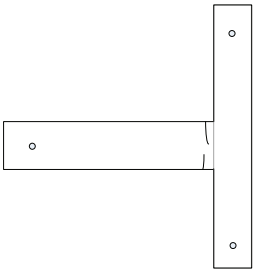
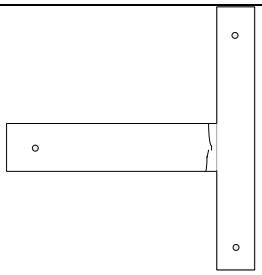
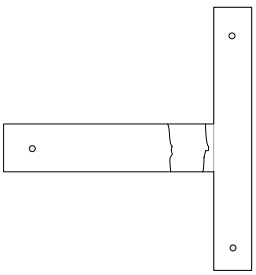
Drift (%)	Observations	Crack pattern
0.15	Maximum lateral load : (+) 17.00 kN (Push) : (-) 26.40 kN (Pull) No apparent cracks occurred.	
0.20	Maximum lateral load : (+) 20.50 kN (Push) : (-) 27.30 kN (Pull) **CR1** : Flexural crack formed at the bottom of the beam, 80 mm away from the column. Length of crack is 190 mm. **CR2** : Flexural crack formed at the upper side of the column, 60 mm away from the column. Length of it is 200 mm.	
0.25	Maximum lateral load : (+) 22.50 kN (Push) : (-) 32.50 kN (Pull) **CR1** : 40 mm extended. **CR2** : 40 mm extended.. **CR1** : Opening at the bottom of beam.	
0.35	Maximum lateral load : (+) 29.70 kN (Push) : (-) 44.00 kN (Pull) **CR1 & CR2 :** joined. **CR3** : Formed at the bottom of the beam, 360 mm away from the column and the length is 300 mm. **CR4** : Formed at the top of the beam, 400 mm away from the column and the length is 190 mm.	

Table 4.2. Observations on specimen US1 (continued)

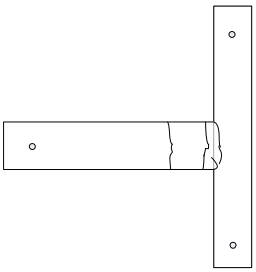
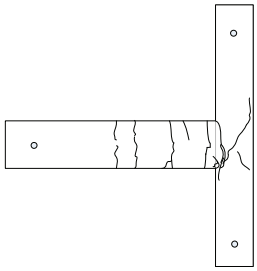
Drift (%)	Observations	Crack pattern
0.50	Maximum lateral load : (+) 40.80 kN (Push) : (-) 55.60 kN (Pull) **CR5** : Diagonal crack formed at the bottom of the joint region with the length of 120 mm. **CR6** : Shear crack formed at the top of the joint region with the length of 250 mm. **CR6** : Extended 180 mm towards to bottom of beam.	
0.75	Maximum lateral load : (+) 55.40 kN (Push) : (-) 68.90 kN (Pull) **CR6** : Extended 90 mm towards to bottom of beam. **CR3** : Doubled at the 45 mm away from the bottom of the beam. **CR7** : Formed at the bottom of the beam, 670 mm away from the column and the length is 270 mm. **CR6** : Doubled (90 mm). **CR8** : Flexural crack formed at the top of the beam, 240 mm away from the column. Length o crack is 190 mm. **CR7** : Reached to the top of the beam. **CR9** : Flexural crack formed at the top of the beam, 820 mm away from the column. Length o crack is 160 mm. **CR10** : Shear crack formed at the joint region, Length is 410 mm. **CR11** : Flexural crack formed at the bottom of the beam, 800 mm away from the column. Length o crack is 220 mm. **CR5** : Doubled. **CR6** : Doubled (70 – 80 mm). **CR10** : Continue to propagation at the top of the beam (100 mm) **CR12** : 150 mm in length shear crack formed at the joint	

Table 4.3. Observations on specimen US1 (continued)

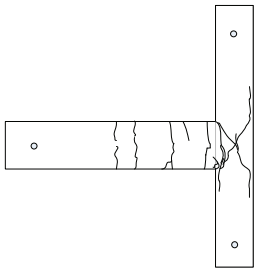
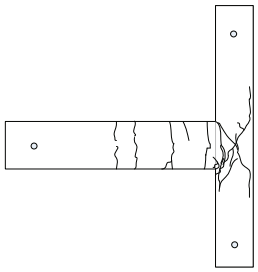
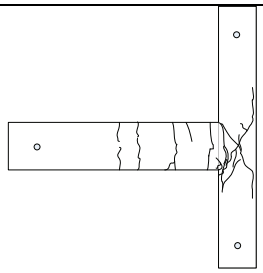
Drift (%)	Observations	Crack pattern
1.00	Maximum lateral load : (+) 60.40 kN (Push) : (-) 74.00 kN (Pull) **CR10 & CR6** : Joined. CR10 extended 200 mm towards to bottom. **CR13** : The symmetry of CR10 at the joint, shear crack. **CR6** : Extended 180 mm towards to bottom of beam. **CR12 :** Extended 150 mm and 100 mm towards to bottom and top of the beam respectiveley. **CR10** : Extended towards to top. **CR6** : Doubled. **CR14** : Occured at the back face of column and the length is 210 mm. **CR10** : Extended 50 mm towards to bottom. **CR12** : Extended en 50 mm towards to bottom.	
1.40	Maximum lateral load : (+) 52.80 kN (Push) : (-) 60.80 kN (Pull) **CR10** : Doubled at the top. **CR15** : Shear crack formed at he joint and bottom column, length is 250 mm. **CR10** : Extended 100 mm towards to bottom. **CR10 & CR15** : Joined. **CR16** : Vertical crack formed at the back face of column and the length is 270 mm. **CR17** : Vertical crack formed at the center of back face of column and the length is 270 mm. **CR18 :** Horizontal crack at the back face of column. **CR14 :** Extended towards to top. **CR17 :** Extended 80 mm towards to top. **CR6 :** Extended 160 mm towards to top. Swelling formed at the joint core	

Table 4.4. Observations on specimen US1 (continued)

Drift (%)	Observations	Crack pattern
1.75	Maximum lateral load : (+) 26.60 kN (Push) : (-) 40.80 kN (Pull) No additional cracks were observed.	

4.2.2. Specimen US2

Main detailing deficiencies of specimen US2 were inadequate anchorage length for the beam bottom longitudinal reinforcement and no shear reinforcement within the joint region. The followings describe the overall behavior of specimen US2.

At the very initial loading cycle, at drift level of 0.15%, a flexural crack formed at the maximum moment region at the bottom of the beam when the specimen was in push direction of loading. The moment value that caused this initial crack was approximately 27 kNm. In the next drift levels, having applied the load both in pull and push directions, additional hairline flexural cracks were observed both at top and the bottom of the beam as shown in Table 4.5. The first crack within the joint region was noticed at the 0.50% drift level at level of the beam bottom longitudinal reinforcement. This crack formed vertically just 5 cm away from the column face as shown in Table 4.5. Vertical formation of the crack was the first indication of slippage of the beam bottom longitudinal reinforcement that was shortly embedded into the joint. Slippage of the beam bottom longitudinal bar was also verified with the readings of the LVDT 15, shown in Figure 3.35, which was measuring the relative movement of the tip of the same reinforcement with respect to the column face. In Figure 4.2 monitored data of the relative movement readings of the rebar are presented. In the consequent drift levels, the slippage increased, and the bottom portion of the beam totally disintegrated from the column as shown in Figure 4.3.

In push direction of loading, between the drift levels of 0.50 % and 0.75 %, a sudden drop of the lateral load carrying capacity was observed as shown in Figure 4.4. This was mainly due the slippage of the beam bottom longitudinal reinforcement which was shortly

embedded into the joint. Maximum force in push direction of loading was approximately 40 kN and the corresponding drift level was 0.50 %.

In pull direction, the mode of failure and the behavior was different than in push direction of loading. Load applied to the top of the specimen in the direction of pull caused a negative moment in the beam which created a tension force in the beam top longitudinal reinforcement. The tensile force in the rebar was transferred to the joint region which created shear force in the joint core. Since the joint was not reinforced for shear, diagonal shear cracks at the joint core were observed as shown in Figure 4.3. Maximum lateral load recorded in pull direction of loading was 77 kN and the drift level corresponding to maximum load was 1.00%.

As mentioned above, mode of failure changes from one direction to another direction of loading as shown in Figure 4.5. In push direction of loading the specimen failed due to slippage of the beam bottom longitudinal reinforcement and in pull direction of loading the governing mode of failure was the excessive damage in the joint core.

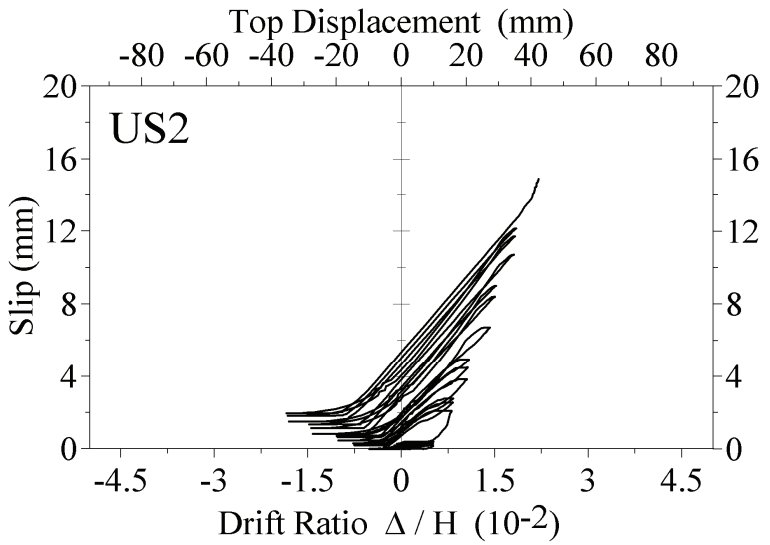


Figure 4.2. Slip vs. drift relationship of the beam positive reinforcement, US2

Table 4.5. Observations on specimen US2

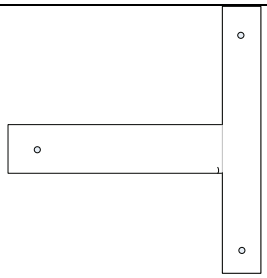
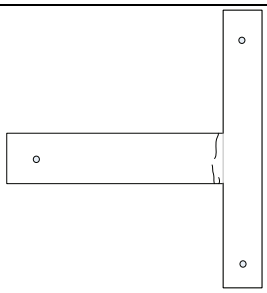
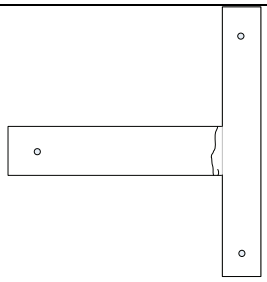
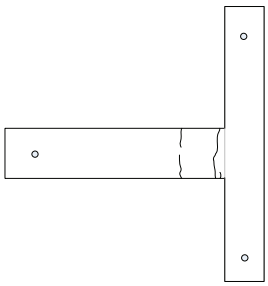
Drift (%)	Observations	Crack pattern
0.15	Maximum lateral load : (+)14.73 kN (Push) : (-)24.50 kN (Pull) **CR1**: Flexural crack formed at the bottom of the beam, 20 mm away from the column. Length of crack is 20 mm.	
0.20	Maximum lateral load : (+)21.60 kN (Push) : (-)31.00 kN (Pull) **CR2**: Flexural crack formed at the bottom of the beam, 60 mm away from the column. Length of crack is 180 mm. **CR3**: Flexural crack formed at the upper side of the beam, 30 mm away from the column. Length of it is 260 mm.	
0.25	Maximum lateral load : (+)25.00 kN (Push) : (-)36.00 kN (Pull) Concrete crushing at the bottom of the column **CR2 & CR3**: Joined	
0.35	Maximum lateral load : (+)29.70 kN (Push) : (-) 44.00 kN (Pull) **CR4**: Flexural crack formed at the bottom of the beam, 350 mm away from the column. Length of crack is 250 mm. **CR5**: Flexural crack formed at the bottom of the beam, 350 mm away from the column. Length of crack is 200 mm	

Table 4.6. Observations on specimen US2 (continued)

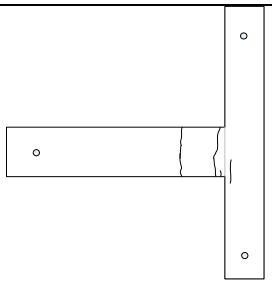
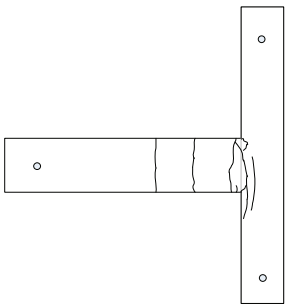
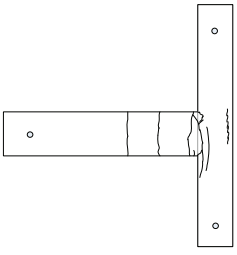
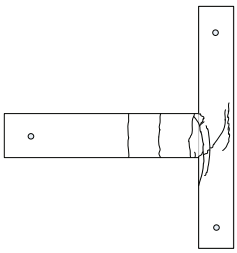
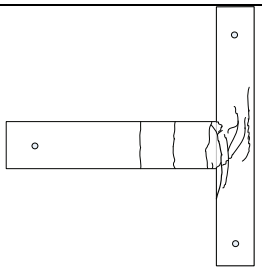
Drift (%)	Observations	Crack pattern
0.50	Maximum lateral load : (+)39.80 kN (Push) : (-)53.90 kN (Pull) **CR4 & CR5**: Joined **CR6**: Vertical crack formed in the joint region	
0.75	Maximum lateral load : (+)39.60 kN (Push) : (-)71.00 kN (Pull) **CR7**: Diagonal crack formed in he joint corner. Length is 100 mm. **CR6**: Extended 60 mm and 120 mm towards to up and down respectively. **CR6 & CR3**: Joined. **CR8**: Vertical crack formed at the joint, 100 mm away from the column. Length of the crack is 500 mm. **CR6**: Doubled. **CR9**: Flexural crack formed at bottom of the beam, 630 mm away from the column. Length o crack is 230 mm. **CR9**: Reached to the upside of the beam **CR7**: Reached to the top corner of the joint **CR8&CR6**: Concrete spalling.	
1.00	Maximum lateral load : (+)22.50 kN (Push) : (-)76.20 kN (Pull) **CR6**: Doubled. **CR10** : Vertical crack formed in the joint. Length is 500 mm. **CR11 :** Formed at the back face of the column, 60 mm away from the column front surface. Length is 280 mm.. **CR8**: Doubled. **CR12** : Horizontal crack formed at the back face of the column,. Length is 100 mm.. **CR6**: Crack width is 3.5 mm	

Table 4.7. Observations on specimen US2 (continued)

Drift (%)	Observations	Crack pattern
1.40	Maximum lateral load : (+)14.80 kN (Push) : (-)75.00 kN (Pull) **CR6** : Crack width is 7.0 mm **CR11**: Extended 70 mm and 30 mm towards to top and bottom of the beam respectively **CR13**: Length is 250 mm. **CR10**: Doubled All the cracks extended **CR12**: Extended 130 mm. **CR13**: Extended 90 mm from top. **CR11**: Doubled (50mm) and pass to the other side. **CR8** : Doubled.	
1.75	Maximum lateral load : (+)10.30 kN (Push) : (-)64.90 kN (Pull) No additional cracks were observed.	

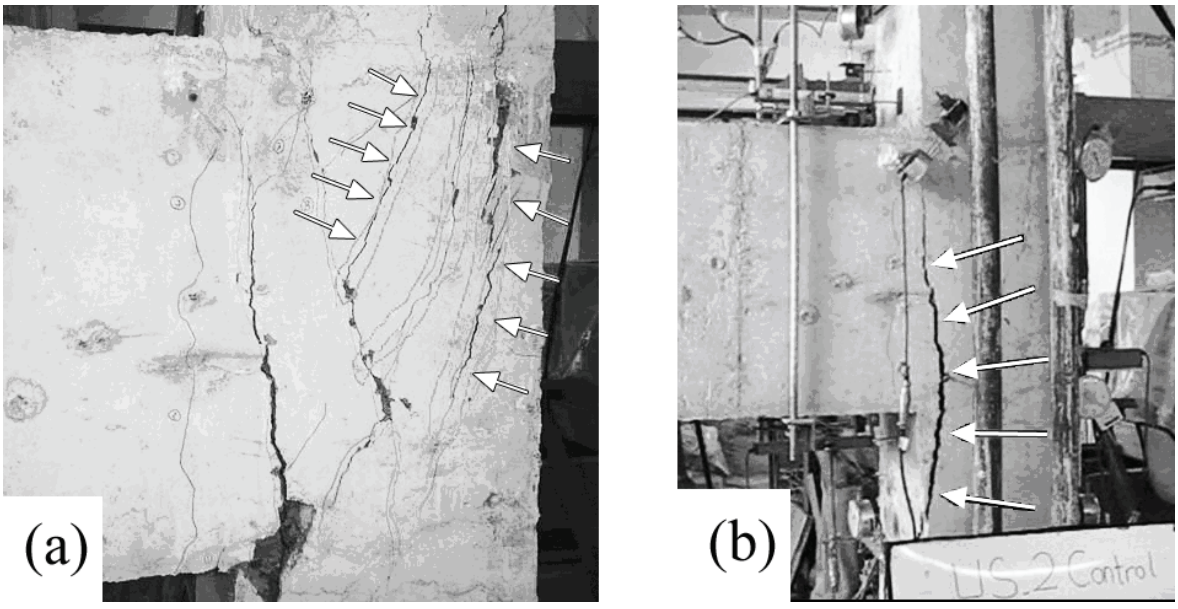


Figure 4.3. Failure modes; (a) pull, (b) push direction of loading

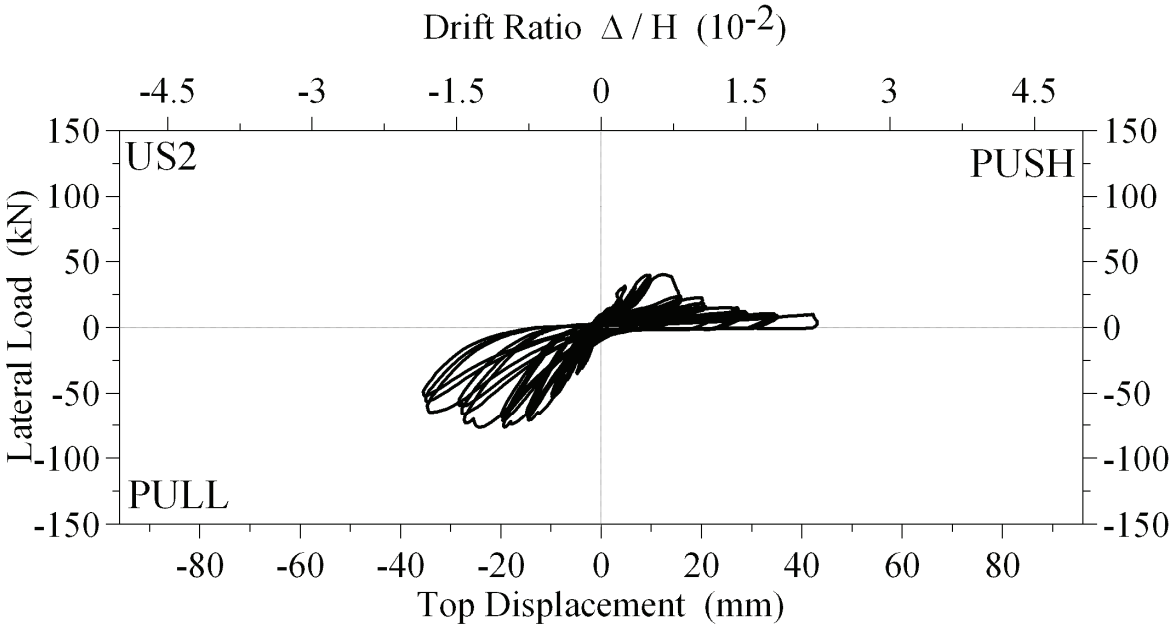


Figure 4.4. Lateral load vs. top displacement, US2

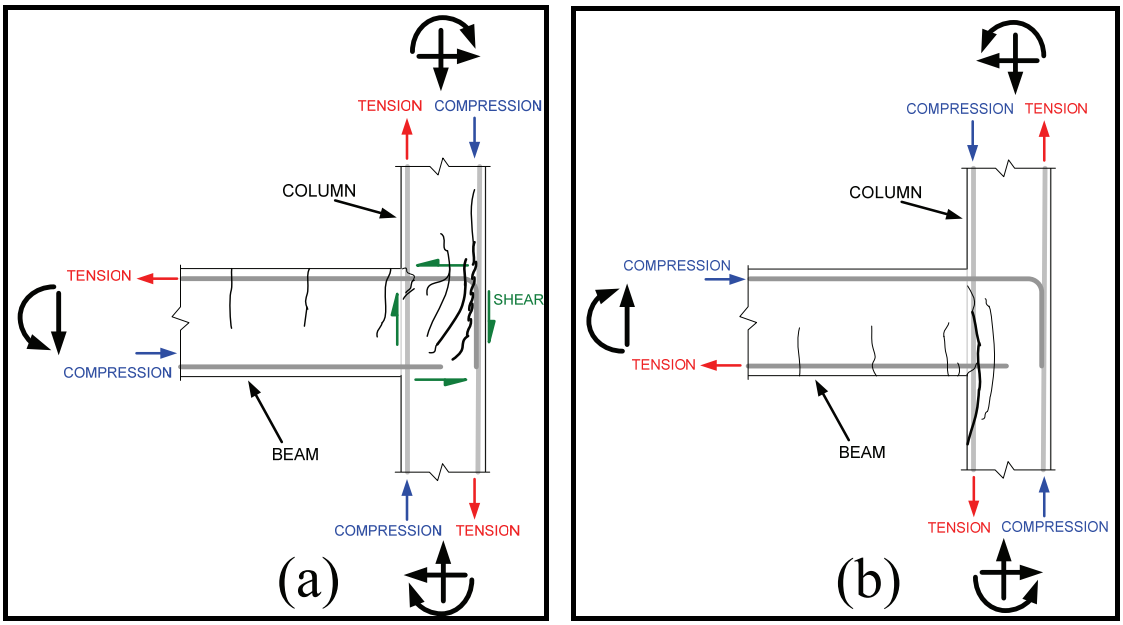


Figure 4.5. Crack pattern and internal forces; (a) pull, (b) push loading direction

4.2.3. Specimen US3

Column lap splicing just above the joint, inadequate embedment length of the beam positive reinforcement and no shear reinforcement within the joint region are the main reinforcement detailing deficiencies of specimen US3. The followings is the description of the specimen during testing.

First, a flexural crack was observed at the bottom of the beam, 70 mm away from the column face when the lateral load was 23 kN and the drift was 0.20%. Up to drift level of 0.50%, flexural cracks were observed only at the beam. In push direction of loading a vertical crack was observed within the joint region, at the level of the beam bottom longitudinal reinforcement. The applied lateral load was 42 kN and the corresponding drift level was 0.50 %. After this drift level the lateral load decreased gradually. The drop in the lateral load was due to the slippage of the beam positive reinforcement. The slippage of the beam positive reinforcement was monitored during the test as shown in Figure 4.6. In pull direction of loading, maximum of 80 kN lateral load was reached at 1.0% drift level. In pull direction of loading, shear damage at the joint core governed the mode of failure. The test was ended at the drift level of 1.75%, where the load carrying capacity decreased up to the 80% of the maximum lateral load. Load versus top displacement hysteretic response is shown in Figure 4.7 and in Table 4.8-Table 4.11 the crack pattern history is provided.

Table 4.8. Observations on specimen US3

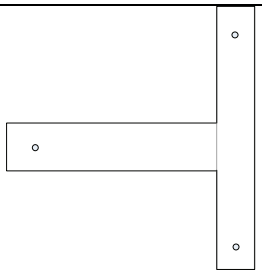
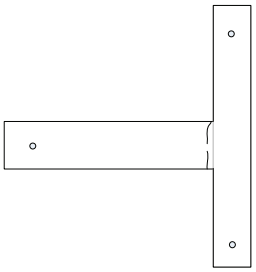
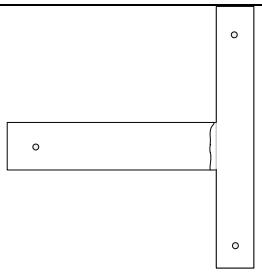
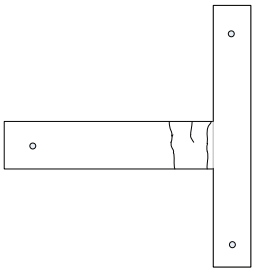
Drift (%)	Observations	Crack pattern
0.15	Maximum lateral load : (+) 17.50 kN (Push) : (-) 27.20 kN (Pull) No apparent cracks were observed.	
0.20	Maximum lateral load : (+) 22.40 kN (Push) : (-) 29.00 kN (Pull) **CR1** : 170 mm in length, flexural crack formed at the bottom of the beam, 70 mm away from the column. **CR2** : Flexural crack formed at the top of the beam, 10 mm away from the column. Length of it is 90 mm. **CR2** : Extended 100mm towards to down.	
0.25	Maximum lateral load : (+) 25.10 kN (Push) : (-) 34.30 kN (Pull) **CR1** : Extended 90 mm **CR1 & CR2** : Joined	
0.35	Maximum lateral load : (+) 32.50 kN (Push) : (-) 44.10 kN (Pull) **CR3** : Flexural crack formed at the bottom of the beam, 330 mm away from the column. Length of crack is 130 mm. The first slip readings in the positive moment rebars of beam **CR4** : Flexural crack formed at the top of the beam, 180 mm away from the column. Length of crack is 100 mm **CR5** : Flexural crack formed at the top of the beam, 370 mm away from the column. Length of crack is 285 mm **CR4** : Extended 40 mm **CR3 & CR5** : Joined	

Table 4.9. Observations on specimen US3 (continued)

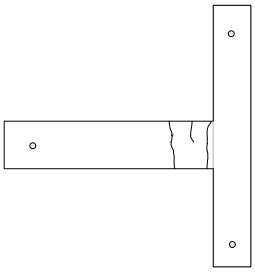
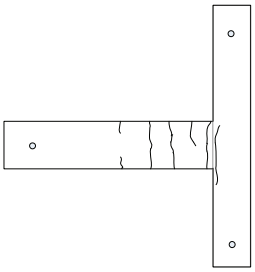
0.35	Maximum lateral load : (+) 32.50 kN (Push) : (-) 44.10 kN (Pull) **CR3** : Flexural crack formed at the bottom of the beam, 330 mm away from the column. Length of crack is 130 mm. The first slip readings in the positive moment rebars of beam **CR4** : Flexural crack formed at the top of the beam, 180 mm away from the column. Length of crack is 100 mm **CR5** : Flexural crack formed at the top of the beam, 370 mm away from the column. Length of crack is 285 mm **CR4** : Extended 40 mm **CR3 & CR5** : Joined	
0.50	Maximum lateral load : (+) 41.70 kN (Push) : (-) 56.00 kN (Pull) **CR6** : Flexural crack formed at the bottom of the beam, 520 mm away from the column. Length of crack is 260 mm. **CR7** : Flexural crack formed at the bottom of the beam, 780 mm away from the column. Length of crack is 110 mm. **CR8** : 225 mm Diagonal crack formed at the top of joint region **CR9** : Flexural crack formed at the top of the beam, 530 mm away from the column. Length of crack is 245 mm and joined to CR6 **CR10** : Flexural crack formed at the top of the beam, 770 mm away from the column. Length of crack is 150 mm **CR8** : Extended 270 mm , extended 130 mm **CR4** : Extended 40 mm.	

Table 4.10. Observations on specimen US3 (continued)

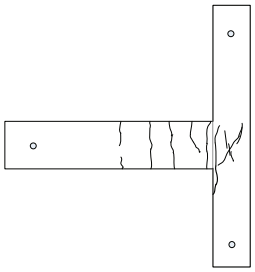
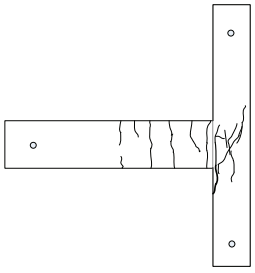
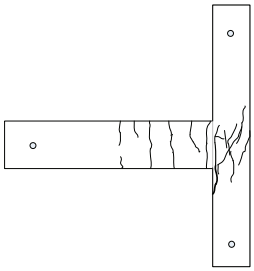
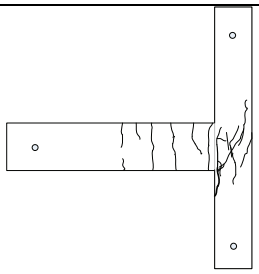
Drift (%)	Observations	Crack pattern
0.75	Maximum lateral load : (+) 38.70 kN (Push) : (–) 71.90 kN (Pull) **CR8** : Extended 60 mm, crack width is 1.0 mm **CR11** : Shear crack formed at the joint, length is 500 mm **CR11** : Doubled (190 mm). **CR12** : 200 mm, shear cracks formed at the joint **CR4** : Extended 110 mm diagonally. **CR10** :Extended 120 mm vertically **CR8** : Crushing	
1.00	Maximum lateral load : (+) 31.60 kN (Push) : (-) 79.00 kN (Pull) **CR12** : Extended 50 mm. **CR11** : Extended 80 mm towards to down. **CR11 :** Crack width is 1.0 mm. **CR13** : Formed in the joint length is 330 mm.. **CR11 :** Crushing. **CR12** : Extended 100 mm **CR14** : Vertical crack formed at the back face of column, 20 mm away from the front face and the length is 220 mm. **CR13& CR8** : Extended towards to down. **CR11** : Extended 150 mm towards to up and crushing. **CR15** : Flexural crack formed at the top of the beam, 660 mm away from the column. Length of crack is 180 mm. **CR14** : Extended 50 mm towards to up and down. **CR8** : Doubled.	

Table 4.11. Observations on specimen US3 (continued)

Drift (%)	Observations	Crack pattern
1.40	Maximum lateral load : (+) 21.00 kN (Push) : (-) 70.00 kN (Pull) **CR4** : Extended 30 mm **CR12** : Extended 160 mm towards to top **CR16** : Diagonal crack formed at the joint, length is 280 mm.	
1.75	Maximum lateral load : (+) 13.70kN (Push) : (-) 59.50 kN (Pull)	 

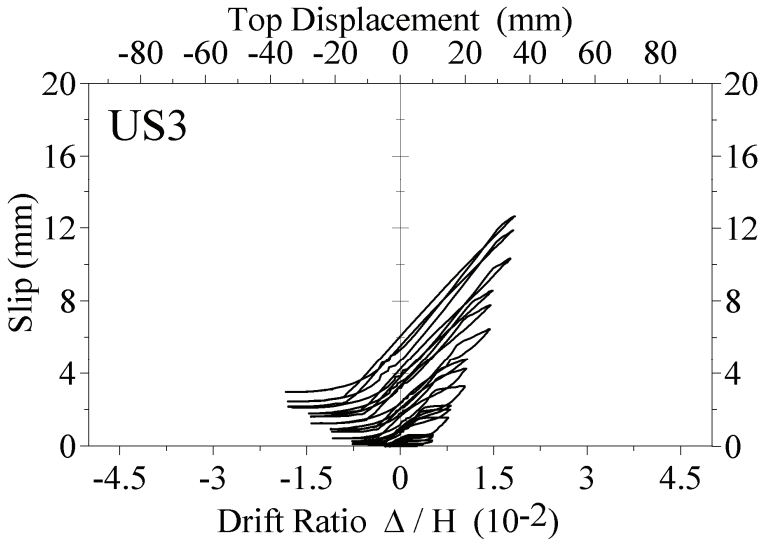


Figure 4.6. Slip vs. drift relationship of the beam positive reinforcement, US3

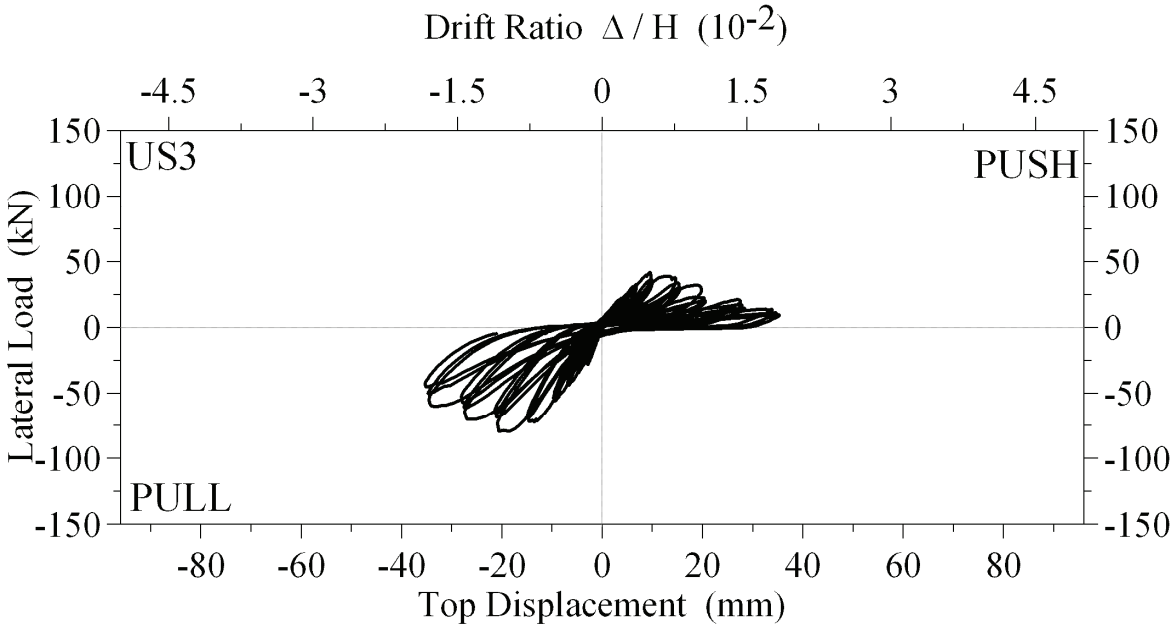


Figure 4.7. Lateral load vs. top displacement, US3

4.2.4. Specimen US4

Reinforcement detailing deficiencies of US4 were exactly the same as those in specimen US3. The only difference was the column axial load levels; 700 kN was applied to specimen US3 and 350 kN was applied to specimen US4.

Up to drift level of 0.75%, only flexural cracks were observed along the faces of the beam. Cracks mainly were formed at the top rather than the bottom of the beam. At drift level of 0.75% significant slippage of the beam bottom longitudinal reinforcement was observed as shown in Figure 4.8. At drift level of 0.75%, in pull direction of loading, the first shear crack inside the joint was observed. The angle of the crack with respect to the horizontal was approximately +60 degree as shown in Figure 4.9. Due to the slippage of the beam bottom longitudinal reinforcement, in push direction of loading, no shear cracks were observed at the joint core, since the beam bottom longitudinal reinforcement was unable to transfer adequate forces from the beam to the joint to cause any shear damage at the joint. An observation of shear cracks inside the joint region forming angles only of +60 degrees (not -60 degree) was not surprising, since the anchorage length provided to the beam top longitudinal reinforcement was adequate to transfer the forces from the beam to the joint. Once the force transfer is achieved with increasing drift levels, observation of

shear cracks inside the joint was unavoidable when there was no transverse reinforcement confining the joint core. The above mentioned phenomena are illustrated in Figure 4.5.

The maximum lateral load recorded during the experiment in push direction of loading was 35 kN which corresponded to drift level of 0.75 %. For pull direction of loading, the recorded maximum lateral load was 75 kN and the corresponding drift level was 1.00 %. As in the test results of US2 and US3, specimen US4 also failed due to slippage of the beam bottom longitudinal reinforcement and shear failure at the joint region, in push and pull direction of loading, respectively. The load versus top displacement hysteretic response is shown in Figure 4.10 and the crack formation history is given in Table 4.12. A picture taken at the end of the test is given in Figure 4.9.

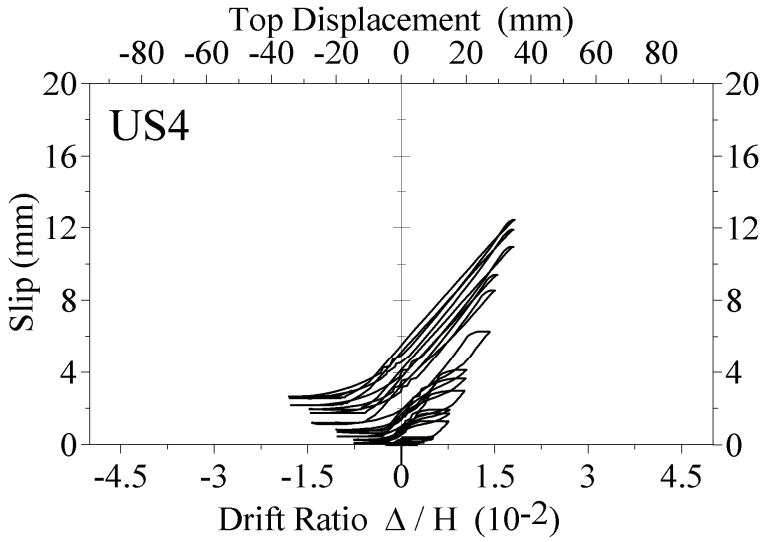


Figure 4.8. Slip vs. drift relationship of the beam positive reinforcement, US4

Table 4.12. Observations on specimen US4

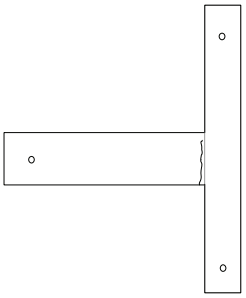
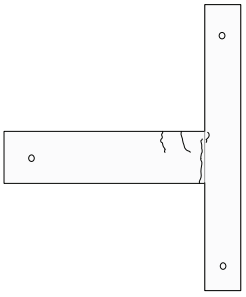
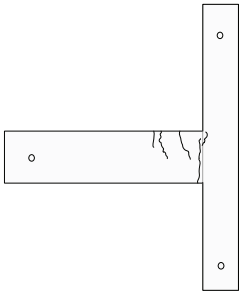
Drift (%)	Observations	Crack pattern
0.25	Max lateral load : (+)20.50 kN (Push) : (-)33.30 kN (Pull) **CR1**: Flexural crack formed at the bottom of the beam, 5 cm away from the column. Length of crack is 25 cm. **CR2**: Flexural crack formed at the middle of the beam, 3 cm away from the column. At the same drift level crack 1 and 2 joined and formed a single crack.	
0.35	Maximum lateral load : (+)24.00 kN (Push) : (-)43.10 kN (Pull) **CR3**: Flexural crack formed at the upper side of the beam, 21 cm away from the column. Length of the crack is 15 cm. **CR4**: Flexural crack formed at the upper side of the beam, 37 cm away from the column. Length of the crack is 21 cm. **CR5**: The first crack at the upper left corner of the joint region at the level of the beam top longitudinal reinforcement.	
0.50	Maximum lateral load : (+)32.20 kN (Push) : (-)55.30 kN (Pull) **CR6:** Flexural crack formed at the upper side of the beam, 53 cm away from the column. Length of the crack is 20 cm. • **CR3, CR4 and CR5:** Extended 8, 10 and 6 cm respectively.	

Table 4.13. Observations on specimen US4 (continued)

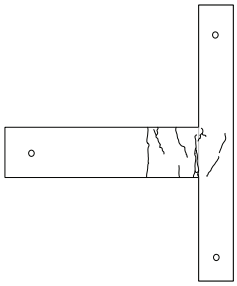
Drift (%)	Observations	Crack pattern
0.75	Maximum lateral load : (+)35.20 kN (Push) : (-)65.20 kN (Pull) **CR7:** A vertical crack formed at the bottom side of the beam, 3 cm away from the column. Length of the crack is 30 cm. Then this crack joined to **CR2**. **CR8:** A flexural crack formed at the bottom side of the beam, 53 cm away from the column. Length of the crack is 23 cm. **CR9:** A flexural crack formed at the bottom side of the beam, 20 cm away from the column. Length of the crack is 13 cm. • **CR1** Split into two cracks. • **CR6** and **CR8** Joined. **CR10:** A shear crack formed at the joint core, approximately 50^{o} with the horizontal. The length of the crack is 50 cm. • **CR3** extended 7 cm. • **CR5** split into two cracks. • **CR4** split into two cracks. • **CR10** split into two cracks. • **CR7** extended to the column face and also spalling of concrete was observed.	

Table 4.14. Observations on specimen US4 (continued)

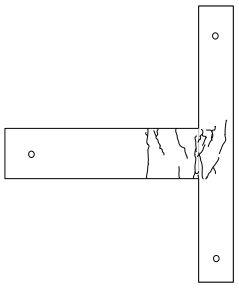
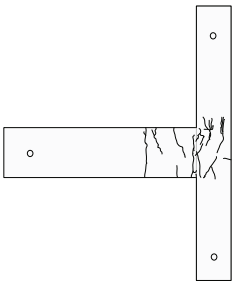
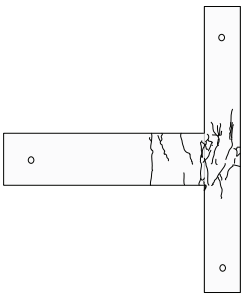
Drift (%)	Observations	Crack pattern
1.00	Maximum lateral load : (+)28.80 kN (Push) : (-)75.00 kN (Pull) **CR10**: Extended both to the up and bottom with 15 cm and 12 cm respectively. The same crack split into two. **CR11**: Shear crack in the joint region with a length of 10 cm. **CR12**: Shear crack in the joint region with a length of 12 cm. • **CR3** extended and **CR6** split into two **CR13**: This crack was observed in the joint region. The orientation was first horizontal but then the crack extended in the vertical direction. Forming a shape of inverted "C". Approximate length of the crack was 15 cm. • Separation between the column and the beam was observed where **CR7** is located. • The upper side of **CR13** split into two and the bottom side of the crack extended 18 cm. • At the interface between the column and the beam, swelling of the concrete cover was observed. **CR14:** On the west face of the column at the level of the bottom longitudinal reinforcement a horizontal crack is observed.	

Table 4.15. Observations on specimen US4 (continued)

Drift (%)	Observations	Crack pattern
1.40	Maximum lateral load : (+)18.20 kN (Push) : (-)64.40 kN (Pull) • Crack **CR13** split into two and extended 20 cm to the upper side. • Crack **CR10** extended 10 cm. • Crack **CR14** split into two and extended to the north and south face of the specimen. **CR15**: Horizontal crack formed at the west face of the column, 30 cm in length. **CR16**: Vertical crack at the west face of the specimen distance from the north face was 25 cm and the length of the crack was 23 cm. • Crack **CR14** extended to the bottom on the north face of the specimen. The extension was 11 cm. • *After this drift level, bottom column curvature readings are not correct. Since the concrete cover at this level expanded (initiation of spalling).*	
1.75	Maximum lateral load : (+)9.80 kN (Push) : (-)52.70 kN (Pull) **CR17**: Vertical crack at the joint region with length of 6 cm.	

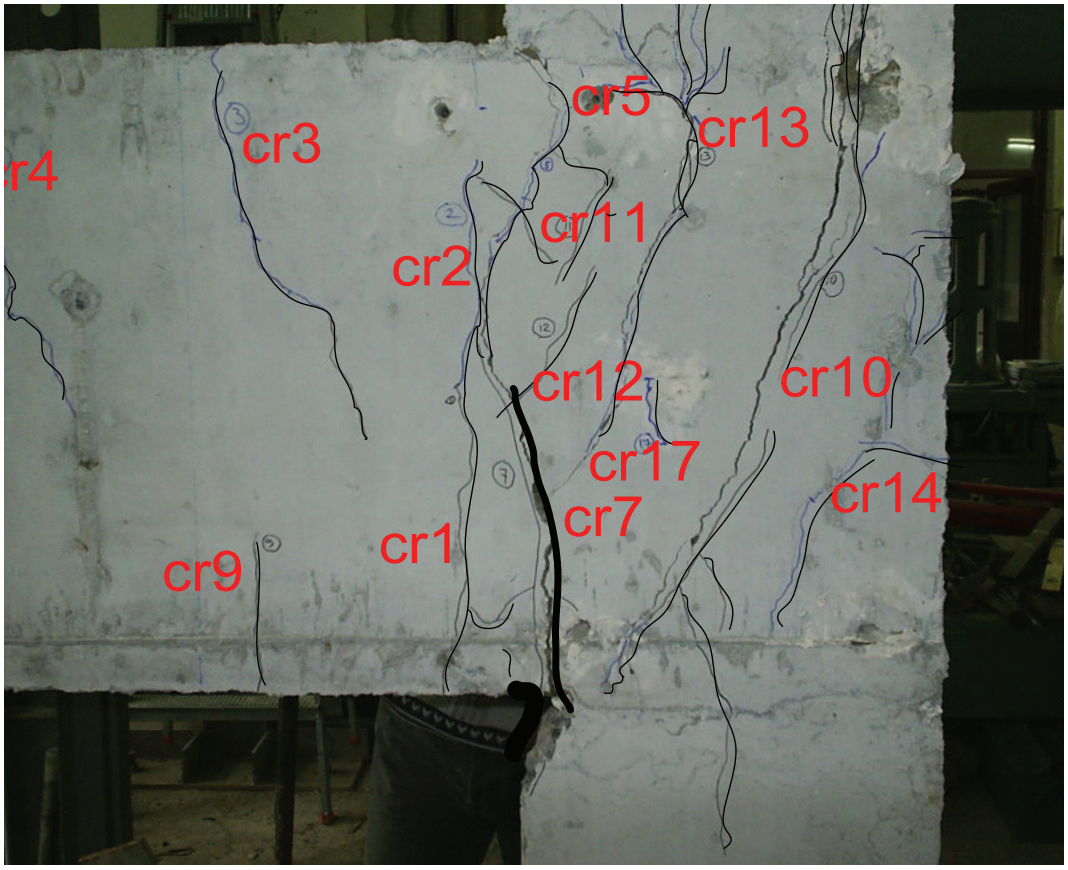


Figure 4.9. Crack pattern at the end of test US4

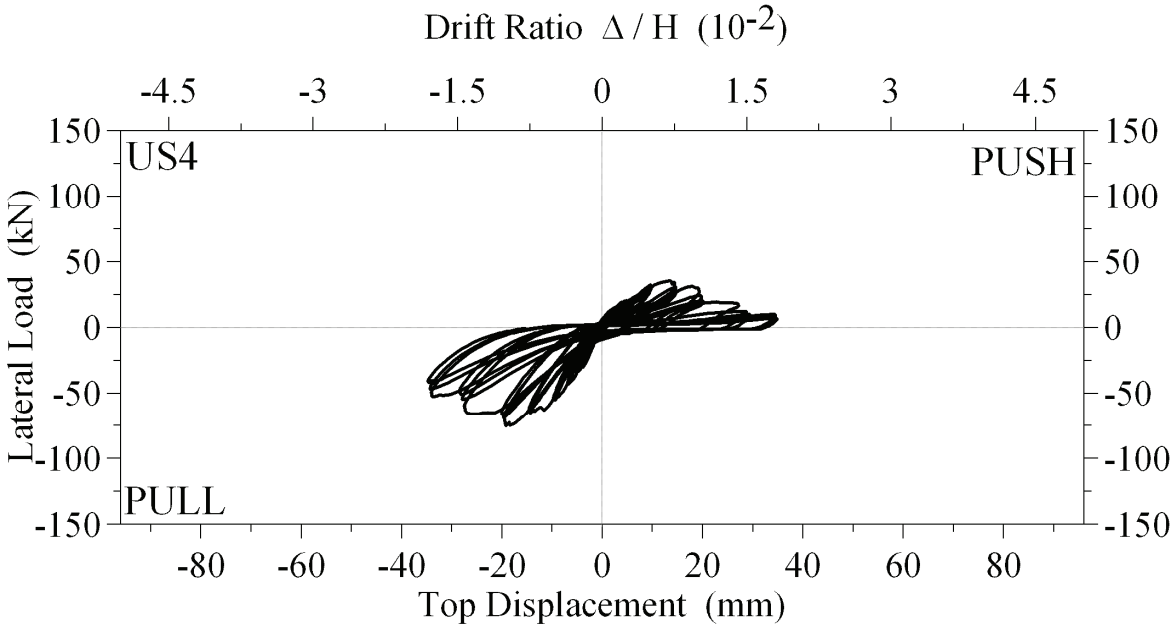


Figure 4.10. Lateral load vs. top displacement, US4

4.2.5. Specimen US1-FRP1

Specimen US1-FRP1 had a reinforcement detailing exactly as US1 and it is strengthened with wrapping configuration FRP1. The followings are the descriptions of the behavior during testing.

Due to the CFRP sheets existence, the cracks formed at the joint region could not be observed. The first observed crack was at the top of the beam, 350 mm away from the column surface just at the end of the wrapped region, in pull direction of loading and at a drift level of 0.25%. Corresponding load was 47 kN. Up to the drift level of 2.20 %, flexural cracks on the beam were observed away from the CFRP wrapped region. In the same drift level, diagonal CFRP sheets debonded from the beam. Some minor rupture of the CFRP sheet was also noted. However, no significant drop in the load was observed. As shown in Figure 4.11, a ductile behavior was achieved with maximum load of 100 kN and 141 kN for push and pull directions respectively. Plastic hinging at the beam formed approximately 110 cm away from beam support. Maximum moment levels observed at the hinging zone were approximately 145 kNm and 203 kNm. Strain response of the beam top longitudinal reinforcement is illustrated in Figure 4.12. Due to the stroke limitations, the test was stopped at the drift level of 3.50% without observing any significant strength degradation. In Table 4.16 observations during and after testing are presented.

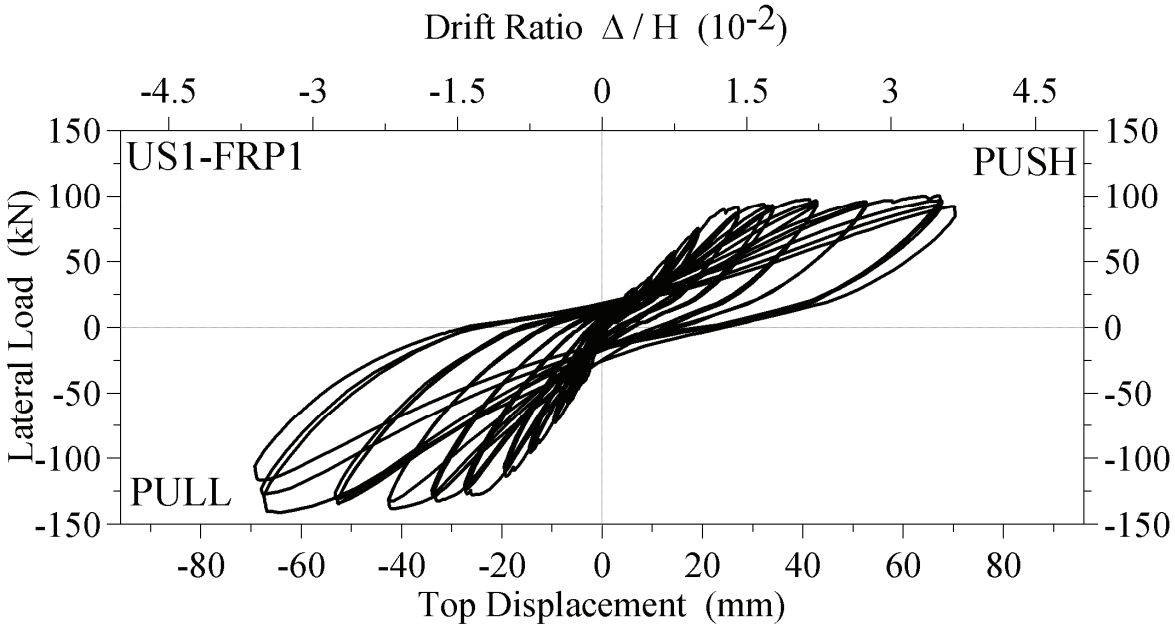


Figure 4.11. Lateral load vs. top displacement, specimen US1-FRP1

Table 4.16. Observations on specimen US1-FRP1

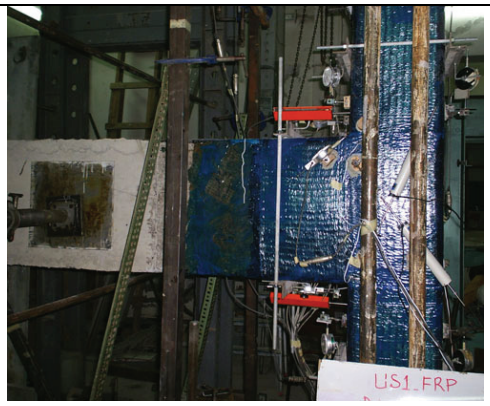
Drift (%)	Observations	Crack patterns & CFRP failure
0.20	Maximum load: + 18 kN (push) - 40 kN (pull) No apparent cracks were observed.	
0.25	Maximum load: + 23 kN (push) - 46 kN (pull) **CR1:** A single flexural crack was observed at the top of the beam where U-shaped CFRP sheet ends.	
0.35	Maximum load: + 29 kN (push) - 58 kN (pull) **CR2:** A flexural crack was observed at the bottom of the beam where U-shaped CFRP sheet ends.	
0.50	Maximum load: + 38 kN (push) - 73 kN (pull) **CR3:** A flexural crack was observed at the top of the beam approximately 48 cm away from the column face.	

Table 4.17. Observations on specimen US1-FRP1 (continued)

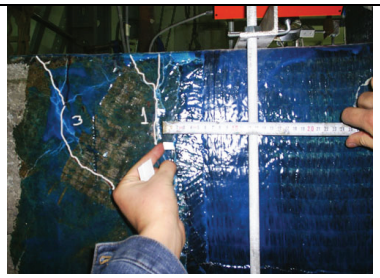
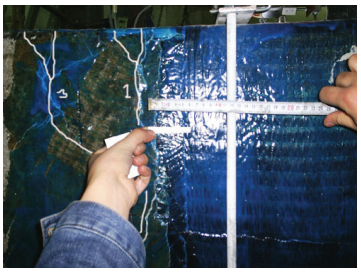
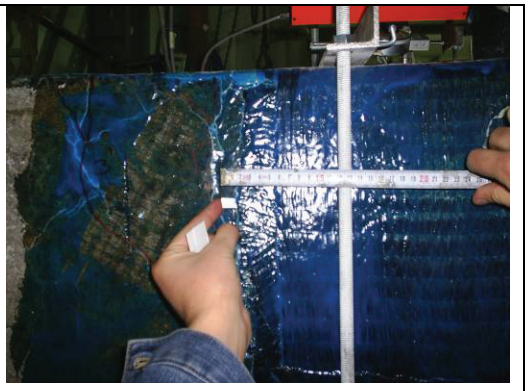
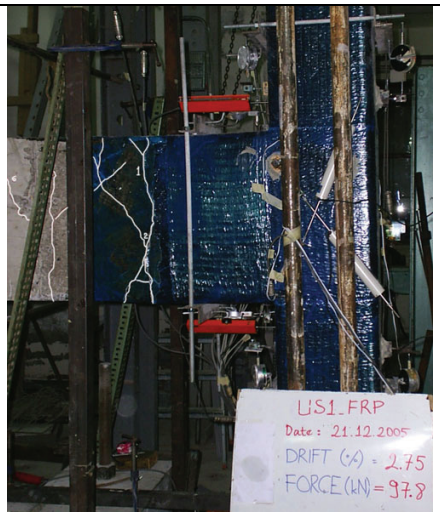
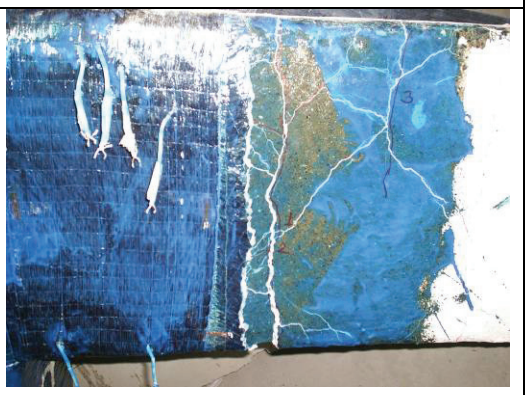
0.75	Maximum load: + 58 kN (push) - 95 kN (pull) No additional cracks were observed	
1.00	Maximum load: + 76 kN (push) - 113 kN (pull) Several flexural cracks were observed at the beam as seen in the figure on the right.	
1.40	Maximum load: + 91 kN (push) - 128 kN (pull) No additional cracks were observed. Crack widths of the existing cracks increased.	
1.75	Maximum load: + 93 kN (push) - 132 kN (pull) No additional cracks were observed. Widths of the existing cracks increased. Local debonding of the CFRP was observed at the face of the beam.	 

Table 4.18. Observations on specimen US1-FRP1 (continued)

2.20	Maximum load: + 96 kN (push) - 139 kN (pull) No additional cracks were observed. Local debonding of the CFRP was observed at the beam face.	
2.75	Maximum load: + 96 kN (push) - 140 kN (pull) No additional cracks were observed. Plastic hinging at the beam was observed as seen in the figure on the right.	
After test	The damage was observed at the beam	
After test	Rupture of CFRP was formed at the bottom corner of beam column intersection	

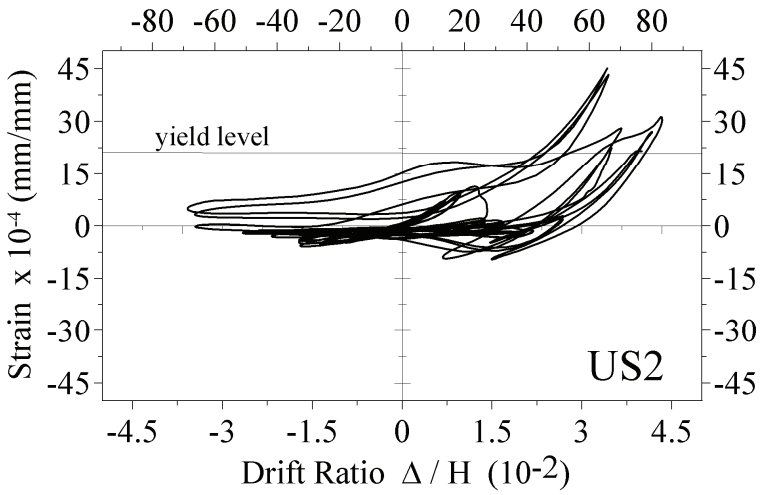


Figure 4.12. Drift vs. strain at beam negative reinforcement, US1-FRP1

4.2.6. Specimen US2-FRP2

Reinforcement detailing of US2-FRP2 is given Section 3.4. This specimen was retrofitted with FRP2 wrapping technique, described in Section 3.5.2 and the followings are the description of the experimental observation during testing. Since CFRP sheets are covered on the surface of the specimen, only CFRP free regions were observed.

In pull direction of loading and at a drift level was 0.50 %, the first flexural crack was noticed at the top side of the beam 67 cm away from the face of the column. In subsequent drift level both in push and pull direction of loading, additional flexural cracks were recorded at the top and bottom faces of the beam within a distance that U-shaped CFRP wrap was extending as shown in Table 4.19. As the experiment proceeded with the next drift levels, no additional cracks were observed up to the rupture of the U-shaped CFRP wrap. Then, at a level of 77 kN of push load, the bottom portion of the beam started disintegrating from the column as shown in Table 4.20. At a drift level of 2.20 % U-shaped ruptured from the bottom regions where the anchorage holes were located. In the same drift level, upper portion of the same CFRP sheet debonded from the face of the beam. In the last drift level, 2.75 %, lateral load carrying capacities for both direction of loading reduced suddenly due to total rupture and debonding of U-shaped CFRP wraps.

Both in push and pull direction of loading, lateral loads reached their maximums at drift level of 2.20%. Maximum lateral loads were approximately 80 kN and 120 kN for

push and pull direction of loading, respectively. In Figure 4.13, lateral load versus top displacement hysteresis are provided. Based on the overall observations and experimental data, it can be concluded that, for push direction of loading the rupture of the U-shaped CFRP was the governing incident. For the pull direction of loading the governing mode of failure was the debonding of the U-shaped CFRP wrap.

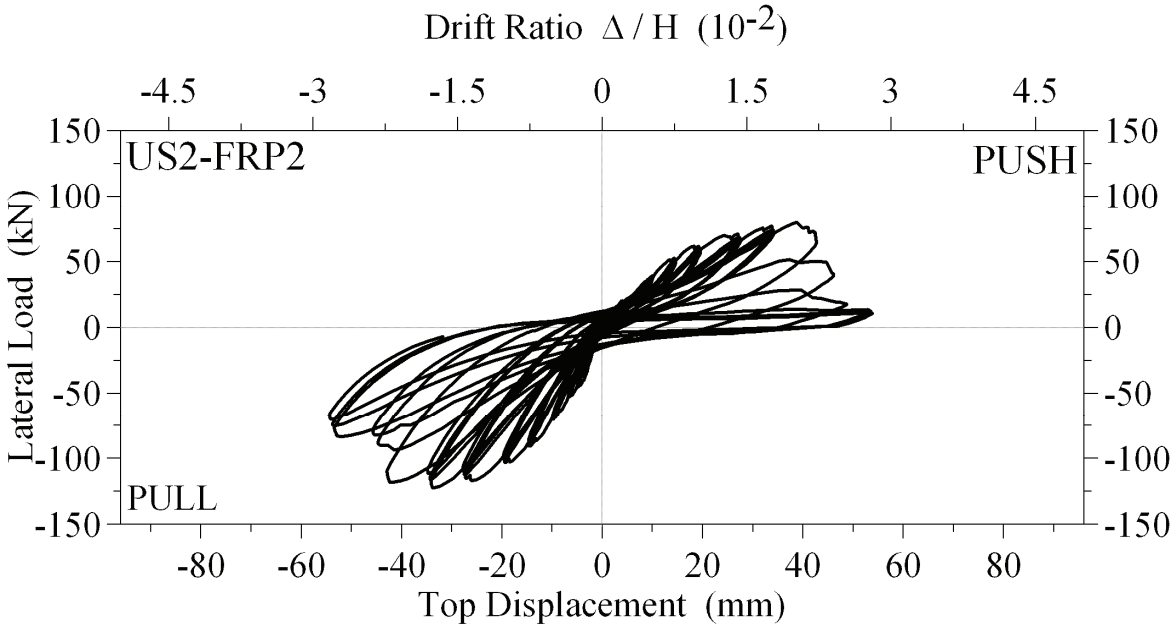


Figure 4.13. Lateral load vs. top displacement, US2-FRP2

Table 4.19. Observations on specimen US2-FRP2

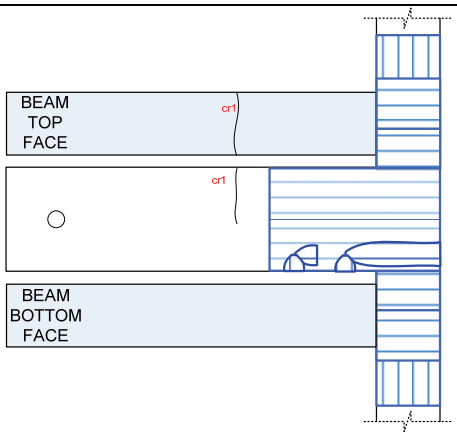
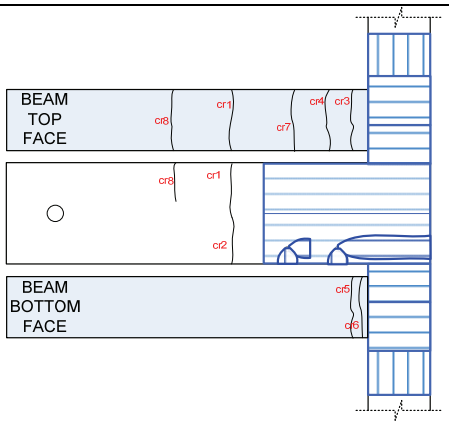
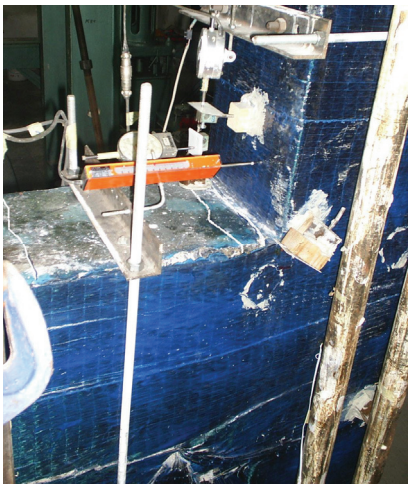
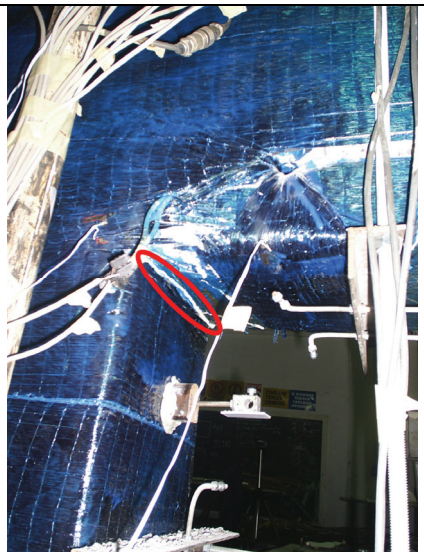
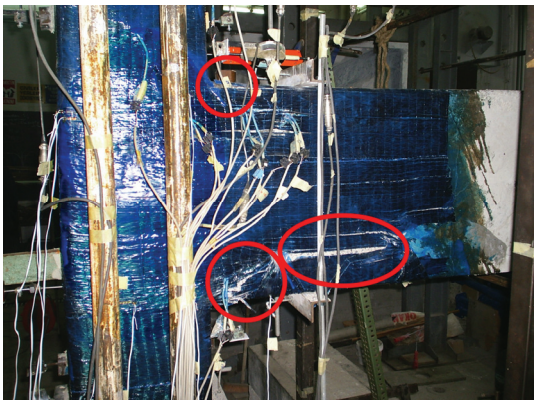
Drift (%)	Observations	Crack patterns & CFRP failure
0.50	Maximum load :(+)38.40 kN (Push) :(-)70.17 kN (Pull) **CR1:** First observable crack, 67 cm away from the column face starting from the top and 32 cm is extending to the bottom	
0.75	Maximum load :(+)52.50 kN (Push) :(-)90.50 kN (Pull) **CR2:** 67 cm away from the column face. **CR3:** At the beam top face 7 cm away from the column. **CR4:** At the beam top face 19 cm away from the column **CR5:** At the beam bottom face 7 cm away from the column **CR6:** At the beam bottom face 2 cm away from the column. **CR7:** At the beam top face 37 cm away from the column. **CR8:** At the beam top face 98 cm away from the column.	 

Table 4.20. Observations on specimen US2-FRP2 (continued)

Drift (%)	Observations	Crack patterns & CFRP failure
1.75	Maximum load :(+)76.83 kN (Push) :(-)122.18 kN (Pull) • Separation of the beam from the column is observed from the bottom.	
2.20	Maximum load :(+)79.75 kN (Push) :(-)118.24 kN (Pull) • U-shape CFRP ruptured, starting from the bottom up to the hole near to the column. • Top fibers of the U-shape CFRP ruptured • Mid section of the U-shape CFRP debonded. • Top portion of the U-shape CFRP debonded. • U-shape CFRP between the two anchorage holes ruptured. • Debonding of the mid section of the U-shape CFRP extended up to the column. U-shape CFRP buckled at the west face of the column, at the joint region.	

4.2.7. Specimen US3-FRP3

Up to drift level of 1.75% there were cracks only at the beam. The first flexural crack formed at top portion of the beam when the lateral load was 52 kN and the drift was 0.35 %. The moment value, causing this initial crack, was calculated as 63 kNm. Since the CFRP was applied on both sides of the beam, cracks that may be formed on the beam faces were not visible.

The debonding of U shape CFRP started from the top side portion of the beam when the drift level was 1.75%. Before the maximum load was reached, noises were heard revealing that there was debonding, and when the maximum load was reached, the CFRP totally debonded. The region of the debonded area and the crack pattern can be seen in Table 4.24 at drift level of 1.75%. This indicated that used anchorage length for the U-shaped CFRP sheet was inadequate.

First rupture of CFRP sheet was noticed at a drift level of 2.20 % on Strip 1. As shown in Table 4.24 the rupture length was approximately 1 cm. The complete rupture of three layers of U-shaped CFRP and a single layer of Strip 1 was observed at the drift level of 3.5%. From this drift level strength degradation initiated as shown in the lateral load versus top displacement relationship in Figure 4.14. The calculated moment that caused the rupture of three layers of U-shaped CFRP and one layer of Strip 1 was approximately 157 kNm.

At the end of testing the CFRP wraps were removed from the concrete surface for visual inspection. Several hairline cracks on the beam were observed. The main crack (the most wide and deep crack) was at the core of the joint region as shown in Figure 4.15. This crack indicated a shear failure at the joint but only in pull direction of loading since the crack was formed in only one diagonal of the joint. After the rupture of the CFRP sheets, inadequately embedment beam bottom longitudinal reinforcement slipped again as it the case of the control specimen US3. Tension force in the bottom rebar was not transferred to the joint, and thus it was unable to create shear forces within the joint.

Table 4.21. Observations on specimen US3-FRP3

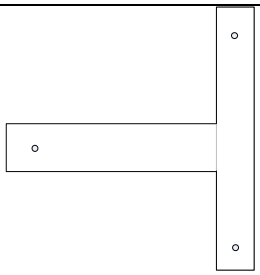
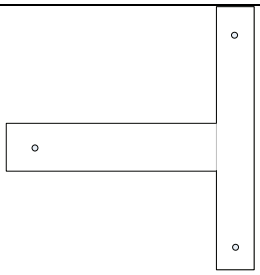
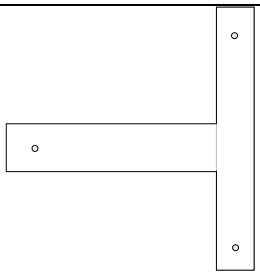
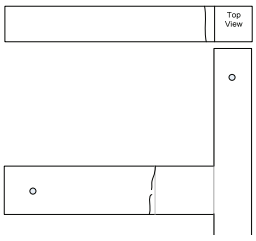
Drift (%)	Observations	Crack patterns & CFRP failure
0.15	Maximum lateral load :(+) 18.40 kN (Push) :(-) 26.60 kN (Pull) No apparent damage was observed.	
0.20	Maximum lateral load :(+) 22.60 kN (Push) :(-) 35.45 kN (Pull) No apparent damage was observed.	
0.25	Maximum lateral load :(+) 26.16 kN (Push) :(-) 42.20 kN (Pull) No apparent damage was observed.	
0.35	Maximum lateral load :(+) 30.60 kN (Push) :(-) 52.50 kN (Pull) **CR1 :** This is a flexural crack, formed in pull direction (at the top of the beam), and the location is 510 mm away from the face of the column. Crack length is 250 mm. **CR2 :** This is another flexural crack in pull direction 70 mm away from the face of the column. This crack was able to be observed only from the top. The crack can not be seen from the faces of the beam since CFRP was bonded. **CR3 :** In the same drift level but now in push direction a symmetrical crack of Cr1 formed.	

Table 4.22. Observations on specimen US3-FRP3 (continued)

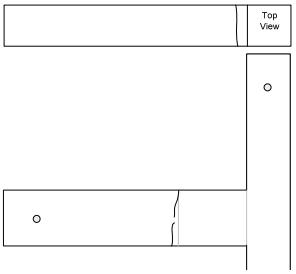
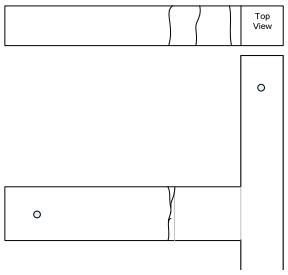
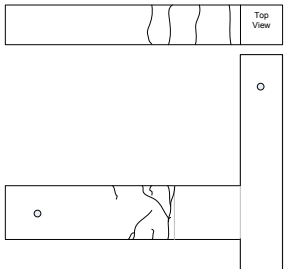
Drift (%)	Observations	Crack patterns & CFRP failure
0.35	Maximum lateral load : (+) 30.60 kN (Push) : (-) 52.50 kN (Pull) **CR1 :** This is a flexural crack, formed in pull direction (at the top of the beam), and the location is 510 mm away from the face of the column. Crack length is 250 mm. **CR2 :** This is another flexural crack in pull direction 70 mm away from the face of the column. This crack was able to be observed only from the top. **CR3 :** In the same drift level but now in push direction a symmetrical crack of Cr1 formed.	
0.50	Maximum lateral load : (+) 40.30 kN (Push) : (-) 68.20 kN (Pull) **CR3 and CR1 :** In this cycle, Cr1 and Cr3, two symmetrical cracks, connected each other (joined). **CR4 :** It was located 350 mm away from the face of the column and it was only visible from the top of the beam.	
0.75	Maximum lateral load : (+) 59.40 kN (Push) : (–) 85.50 kN (Pull) **CR5 :** In push direction a flexural crack formed. The distance from the face of the column is 660 mm and its length is 110 mm **CR6 :** In push direction, another flexural crack formed 820 mm away from the face of the column. The length of the crack was 290 mm. **CR7 :** In pull direction a flexural crack formed. The distance from the face of the column is 680 mm and its length is 310 mm. **CR8** : In pull direction a flexural crack formed. The distance from the face of the column is 650 mm. **CR9 :** It started from the top of the beam. The distance from the face of the column is 1000 mm and its length is 100 mm.	

Table 4.23. Observations on specimen US3-FRP3 (continued)

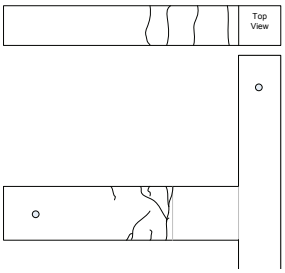
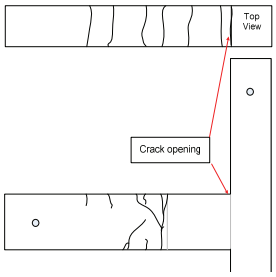
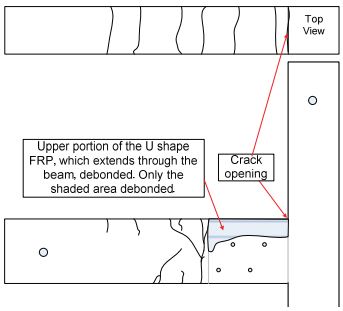
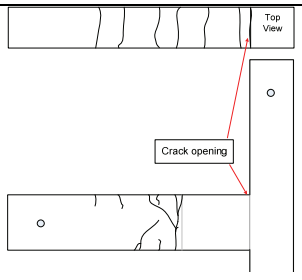
Drift (%)	Observations	Crack patterns & CFRP failure
0.75	Maximum lateral load : (+) 59.40 kN (Push) : (–) 85.50 kN (Pull) **CR5 :** In push direction a flexural crack formed. The distance from the face of the column is 660 mm and its length is 110 mm **CR6 :** In push direction, another flexural crack 160 mm away from Cr 5 or in other words 820 mm away from the face of the column formed. The length of the crack is 290 mm and in the subsequent cycles it forked. **CR7 :** In pull direction a flexural crack formed. The distance from the face of the column is 680 mm and its length is 310 mm. **CR8** : In pull direction a flexural crack formed. The distance from the face of the column is 650 mm. **CR9 :** It started from the top of the beam. The distance from the face of the column is 1000 mm and its length is 100 mm.	
1.00	Maximum lateral load : (+) 69.40 kN (Push) : (-) 101.30 kN (Pull)	
1.40	Maximum lateral load :(+) 83.70 kN (Push) :(-) 117.00 kN (Pull) **CRX :** Just at the connection of the beam and the column, a crack opening was observed. This crack was exactly at the top connection line see the sketch on the right. **CR10 :** 1150 mm away from the face of the column and 100 mm in length Cr10 was observed.	

Table 4.24. Observations on specimen US3-FRP3 (continued)

Drift (%)	Observations	Crack patterns & CFRP failure
1.75	Maximum lateral load : (+) 90.10kN (Push) : (-) 118.00 kN (Pull) Debonding was observed before the maximum drift level was reached It was about 200 mm away from the face of the column. Eventually at maximum drift level CFRP debonded totally as it is shown in the figure below.	
2.20	Maximum lateral load : (+) 92.70 kN (Push) : (-) 118.90 kN (Pull) Crack opening was measured as 3 mm at the connection, upper left corner of the joint shown on the table above, drift level 1.40%, as crack CrX. 10 mm from the bottom end of CFRP strip, which surrounds the column as belt ruptured.	
2.75	Maximum lateral load : (+) 93.00kN (Push) : (-) 110.70 kN (Pull) **CR3 :** The crack opening of Cr3 was noted as 4 mm. 50 mm from the bottom of CFRP strip, which surrounds the column as belt , and U shape CFRP that extends to the beam ruptured at this drift level.	
3.50	Maximum lateral load : (+) 62.87kN (Push) : (-) 87.96 kN (Pull) FRP strip, which surrounds the column as belt, and U shape CFRP that extends to the beam totally ruptured	

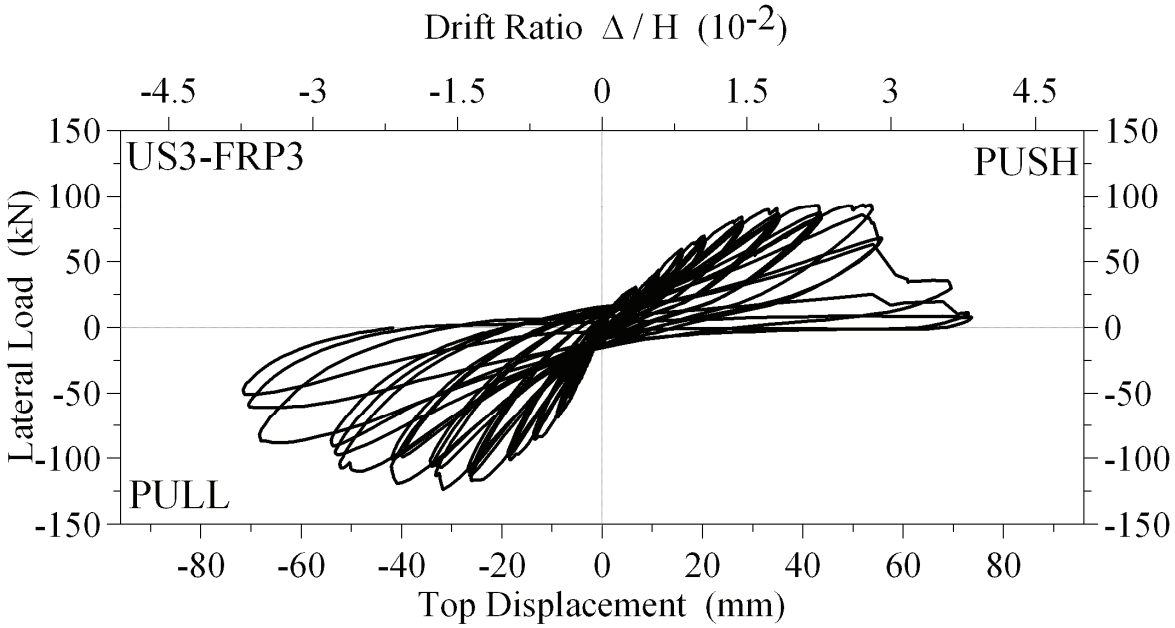


Figure 4.14. Lateral load vs. top displacement, US3-FRP3



Figure 4.15. Damage at the joint region after removal of the CFRP sheets

4.2.8. Specimen US4-FRP3

Reinforcement detailing and wrapping configuration of specimen US4-FRP3 was exactly the same as the detailing and wrapping configuration of specimen US3-FRP3. The only difference between these specimens was the level of column axial loads; column axial load for US4-FRP3 was loaded 350 kN and axial load of US3-FRP3 was 700 kN. Below, the overall behavior of specimen US4-FRP3 is presented.

As in the all CFRP wrapped specimens, during the experiment, it was possible only to observe the damage where no CFRP sheet was applied. These locations were the top and bottom of the beam and north and south faces of the beam but 45 cm away from the east face of the column as seen in Figure 3.26.

Up to drift level of 1.40 % several flexural cracks were observed from the south and north face of the beam. All of the cracks were at least 45 cm away from the column east face. In other words the cracks were not in the region where the U-shape CFRP sheet was applied. This indicated that the CFRP wrapped region is well strengthened. Up to 1.40 % drift level no debonding between the CFRP and concrete was observed. At drift level of 1.75% and when the specimen was in push direction of loading, the U-shaped CFRP debonded from the concrete at the region which is in between the top and bottom anchorage holes as shown in Table 4.25.

Prior to the debonding at the top portion of the U-shaped CFRP sheet, hairline cracks formed at the top face of the beam. This implied that the strain level just prior to the debonding was higher than the cracking strain of the concrete which caused cracking at the top face of the beam and no debonding of the U-shape CFRP sheet. At drift level of 2.20%, top portion of the U-shape CFRP sheet debonded from the top of the beam. When the U-shaped CFRP sheet debonded, a block of concrete, bonded to the CFRP sheet, came out from the beam. This indicated that the bond between the concrete and the CFRP sheet did not fail rather than that concrete failed from tension. In pull direction of loading, the maximum lateral load was 127 kN and in push direction of loading the maximum lateral load was 83 kN.

As shown in Figure 4.16, the direction of the cracks caused due to tensile stresses coming from the U-shaped CFRP sheet was not in the direction of a regular flexural crack. From this figure it is also possible to visualize the direction of the maximum stresses formed due to the bond stress between U-shaped CFRP sheet and the concrete of the beam.

At the same drift level (2.20% drift) rupture of the U-shape CFRP sheet started from the bottom of the beam. The location of the rupture was at the section where the maximum moment is observed when the specimen was in push direction of loading. The moment value caused the initiation of rupture was approximately 120 kNm.

After drift level of 2.20%, both in push and pull direction of loading the specimen started degrading. In push direction of loading the cause for the strength decrease was the rupture of the U-shaped CFRP from the bottom.

At drift level of 2.75% the rupture length of the U-shaped CFRP increased and that caused the initiation of the slippage of the beam bottom longitudinal reinforcement as shown in Figure 4.17. This was also the reason for the sudden drop of the load versus displacement relationship shown on Figure 4.18.

The failure mode for pull direction of loading was the debonding of the U-shape CFRP sheet from the top of the beam. Once the top portion of the U-shaped CFRP debonded, the damage started to propagate inside the joint core from the upper east corner of the joint. Thus, shear failure of the joint can be considered as a secondary failure mode for the pull direction of loading.

The experiment was continued up to drift level of 4.00 % at which the specimen have lost approximately 71 % and 52 % of its lateral load carrying strength for push and pull direction of loading, respectively. In Table 4.25 summary of the test observations is presented.

Table 4.25. Observations on specimen US4-FRP3

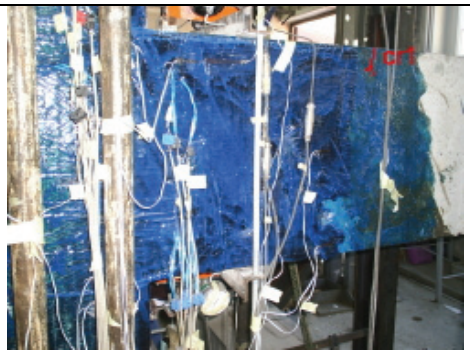
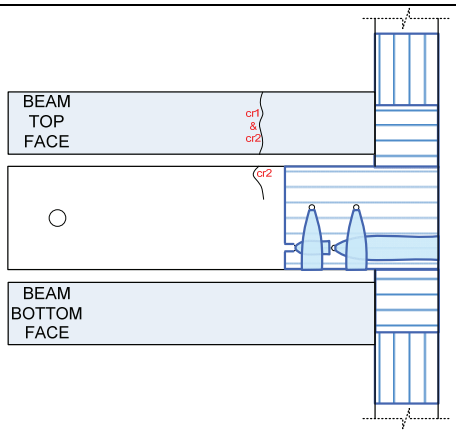
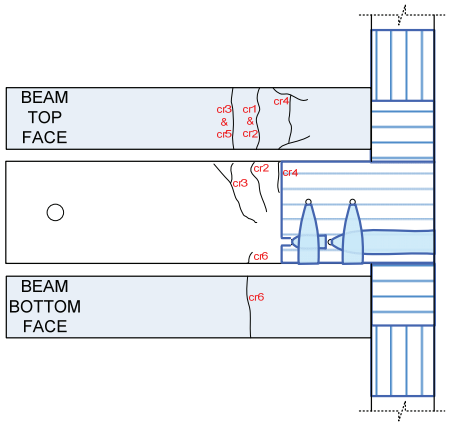
Drift (%)	Observations	Crack patterns & CFRP failure
0.35	Maximum load :(+)29.40 kN (Push) :(-)55.17 kN (Pull) **CR1:** First observable crack at the south face of the beam, 55 cm away from the column east face, which is starting from the top and it is extending 7 cm to the bottom.	
0.50	Maximum load :(+)37.07 kN (Push) :(-)65.19 kN (Pull) **CR2:** Flexural crack at the beam top side. This crack is approximately 55 cm away from the column east face and is 15 cm in length. The same as crack CR1 but on the north face of the beam.	
1.40	Maximum load :(+)72.54 kN (Push) :(-)118.40 kN (Pull) **CR3**: Occurred at the north face of the beam. This crack is 67 cm away from the face of the column with approximate length of 30 cm. **CR4**: Flexural crack of length 13.5 cm which formed at the top side of the beam. Adjacent to the U-shape CFRP sheet end. **CR5**: Its length and distance from the east face of the column is the same as CR3, but formed on the south face. **CR6**: This is a flexural crack which formed at the beam bottom side. Its length is approximately 5 cm and its distance from the column east face is 57 cm.	

Table 4.26. Observations on specimen US4-FRP3 (continued)

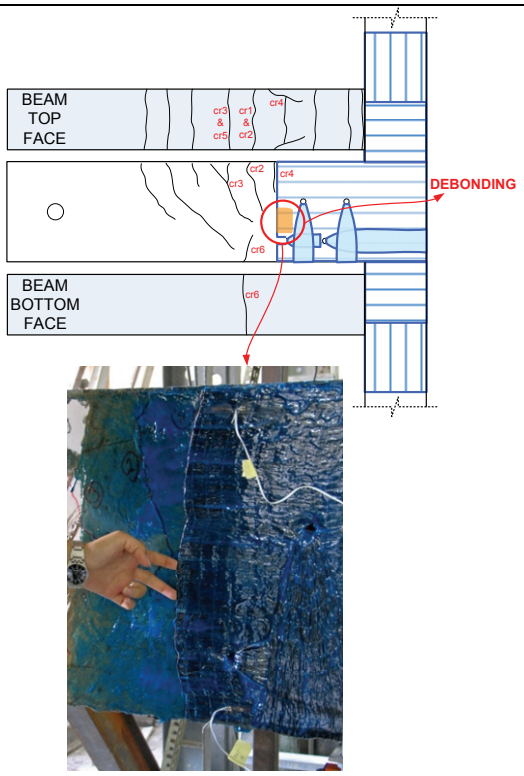
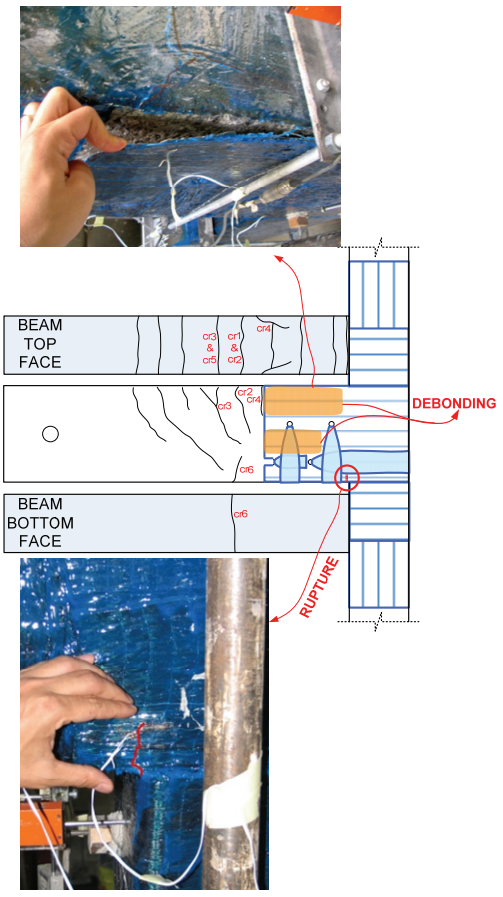
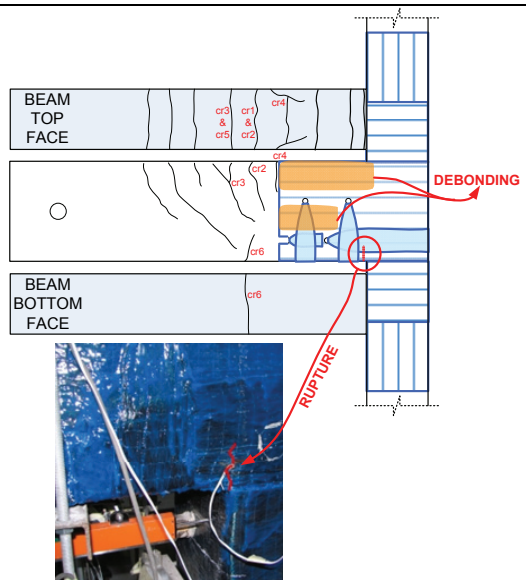
Drift (%)	Observations	Crack patterns & CFRP failure
1.75	Maximum load :(+)81.77 kN (Push) :(-)126.50 kN (Pull) • The middle portion of the U-shape CFRP sheet, between the top and bottom anchorage holes, debonded from the concrete of the north face of the beam. This was observed when the specimen was in push direction of loading	
2.20	Maximum load :(+)83.00 kN (Push) :(-)122.00 kN (Pull) • In pull direction of loading, when the lateral load was approximately 120 kN, the top portion of the U-shape CFRP sheet debonded from the concrete of the north face of the beam. • When the load increased to 122 kN also the U-shape CFRP sheet debonded from the concrete of the south face of the beam. • 3 cm from the bottom portion of the U-shape CFRP sheet ruptured. • Except regions around the anchorage holes, totally the U-shape CFRP sheet debonded from the concrete of the beam.	

Table 4.27. Observations on specimen US4-FRP3 (continued)

Drift (%)	Observations	Crack patterns & CFRP failure
2.75	Maximum load :(+)71.00 kN (Push) :(-)112.15 kN (Pull) • U-shape CFRP sheet ruptured from the bottom near to the beam column interface. Rupture was observed at both faces of the beam north and south. On the north face, the length of the rupture was 7 cm. On the south face rupture length was14 cm at the first cycle and 17 cm at the second cycle.	

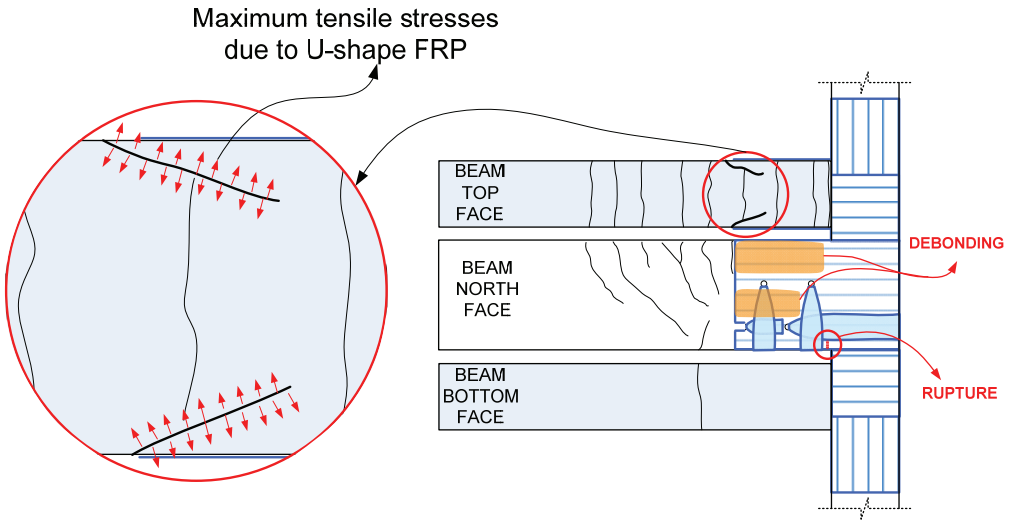


Figure 4.16. Stress distribution due to U-shaped CFRP

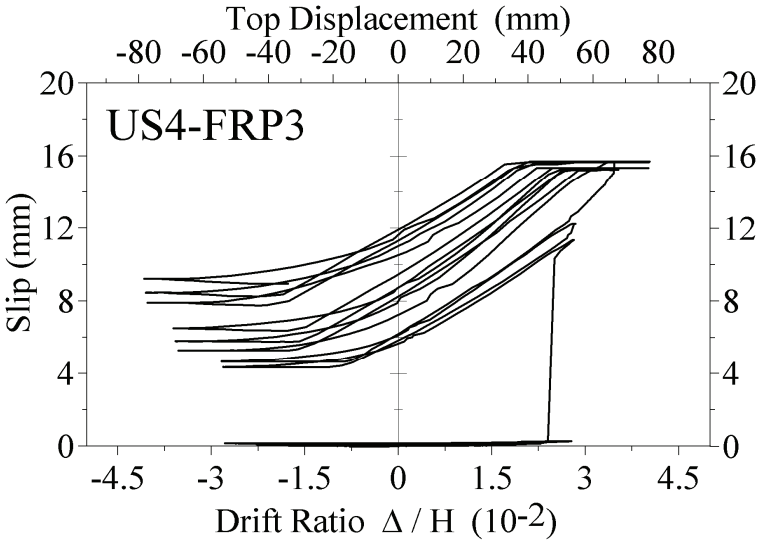


Figure 4.17. Slippage of the beam positive reinforcement, US4-FRP3

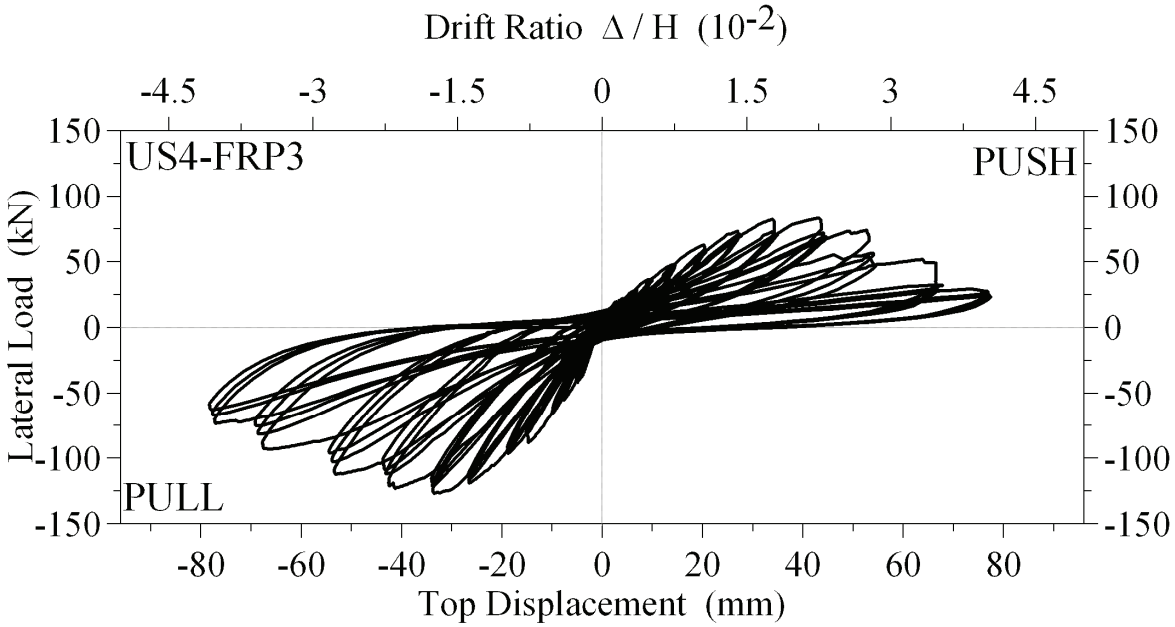


Figure 4.18. Lateral load vs. top displacement, US4-FRP3

4.2.9. Specimen US1-R-FRP1

The first flexural crack was observed at the beam at the drift level of 0.25%, when the lateral loads were 38 kN and 44 kN in push and pull direction. At the drift level of 0.50 %, second crack was formed at the bottom of the beam, 70 cm away from the column face.

Diagonal CFRP sheets started to debond from the beam at drift level of 1.40 %. At drift level of 1.75 % maximum lateral of 128 kN was acfhieved. During the cycles of drift level 2.20%, 2 cm portion of the CFRP was ruptured from the bottom corner resulting in a crack opening at the top corner of the beam column intersection. In the same drift level, debonding of the diagonal CFRP sheets from the beam was observed. In push direction of loading, maximum lateral load of 95 kN was achieved at drift level of 2.20 %. Load-displacement response is presented Figure 4.19 and a picture illustrating the condition of the test specimen at drift level of 1.75 % is show in Figure 4.20.

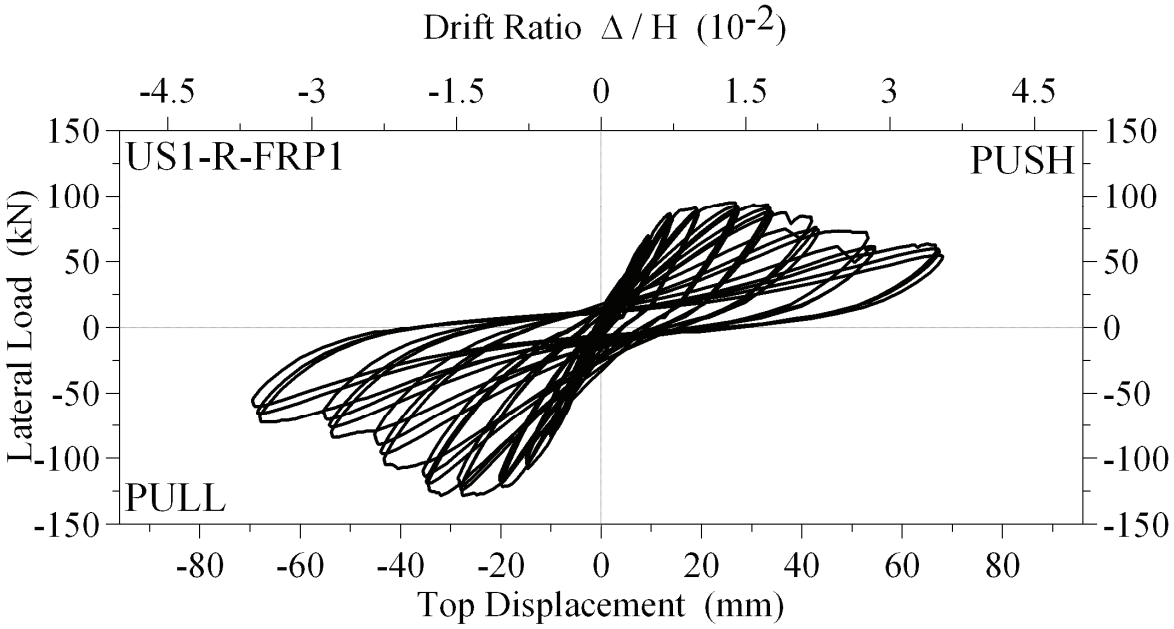


Figure 4.19. Lateral load vs. top displacement, US1-R-FRP1



Figure 4.20. Lateral load vs. top displacement, US1-R-FRP1

4.2.10. Specimen US2-R-FRP2

Specimen US2-R-FRP2 was first repaired and then retrofitted with FRP2 wrapping configuration. The followings are description of test observations of this specimen.

Up to drift level of 0.75 % only flexural cracks were observed along the beam, as shown in Table 4.28. In pull direction of loading, debonding of U-shaped CFRP initiated at drift level of 1.00 % corresponding to a load level of approximately 90 kN. Maximum load in this direction of loading was achieved at drift level of 1.75 % corresponding to a load level of 105 kN. At drift level of 2.75 % U-shaped CFRP totally debonded from the beam.

In push direction of loading ductile behavior was achieved as shown in Figure 4.21. Up to a drift level of 4.00 % no significant drop in the load carrying capacity was observed. At this drift level CFRP Strip 1 ruptured and this caused a sudden drop in the load-top displacement response of the specimen. A detailed observation noted during testing is presented in Table 4.29.

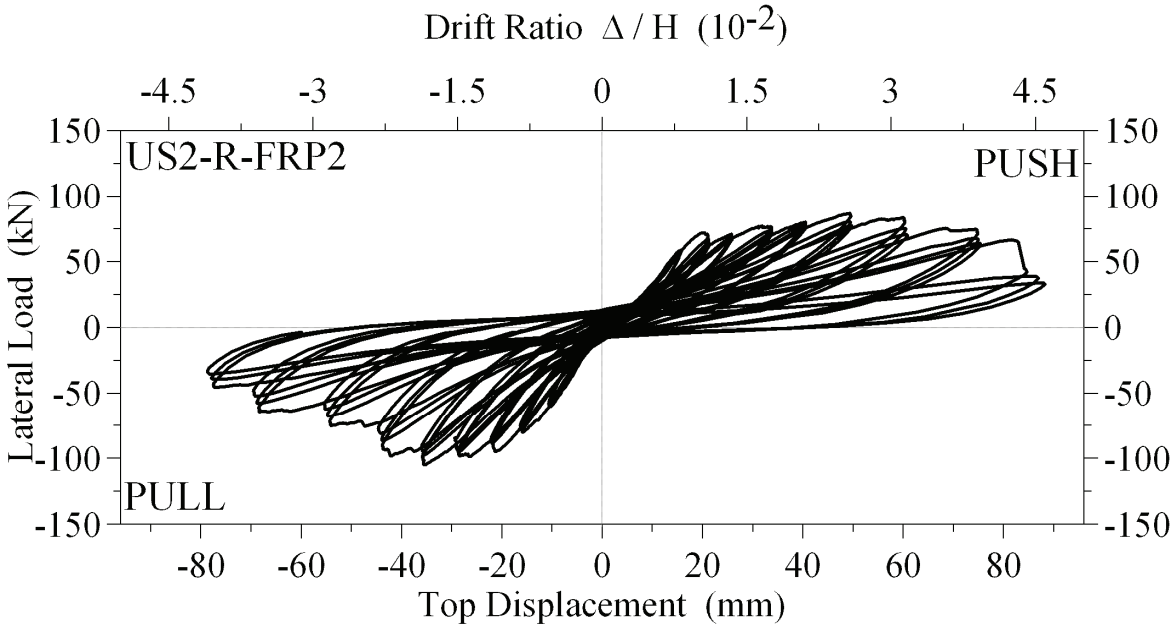


Figure 4.21. Lateral load vs. top displacement, US2-R-FRP2

Table 4.28. Observations on specimen US2-R-FRP2

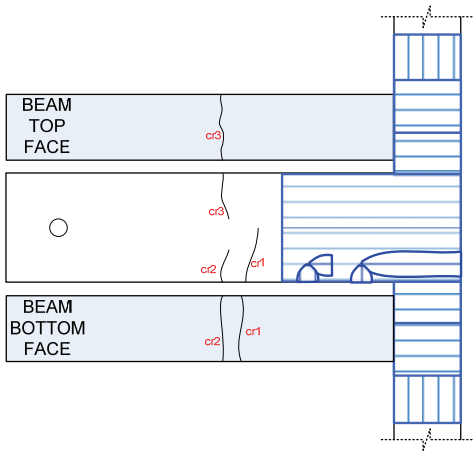
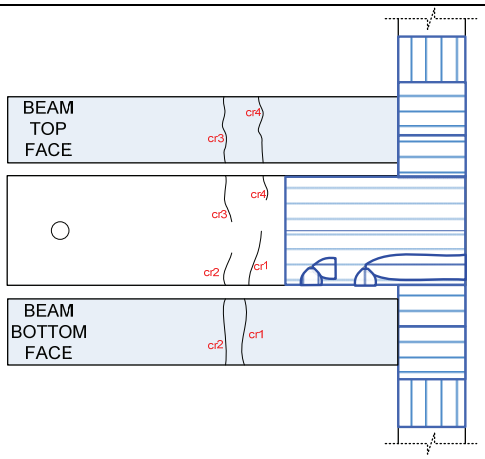
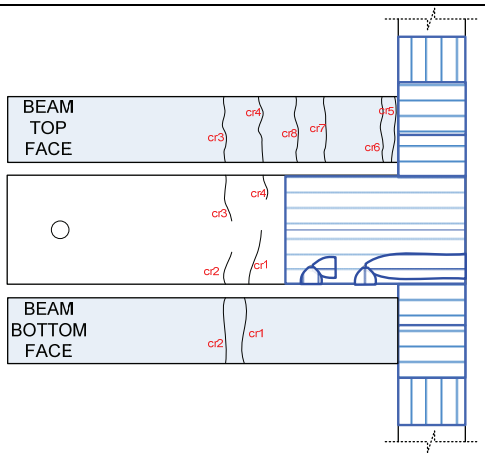
Drift (%)	Observations	Crack patterns & CFRP failure
0.15	Maximum load:(+)15.61 kN (Push) :(-)18.30 kN (Pull) **CR1**: 72 cm away from the beam support a flexural crack was observed at the bottom of the beam (crack length was approx. 20 cm). **CR2**: 60 cm away from the beam support a second flexural crack was observed at the bottom of the beam **CR3**: 80 cm away from the column face a flexural crack was observed at the top of the beam.	
0.25	Maximum load :(+)28.00 kN (Push) :(-)32.20 kN (Pull) **CR4**: 65 cm away from the column face a flexural crack was observed at the top of the beam (crack length approximately 11 cm)	
0.50	Maximum load :(+)58.40 kN (Push) :(-)59.40 kN (Pull) **CR5**: At the top of the beam 5 cm away from the column face, flexural crack was observed. **CR6**: At the top of the beam 7 cm away from the column face, flexural crack was observed.	

Table 4.29. Observations on specimen US2-R-FRP2 (continued)

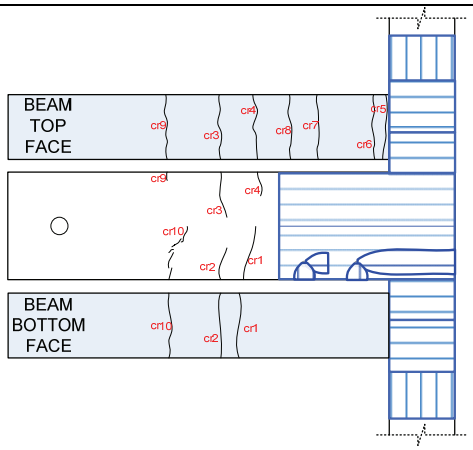
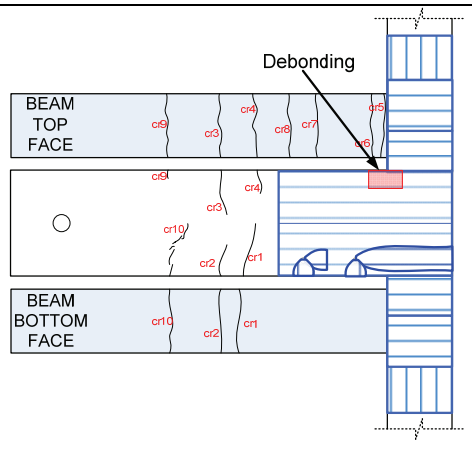
Drift (%)	Observations	Crack patterns & CFRP failure
0.50 (continued)	Another flexural crack was observed at the bottom of the beam 2 cm away from the column face. **CR7**: At the top of the beam 34 cm away from the column face, flexural crack was observed **CR8**: At the top of the beam 48 cm away from the column face, flexural crack was observed	
0.75	Maximum load :(+)71.6 kN (Push) :(-)80.3 kN (Pull) **CR9**: At the top of the beam 106 cm away from the column face, flexural crack was observed. **CR6**: At the bottom of the beam 104 cm away from the column face, flexural crack was observed.	
1.00	Maximum load :(+)71 kN (Push) :(-)93 kN (Pull) Starting from the joint region and extending to the mid length of the U-shape FRP, debonding was observed at the top of the U-shape FRP	

Table 4.30. Observations on specimen US2-R-FRP2 (continued)

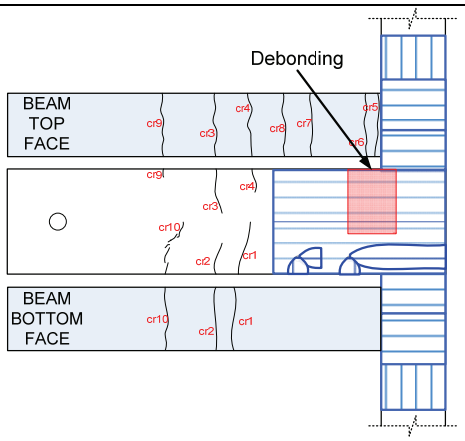
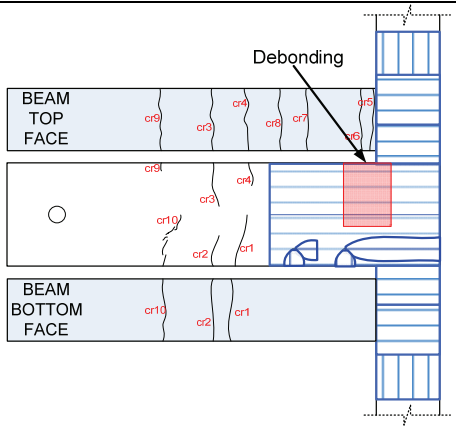
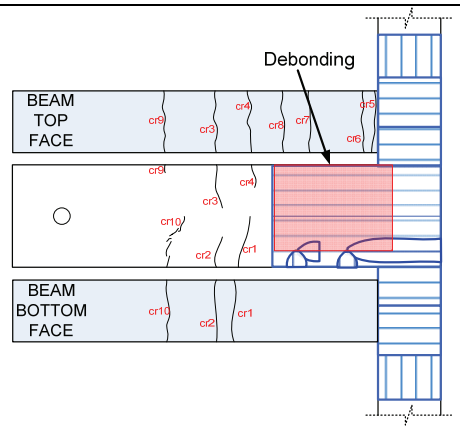
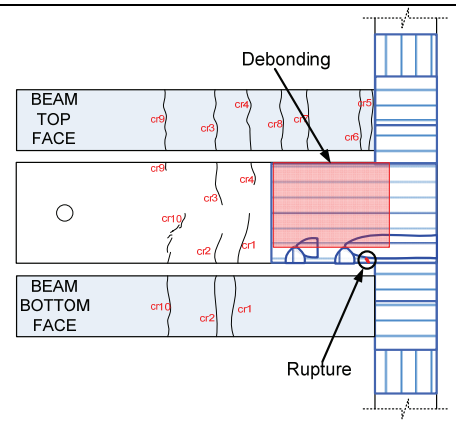
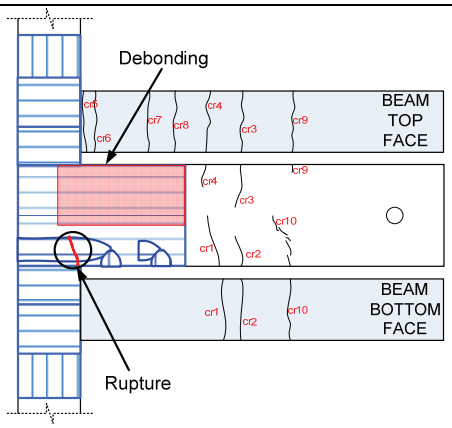
Drift (%)	Observations	Crack patterns & CFRP failure
1.40	Maximum load :(+)77 kN (Push) :(-)98 kN (Pull) **CR11**: At the top of the beam 92 cm away from the column face, flexural crack was observed (approximate length of the crack was 19 cm).	
2.20	Max lat. Load (+)87 kN (Push) (-)98 kN (Pull) The upper portion (up to 30 cm from the beam top face) of the U-shape CFRP debonded. The lateral load that caused debonding was 95 kN(Pull direction of loading)	
2.75	Max lat. Load (+)83 kN (Push) (-)75 kN (Pull) The upper portion (starting from the top of the beam up to the anchorage holes) of the U-shape CFRP totaly debonded	

Table 4.31. Observations on specimen US2-R-FRP2 (continued)

Drift (%)	Observations	Crack patterns & CFRP failure
3.50	Max lat. Load (+)75 kN (Push) (-)64 kN (Pull) 3 cm starting from the bottom of the belt CFRP ruptured.	
4.00	Max lat. Load (+)66 kN (Push) (-)46 kN (Pull) FRP belt totally ruptured.	

4.2.11. Specimen US3-R-FRP3

The damaged control specimen was repaired as specified in Section 3.6 and was strengthened with FRP3 wrapping configuration, as described in Section 3.5.3.

The behavior of repaired specimen US3-R-FRP3 was similar to that of undamaged CFRP strengthened specimen US3-FRP3. The first crack formed at the top portion of the beam at the end of the U-shaped CFRP when the lateral load was 32 kN and the drift was 0.25%. Since the repaired area is at the joint region, there were still hairline cracks existing at the unwrapped part of the beam. The cracks observed in the test of US3-R-FRP3 followed the same cracking paths. Up to drift level of 1.40% there were cracks only in the beam.

The debonding of U-shaped CFRP was observed first at the top portion of the beam at the drift level was 1.40%. The figure illustrating the debonded area of the U-shaped CFRP is given in Table 4.32. During the 1.75% drift level, debonding of U-shaped CFRP was observed at the other side of the beam. At the maximum load level, 126 kN and drift level of 1.75 % the U-shaped CFRP totally debonded from the faces of the beam. After that drift level, in pull direction of loading strength degradation was observed.

In push direction of loading, as in the specimen US3-FRP3, the rupture started first in the CFRP Strip 1 at a drift level of 2.20 %. The rupture length was approximately 2 cm. Total rupture of three layers of U shapes and a single layer of CFRP Strip 1 layer was observed in the second cycle of the 3.5% drift level at a load level of 85 kN. Load-top displacement response is shown in Figure 4.22. Lateral load vs. top displacement, US3-R-FRP3 and detailed description of the crack pattern and CFRP failure history is presented in Table 4.33.

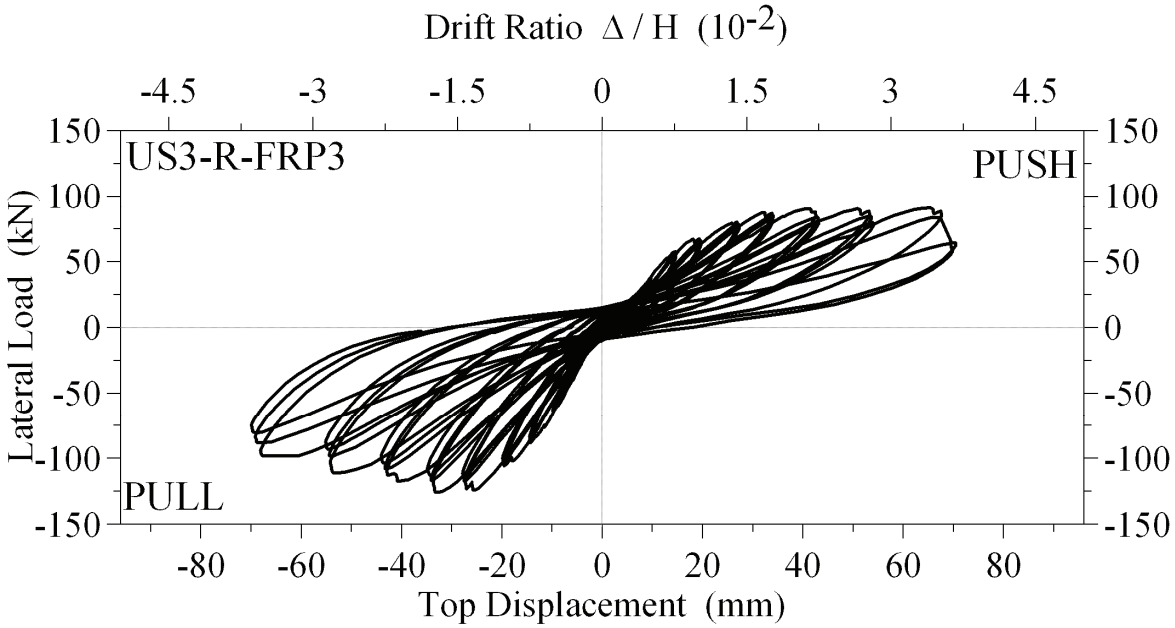


Figure 4.22. Lateral load vs. top displacement, US3-R-FRP3

Table 4.32. Observations on specimen US3-R-FRP3

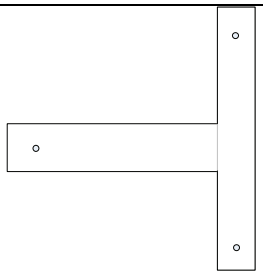
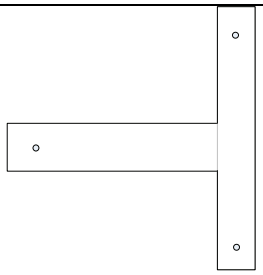
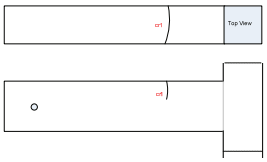
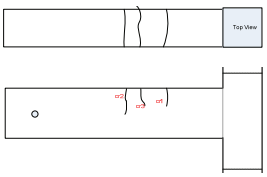
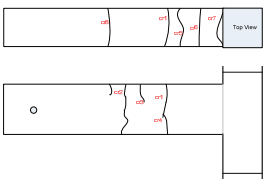
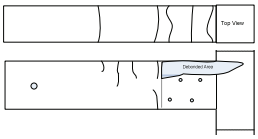
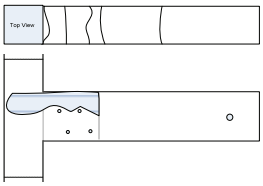
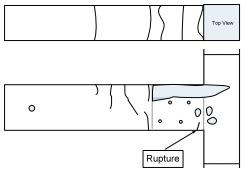
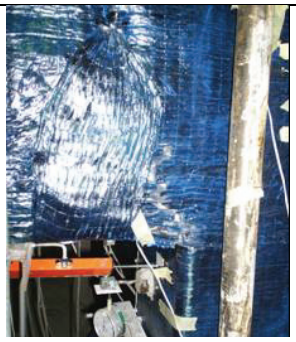
Drift (%)	Observations	Crack patterns & CFRP failure
0.15	Maximum lateral load : (+) 13.00 kN (Push) : (-) 18.40 kN (Pull) No apparent cracks were observed.	
0.20	Maximum lateral load : (+) 16.40 kN (Push) : (-) 25.20 kN (Pull) No apparent cracks were observed.	
0.25	Maximum lateral load : (+) 18.80 kN (Push) : (-) 32.00 kN (Pull) **CR1** : This is a flexural crack, formed in pull direction (at the top of the beam), and the location is 510 mm away from the face of the column. Crack length is 150 mm. (cr9 in US3-Control)	
0.35	Maximum lateral load : (+) 25.20 kN (Push) : (-) 45.74 kN (Pull) **CR2** : Flexural crack formed at the top of the beam, 770 mm away from the column. (cr10 in US3-Control) **CR3** : Flexural crack formed at the top of the beam, 660 mm away from the column.. (CR15 in US3-Control)	
0.50	Maximum lateral load : (+) 37.70 kN (Push) : (-) 64.10 kN (Pull) **CR4** **:** This is a flexural crack, formed in push direction (at the bottom of the beam), and the location is 510 mm away from the face of the column.	
0.75	Maximum lateral load : (+) 57.68 kN (Push) : (-) 88.30 kN (Pull) **CR1-CR4** **:** Joined **CR2-CR7** **:** Joined	

Table 4.33. Observations on specimen US3-R-FRP3 (continued)

Drift (%)	Observations	Crack patterns & CFRP failure
1.00	Maximum lateral load : (+) 67.30 kN (Push) : (-) 105.50 kN (Pull)	
1.40	Maximum lateral load : (+) 80.00 kN (Push) : (-) 124.00 kN (Pull) Debonding formed at the south side of the specimen	
1.75	Maximum lateral load : (+) 86.80 kN (Push) : (-) 125.89 kN (Pull) Debonding was observed at the north side of the specimen before the maximum drift level was reached	
2.20	Maximum lateral load : (+) 89.60 kN (Push) : (-) 112.60 kN (Pull) **CR3 :** Diagonally extended 200 mm. 20 mm from the bottom end of CFRP strip, which surrounds the column as belt ruptured.	 
2.75	Maximum lateral load : (+) 89.00 kN (Push) : (-) 107.70 kN (Pull)	
3.50	Maximum lateral load : (+) 90.00 kN (Push) : (-) 97.70 kN (Pull) FRP strip, which surrounds the column as belt, and U shape CFRP that extends to the beam totally ruptured (See the picture below)	

4.2.12. Specimen US4-R-FRP3

The structural response of the US4-R-FRP3 specimen under the reversed cyclic loading was close to the response of specimen US4-FRP3. In the initial drift levels several flexural cracks were observed at the beam. These cracks were generally located between the beam roller support and the end of the U-shaped CFRP sheet. Mainly, cracks were observed at the top side of the beam.

One of the essential improvements in the strengthening of the specimen was that the slippage was reduced noticeably such that only after 2.00 % drift level the slippage of the beam bottom longitudinal reinforcement initiated. Furthermore, even if the rebar started to slip, the slippage did not exceed 2.5 mm. Although the CFRP strengthening strategy was the same as US4-FRP3, the improvement in the reduction of the slippage was due to the higher bond strength of the repair material (compared to the concrete) with steel reinforcement.

The failure mechanisms in push and pull direction of loading were the same as the failure modes of US4-FRP3 specimen. In push direction of loading the U-shaped CFRP sheet and the CFRP Strip 1 ruptured from the bottom and then the slippage of the beam bottom longitudinal reinforcement initiated. Thus degradation in the lateral load resistance of the specimen was observed. On the other hand for pull direction of loading, U-shape CFRP sheet debonded from the top which then allowed the damage to propagate to the joint and cause shear failure in the joint region. Hysteretic load-top displacement response of the specimen is shown in Figure 4.23 and detailed test observations are given in Table 4.34.

Table 4.34. Observations on specimen US4-R-FRP3

Drift (%)	Observations	Crack patterns & CFRP failure
0.50	Maximum load :(+)37.90 kN (Push) :(-)68.80 kN (Pull) **CR1**: Flexural crack formed at the top, 110 cm away from the east face of the column. The length of the crack was 16.5 cm.	
0.75	Maximum load :(+)59.10 kN (Push) :(-)89.34 kN (Pull) **CR2**: Flexural crack formed at the top, 80 cm away from the east face of the column. The length of the crack is 17 cm. **CR3**: Flexural crack formed at the top, 65 cm away from the east face of the column. The length of the crack is 16 cm. **CR4**: Flexural crack formed at the top, 94 cm away from the east face of the column. The length of the crack is 24 cm. **CR5**: Flexural crack formed at the top, 110 cm away from the east face of the column. The length of the crack is 16 cm.	

Table 4.35. Observations on specimen US4-R-FRP3 (continued)

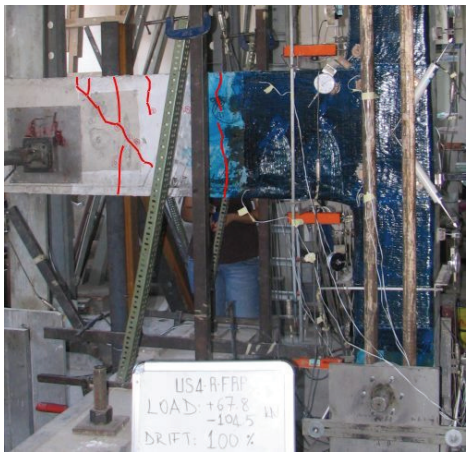
Drift (%)	Observations	Crack patterns & CFRP failure
1.00	Maximum load :(+)67.81 kN (Push) :(-)104.50 kN (Pull) **CR6**: Flexural crack formed at the top, 80 cm away from the east face of the column. The length of the crack is 17 cm. • **CR5** split and extended to the U-shape CFRP sheet. **CR7**: Shear crack between the beam support and U-shape CFRP sheet. Approximately 100 cm away from the east face of the column. The length of the crack was 39 cm. **CR8**: Flexural crack formed at the top, just at the interface between the column and the beam (1 cm away from the column east face). The crack started from the top of the beam and extended into the joint core. This crack was only observable from the beam top face. • The crack pattern at south face of the beam, between the beam support and the U-shape CFRP sheet, was like a cross shape (+) and (–) 45^{o} degrees indicating shear damage at this region.	

Table 4.36. Observations on specimen US4-R-FRP3 (continued)

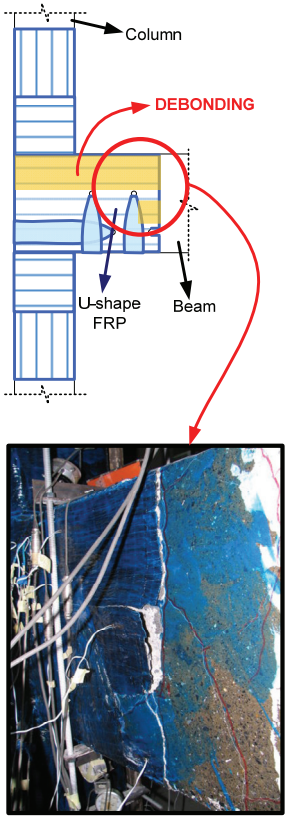
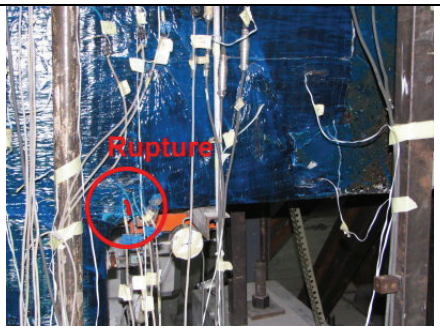
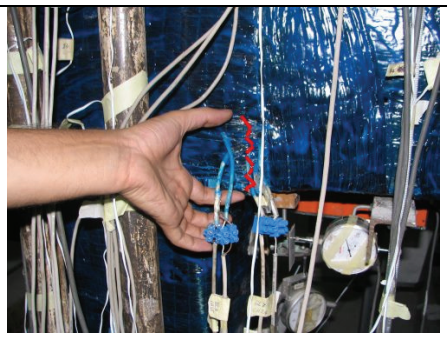
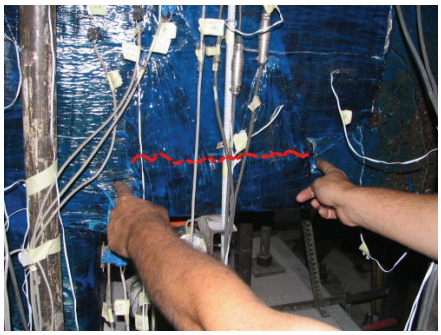
Drift (%)	Observations	Crack patterns & CFRP failure
1.40	Maximum load :(+)79.50 kN (Push) :(-)124.80 kN (Pull) **CR9:** Flexural crack formed at the bottom, approximately 1 cm away from the east face of the column. This crack was only observable from the beam bottom face. • In pull direction of loading top portion (17 cm within the height of the beam) of the U-shape CFRP sheet debonded from the concrete of the beam.	
2.20	Maximum load :(+)91.12 kN (Push) :(-)132.00 kN (Pull) • Debonding of U-shape CFRP sheet was observed on the south face of the beam. At the first cycle, top portion debonded and the second cycle mid-portion debeonded (Between the upper and bottom anchorage holes).	

Table 4.37. Observations on specimen US4-R-FRP3 (continued)

Drift (%)	Observations	Crack patterns & CFRP failure
3.50	Maximum load :(+)91.30 kN (Push) :(-)113.50 kN (Pull) • In push direction of loading, bottom portion of the U-shape CFRP ruptured 1 cm.	
4.00	Maximum load :(+)85.10 kN (Push) :(-)99.20 kN (Pull) • In push direction of loading U-shape CFRP sheet and the CFRP strip 1 ruptured from the bottom. Rupture length was approximately 6 cm. • Both sides of the U-shape CFRP sheet debonded from the top up to the bottom level anchorage holes. • Rupture in the direction of the fibers of U-shape CFRP (horizontal rupture) was observed from the south face of the beam.	 

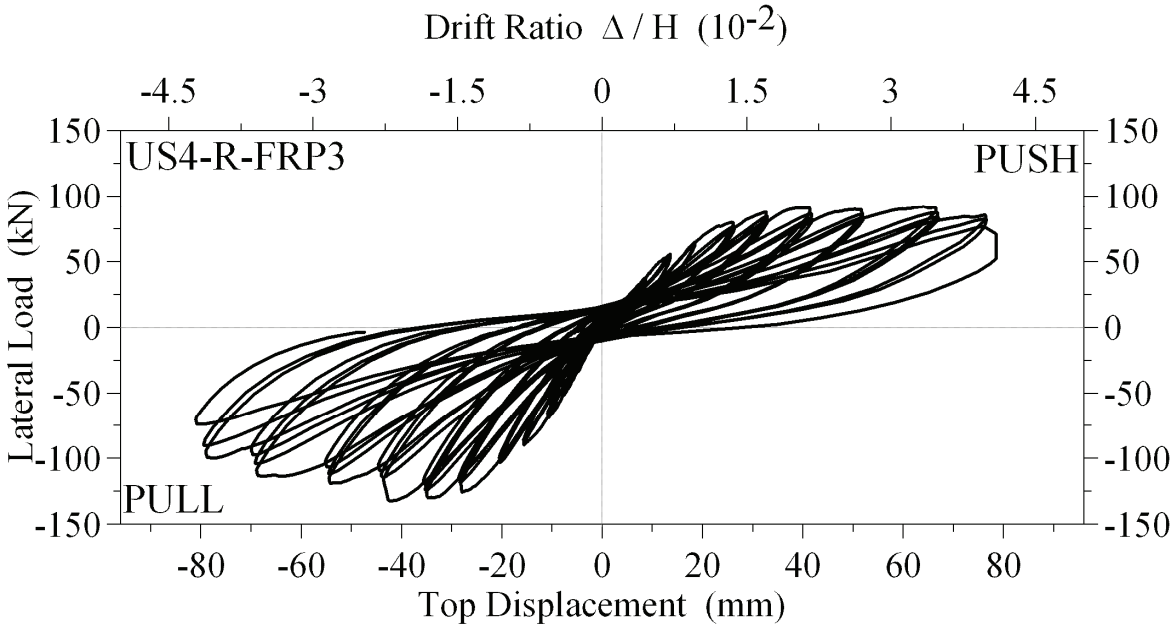


Figure 4.23. Lateral load vs. top displacement, US4-R-FRP3

4.3. Shear Deformation of the Joints

Deformed and undeformed configuration of the joint shear panel is illustrated in Figure 4.24. Joint shear deformation value, γ, shown in Figure 4.24 was calculated as follows:

$$\gamma = \arctan\left(\frac{x}{h}\right) \tag{3.2}$$

where

$$x = \frac{\left(\sqrt{(d_1')^2 - h^2}\right) - z}{2}, \tag{3.3}$$

and

$$z = \sqrt{(d_2')^2 - h^2}\ . \tag{3.4}$$

By assuming the height of the joint, h to be constant and by substituting Equations (3.3) and (3.4) into Eq. (3.2), the shear deformation value in radians is obtained as follows:

$$\gamma = \arctan\left(\frac{\sqrt{(d_1')^2 - h^2} - \sqrt{(d_2')^2 - h^2}}{2h}\right) \tag{3.5}$$

The terms d'_1 and d'_2 are the diagonal distances of deformed shape measured through the use of LVDTs placed diagonally at the joint shear panel.

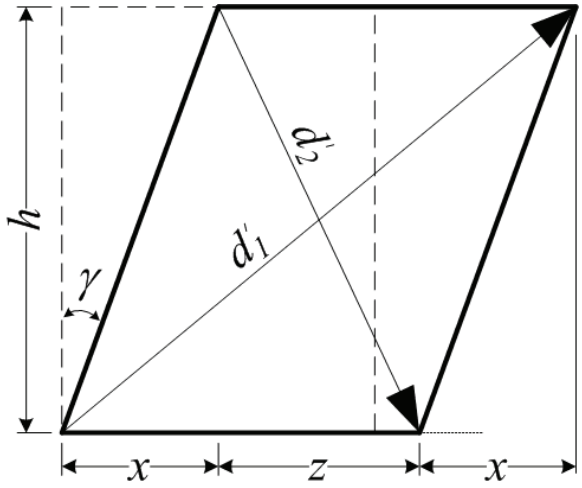


Figure 4.24. Joint panel shear deformation

Below shear deformation versus applied lateral load plots are presented. In all control specimens shear deformations corresponding to the same amount of applied lateral load were higher than the deformations of those in the CFRP retrofitted and repaired and CFRP retrofitted specimens. Especially in US1-FRP1 specimen shear deformations remained almost elastic. The proposed CFRP wrapping configurations restricted the shear deformation at the joint core. This indicates that CFRP wrapping configurations were able to increase the joint shear strength and stiffness.

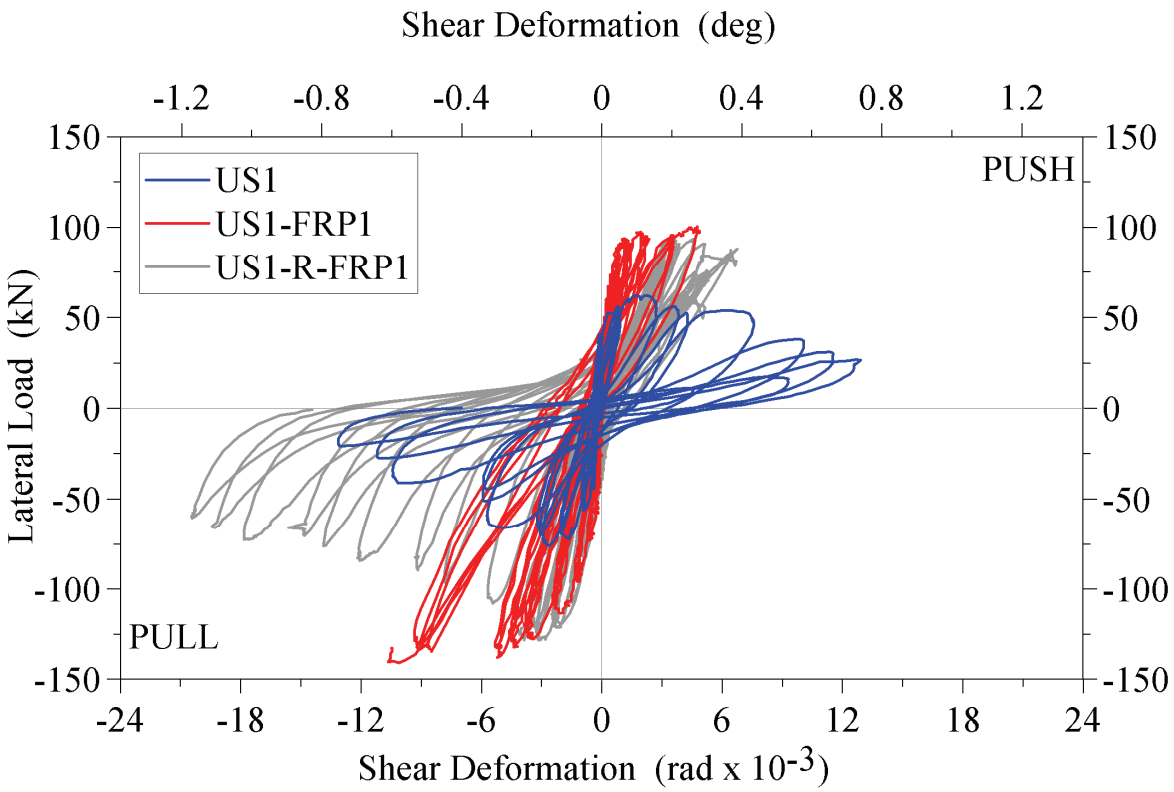


Figure 4.25. Shear deformation vs. load, US1, US1-FRP1 and US1-R-FRP1

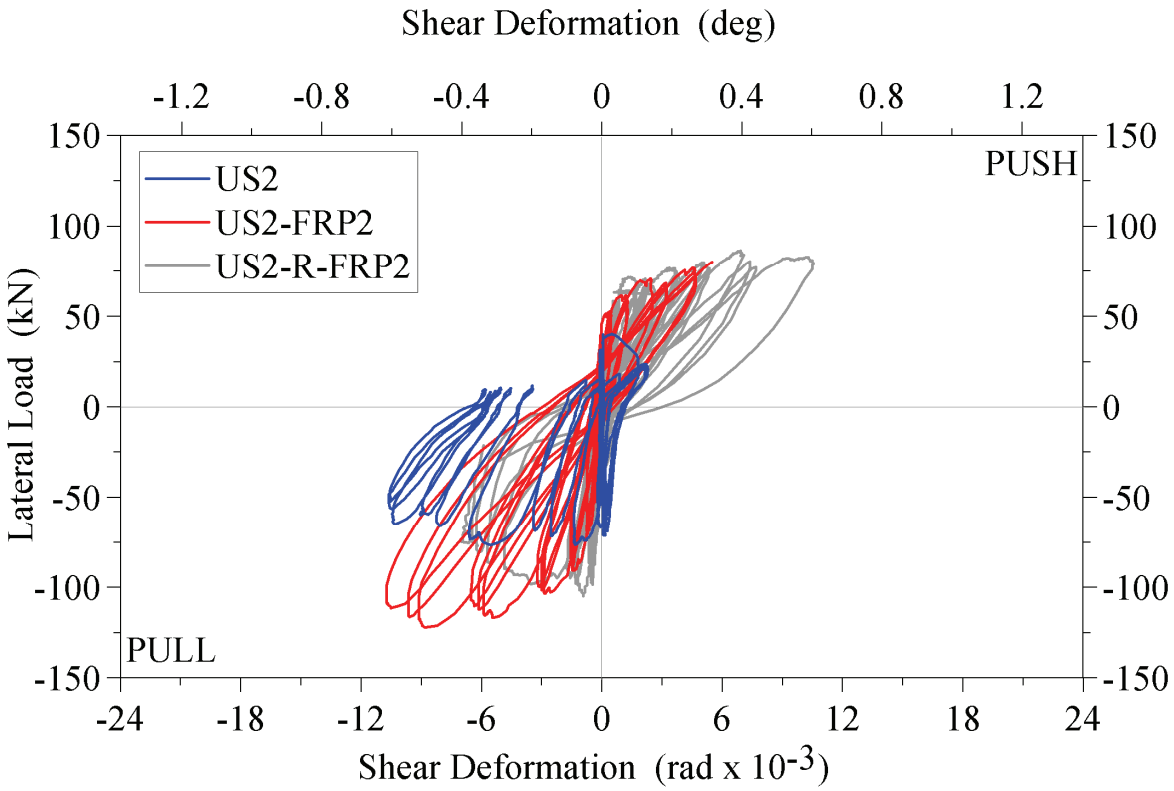


Figure 4.26. Shear deformation vs. load, US2, US2-FRP2 and US2-R-FRP2

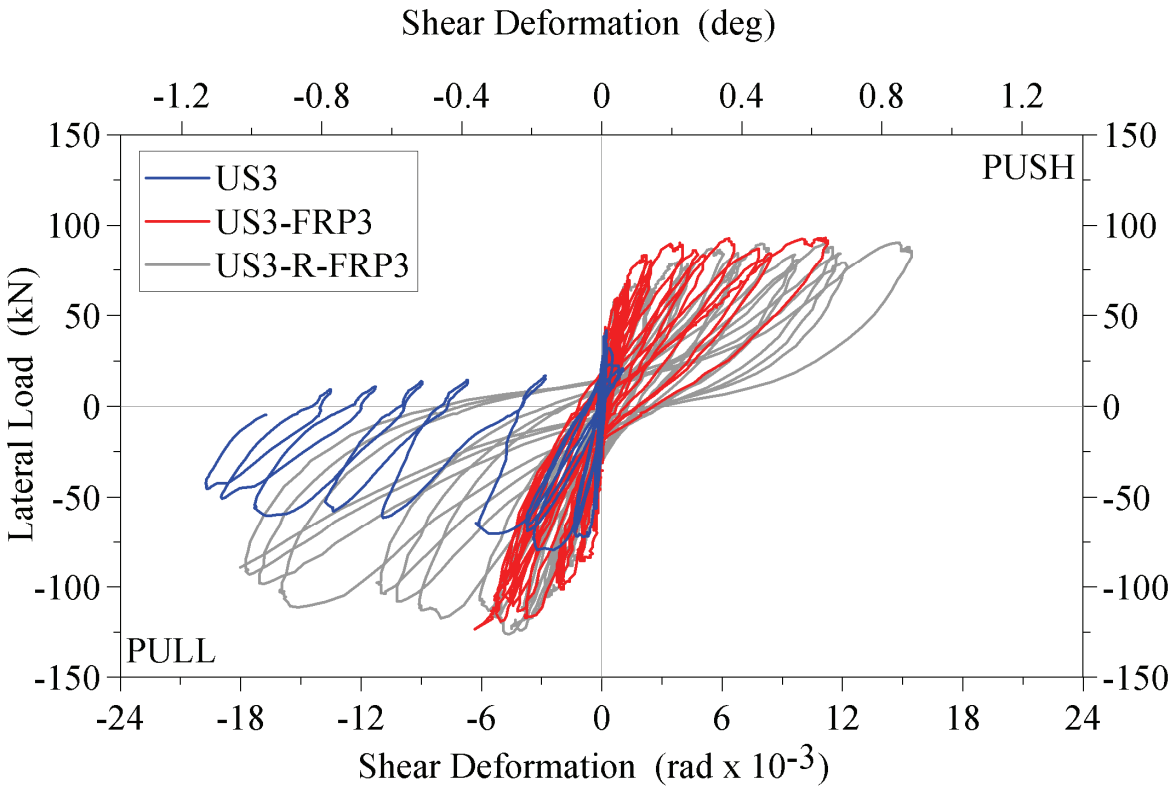


Figure 4.27. Shear deformation vs. load, US3, US3-FRP3 and US3-R-FRP3

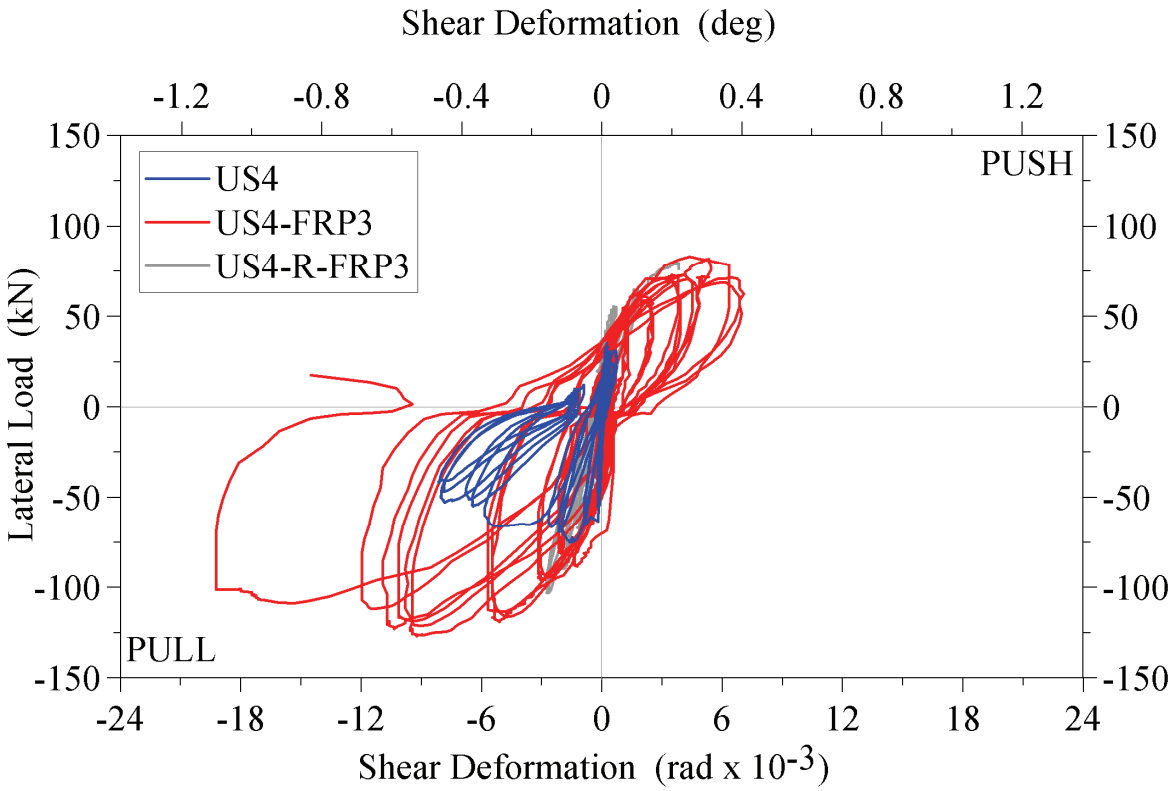


Figure 4.28. Shear deformation vs. load, US4, US4-FRP3 and US4-R-FRP3

4.4. Stiffness Degradations of the Subassemblies

Under reversed cyclic loading, almost all specimens behaved differently when the loading direction is under consideration. In push direction of loading control specimens, except US1, failed due to slippage of the beam bottom longitudinal reinforcement. In pull direction of loading, all control specimens failed from excessive shear damage at the joint core. CFRP strengthened and repaired and CFRP strengthened specimens failed due to rupture of the U-shaped CFRP and debonding of CFRP sheets in push and pull direction respectively. Therefore in this study stiffness degradation of each specimen was calculated for push and pull directions of loading, separately.

In this study, secant stiffness was utilized as a tool to investigate the behavior of the beam-column subassemblies. Secant stiffness, K, is defined as the slope of the line that passes from the origin to a point of interest on a lateral load versus top displacement relationship. Figure 4.29 illustrates the definition for the secant stiffness.

Top displacement-stiffness relationships are presented in Figures 4.30-4.33. Each figure consists of overlapped three plots of the control, retrofitted and repaired and retrofitted specimens. As seen from the figures, stiffness levels of the retrofitted and repaired and retrofitted specimens are higher than those of the control specimens. Especially, at higher drift levels discrepancies between the stiffness values of the control specimen and CFRP retrofitted specimens is increasing. This indicates that CFRP retrofitted beam column joints may resist to higher drift demands under earthquake type of cyclic loading.

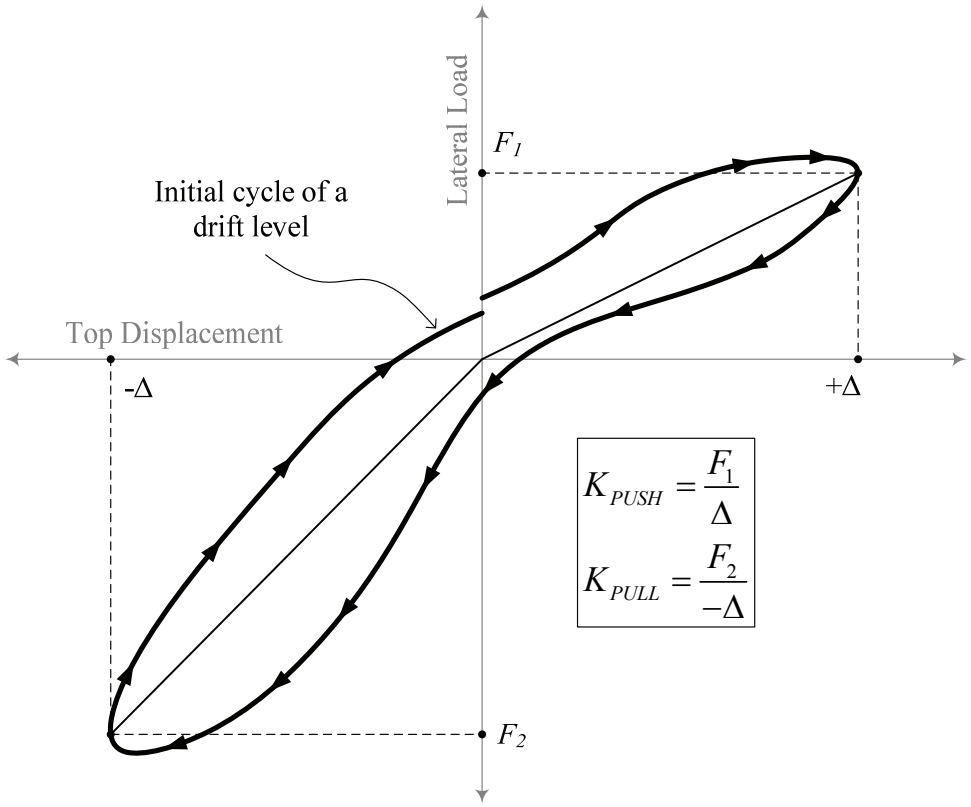


Figure 4.29. Secant stiffness

It should be noted that stiffness values in pull direction of loading are higher than those in push direction of loading. This was mainly due to two reasons; the amount of beam top reinforcement was higher compared to the bottom and the load required to cause slippage to the beam bottom longitudinal was lower compared to the load required to cause shear failure at the joint. Slopes of the stiffness degradation plots indicate the rate of deterioration. From the figure it can be observed that the deterioration in the push direction was more abrupt than the pull direction of loading. This also implies that slippage of the beam bottom longitudinal reinforcement resulted in more sudden type of failure compared to the shear failure at the joint.

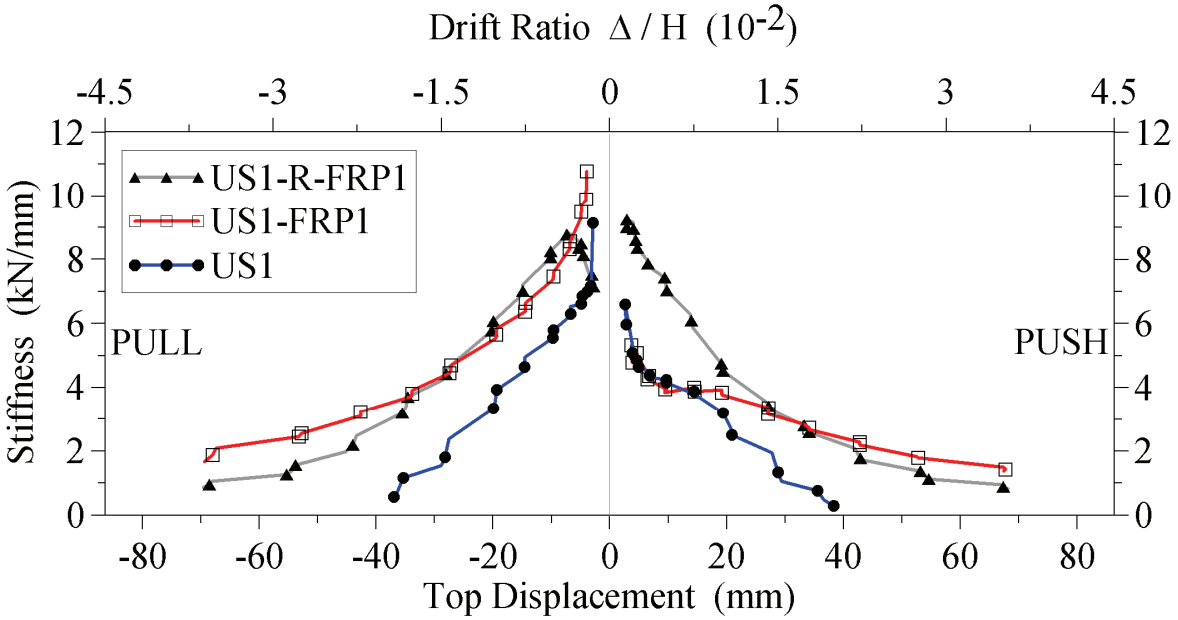


Figure 4.30. Stiffness degradation, US1, US1-FRP1 and US1-R-FRP1

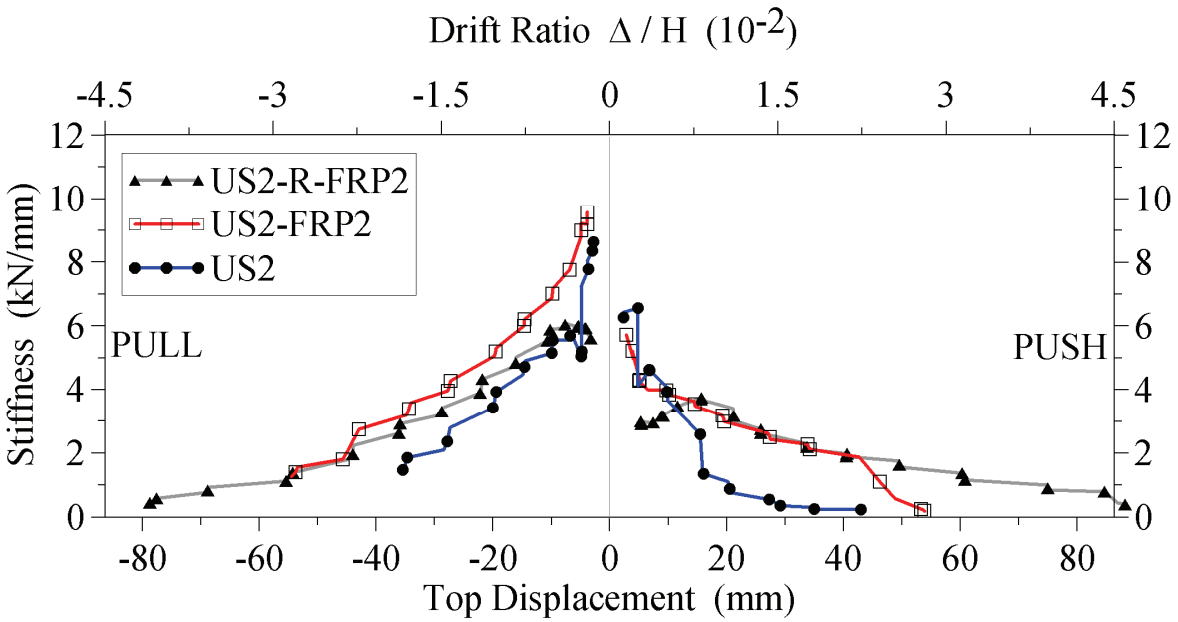


Figure 4.31. Stiffness degradation, US2, US2-FRP2 and US2-R-FRP2

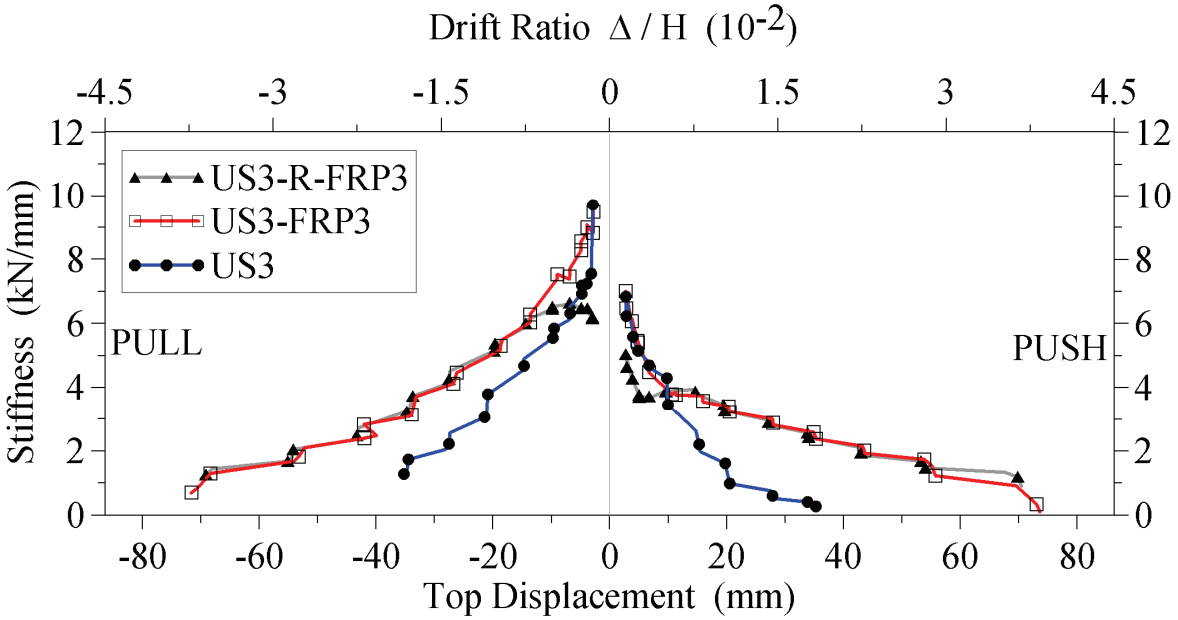


Figure 4.32. Stiffness degradation, US3, US2-FRP3 and US3-R-FRP3

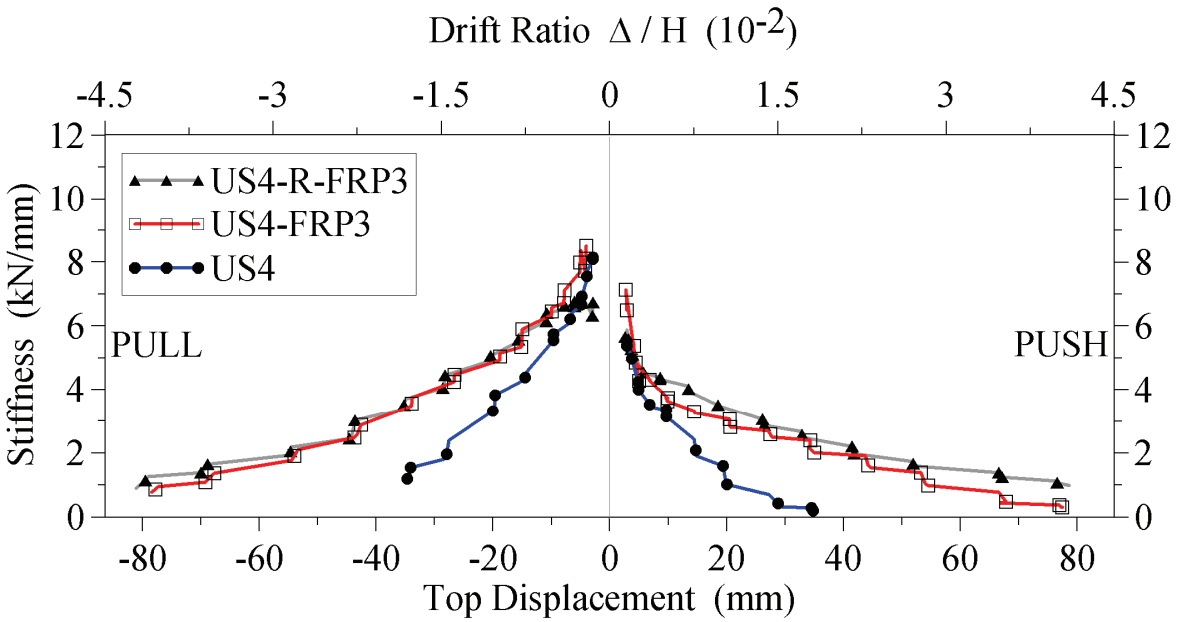


Figure 4.33. Stiffness degradation, US4, US4-FRP3 and US4-R-FRP3

In overall, the CFRP wrapping configurations increased the stiffness values of the beam-column joints. Especially at high drift levels, the difference in the stiffness values between the control and CFRP retrofitted specimens is gradually increasing indicating the effectiveness of the CFRP wrapping configurations.

4.5. Energy Dissipation of the Beam-Column Joints

Cumulative dissipated energy, *CDE*, is specified as the cumulative area under hysteresis loops of a load vs. top displacement relationships and is defined with the following equation;

$$CDE = \sum_{j=1}^{n} \left(\oint_{cycle\ j} (H)du \right) \tag{4.1}$$

where n is the number of response cycles and H is the applied lateral load corresponding to the top displacement u. Shaded area in Figure 4.34 illustrates the physical interpretation of Equation 4.1.

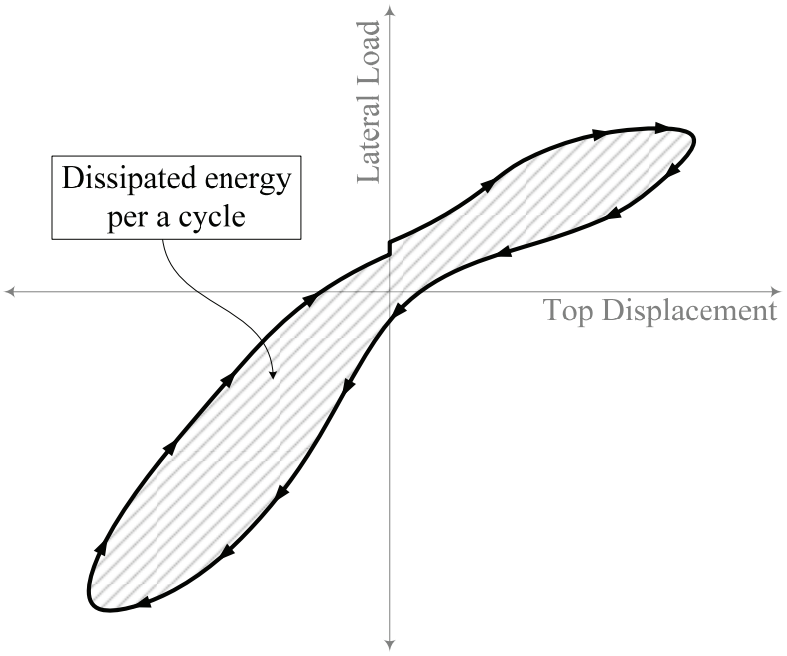


Figure 4.34. Energy dissipation per cycle

Below, dissipated energy plots for all specimens are presented in Figure 4.35. As seen in the figures the amount dissipated energies in the CFRP retrofitted and repaired and CFRP retrofitted specimen were much higher. The increase in energy dissipation of CFRP retrofitted specimens ranges from 350% to 500 %.

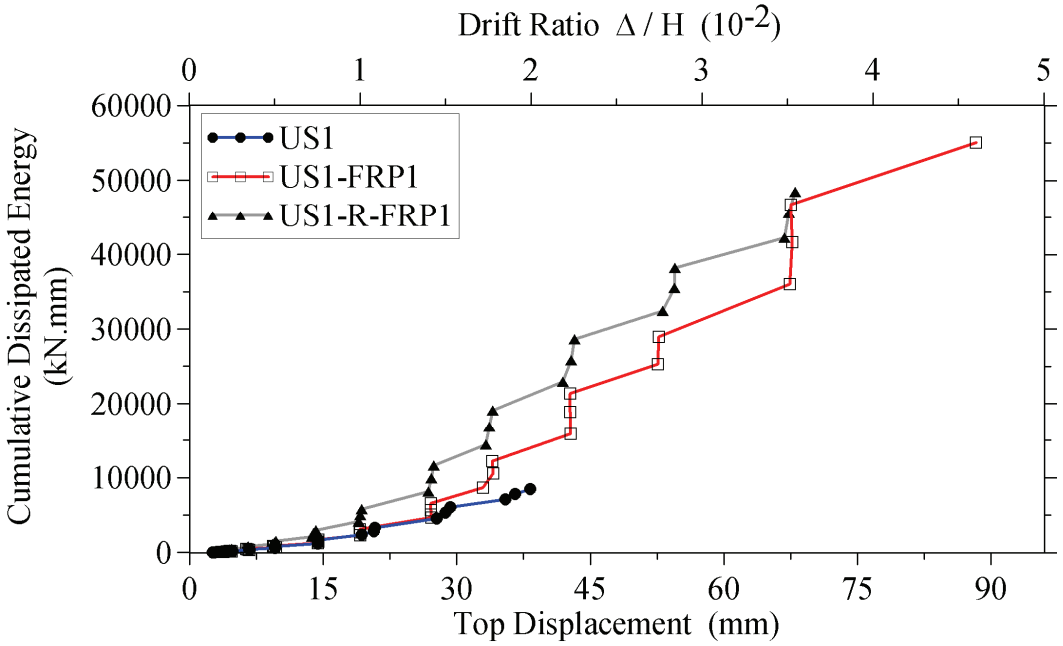


Figure 4.35. Energy dissipation, US1, US1-FRP1, US1-R-FRP1

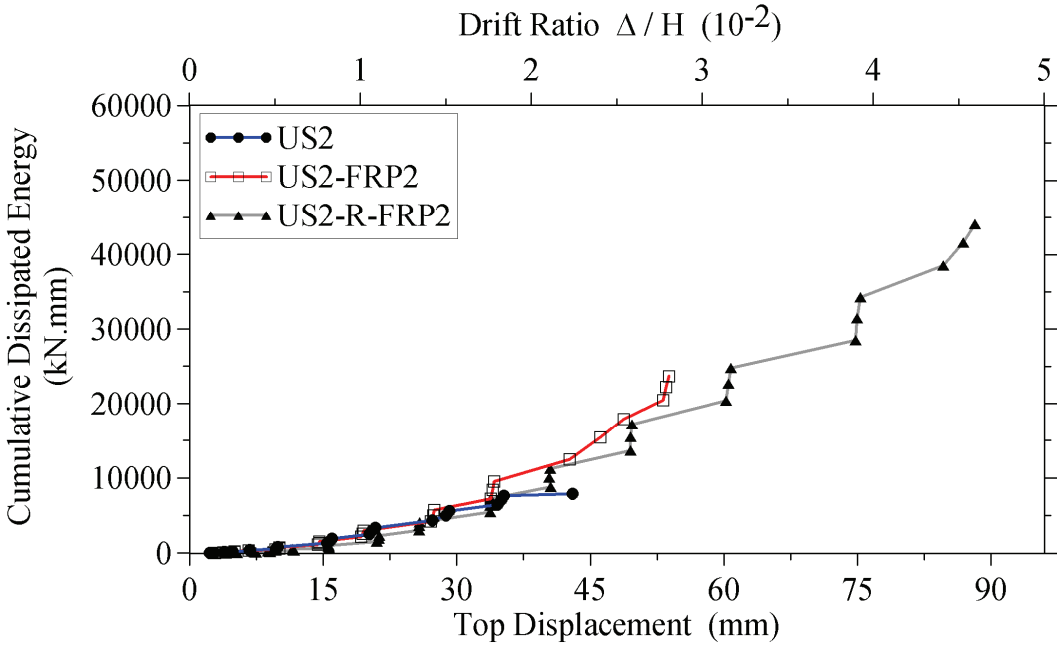


Figure 4.36. Energy dissipation, US2, US2-FRP2, US2-R-FRP2

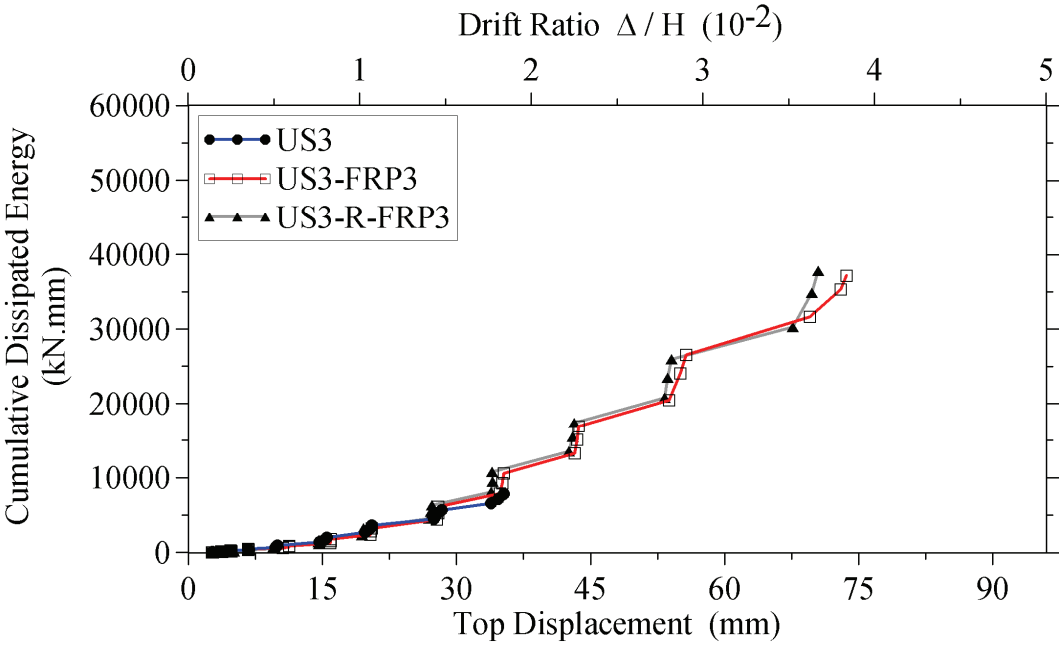


Figure 4.37. Energy dissipation, US3, US3-FRP3, US3-R-FRP3

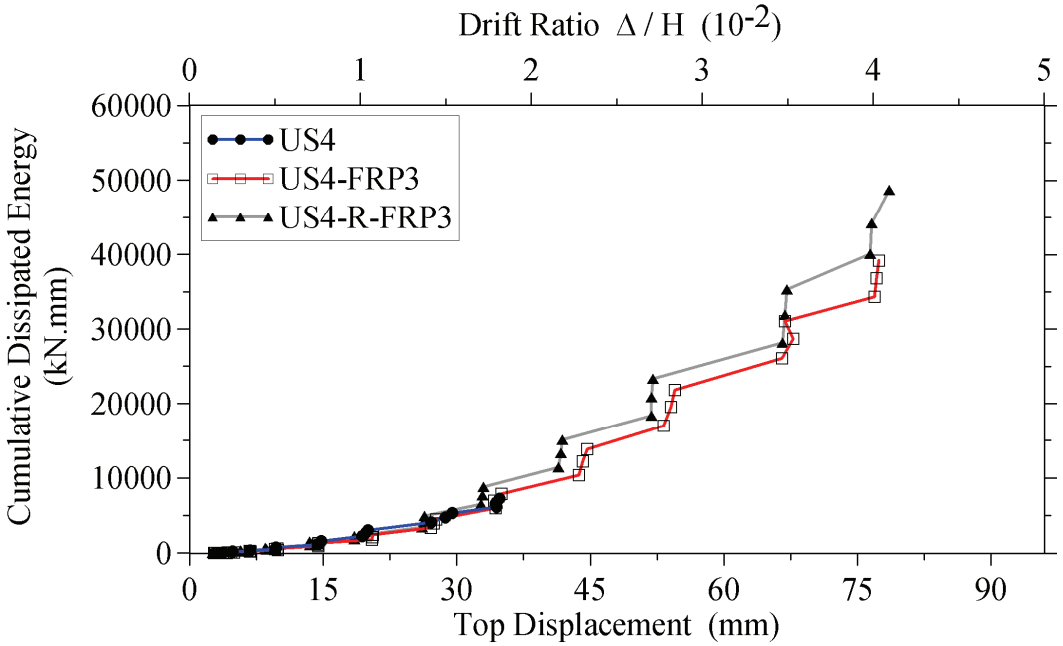


Figure 4.38. Energy dissipation, US4, US4-FRP3, US4-R-FRP3

In overall, the CFRP wrapping configurations increased the energy dissipation capacities of the beam-column joints. Almost all CFRP retrofitted specimens were able to dissipate energy up to drift level of 3.50 % which indicates that the displacement capacities are also increased.

5. FINITE ELEMENT MODELING OF THE BEAM-COLUMN JOINTS

5.1. Introduction

In order to understand the cyclic behavior of 3-D beam-column subassemblages, three different finite element modeling tools were utilized. MSC. Marc Mentat [62] was used as pre-processor, LS-Dyna [63] was utilized as a solver of the finite element models and LS-PrePost [64] was used both as pre and post processor. This chapter presents the procedures followed for the numerical modeling of the reinforced concrete beam-column joints. Discussion for the chosen solution procedure, information for the material models, boundary conditions and mesh generation are also given in this chapter. In order to verify the followed numerical procedure and be able to discuss the behavior of the beam column joints through finite element analysis, experimentally obtained results are used as benchmarks.

5.2. Solution Procedures

In this study, initially MSC. Marc [65] software package was used as a modeling tool. It has an implemented implicit solution scheme [66-68] and as in the case of other implicit solvers it requires iterations to obtain solutions for nonlinear problems. However, the implemented iteration procedures such as Newton-Raphson, Modified Newton-Raphson [66, 69] and Arc-Length [66-67] methods are not always able to provide a converged solution. Instabilities, especially maxima and minima points of the force-displacement response, due to concrete cracking and sudden changes in the magnitude and/or sign of the stiffness arise complexities and sometimes partial impossibilities for a solution with iterations. Due to some of the above mentioned difficulties, the solver of MSC. Marc has failed to provide a full solution for the finite element model of beam-column joints. In order to investigate the nonlinear behavior of the beam-column subassemblages, an explicit finite element code LS-Dyna was employed. On the contrary to the implicit codes, explicit solvers utilize central difference method [69-70] as a solution scheme. Explicit solution schemes [70-71] do not have to form the stiffness

matrix of the finite element model, which enables explicit codes generally to obtain a solution. However, in order to obtain a correct solution within the acceptable range, explicit schemes require much smaller time steps when compared to implicit solvers.

5.3. Concrete Model

LS-Dyna finite element code offers a variety of non-linear material models for simulating concrete behavior [72]. These models differ from each other in terms of defined failure or yield criterion, consideration of the tri–axial state of stress, cyclic behavior under tension and compression, compression strain softening, post–cracking response such as shear transfer after cracking or tension stiffening. In order to decide on which specific model to utilize in simulation of concrete, several material tests were conducted on a single hexahedral element with a single integration point used for monitoring stress-strain states. Under uniaxial cyclic loading, the above mentioned features of the material models were examined. As a result of the single finite element test, the Winfrith concrete model [72] was chosen to represent the concrete medium. This model employs a smeared-crack approach and is able to display the cracks on the faces of the 3-D solid finite elements. Thus, in the post–processor, the user can visualize the damage observed on the model during the simulation and interpret the possible failure modes. Although it has a simple stress-strain shape, the complex tri-axial state of stress is considered in the model, [73-74].

5.3.1. Ottosen Failure Surface

The Winfrith concrete model utilizes Ottosen failure surface [44, 75-79] as a limiting ultimate strength for the concrete. The failure surface is considered as a four–parameter criterion which involves the stress invariants I_1, J_2, $\cos(3\theta)$. The Ottosen failure surface is defined with the following function;

$$f(I_1, J_2, \cos 3\theta) = A\frac{J_2}{(f_c^{'})^2} + \lambda\frac{\sqrt{J_2}}{f_c^{'}} + B\frac{I_1}{f_c^{'}} - 1 = 0 \qquad (5.1)$$

where,

if $\cos 3\theta \geq 0$, $$\lambda = K_1 \cos\left[\frac{1}{3}\arccos(K_2 \cos 3\theta)\right] \quad (5.2)$$

and if $\cos 3\theta \leq 0$, $$\lambda = K_1 \cos\left[\frac{\pi}{3} - \frac{1}{3}\arccos(-K_2 \cos 3\theta)\right] \quad (5.3)$$

and A, B, K_1 and K_2 are the constants and depend on the uniaxial tensile and compressive strengths of the concrete and θ is the Lode angle [78]. It should be noted that when A, B and K_2 are set to zero, the function defining the Ottosen failure surface converts to Von Mises failure criteria [44].

In the analyses, the ratio of tensile to compressive strength of concrete, $f_t / f_c^{'}$, was assumed to be approximately 10%. A, B, K_1 and K_2 values for 0.10 tensile to compressive strength ratio are best fitted to experimental results of Kupfer et al. [80] by Ottosen. In the analyses, the assumed values of these parameters are presented in Table 5.1.

Table 5.1. Ottosen failure surface parameters

$f_t / f_c^{'}$	A	B	K_1	K_2
0.10	19.1382	42.7629	15.037	0.9928

The failure surface has a close fit to the bi–axial test results of Kupfer et al. [80] and tri–axial test results of Richart et al. [81]. It is a smooth and monotonically curved surface without inflection points. The deviatoric section of the surface is expandable with increasing hydrostatic pressure from nearly triangular to circular shape. The 3-D shape of the Ottosen failure surface was plotted using Mathemetica computing software [82] as shown in Figure 5.1. In this figure, σ_1, σ_2, and σ_3 are the principal stresses and the red line with an arrow shows the hydrostatic axis. The intersection between the plane, σ_3=0 (the plane in blue in Figure 5.1) and the failure surfaces shows the biaxial failure criterion which is very similar in shape to the one presented by Kupfer et al. [80].

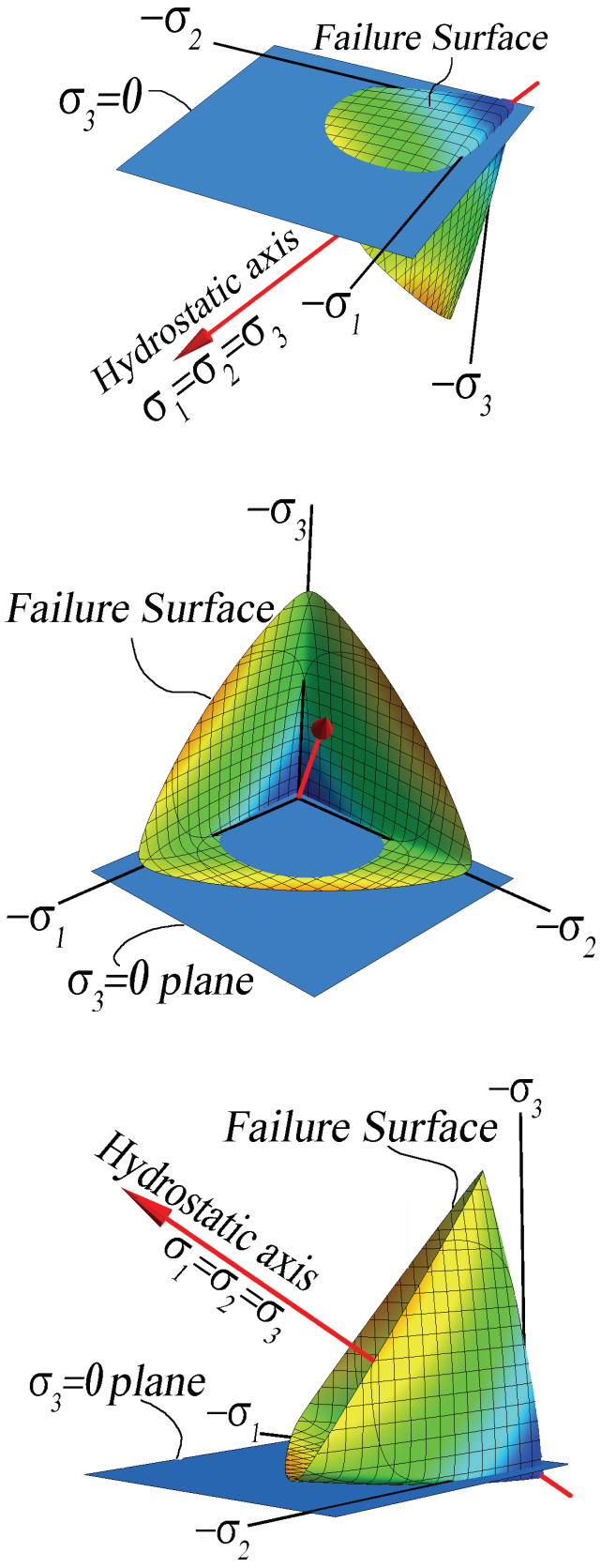


Figure 5.1. Views of the Ottosen failure surface

5.3.2. Behavior of the Concrete Model in Tension

Concrete in tension is assumed to follow a tri-linear relationship. The slope of the ascending branch (prior to cracking) is equal to the elastic modulus of the concrete. The descending branch (after cracking) is a stress function dependent on the crack width. After occurrence of a cracking, the crack normal stress degrades following a bilinear decay function, which is an approximation of the tension–softening property of the concrete. Schematic view displaying the cyclic behavior of concrete under tensile loading is shown in Figure 5.2. Plain concrete physically exhibits strength degradation during unloading after cracking. However the concrete model forms a linear elastic path during unloading and reloading. Failure in tension is achieved after tracing the decay function when the strain in the element reaches to the ultimate strain level defined by the user.

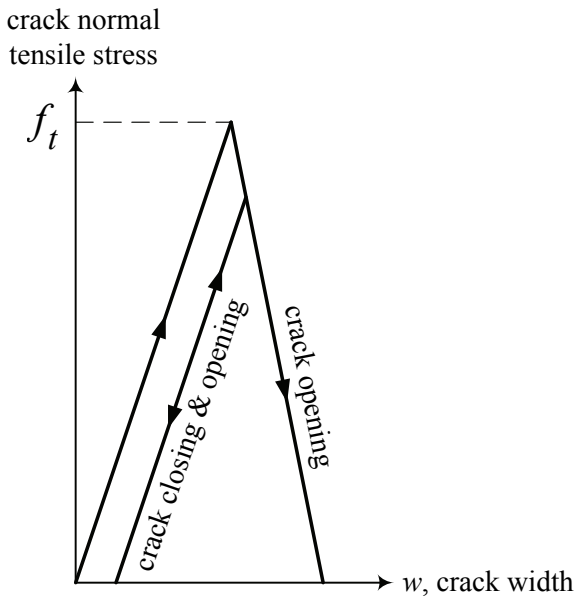


Figure 5.2. Crack width-tensile stress [73]

Smeared rotating cracking procedure is implemented in the model such that the orientation of the cracks is adjusted to remain orthogonal to the maximum principal stress. During the experiment of the control beam column joint specimens softening response was observed due to the large shear cracks at the shear panel. Since the rotating crack model adjusts the plane of degradation orthogonal to the direction of the principal stresses it was expected that the softening response due to concrete cracking would be captured.

5.3.3. Concrete in Compression

Under compression loading, the stress-strain relationship of the concrete model has a very simple shape which is formed with a bilinear curve. The ultimate compressive strength, $f_c^{'}$, is limited with the Ottosen failure surface that takes into account the tri-axial state of stress. An increase in compressive stresses in the direction of two orthogonal axes results in an increase on the compressive strength in the third direction. This indicates that the effect of confinement is incorporated in the model. On the contrary of the effect of confinement, suction stresses in the direction of two orthogonal axes causes a reduction on the compressive strength in the direction of the third axis perpendicular to the other two orthogonal axes. Concrete in compression during unloading and reloading is assumed to behave linearly elastic with a slope equal to the elastic modulus of concrete defined by the user. Sketch of the stress-strain relationship of the model under cyclic compression is shown in Figure 5.3. Failure under compression is achieved by defining an ultimate compressive strain, ε_u, as an input. The effect of crushing and spalling of the concrete could be included in the analysis through a deletion of a finite element exceeding the maximum compressive strain provided by the user.

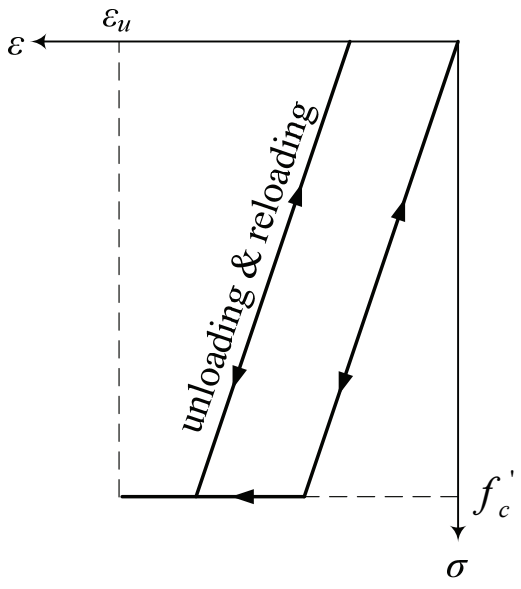


Figure 5.3. Constitutive model for concrete under compression

5.3.4. Shear Transfer across Crack Face

Shear force transfer due to aggregate interlock parallel to the cracked section is considered in the model. Transferred shear stress is reduced by multiplying the shear stress at the finite element by a coefficient which is dependent on the crack width and consequently on the aggregate diameter. Above mentioned shear stress modification coefficient, SSC, versus crack width relationship is defined with the following parabolic function:

$$SSC = \frac{(a - w_i)^2}{a^2} \tag{5.4}$$

Here, a is the aggregate diameter defined by the user and w is the crack width at time step i. Figure 5.4 exhibits a schematic view of the function. In this figure, it should be noticed that once the crack width exceeds the aggregate diameter no shear stress is transferred. On the other hand, if the crack is closed, the shear stress is transferred without any reduction.

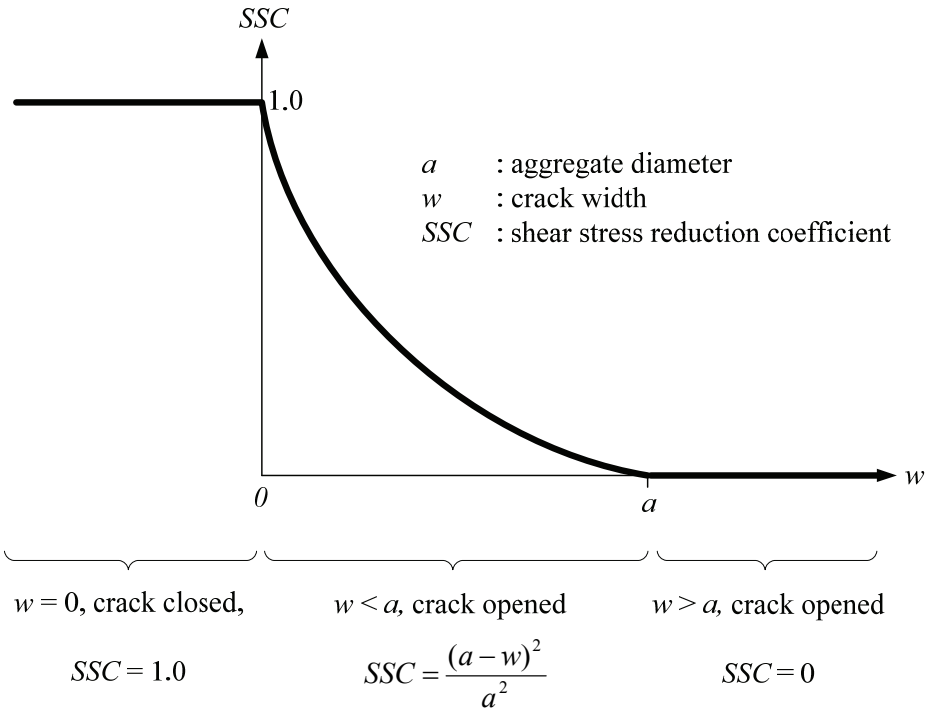


Figure 5.4. Shear stress modification function [74]

In the simulations, concrete properties were taken as follows; elasticity modulus, E_c=28 GPa; uniaxial compressive stress, $f_c^{'}$=26 MPa; poison ratio, η=0.2; crack width, w=0.2 mm; aggregate size, a=20 mm.

5.4. Model for the Steel Reinforcement

Stress-strain constitutive relationship of the reinforcing steel is simulated with a bilinear curve, whose initial slope is equal to the Young's Modulus of the steel. Yield stress provided by the user as an input is the limiting stress value of the first portion of the bilinear curve which simulates the elastic behavior of the steel material. The second portion of the bilinear curve is assumed to simulate the behavior after yielding of the steel and its slope was assumed to be equal to 1% of the Young's Modulus of the steel. After yielding, plastic deformations are allowed and the slope of the unloading-reloading stress-strain curve is kept equal to the Young's Modulus of the steel material. Under cyclic loading the model displays an isotropic hardening rule. This enables the yield surface to expand under plastic cyclic deformations. Schematic view of the stress-strain model and the yield surface under cyclic loading is shown in Figure 5.5 and Figure 5.6, respectively.

In the simulations, the Young's modulus, E_s, was assumed to be 200 GPa, tangent modulus, E_t, was assumed to be 2 GPa, yield stress, σ_y, was assumed to be 450 MPa and the poison ratio was assumed to be 0.3.

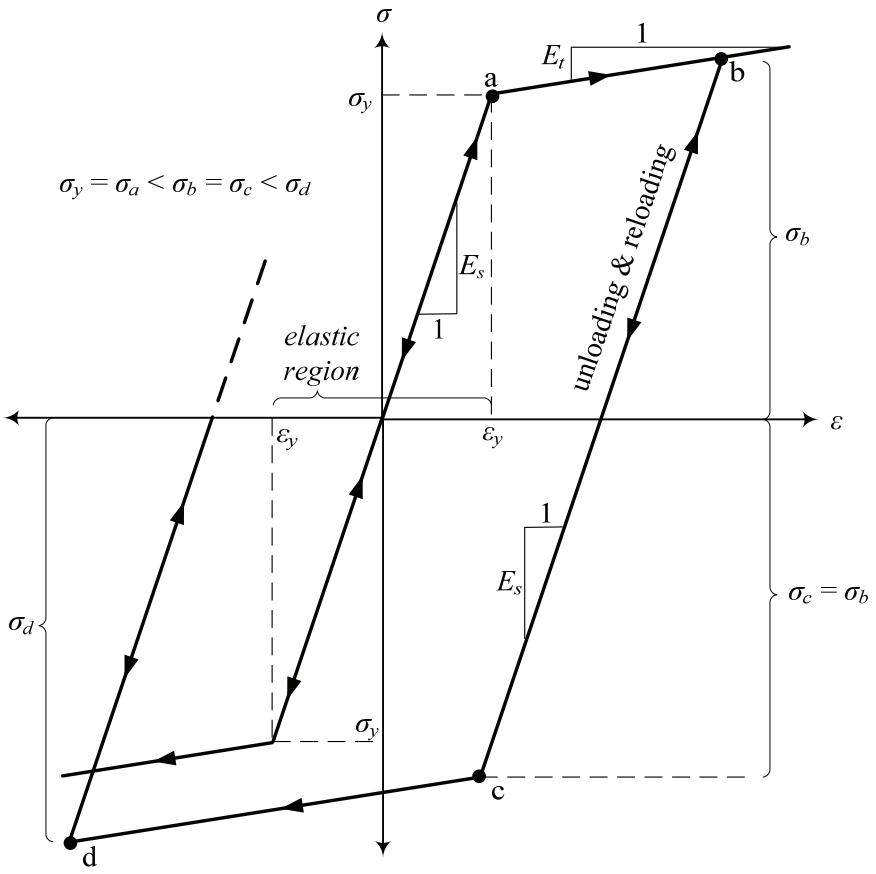


Figure 5.5. Stress-strain model for steel under cyclic loading

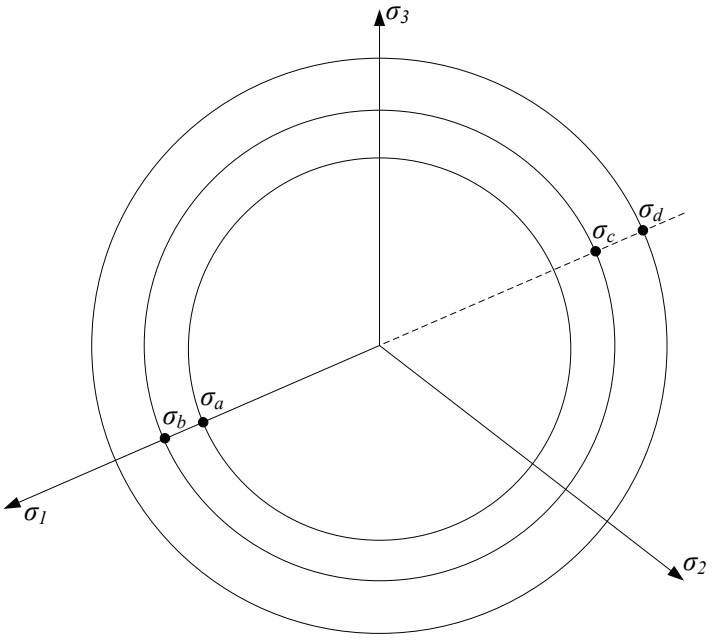


Figure 5.6. Deviatoric section of the yield surface for steel

5.4.1. Treatment of the Rebar Slip

Except the beam bottom longitudinal reinforcement all steel reinforcements were assumed to be fully bonded to the concrete such that all nodes defining the steel reinforcement elements were shared with those of the solid elements of the concrete. In order to simulate the slippage of the beam bottom longitudinal reinforcement, constitutive material model of the shortly embedded portion of the reinforcement was modified such that the ultimate tensile stress developed in the reinforcement was limited with an average stress level of 140 MPa extracted from the experimental data of a slipping rebar. Thus the cyclic behavior of the slipping rebar was exactly the same as the behavior shown Figure 5.5, except that the tensile yield stress was set to 140 MPa whereas the compressive yield stress remained the same as 450 MPa.

5.5. FRP Material Model

Unidirectional CFRP material was modeled in LS-Dyna with an arbitrary orthotropic material MAT_ENHANCED_COMPOSITE_DAMAGE [71-72]. The constitutive model was assumed to be linear elastic up to rupture. After rupture is observed, its strength is reduced with a damage decay function based on a study by Chang and Chang [83]. In order to simulate the uniaxially woven CFRP fabric, the CFRP was modeled as an orthotropic material. The tensile strength in the direction of the fibers, from now on referred as longitudinal direction, was defined to be much higher than the tensile strength in the transverse direction. Also, in both longitudinal and transverse directions the compressive strengths were defined to be almost equal to zero. An approximate assumption was made also for the shear strength of the CFRP material, such that the shear strength was much lower then the tensile strength in longitudinal direction.

In the simulations the following CFRP material properties were taken; tensile strength in the direction of fibers, XT =3800 MPa; tensile strength in transverse direction, YT =60 MPa; compressive strength in fiber direction, XC =80 MPa; compressive strength in transverse direction, YC =80 MPa; Young's modulus in fiber direction, EA =210 GPa; Young's modulus in transverse direction, EB =0.1 MPa; shear modulus for each direction was assumed to be only 10 Pa.

5.6. Mesh Generation

Finite element meshes were created through the use of MSC. Marc Mentat preprocessor routines. Then, these meshes were exported to LS-PrePost and saved as text files. After some intensive text editing, the input data for LS-Dyna was created. FE components created explicitly during the mesh generation process are shown in Figure 5.7.

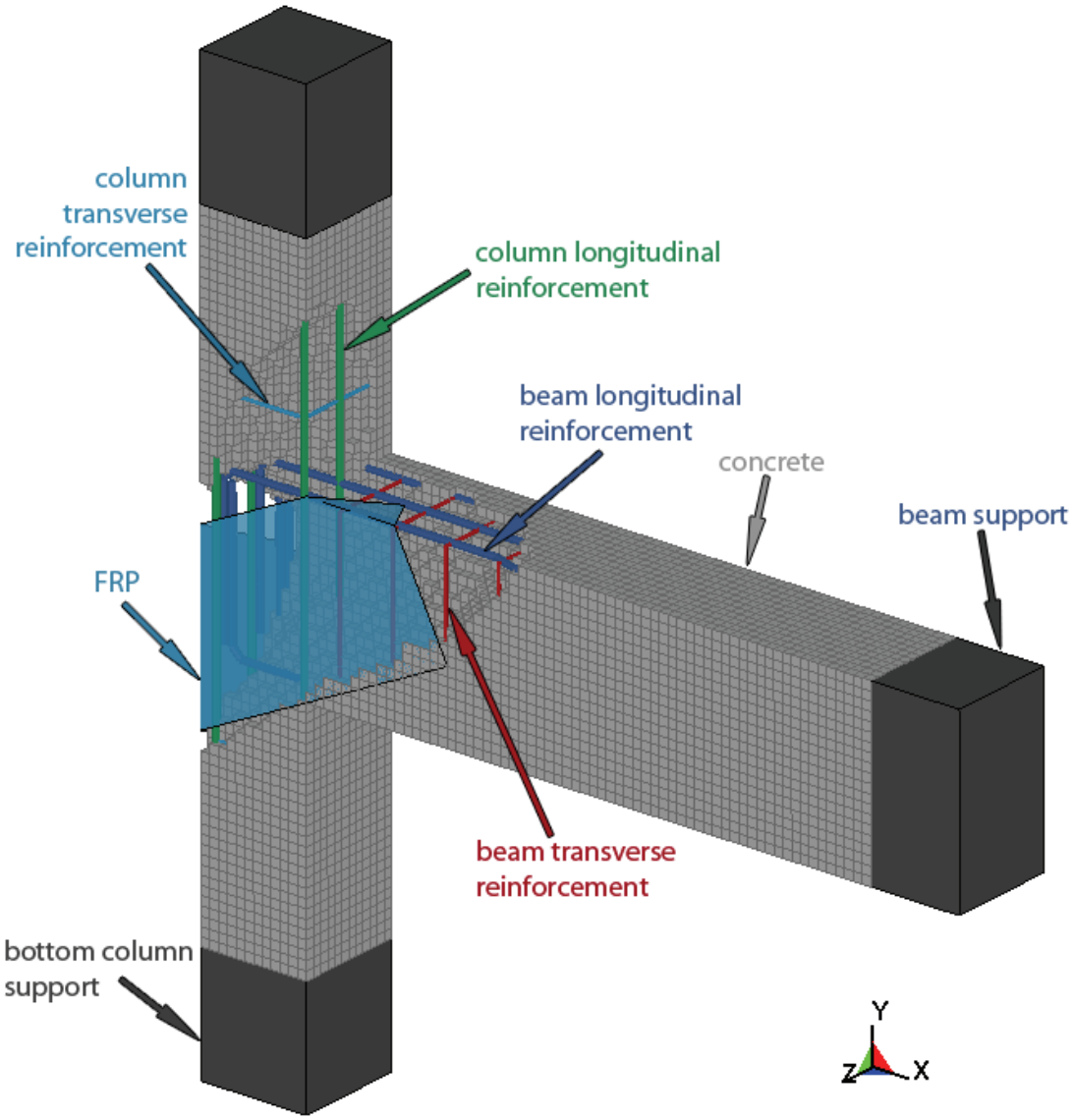


Figure 5.7. Finite element components

The dimensions of the FE models were exactly the same as the dimensions of the test specimens. General dimensions are already given in Figure 3.7.

Total number of finite elements used for the control specimen models was 34733, where 32160 of which were solid and 2573 were beam elements. Additional 5248 shell elements were used for the CFRP retrofitted finite element model and that increased the total number of elements in this model to 39981.

The concrete material was modeled with 8-node, single integration point solid elements with equal edge dimensions, 25 x 25 x 25 mm. Errors that could accumulate due to bad aspect ratio of the edge dimensions of the solid elements were prevented by keeping the aspect ratio to be equal to unity.

Longitudinal and transverse rebars were modeled with 2-node beam elements with lengths of 25 mm. Nodes of the beam elements were shared with the nodes of the solid elements. Two different sections were defined for the beams since the diameter of the longitudinal and transverse reinforcement were different. Beam element formulation was Belytschko-Schwer tubular beam with cross-section integration [71-72].

FRP material was modeled with 3 and 4 node shell elements with edge dimensions varying from 25 mm to 75 mm. In order to decide on which element formulation to be used for the shell elements, single shell element was tested under cyclic loading both in the direction of the fibers and in the transverse direction. As a result of the single element test, Belytschko-Tsay element formulation [71-72] was chosen, since it provided a stress-strain relationship close to the mechanical data supplied by the manufacturer [58].

In order to simulate the supports, column and beam free ends were modeled with solid elements with the same dimension of the solid elements used for modeling of the concrete. In order to represent the well confined region of the supports, these regions were modeled with rigid material.

The finite element mesh for concrete and supports used in the simulations of specimens US1-US4, US1FRP1, US2FRP2, US3FRP3 and US4FRP3 is shown in Figure 5.8.

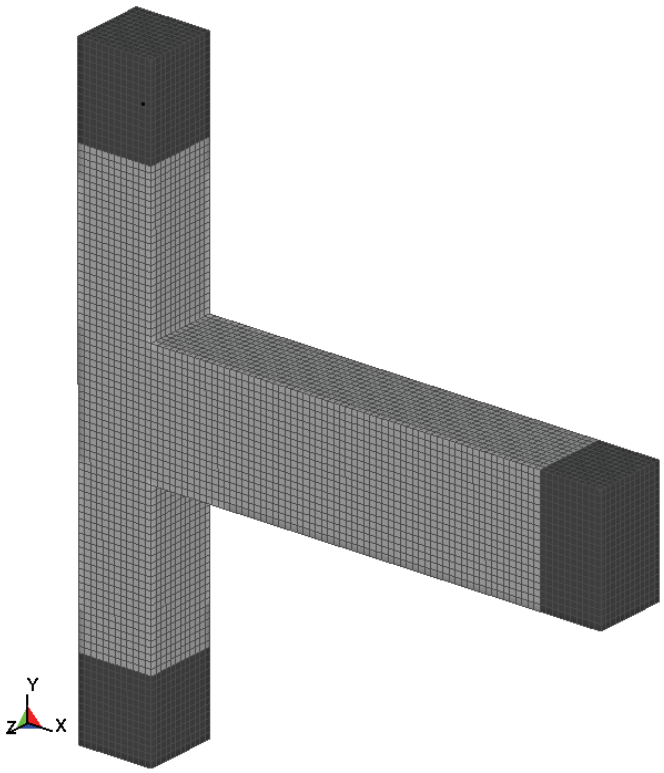


Figure 5.8. Mesh for concrete and supports

Steel reinforcement mesh created for specimens US1 and US1FRP1, is shown in Figure 5.9 and Figure 5.10 displays the steel reinforcement mesh created for the all other specimens, namely, US2-US4, US2FRP2, US3FRP3 and US4FRP3.

FRP meshes created for specimens US1FRP1, US2FRP2, US3FRP3 and US4FRP3 are shown in Figure 5.11-Figure 5.16. It should be noticed that each CFRP plane is modeled separately. For instance, the south face +α CFRP diagonal, shown on the top left in Figure 5.11, was modeled with four different material properties. Each CFRP plane is defined in the global coordinate system with unit vectors in the direction of the fibers. Total number of CFRP materials defined for specimen US1FRP1 is 24, since there are 4 different CFRP planes for a single CFRP diagonal and 2 different planes for each U-shaped FRP, L-shaped FRP, beam wrap and column wraps. Due to the assumption of full bond between CFRP and concrete, each node of a shell element was coincided with a node of a solid element.

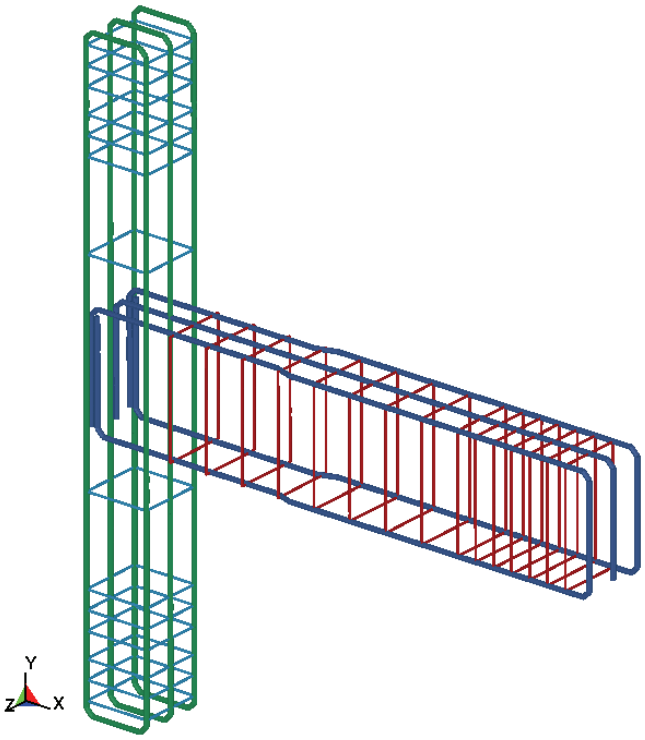


Figure 5.9. Steel reinforcement mesh for US1 and US1FRP1

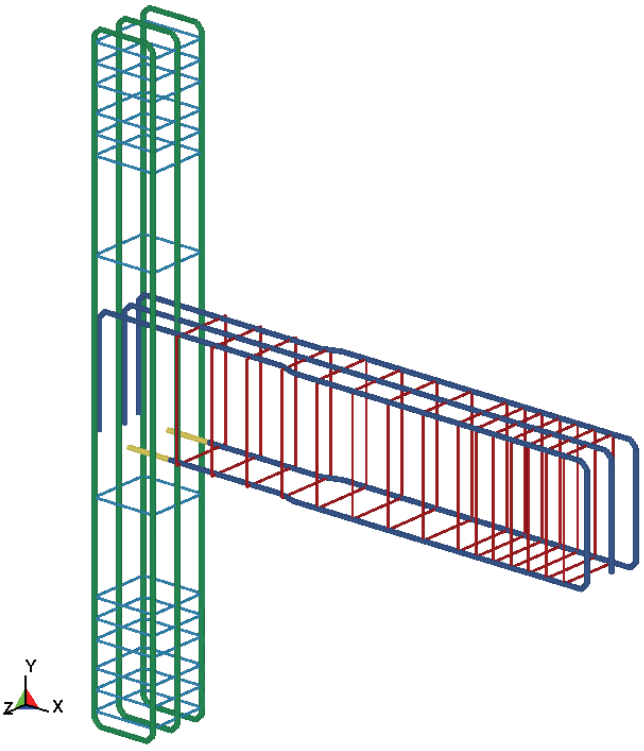


Figure 5.10. Steel reinforcement mesh for US2-US4, US2FRP2, US3FRP3 and US4FRP3

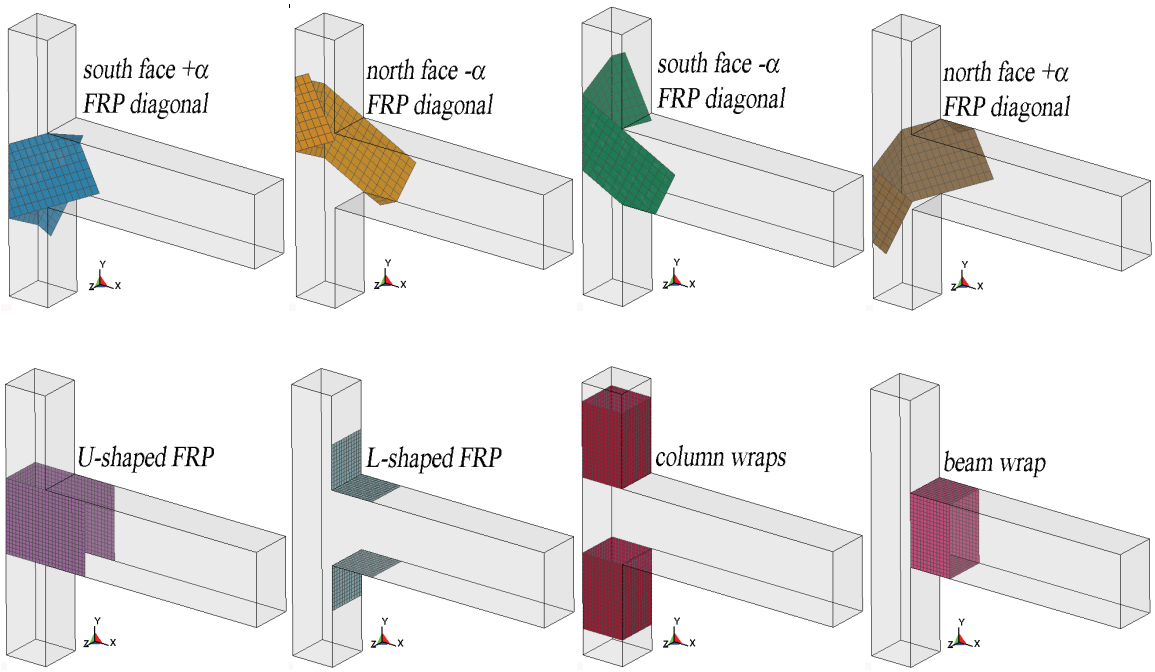


Figure 5.11. CFRP mesh components for US1FRP1

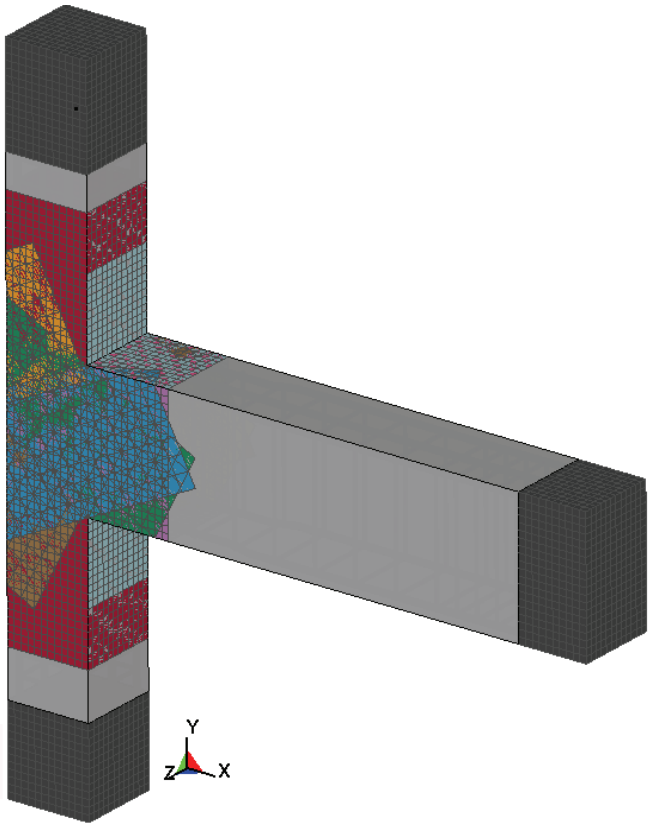


Figure 5.12. CFRP mesh for US1FRP1

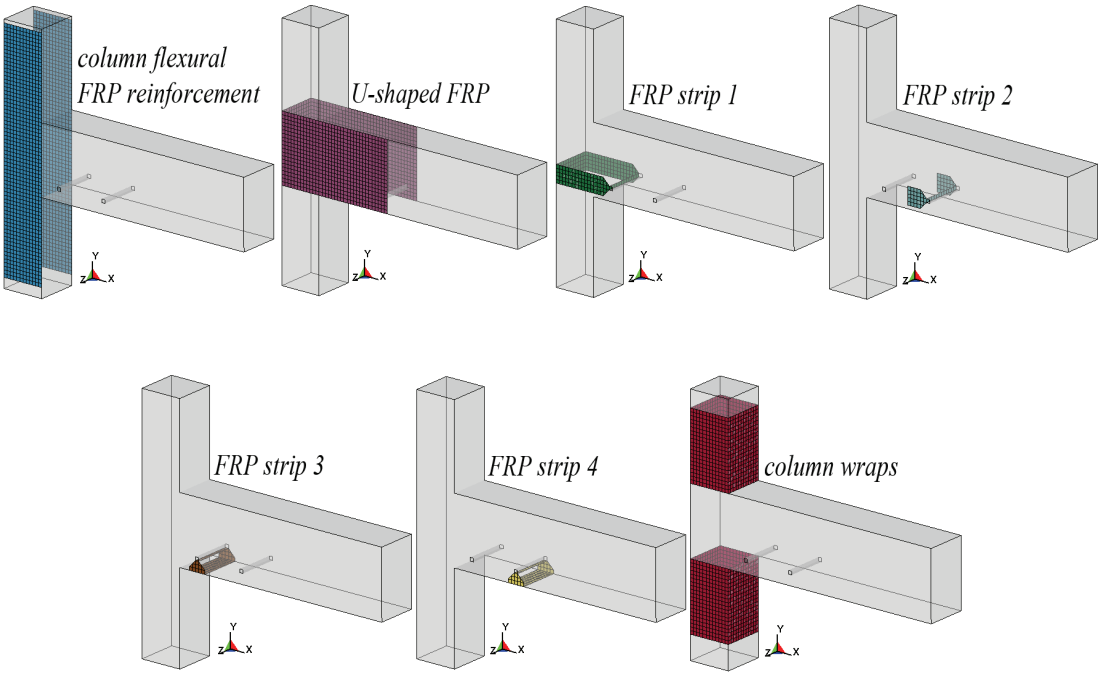


Figure 5.13. CFRP mesh components for US2FRP2

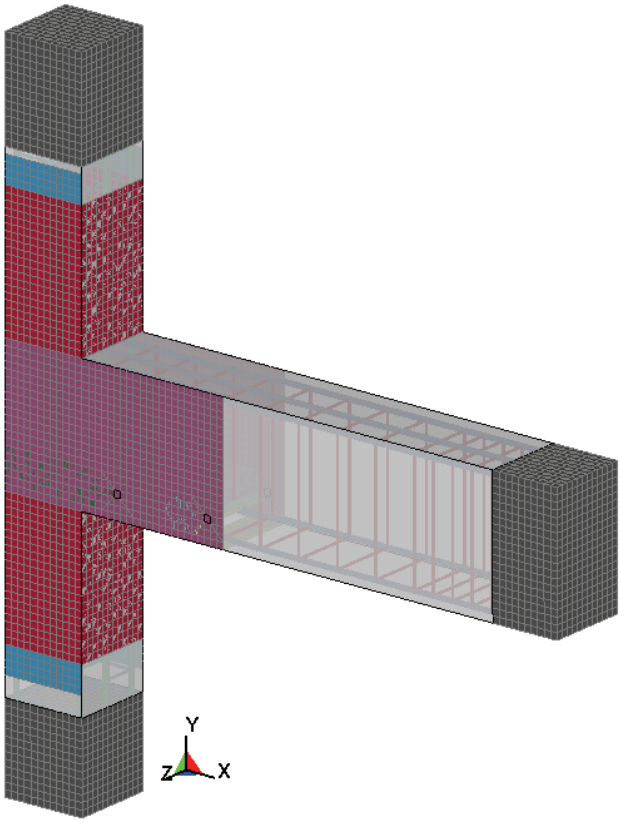


Figure 5.14. CFRP mesh for US2FRP2

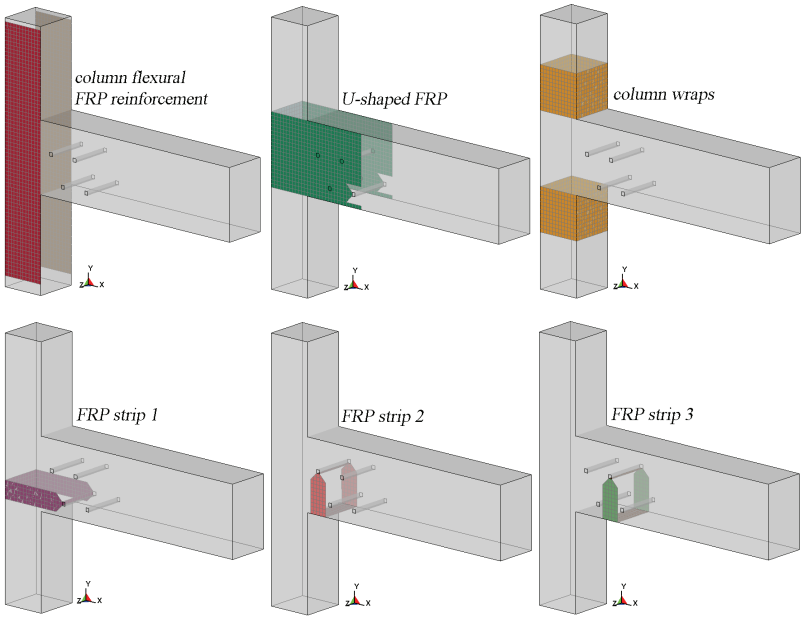


Figure 5.15. CFRP mesh components for US3FRP3 and US4FRP3

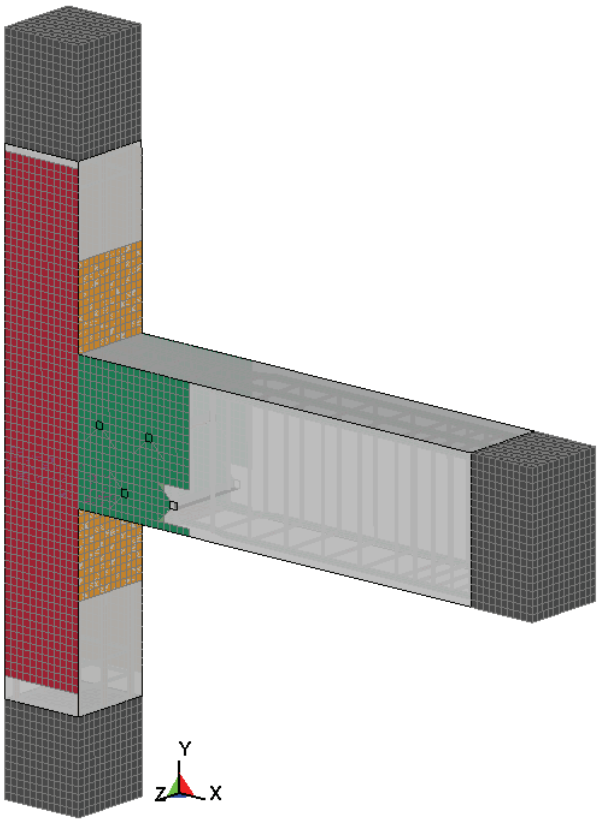


Figure 5.16. CFRP mesh for US3FRP3 and US4FRP3

5.7. Boundary and Loading Conditions

Bottom column free-end nodes, shown in Figure 5.17 (a), were fixed in translation in the global X, Y and Z directions. The same nodes were also fixed to rotate about X and Y axes to account for any out of plane action and were allowed to rotate freely about Z axis to simulate a simple support boundary condition in the direction of loading. The beam free-end nodes, shown in Figure 5.17 (b), were fixed in all translational and rotational directions, except the global translational X and rotational Z directions. This type of boundary condition defined for the beam free-end simulates a roller support in the loading direction.

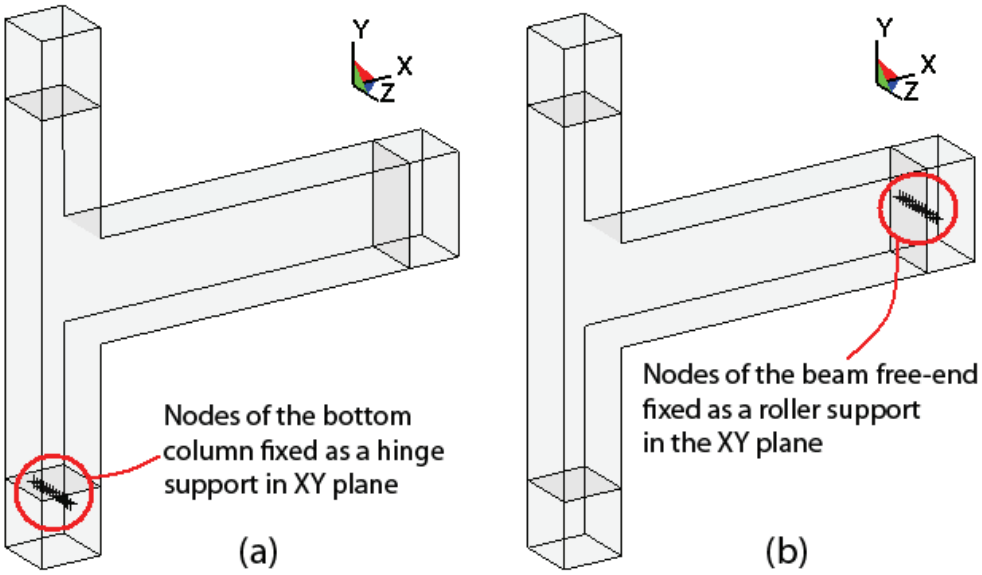


Figure 5.17. Boundary conditions

The lateral loading was applied to the top column free-end in the global X direction, as shown in Figure 5.18. The same target displacement levels as those used in the experiments were used for the loading in the finite element simulations, except that during the simulation in each target drift level a single displacement cycle was imposed where in the experiments three cycles per drift level was applied. The analyses can be considered as quasi-static since the cyclic displacement loading was applied dynamically with long loading duration such that no inertial effects were observed in the simulation.

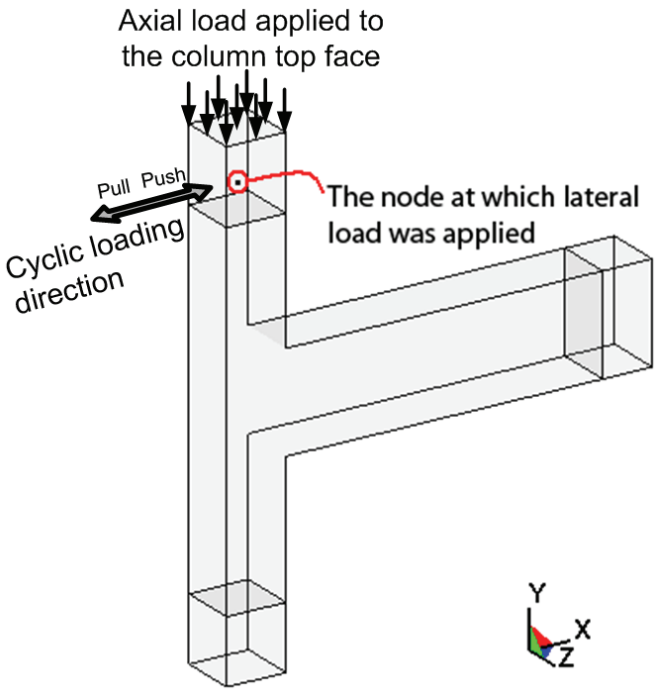


Figure 5.18. Applied loading

In the simulation prior to the application of the lateral loading, 700 kN of axial load was applied, as shown in Figure 5.18, to the top of the column face as an equivalent pressure. In this way, the direction of the axial load was kept always in the longitudinal direction of the column as it was the same in the experiments.

5.8. Run Time of the Simulations

In order to provide a general understanding for the run time of the FE simulations the following example is given.

The time needed to complete an analysis of a single CFRP retrofitted beam column joint simulation (total number of finite elements was 39981) on a PC with single-core, Intel Pentium 4, 3.4 GHz CPU and 2 GB of RAM was approximately 1008 hours (42 days). The same model was then analyzed on HP DL360G5 server with 8-core, Xeon 2.50 GHz CPU with 8 GB of RAM and the run time was reduced to approximately 121 hours (5 days). The same model was again analyzed on a compute cluster with 32-core, Xeon 2.50 GHz CPU with 40 GB of RAM and the run time was reduced substantially to approximately 22 hours

(less than a day). This fact shows that the use of a cluster with parallel computing was an indispensable tool in this type of study.

5.9. Verification of the Finite Element Models with Experimental Results

The reliability of the finite element simulations was discussed through a comparison between the experimental and numerical results. Mainly, lateral load vs. top displacement responses, damage observations during testing and simulation, and modes of failure are discussed. In this section, also, additional information which could not be easily obtained from an experimental study is aimed to be presented; such as damage development in the concrete medium beneath the FRP, stress distribution in the core of the concrete, possible locations of the rebar yielding, etc.

5.9.1. Specimen US1

Although the loading was applied dynamically, the FE analysis could be assumed as quasi-static since the kinetic energy throughout the analysis is zero and the total energy is almost equal to internal energy. The recorded energy data during the simulation is shown in Figure 5.19. In this figure, kinetic energy is the energy created due to inertial forces; internal energy is the energy created due to strain developed in the finite elements; hourglass energy, which is provided by the finite element code, is an artificial energy provided to the highly deformed elements for stability; and the total energy is the summation of the kinetic, internal and hourglass energies.

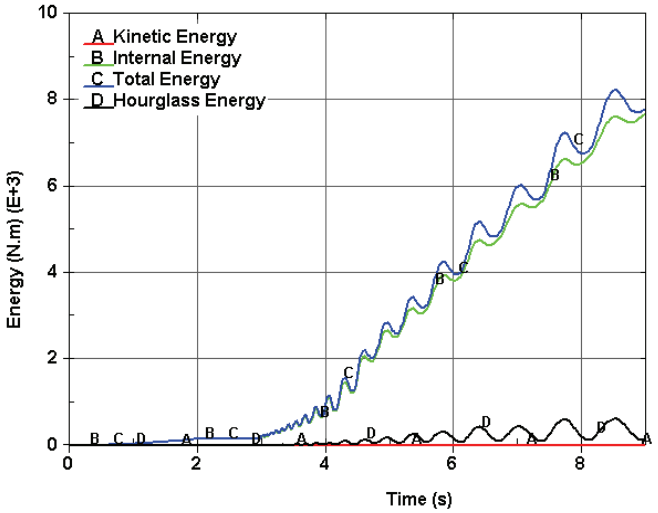


Figure 5.19. Energy vs. time, output from LS-Dyna [72], US1

The comparison between the experimentally and numerically obtained lateral load versus top displacement relationships is shown in Figure 5.20. In both directions of loading numerically obtained ultimate loads (70 kN in push and 80 kN in pull directions of loading) are in good agreement with the experimental loads (62 kN in push and 76 kN in pull directions of loading). The shape of the hysteretic response of the lateral load versus top displacement relationship is in good agreement with the experimentally obtained lateral load top displacement relationship, as seen from the same figure. The pinched shape near the origin of the hysteretic response due to crack closures at the joint core and the beam is well predicted through the FE modeling. The post peak softening response, which is a critical and challenging region for most of the finite element solvers, is also captured.

In the experimental testing of specimen US1, heavy damage at the joint region was observed due to excessive shear deformations at joint core. The FE simulation of specimen US1 showed very similar failure mode as seen in Figure 5.21.

Furthermore, Figure 5.23 shows the crack patterns at the initial drift levels obtained from the numerical and experimental observations. Locations of the initial flexural cracks at the beam face are also in agreement with locations of the cracks observed during experimental testing.

At the initial drift levels, especially prior to cracking, FE results exhibit higher stiffness compared to the experimental findings. This could be due to the fact that full bond between the steel reinforcement and concrete was assumed.

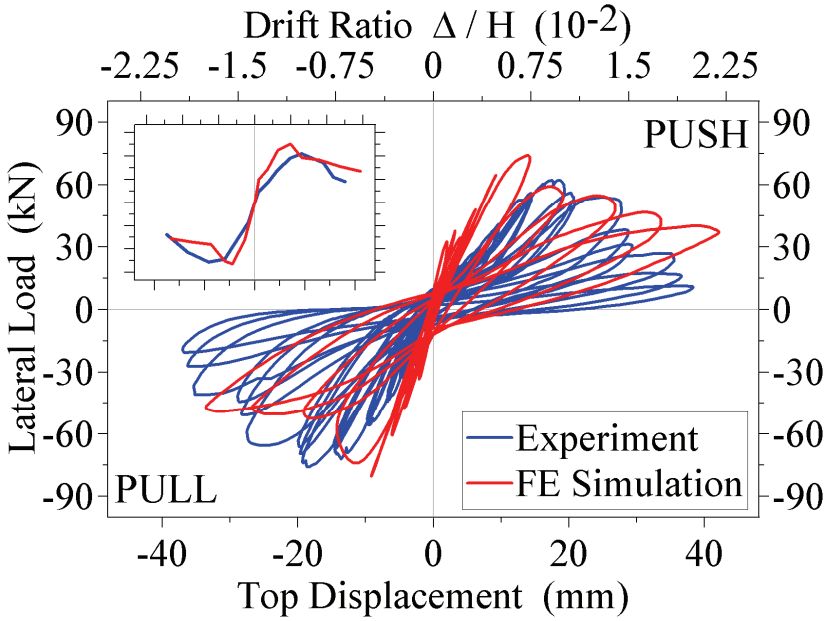


Figure 5.20. Lateral load vs. top displacement comparison, US1

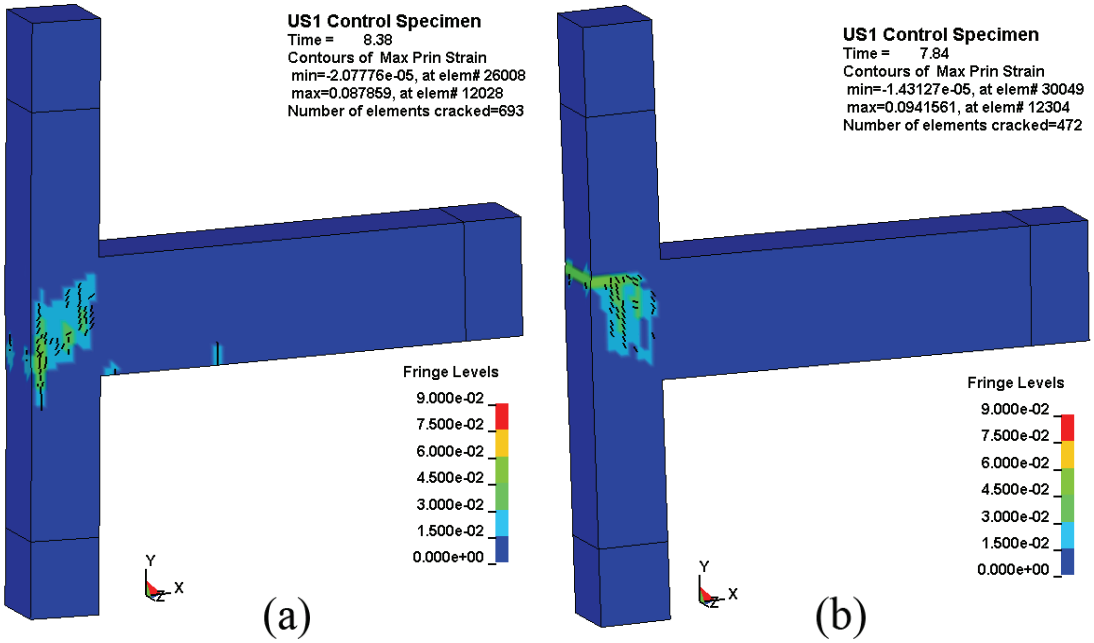


Figure 5.21. Shear failure at the joint; (a) push, (b) pull direction of loading



Figure 5.22. Shear failure at the joint core

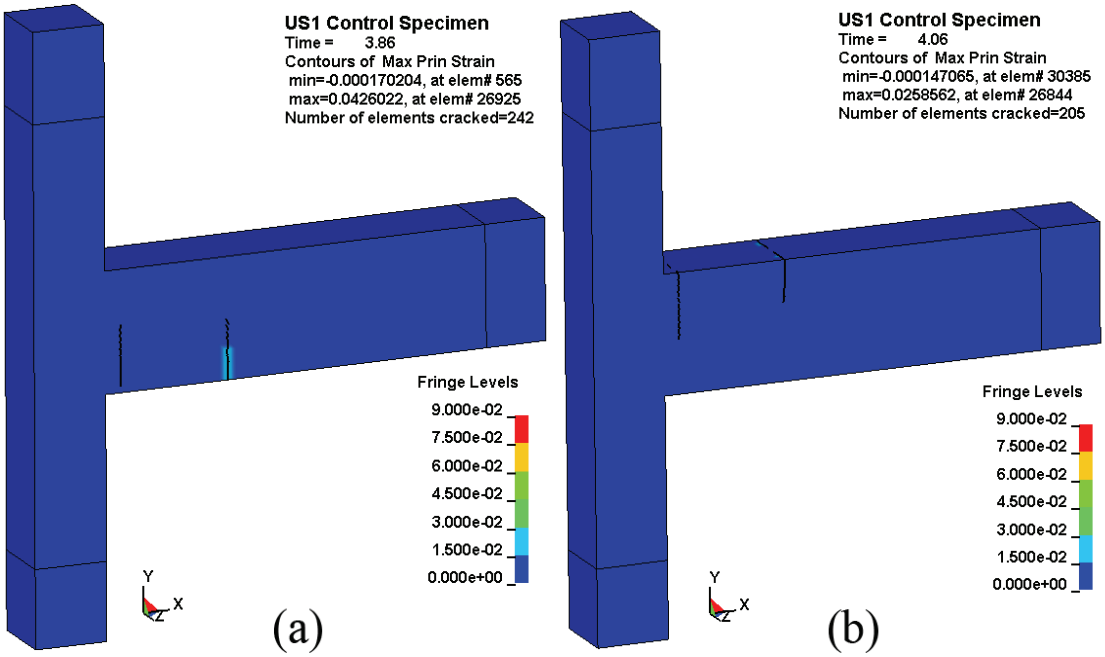


Figure 5.23. Flexural cracks at the beam; (a) push, (b) pull direction of loading

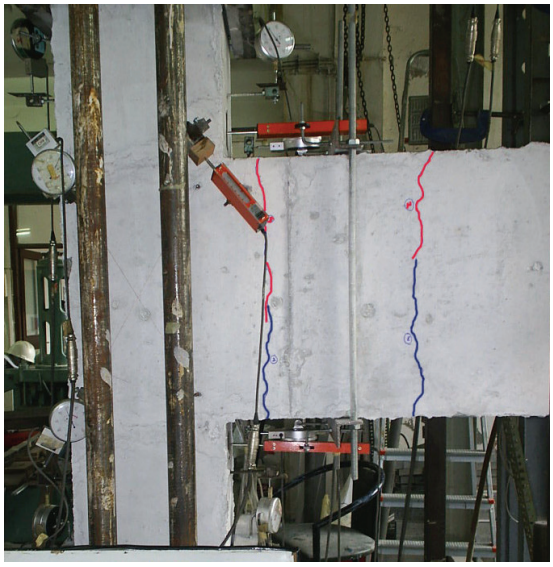


Figure 5.24. Flexural cracks at the beam

A comparison was also made between the joint shear deformation versus lateral load relationships of the numerical and experimental results as shown in Figure 5.25. In the experiment shear deformations calculated as described in Section 4.3. In the FE simulations, shear deformation, ε_{xy}, was extracted from LS-Dyna outputs and were compared each other. At the initial drift levels, there are almost no shear deformations and with an increasing lateral load shear deformations at the joint core are also increasing. It should be noticed that the shear deformations are lesser in the numerically obtained results. This could be due to the hourglass control implemented in LS-Dyna code that impedes the shear deformations of the solid elements by providing additional stiffness [70-72]. Especially solid elements with single point of integration, as in the current study, could exhibit spurious hourglassing modes shapes and that could trigger the hourglass control feature of the code and thus dissipate additional hourglassing energy as shown in Figure 5.19. This figure also explains the stiffer response of the numerically obtained lateral load versus top displacement relationship at the higher drift levels since the hourglass energy increases with an increased time and thus with an increased top displacement.

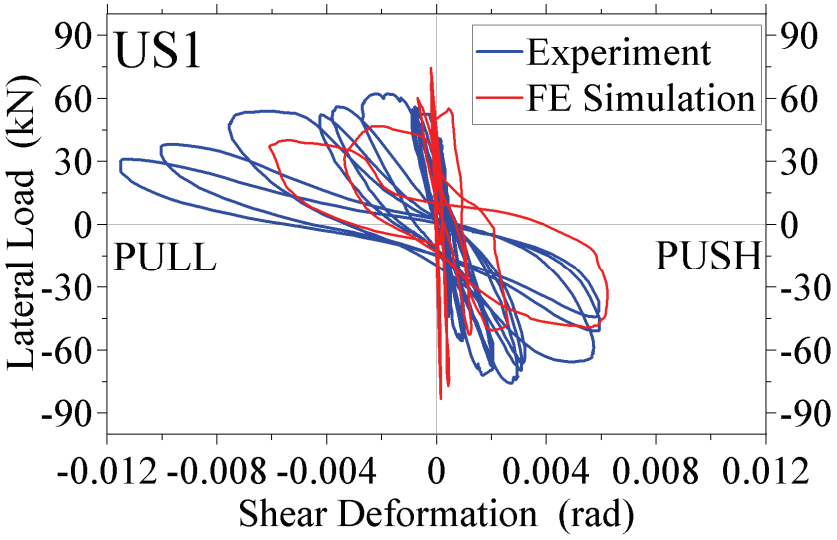


Figure 5.25. Joint shear deformation vs. lateral load

In terms of ultimate load level, damage locations, failure modes and hysteretic response, in overall, the FE simulation results are in good agreement with the experimental findings.

5.9.2. Specimen US1FRP1

Firstly, to show that the FE simulation of specimen is a quasi-static simulation and no inertial effects are included in the analysis, the energy versus time relationship is given in Figure 5.26. As seen from the figure the kinetic energy of the system is equal to zero showing that inertial effects are not included. Throughout the analysis the total energy is maintained mainly with the internal, strain energy and minimum amount of hourglass energy is dissipated through the control of hourglass mode shapes as shown in Figure 5.26.

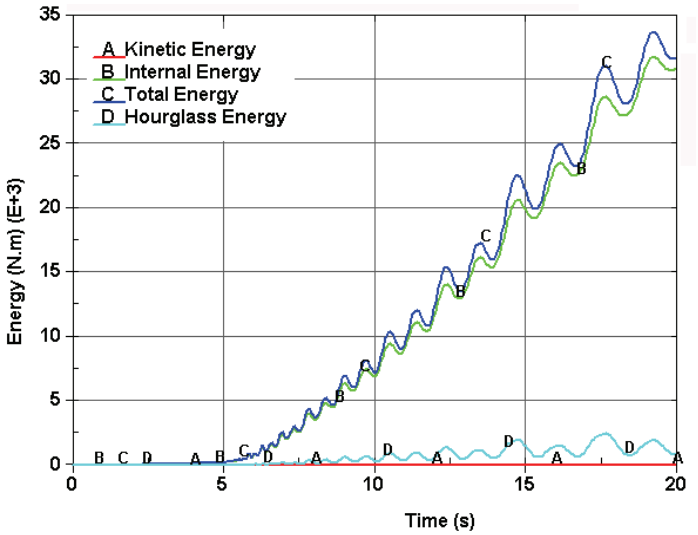


Figure 5.26. Energy vs. time, output from LS-Dyna [72], US1FRP1

The comparison between the experimentally and numerically obtained lateral load versus top displacement relationships is shown in Figure 5.27. In both directions of loading numerically obtained ultimate loads (110 kN in push and 140 kN in pull directions of loading) are in good agreement with the experimental loads (98 kN in push and 134 kN in pull directions of loading). The shape of the hysteretic response of the lateral load versus top displacement relationship is in good agreement with the experimentally obtained lateral load top displacement relationship, as seen from the same figure. The pinched shape near the origin of the hysteretic response of the experimental load versus displacement relationship is much higher than the numerical results. Baushinger effect of the steel model and the compression softening effect of the concrete model were not modeled. Thus this could create such a difference between the pinched shapes of the hysteretic responses.

In the experimental testing of specimen US1FRP1, plastic hinging at the beam face was observed just at the end of CFRP application as shown in Figure 5.28. The same type of damage was also observed in the FE simulation. The maximum principal strain contours indicating the excessive deformations in the FE model are shown for comparison in Figure 5.29.

Stress levels in the beam longitudinal reinforcement supports the conception of plastic hinging at the beam. Stress contours in the steel reinforcement are shown in Figure 5.30. Defined yield stress was 450 MPa and it is seen from the figure that this stress level

is reached. The strain readings of beam top longitudinal reinforcement recorded during testing of specimen US1FRP1 is shown in Figure 5.31 for comparison.

As in the case of the control specimen simulation in the CFRP retrofitted model the initial stiffness is higher than the stiffness observed in the experiment. This could be due to the fact that full bond between the steel reinforcement and concrete was assumed.

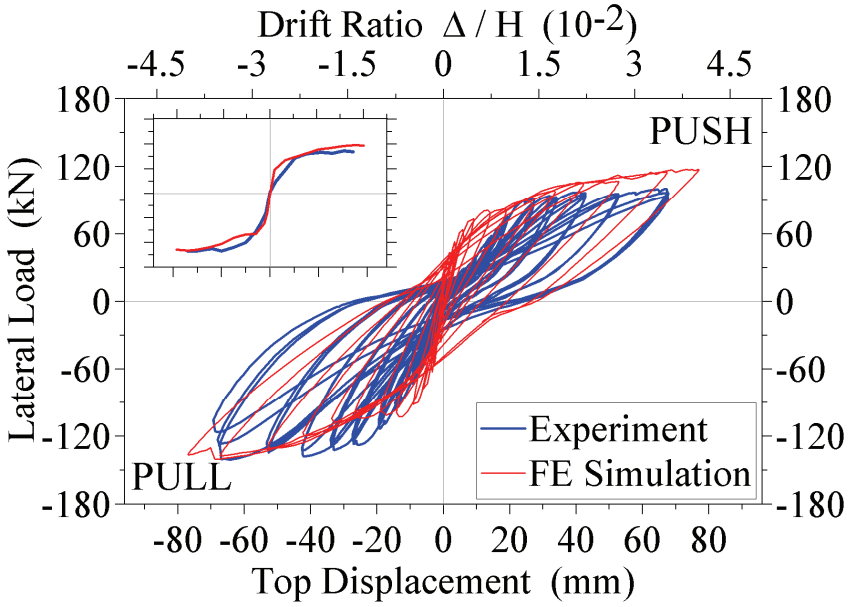


Figure 5.27. Lateral load vs. top displacement comparison, US1FRP1

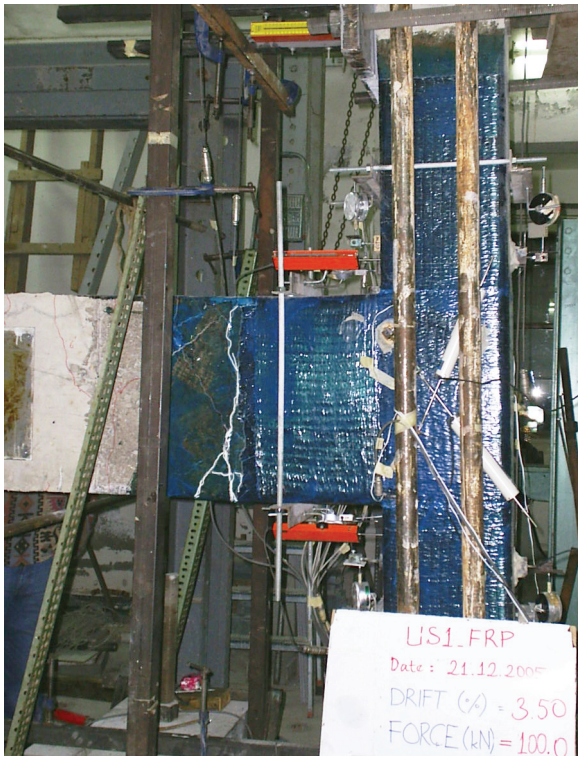


Figure 5.28. Plastic hinge at the beam

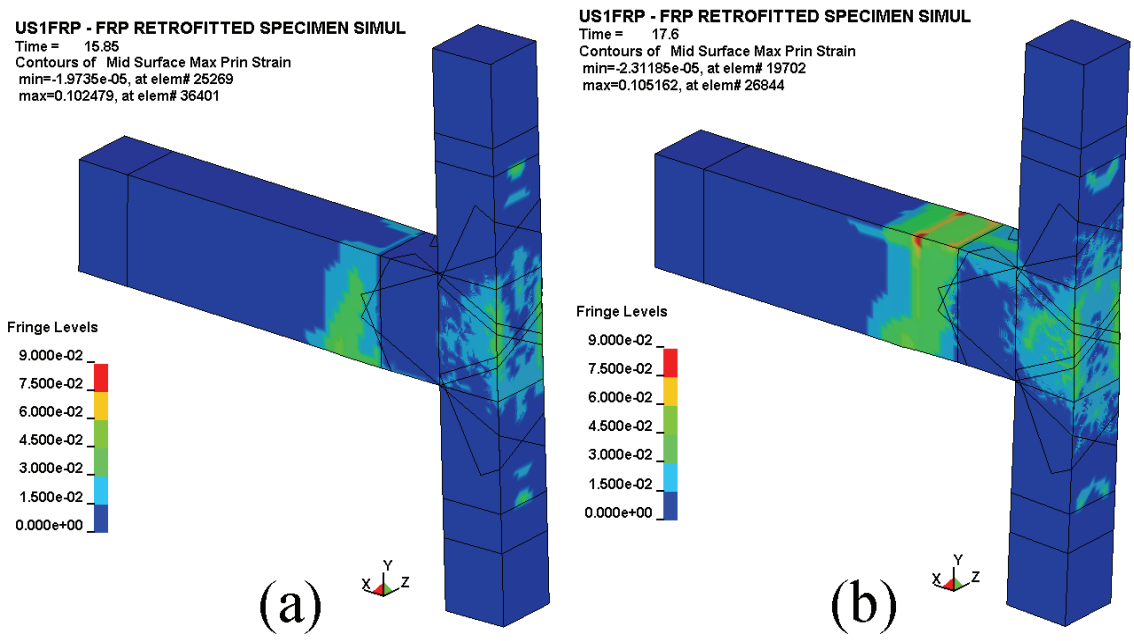


Figure 5.29. Maximum principal strain contours showing the plastic hinging at the beam; (a) push, (b) pull direction of loading

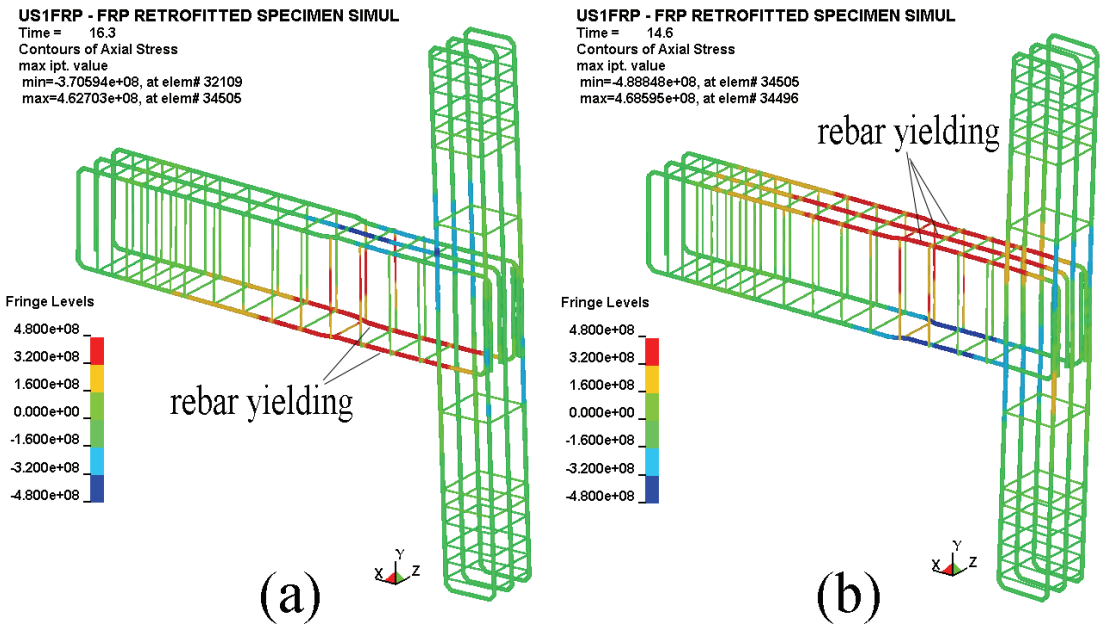


Figure 5.30. Stress at the steel reinforcements showing yielding of the beam longitudinal reinforcements; (a) push, (b) pull direction of loading

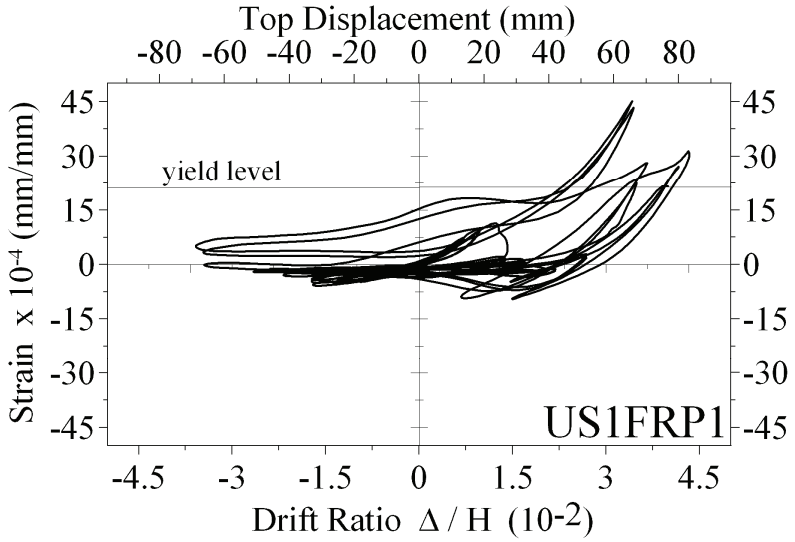


Figure 5.31. Strain readings of beam top longitudinal reinforcement, US1FRP1

A comparison also is made between the joint shear deformation versus lateral load relationships of the numerical and experimental results as shown in Figure 5.32. At the initial drift levels, numerical and experimental shear deformations are in agreement. However, with increasing load level FE simulation results deviate from the experimental results. In the modeling of concrete, utilized solid elements were with single point of integration elements which a single element is poor in simulation of shear deformations.

This could be a reason for the discrepancy between the experimentally and numerically obtained shear deformations

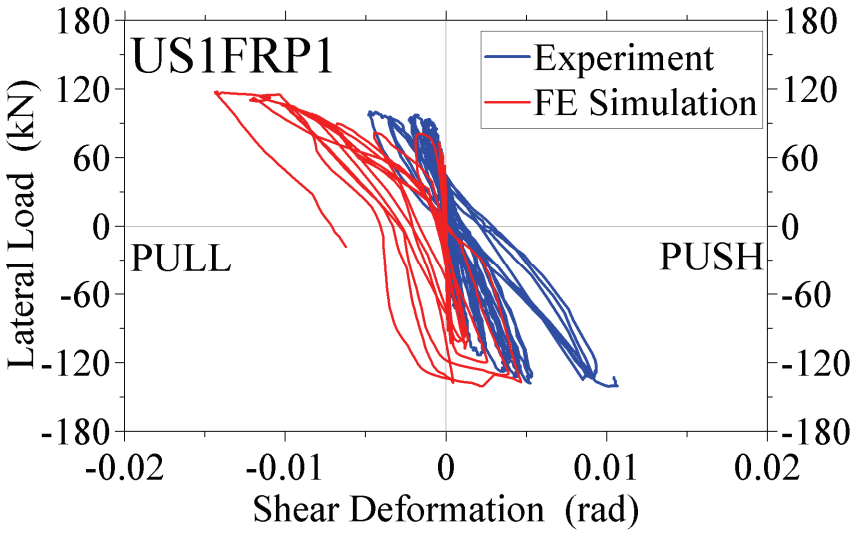


Figure 5.32. Joint shear deformation vs. lateral load

5.9.3. Specimens US2 and US3

The US2 specimen with no shear reinforcement and short embedment length for beam bottom longitudinal reinforcement was simulated under cyclic loading. The finite element model created for modeling specimen US2 was also used to simulate specimen US3, since through the comparison of experimental data of specimens US2 and US3 the lapped splice region of the column longitudinal reinforcement had no effect on the overall behavior. Figure 5.33 shows the comparison between the experimental and numerical lateral load versus top displacement relationships. The ultimate load levels were well predicted. However, the load level in descending branch in push direction of loading is over estimated. This was expected since in the bond stress slip model the descending branch was not defined and the stress that causes slippage was kept constant. Also, the hysteretic loops are fatter compared to hysteretic loops obtained from the experiment. In the bond stress slip model the softening behavior was not defined and this could be a possible reason for the discrepancy between the shapes of the loops. However, in overall the FE simulations are in agreement with the experimental results. Figure 5.34 shows the maximum principal stress contours which indicate the possible failure locations.

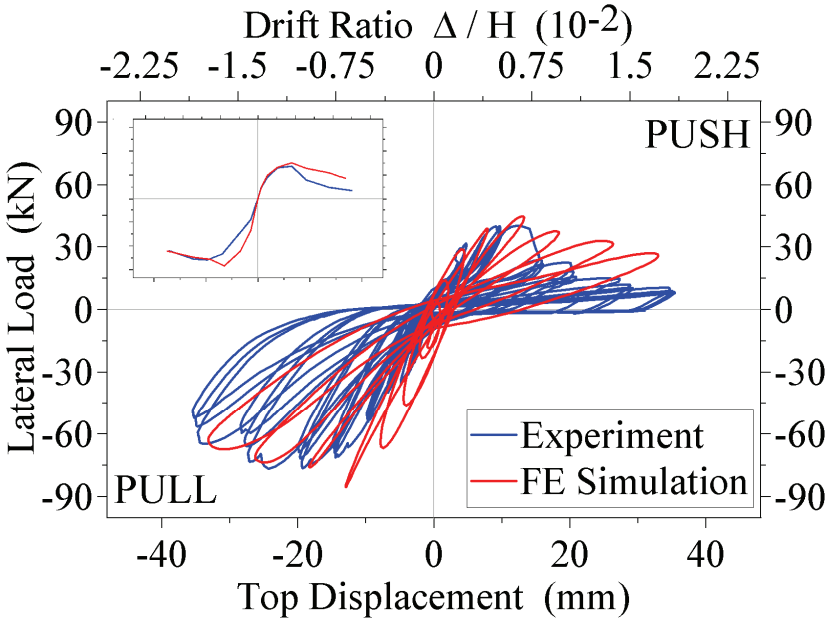


Figure 5.33. Lateral load vs. top displacement comparison, US2 and US3

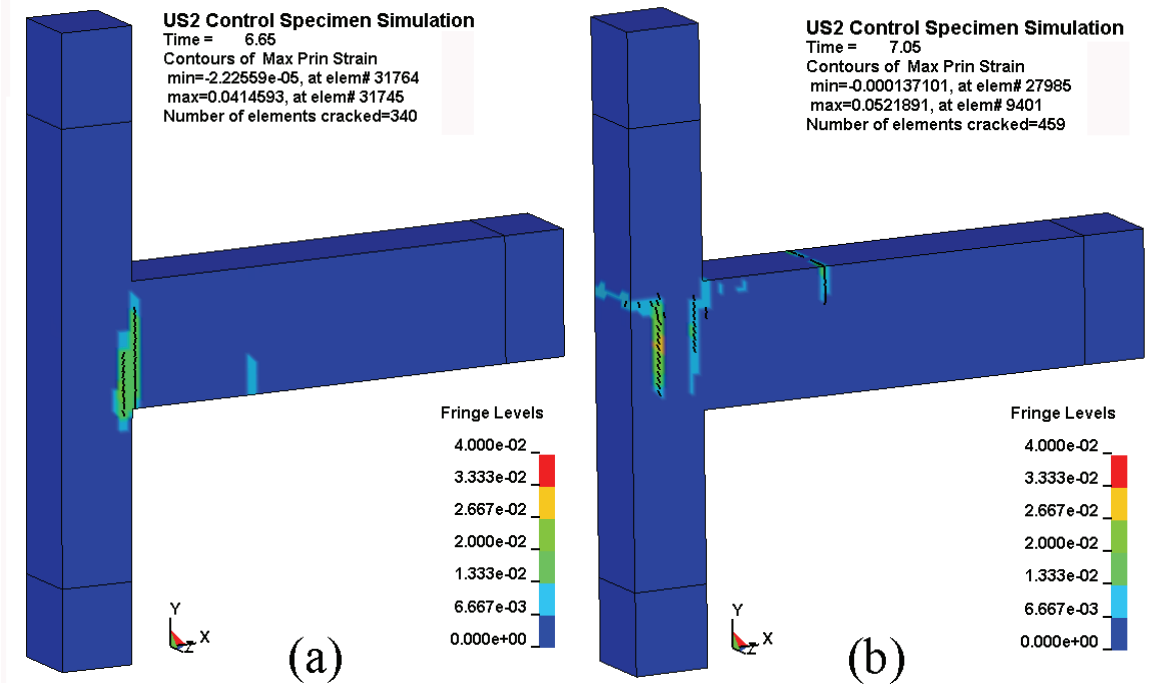


Figure 5.34. Maximum principal strain contours and crack pattern; (a) push, (b) pull direction of loading

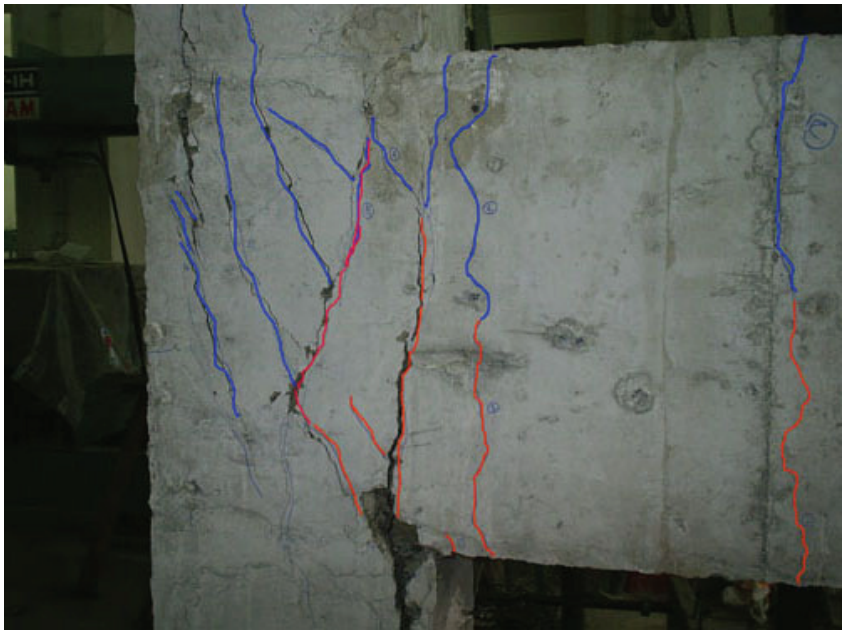


Figure 5.35. Observed damage at the end of the experiment of US2

5.9.4. Specimen US2FRP2

Specimen with no shear reinforcement and short embedment length for beam bottom longitudinal reinforcement which is wrapped with FRP2 technique was simulated under cyclic loading. Figure 5.36 shows the comparison between the experimental and numerical lateral load versus top displacement relationships. On the left upper part of the figure, a comparison of the backbone curves is shown. As seen from the figure, both in push and pull directions of loading the ultimate load levels were under estimated. In the simulation, shell elements are connected only to one of the faces of the solid elements and any differential stress between shell and solid elements creates moments and shearing forces to the solid elements. Thus, the amount of internal forces transferred between shell (FRP material) and solid elements (concrete media) was limited with the shear strength and moment capacity of solid elements. A single integration point solid element may not represent the actual strength of the concrete which could be the reason for the discrepancy between the experimental end numerical results.

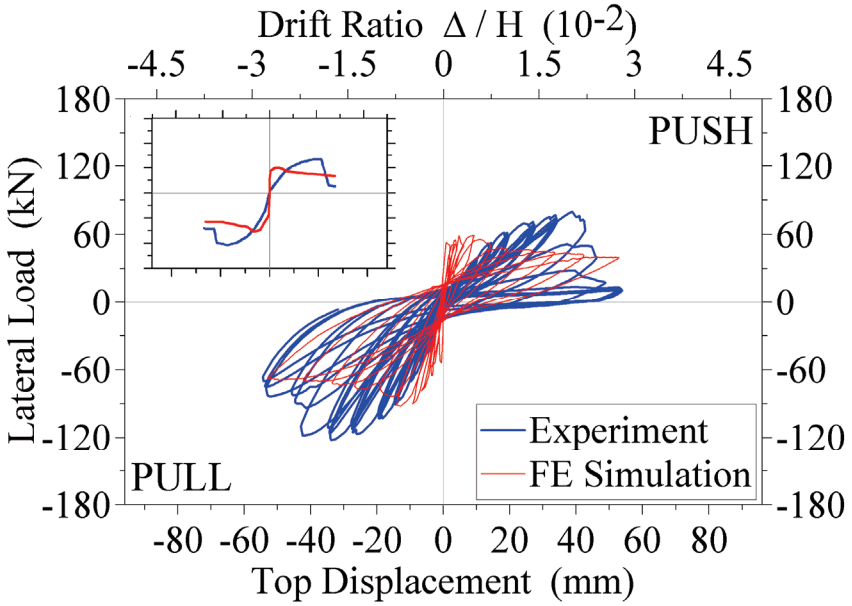


Figure 5.36. Lateral load vs. top displacement comparison, US2FRP

5.9.5. Specimen US3FRP3

In the numerical simulation of specimen US3FRP3 the finite element mesh was generated as described in section 5.6 and the load was applied as described in section 5.7. Hysteretic responses obtained from experimental and numerical investigations are compared in Figure 5.37. The ultimate loads in push and pull directions of loading are underestimated. The use of single integration point solid element could be the reason for the discrepancies between the experimental and numerical results. In LS-Dyna, the utilized Winfrith concrete model is applicable only on single integration point solid element which is poor in representing the internal force transfers between solid and shell elements. Different contact algorithms between FRP and concrete materials or outer and inner nodes could be utilized to simulate the actual behavior.

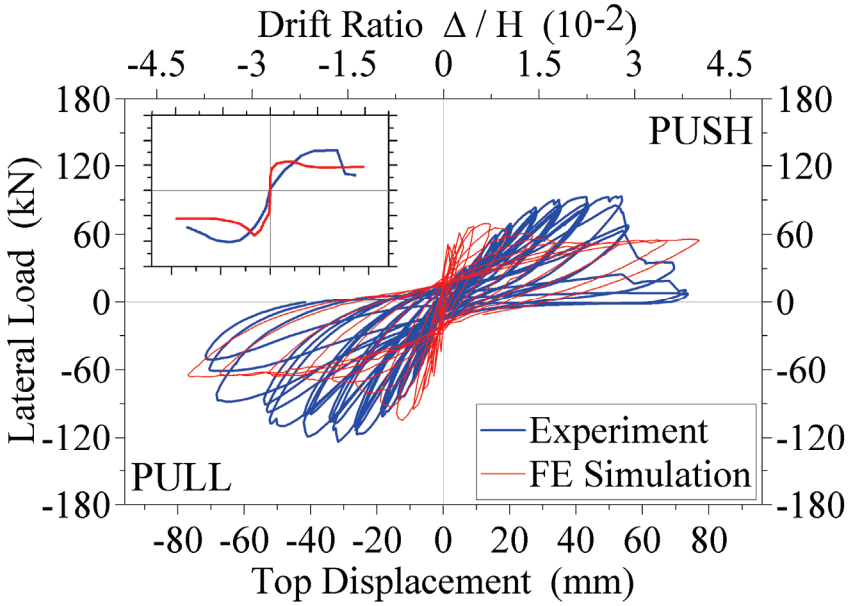


Figure 5.37. Lateral load vs. top displacement comparison, US3FRP3

5.9.6. Specimen US4

The comparison between the experimentally and numerically obtained lateral load versus top displacement relationships is shown in Figure 5.38. In both directions of loading numerically obtained ultimate loads (40 kN in push and 64 kN in pull directions of loading) are in good agreement with the experimental loads (35 kN in push and 75 kN in pull directions of loading). The shape of the hysteretic response of the lateral load versus top displacement relationship is in good agreement with the experimentally obtained lateral load top displacement relationship, as seen from the same figure. The pinched shape near the origin of the hysteretic response due to crack closures at the joint core and the beam is well predicted through the FE modeling. The post peak softening response in push direction of loading which was governed with the slippage of beam bottom longitudinal reinforcement was slightly overestimated. This was due the fact that in the finite element simulation the bond stress was defined elastic perfectly plastic with no descending branch. As already described in the literature [84], the backbone curve of the bond stress slip models under cyclic loading, has a descending branch in fact.

In the experimental testing of specimen US4, heavy damage at the joint region was observed due to excessive shear deformations at joint core. The FE simulation of specimen US4 showed very similar failure mode as seen in Figure 5.39.

At the initial drift levels, especially prior to cracking, FE results exhibit higher stiffness compared to the experimental findings. This could be due to the fact that full bond between the steel reinforcement and concrete was assumed.

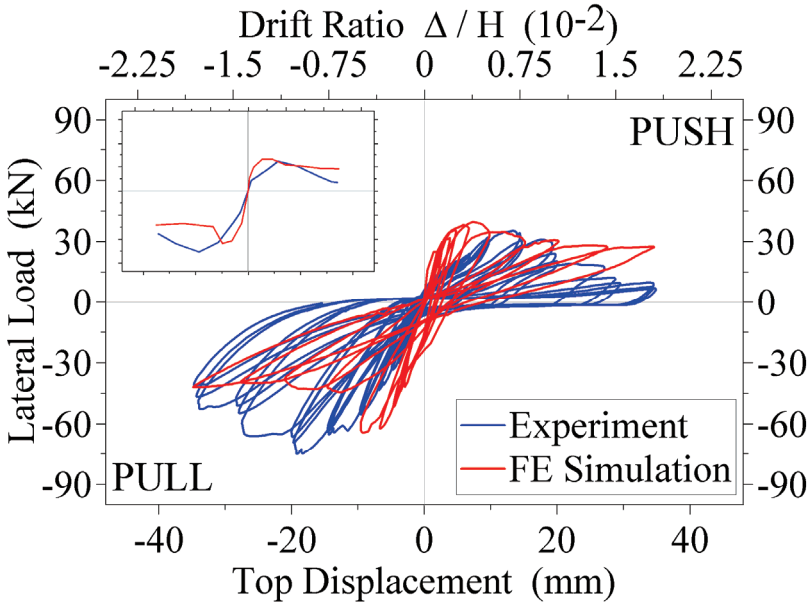


Figure 5.38. Lateral load vs. top displacement comparison, US4

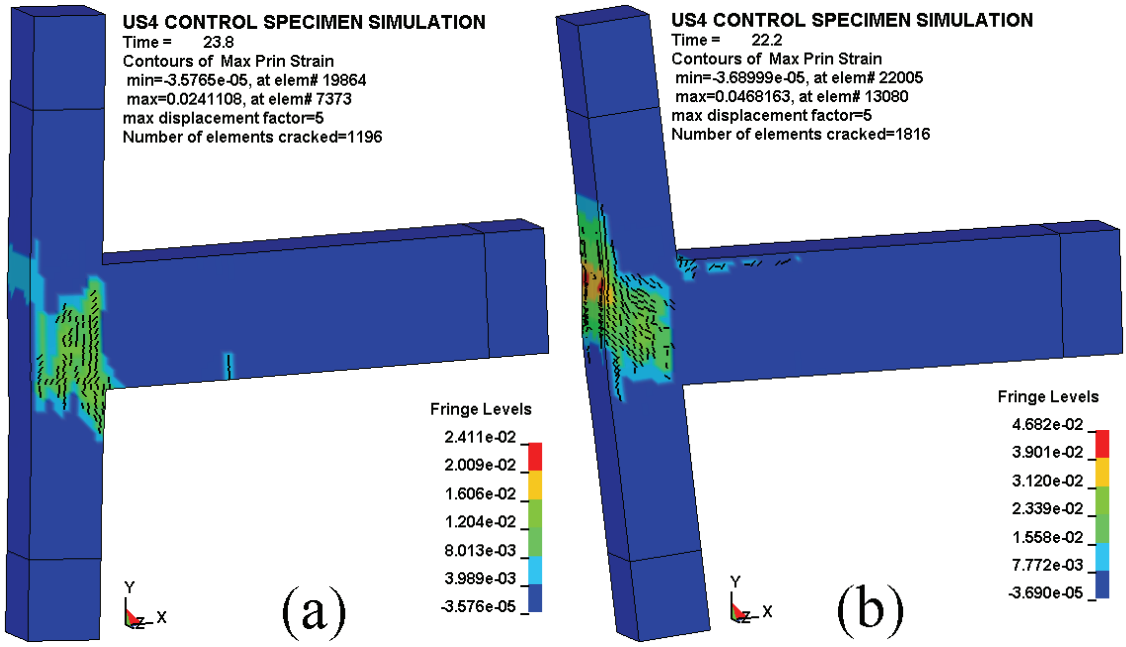


Figure 5.39. Crack pattern; (a) push, (b) pull direction of loading

5.9.7. Specimen US4FRP3

The comparison between the experimentally and numerically obtained lateral load versus top displacement relationships is shown in Figure 5.40. In both directions of loading numerically obtained ultimate loads (87 kN in push and 110 kN in pull directions of loading) are in good agreement with the experimental loads (83 kN in push and 127 kN in pull directions of loading). However the shape of the hysteretic response of the lateral load versus top displacement relationship is not in good agreement with the experimentally obtained lateral load top displacement relationship. As the discussed in sections 5.9.4 and 5.9.5, the use of single integration point solid element may be the reason for the discrepancies between experimental and numerical results. Baushinger effect of the steel model and the compression softening effect of the concrete model were not modeled. Thus this could be another reason for the difference between the hysteretic responses. The pinched shape near the origin of the hysteretic response of the numerical load versus displacement relationship is in agreement with the experimental measurements.

As in the case of the US4 control specimen simulation, in the US4FRP3 model the initial stiffness is higher than the stiffness observed in the experiment. This could be due to the fact that full bond between the steel reinforcement and concrete was assumed.

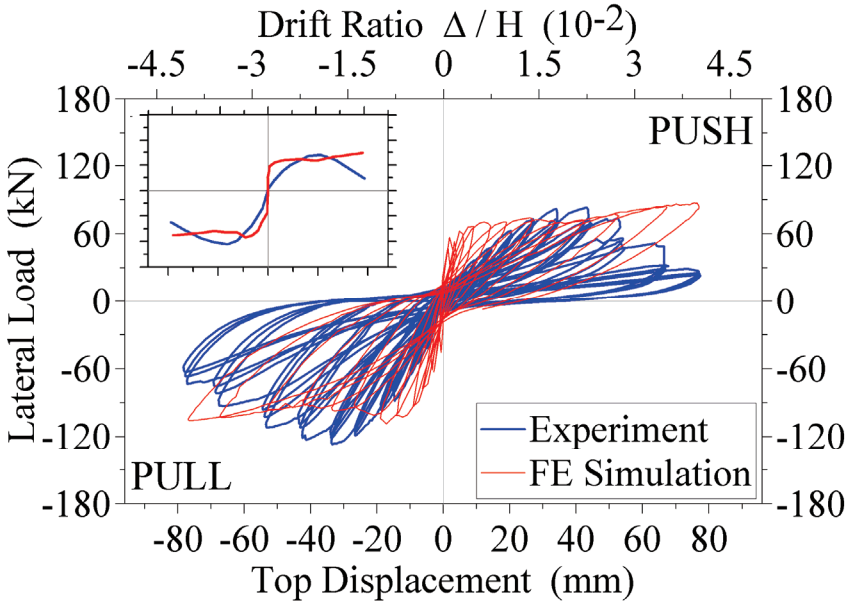


Figure 5.40. Lateral load vs. top displacement comparison, US4FRP3

6. SUMMARY, CONCLUSIONS AND RECOMMENDATIONS

In the light of the experimental and numerical results and observations the following conclusions were identified;

As-built specimen US1 with no shear reinforcement within the joint, failed due to excessive shear deformations at the joint core. Under cyclic loading as-built specimens with no shear reinforcement and short embedment length of bottom beam reinforcement behaved poorly in terms of lateral load top displacement relationship. Two different modes of failure were observed; shear failure at the joint and slippage of beam bottom longitudinal reinforcement. The slippage of the beam positive reinforcement is more critical than that of joint shear failure. Bond failure at the beam positive reinforcements resulted in lower drift, lower lateral load carrying capacities, and lower stiffness in the control specimens US2, US3 and US4.

In retrofitting of beam column joints with no shear reinforcement at the joint and short embedment length for the beam positive reinforcement, priority to the possible reinforcement slippage should be given and then the joint should be strengthened for shear.

FRP retrofitted specimens increased the ultimate lateral load levels of the specimens of approximately 50% to 60 %. This effect in general shows the effectiveness of the CFRP wrapping configurations in terms of ultimate loads.

FRP1 wrapping configuration prevented the joint shear failure and caused a desired failure mode which is plastic hinging at the beam. Beam column joints with reinforcement detailing as specimen US1 could be retrofitted effectively with the proposed wrapping configuration, FRP1.

Both FRP2 and FRP3 configurations substantially enhanced the structural performance of the beam-column joints in terms of lateral load capacity, drift, dissipated energy, and stiffness as compared to as-built joints. FRP3 wrapping configuration performed better than FRP2 retrofitted specimen in terms of ultimate load and

displacement due to higher number of CFRP layers employed in the U-shape application and the additional anchorages provided for the U-shaped FRP.

Wrapping configurations FRP2 and FRP3 were able to control the slippage of the beam bottom longitudinal reinforcement up to drift level of 2.00% and 2.80%, respectively. However after that drift level ruptures of the CFRP strip 1 have caused undesired sudden failure in push direction of loading. The proposed amount of CFRP was inadequate to stop the rupture of the strip 1. Thus, additional layers should be considered or at least small pieces of CFRP (CFRP strips) could be used as patches at high stress concentration locations to prevent the rupture.

FRP rupture strain levels were approximately 60 % lower than those provided by the manufacturer. In the design of CFRP applications, ultimate design strain level should be reduced at least by a factor of 0.60.

In pull direction of loading, the governing mode of failure for FRP2 and FRP3 wrapping configurations was debonding of U-shaped FRP. Thus, effective anchorage techniques should be provided for the CFRP bonded to the beam.

Especially at higher drift levels, stiffness values of the CFRP retrofitted specimens are doubled when compared to the stiffness of the control specimens. Compared to the control specimens, strength degradation rate of CFRP retrofitted specimens was considerably reduced. This effect was more significant in the repaired and retrofitted specimens due to high strength repair materials.

Repaired and CFRP retrofitted specimens performed almost exactly the same as the CFRP retrofitted specimens. This indicates that even a heavily damaged joint could be repaired and then retrofitted to resist extreme seismic loadings.

In general, the increase in the axial load resulted in an increase in the lateral load capacity and the stiffness of the control and CFRP-retrofitted joints.

Up to ultimate drift level of the control specimens (approximately 1.75 % drift level), CFRP retrofitted specimens dissipated almost equal amount energy as those of the control specimens. However, after that drift level, CFRP retrofitted specimens dissipated a significant amount of energy. The increase in energy dissipation of CFRP retrofitted and repaired and CFRP retrofitted specimens, compared to control specimens, ranged from 350 % to 500 %.

In terms of ultimate load level, damage locations, shear deformations at the joint core, failure modes and hysteretic response, the FE simulation results of as-built specimens in overall are in good agreement with the experimental findings. Discrepancies between the numerical and experimental FE simulations of FRP retrofitted specimens range from slight to moderate. Reasons for the discrepancies could be due to the use of poorly behaved single integration point solid elements. Different contact algorithms could be utilized between shell (FRP material) and solid (concrete media) elements.

Design guidelines for CFRP retrofitting of beam-column joints could be developed with additional FE simulations and experimental and numerical results presented in this study.

Herein presented FE simulations are unique in terms of finite element modeling of a 3-D reinforced concrete beam-column joint under cyclic loading with the inclusion of concrete cracking, shear transfer due to aggregate interlocking and tri-axial state of stress effects.

The same FE simulation methodology, explicit finite element modeling, could be applied also to other type of structural members, e.i. beams, columns, slabs etc. for predicting the nonlinear cyclic response, since the herein presented simulations involve complex failure modes such as shear failure at the joint core and flexural plastic hinging at the beam.

Utilized concrete constitutive model which is elastic perfectly plastic could be improved such that the shape of the stress-strain relationship is similar to the actual concrete behavior which is more like a parabolic function. Both concrete under

compression and tension material behavior could be developed accordingly and this may improve the hysteretic response predictions of the reinforced concrete beam column joints.

APPENDIX A. MOMENT CURVATURE RELATIONSHIPS

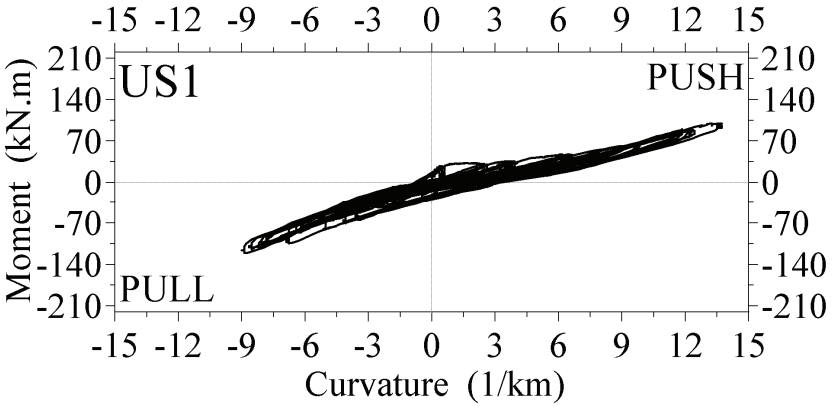


Figure A.1. Beam moment curvature for US1

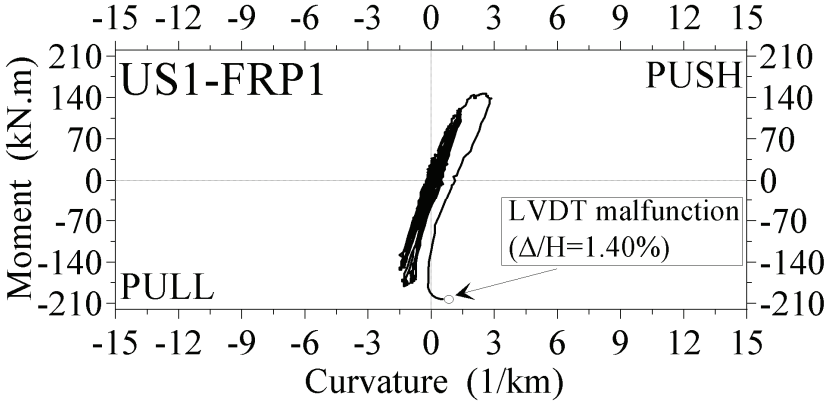


Figure A.2. Beam moment curvature for US1FRP1

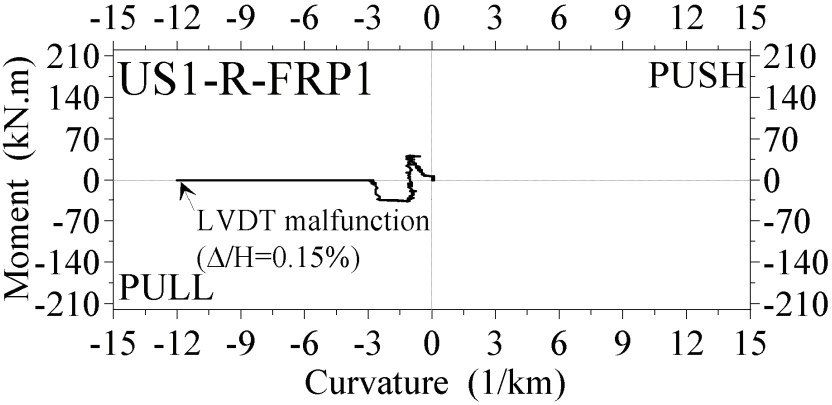


Figure A.3. Beam moment curvature for US1RFRP1

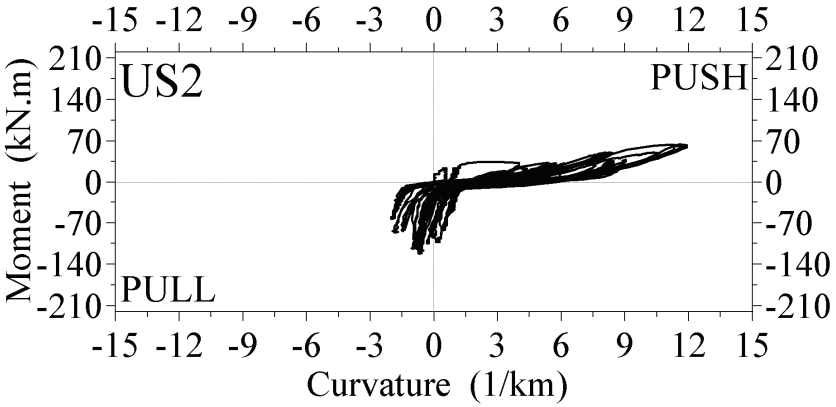


Figure A.4. Beam moment curvature for US2

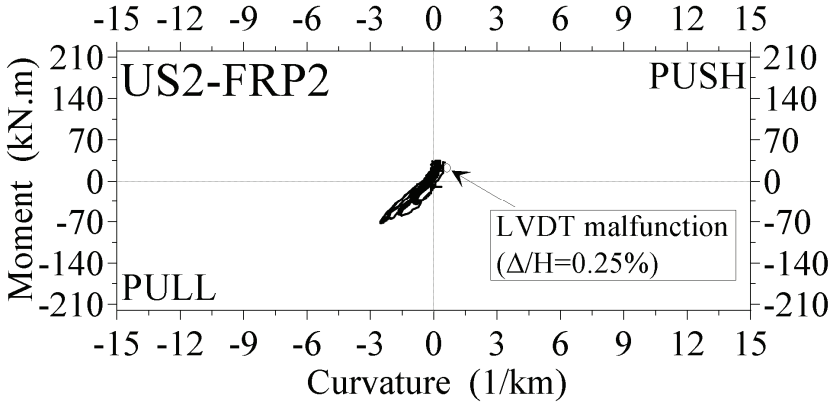


Figure A.5. Beam moment curvature for US2FRP2

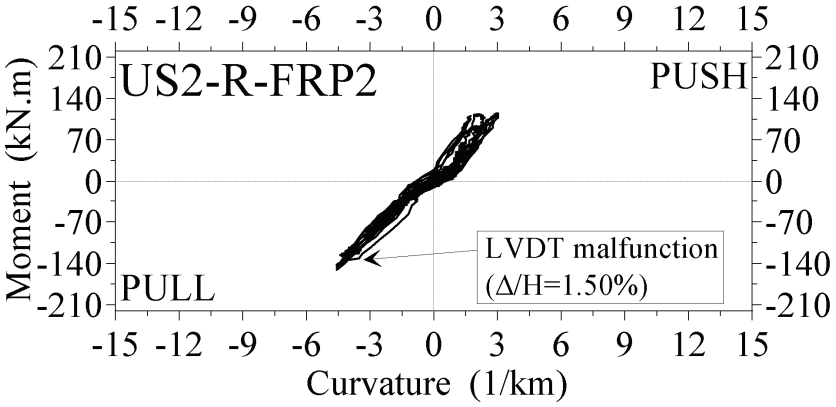


Figure A.6. Beam moment curvature for US2RFRP2

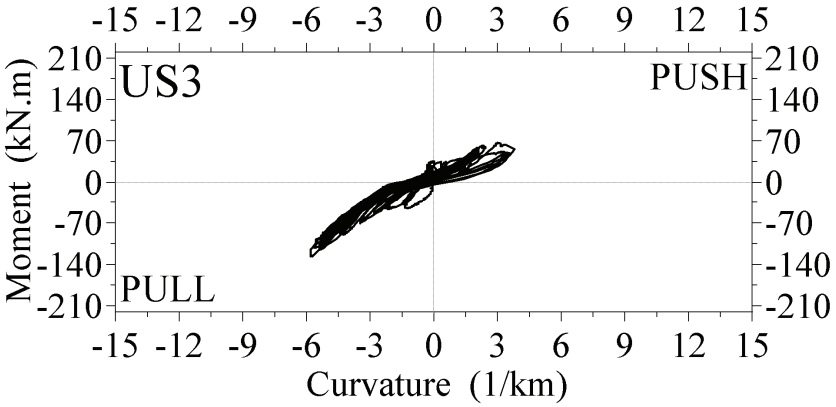


Figure A.7. Beam moment curvature for US3

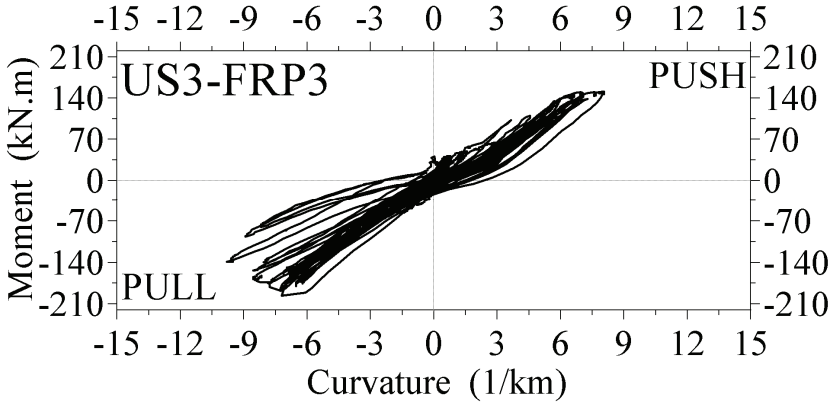


Figure A.8. Beam moment curvature for US3FRP3

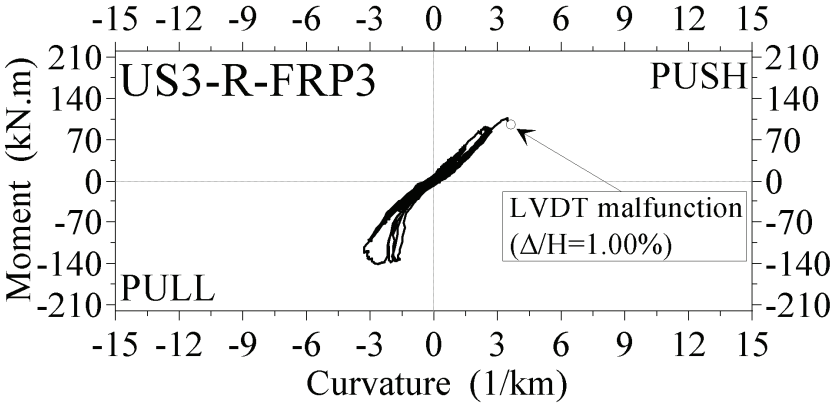


Figure A.9. Beam moment curvature for US3RFRP3

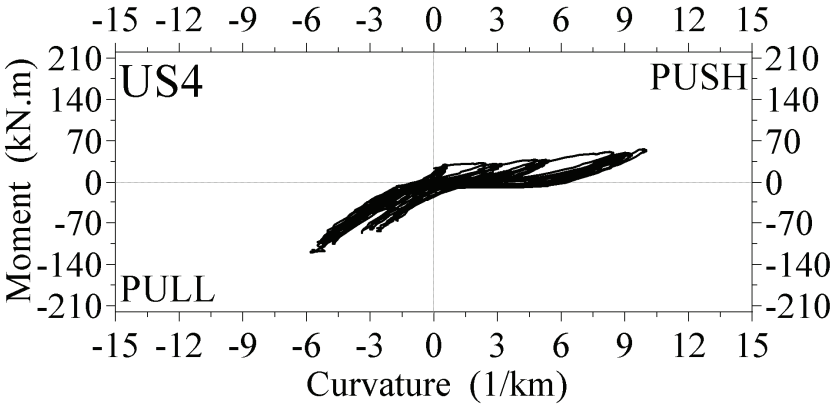


Figure A.10. Beam moment curvature for US4

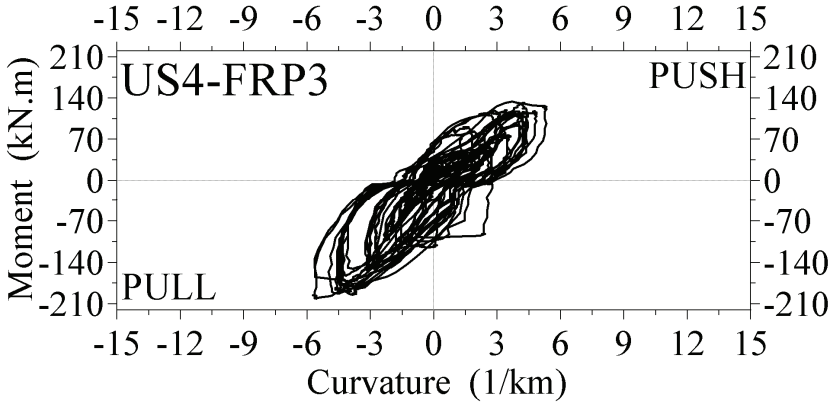


Figure A.11. Beam moment curvature for US4FRP3

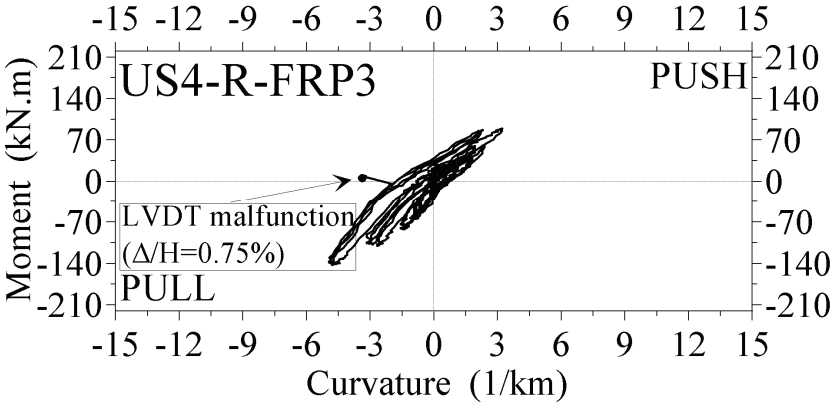
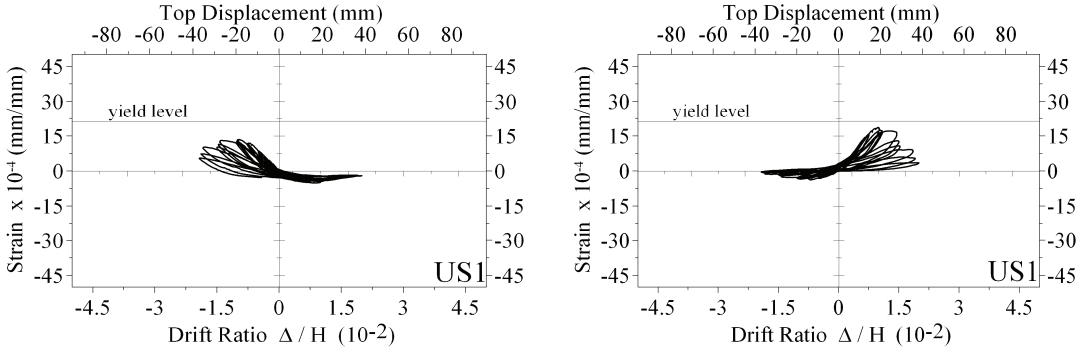


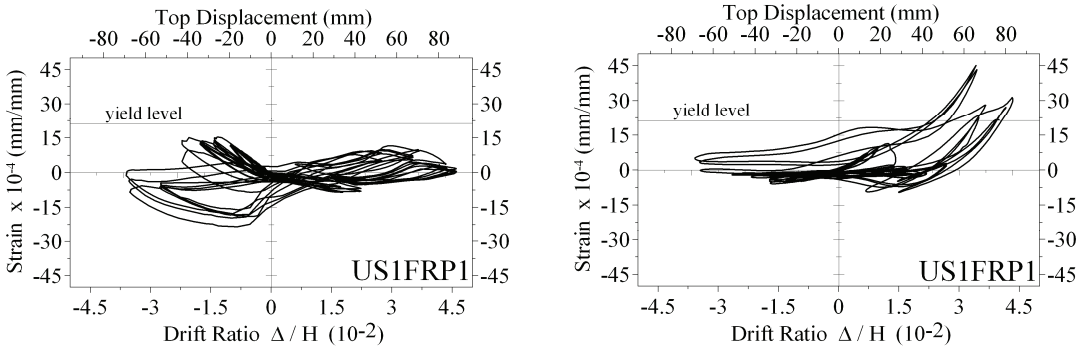
Figure A.12. Beam moment curvature for US4RFRP3

APPENDIX B. BEAM LONGITUDINAL REINFORCEMENT STRAINS



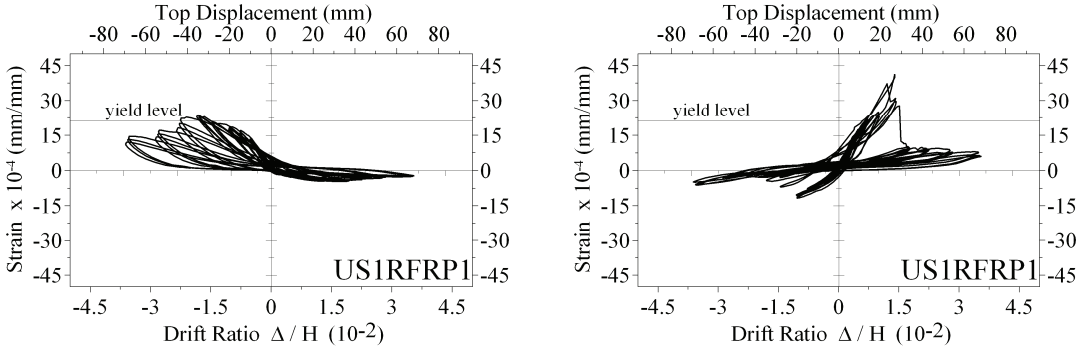
(a) (b)

Figure B.1. US1 ;(a) bottom (b) top longitudinal reinforcement



(a) (b)

Figure B.2. US1FRP1 ;(a) bottom (b) top longitudinal reinforcement



(a) (b)

Figure B.3. US1RFRP1 ;(a) bottom (b) top longitudinal reinforcement

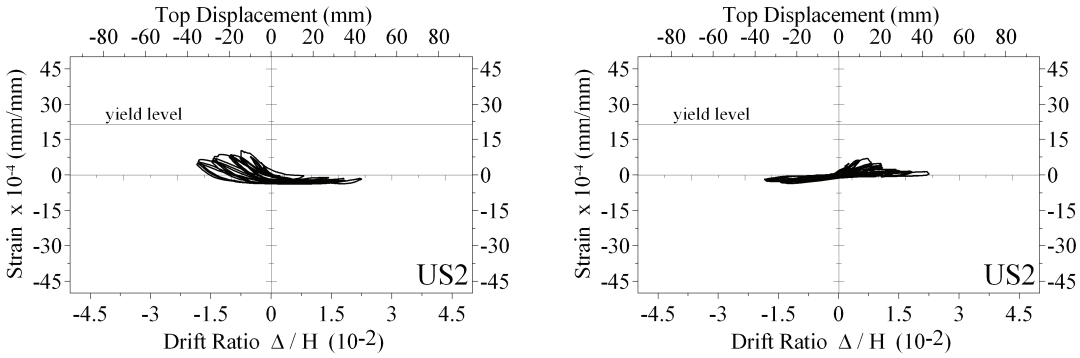


Figure B.4. US2 ;(a) bottom (b) top longitudinal reinforcement

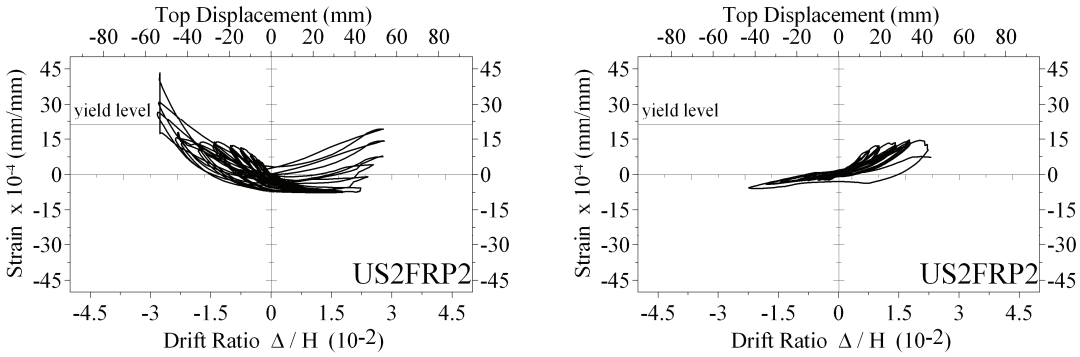


Figure B.5. US2RFRP2 ;(a) bottom (b) top longitudinal reinforcement

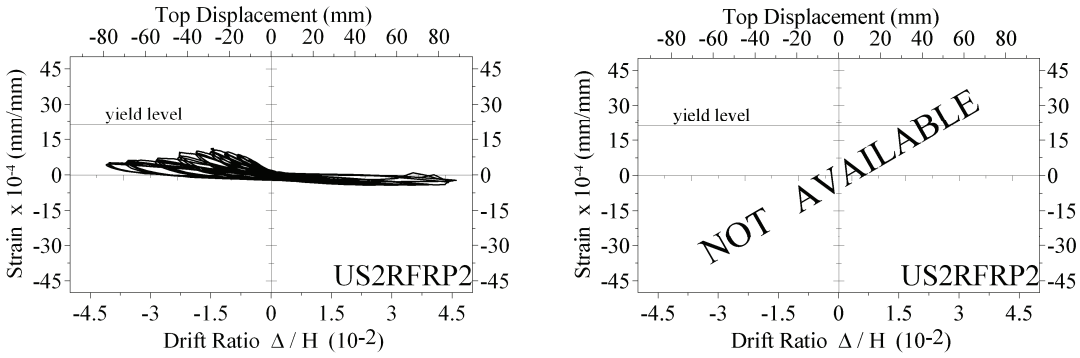


Figure B.6. US2RFRP2 ;(a) bottom (b) top longitudinal reinforcement

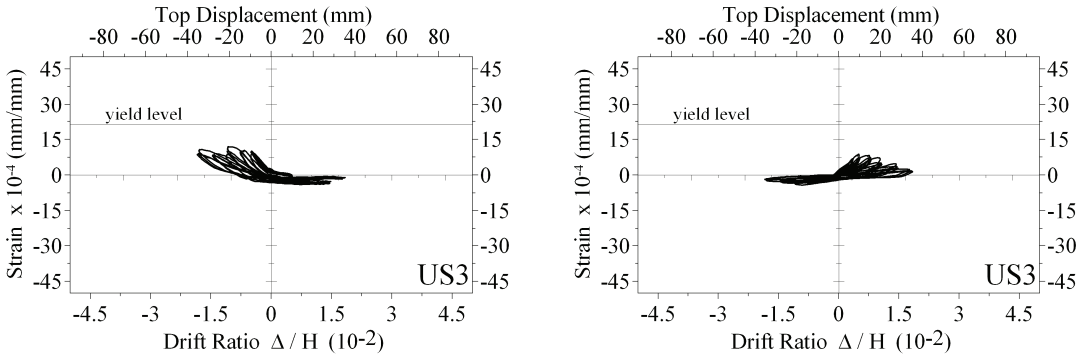


Figure B.7. US3 ;(a) bottom (b) top longitudinal reinforcement

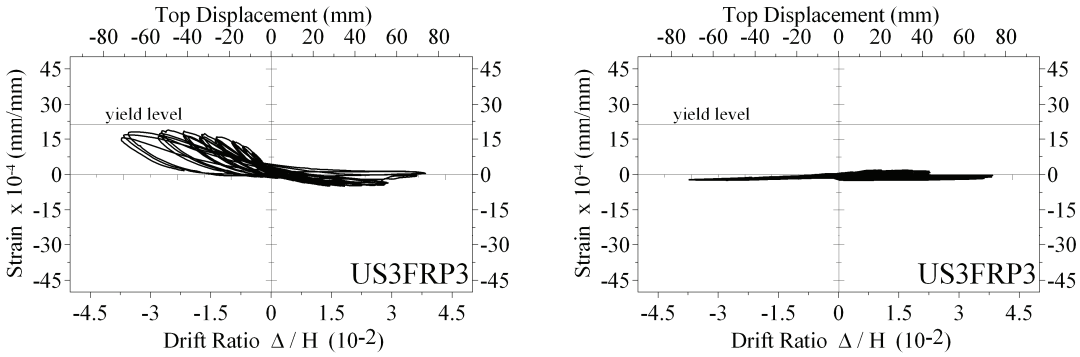


Figure B.8. US3RFRP3 ;(a) bottom (b) top longitudinal reinforcement

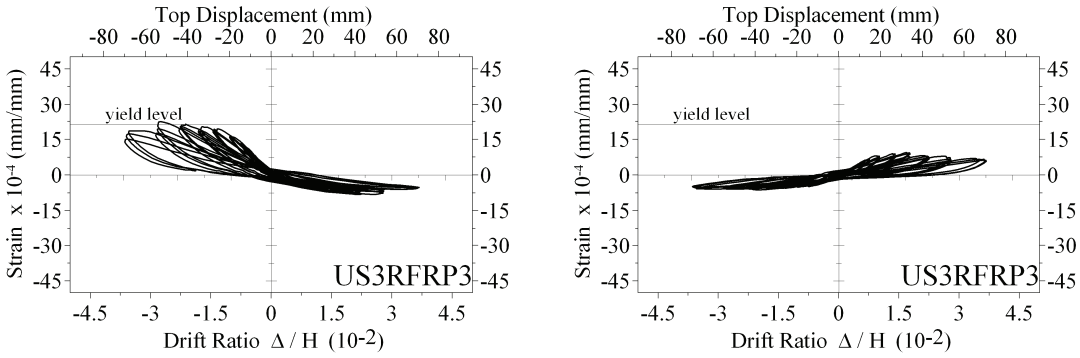


Figure B.9. US3RFRP3 ;(a) bottom (b) top longitudinal reinforcement

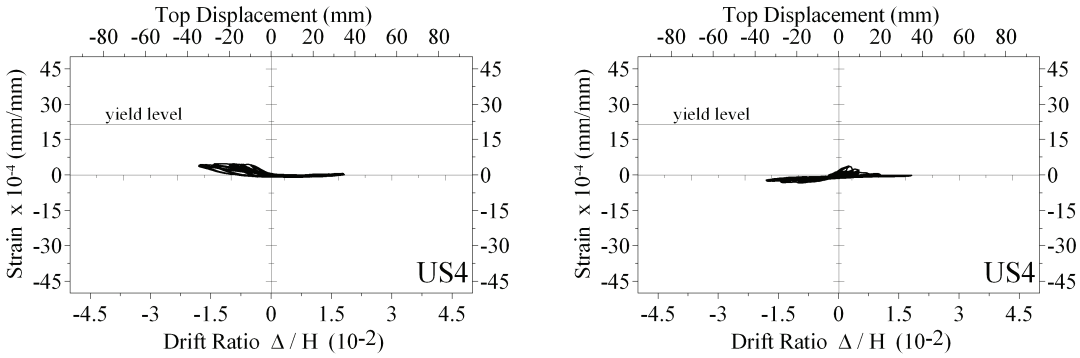


Figure B.10. US4 ;(a) bottom (b) top longitudinal reinforcement

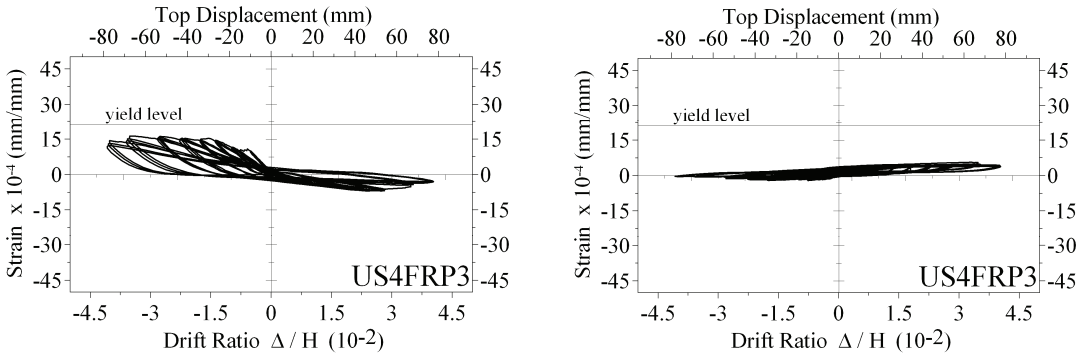


Figure B.11. US4FRP3 ;(a) bottom (b) top longitudinal reinforcement

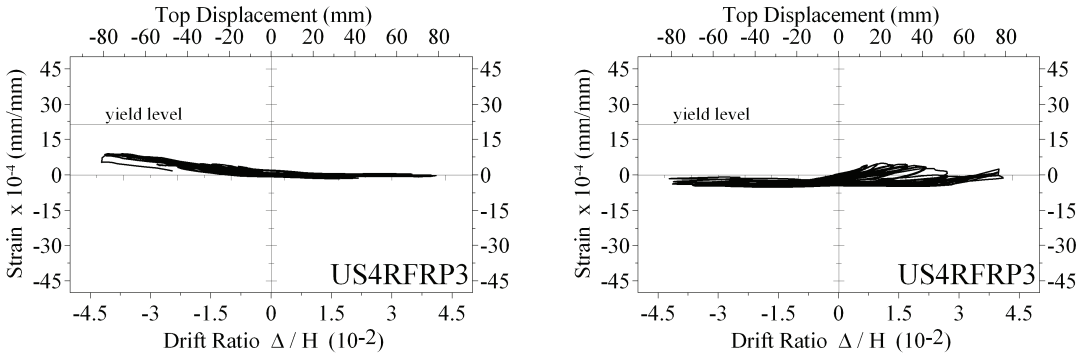


Figure B.12. US4RFRP3 ;(a) bottom (b) top longitudinal reinforcement

REFERENCES

1. Amoury, T. and A. Ghobarah, “Seismic Rehabilitation of Beam-Column Joint Using GFRP Sheets”, *Engineering Structures*, Elsevier, Vol. 24, pp. 1397-1407, 2002.

2. Ghobarah, A. and A. Said, “Shear Strengthening of Beam-Column Joints”, *Engineering Structures*, Elsevier, Vol. 24, pp. 881-888, 2002.

3. Park, R. and T. Paulay, *Reinforced Concrete Structures*, John Wiley and Sons, New York, pp. 730-733, 1975.

4. Beres, A. B., *Experimental and Analytical Study of the Performance of Reinforced Concrete Frames with Non-Ductile Details*, Ph.D. Dissertation, School of Civil and Environmental Engineering, Cornel University, Ithaca, NY., 1994.

5. Engindeniz, M., L. F. Kahn and A. H. Zureick, "Repair and Strengthening Of Reinforced Concrete Beam-Column Joints: State Of The Art”, *ACI Structural Journal*, Vol. 102, No. 2, pp. 187-197, 2005.

6. Alcocer, S. and J. O. Jirsa, ‘‘Strength of Reinforced Concrete Frame Connections Rehabilitated by Jacketing’’, *ACI Structural Journal*, Vol. 90, No. 3, pp. 249-261, 1993.

7. Beres ,A., S. El-Borgi, R. N. White and P. Gergely, *Experimental Results of Repaired and Retrofitted Beam-Column Joint Tests in Lightly Reinforced Concrete Frame Buildings*, Technical Report NCEER-92-0025 , National Center for Earthquake Engineering Research, State University of New York at Buffalo, 1992.

8. Gergely, J., C. P. Pantelides and L. D. Reaveley, “Shear strengthening of RCT-Joints Using CFRP Composites”, *Journal of Composites for Construction*, ASCE, Vol. 4, No. 2, pp. 56-64, 2000.

9. Hanson, N. W. and H. W. Connor, "Seismic Resistance of Reinforced Concrete Beam-Column Joints", *Journal of the Structural Division*, Proceedings of the American Society of Civil Engineers, Vol. 93(ST5), pp. 533-560, October 1967.

10. Hanson, N. W., "Seismic Resistance of Concrete Frames with Great 60 Reinforcement", *Journal of the Structural Division*, Proceedings of the American Society of Civil Engineers, Vol. 97(ST6), pp. 1685-1700, June 1971.

11. ACI Committee 318, *Building Code Requirements for Reinforced Concrete (ACI 318-71)*, American Concrete Institute, Detroit, 1971.

12. Paulay, T., R. Park and M. J. N. Priestley, "Reinforced Concrete Beam-Column Joints Under Seismic Actions", *ACI Journal*, Vol. 75, Issue 11, Title No. 75-60, pp. 585-593, 1978.

13. Ehsani, M. R. and J. K. Wight, "Exterior Reinforced Concrete Beam-to-Column Connections Subjected to Earthquake-Type Loading", *ACI Journal*, Vol. 82, Issue 4, Title No. 82-43, pp. 492-499, July-August 1985.

14. Popov, E. P., V. V. Bertero and S. Viwathanatepa, "Analytical and Experimental Hysteretic Loops for R/C Subassemlages", *Fifth European Conference on Earthquake Engineering*, Istanbul, 89, 1975.

15. Üzümeri, S. M. and M. Seçkin, "Behaviour of Joints and Ductility of Reinforced Concrete Frames", *Fifth European Conference on Earthquake Engineering*, Istanbul, 94, 1975.

16. Meinheit, D. F. and J. O. Jirsa, *The Shear Strength Of Reinforced Concrete Beam-Column Joints*, CESRL Report, 1977.

17. Jirsa, J. O., D. F. Meinheit and J. W. Woolen, "Factors Influencing the Shear Strength of Beam-Column Joints", *Proceedings of the U.S. National Conference on Earthquake*

Engineering, Earthquake Engineering Research Institute, EERI, Ann Arbor, Michigan, pp. 297-305, June 1975.

18. Beres ,A., R. N. White and P. Gergely, *Seismic Behavior of Reinforced Concrete Frame Structures with Nonductile Details: Part I*, Technical Report NCEER-92-0024 , National Center for Earthquake Engineering Research, State University of New York at Buffalo, 1992.

19. Beres, A., S. P. Pessiki, R. N. White and P. Gergely, "Behavior of Existing Reinforced Concrete Frames Designed Primarily for Gravity Loads", *Proceedings of the International Meeting on Earthquake Protection of Buildings*, Universita Degli Studi di Ancona, Italy, 1991.

20. Beres, A., S. P. Pessiki, R. N. White and P. Gergely, "Seismic Performance of Existing Reinforced Concrete Frames Designed Primarily for Gravity Loads", *6th Canadian Conference on Earthquake Engineering*, Toronto, Canada, 1991.

21. Beres, A., S. Pessiki, R. N. White and P. Gergely, "Implications of Experiments on the Seismic Behavior of Gravity Load Designed RC Beam-to-Column Connections", *Earthquake Spectra*, Vol. 12, No. 2, pp. 185-198, 1996.

22. Beres ,A., *Experimental and Analytical Study of the Performance of Reinforced Concrete Frames with Non-Ductile Details*, Ph.D. Dissertation, School of Civil and Environmental Engineering, Cornel University, Ithaca, NY., 1994.

23. Lee, L. N., J. K. Wight and R. D. Hanson, "Repaired Beam-Column Subassemblages Subjected to Earthquake Type Loads", *Fifth European Conference on Earthquake Engineering*, Istanbul, 95, 1975.

24. Adin, M. A., D. Z. Yankelevsky and D.N. Farhey, "Cyclic Behavior of Epoxy-Repaired Reinforced Concrete Beam-Column Joints", *ACI Structural Journal*, Vol. 90, Issue 2, pp. 170-179, 1993.

25. Alcocer S. M., “RC Frame Connections Rrehabilitated by Jacketing”, *Journal of Structural Engineering*, ASCE, Vol. 119, No. 5, pp. 1413-1431, 1993.

26. Alcocer, S. M., "RC Frame Connections Rehabilitated By Jacketing”, *Journal of Structural Engineering,* ASCE, Vol. 119, No. 5, pp. 1413-1431, 1993.

27. Alcocer, S. M. and J. O. Jirsa, "Strength Of Reinforced-Concrete Frame Connections Rehabilitated By Jacketing”, *ACI Structural Journal*, Vol. 90, Issue 3, pp. 249-261, 1993.

28. Alcocer, S. M. and J. O. Jirsa, *Reinforced Concrete Frame Connections Rehabilitated by Jacketing*, PMFSEL Report 221, 1991.

29. Ghobarah, A., T. S. Aziz and A. Biddah, ‘‘Rehabilitation of Reinforced Concrete Frame Connections Using Corrugated Steel Jacketing’’, *ACI Structural Journal*, Vol. 4, Issue 3, pp. 283-294, 1997.

30. Biddah, A., A. Ghobarah and T. S. Aziz, "Upgrading of Nonductile Reinforced Concrete Frame Connections”, *Journal of Structural Engineering*,-ASCE, Vol. 123, No. 8, pp. 1001-1010, 1997.

31. ACI-ASCE Committee 352, *Recommendations for Design of Beam-Column Joints in Monolithic Reinforced Concrete Structures (ACI 352R-76) (Reaffirmed 1981)*, American Concrete Institute, Detroit, 1976

32. Tsonos, A. G., “Lateral Load Response of Strengthened Reinforced Concrete Beam-to-Column Joints”, *ACI Structural Journal*, Vol. 96, Issue 1, pp. 46-56, 1999.

33. Gergely, I, C. P. Pantelides, R.J. Nuismer and L. D. Reaveley, “Bridge Pier Retrofit Using Fiber-Reinforced Plastic Composites”, *Journal of Composites for Construction*, Vol. 2, No 4, pp. 165-174, 1998.

34. Pantelides, C. P., I. Gergely and L. D. Reaveley, “In-Situ Verification of Rehabilitation and Repair of Reinforced Concrete Bridge Bents under Simulated Seismic Loads”, *Earthquake Spectra*, Vol. 17, No. 3, pp. 507-530, August 2001.

35. Pulido, C., M. S. Saiidi, D. Sanders, A. Itani and S. El-Azazy, “Seismic Performance of Two-Column Bents-Part I: Retrofit with Carbon Fiber-Reinforced Polymer Fabrics”, *ACI Structural Journal*, Vol. 101, Issue 4, Document No. 101-S56, pp. 558-568, 2004.

36. Granata, P. J. and A. Parvin, “An Experimental Study on KevlarS of Beam-Column Connections”, *Composite Structures*, Elsevier, 53, pp. 163-171, 2001.

37. Parvin, A. and P. J. Granata, "Investigation on the Effects of Fiber Composites at Concrete Joints”, *Composites Part B: Engineering Journal*, Vol. 31B, No. 6-7, pp. 499-509, November 2000.

38. Parvin, A. and S. Wu, "Evaluation of Wrap Thickness in CFRP-Strengthened Concrete T-Joints", *Proceedings of the Second International Conference on FRP Composites in Civil Engineering*, CICE 2004, Adelaide, Australia, pp. 643-646, December 2004.

39. Antonopoulos, C. P. and T. C. Triantafillou, “Experimental Investigation of FRP-Strengthened RC Beam-Column Joints Analysis of FRP Strengthened RC Beam-Column Joints”, *Journal of Composites for Construction*, ASCE, Vol. 7, No. 1, pp. 39-49, 2003.

40. Antonopoulos, C. P. and T. C. Triantafillou, “Analysis of FRP Strengthened RC Beam-Column Joints”, *Journal of Composites for Construction*, ASCE, Vol. 6, No. 1, pp. 41-51, February 2002.

41. Prota, A., A. Nanni, G. Manfredi and E. Cosenaza, “Seismic Upgrade of Beam-Column Joints with FRP Reinforcement”, *Industria Italiana del Cemento*, 2000.

42. Ngo, D. and A. C. Scordelis, “Finite Element Analysis of Reinforced Concrete Beams”, *ACI Journal*, Vol. 64, Issue 3, Title No. 64-14, pp. 152-163, March 1967.

43. Vidosa, F. G., M. D. Kotsovos and M. N. Pavlovic, "Nonlinear Finite Element Analysis of Concrete Structures: Performance of a Fully Three-Dimensional Brittle Model", *Computers and Structures*, Vol. 40, pp. 1287-1306, 1991

44. Chen, W. F, *Plasticity in Reinforced Concrete*, McGraw-Hill, New York, pp. 394-459, 1982.

45. Stevens, N. J. and S. M. Uzumeri, M.P. Collins and G.T. Will, "Constitutive Model for Reinforced Concrete Finite Element Analysis", *ACI Structural Journal*, Vol. 88, Issue 1, Title No. 88-S7, pp. 49-59, 1991.

46. Balakrishnan, S. and D. Murray, "Concrete Constitutive Model for NLFE Analysis of Structures", *Journal of Structural Engineering*, ASCE, Vol. 114, No. 7, pp. 1449-1466, 1988.

47. Balakrishnan, S. and D. Murray, "Effect of Modeling on NLFE Analysis of Concrete Structures", *Journal of Structural Engineering*, ASCE, Vol. 114, No. 7, pp. 1467-1487, 1988.

48. Yamaguchi, E. and W. F. Chen, "Cracking Model for Finite Element Analysis of Concrete Materials", *Journal of Engineering Mechanics*, ASCE, Vol. 116, No. 6, pp. 1242-1260, 1990.

49. Bashur, F. K. and D. Darwin, "Nonlinear Model for Reinforced Concrete Slabs", *Journal of the Structural Division*, Proceedings of the American Society of Civil Engineers, ASCE, Vol. 104, No. ST1, pp. 157-170, January 1978.

50. Crisfield, M. A. and J. Wills, "Analysis of R/C Panels Using Different Concrete Models", *Journal of Engineering Mechanics*, ASCE, Vol. 115, No. 3, pp. 578-597, Mart 1989.

51. Baglin, P. S. and R. H. Scott, “Finite Element Modeling of Reinforced Concrete Beam-Column Connections”, *ACI Structural Journal*, Vol. 97, Issue 6, Title No. 97-S90, pp. 886-894, 2000.

52. Hegger, J., A. Sherif and W. Roeser, “Nonlinear Finite Element Analysis of Reinforced Concrete Beam-Column Connections”, *ACI Structural Journal*, Vol. 101, No. 5, Title No. 101-S59, pp. 604-614, 2004.

53. Chansawat, K., S. C. S. Yim and T. H. Miller, “Nonlinear Finite Element Analysis of a FRP-Strengthened Reinforced Concrete Bridge”, *Journal of Bridge Engineering*, ASCE, Vol. 11, Issue 1, pp. 21-32, January-February 2006.

54. Sritharan, S., M. J. N. Priestley and F. Seible, “Nonlinear Finite Element Analyses of Concrete Bridge Joint Systems Subjected to Seismic Actions”, *Finite Elements in Analysis and Design*, Vol. 36, pp. 215-233, 2000.

55. Noguchi, H., "Three-Dimensional FEM Analysis of RC Beam-Column Joints Subjected to Two-Directional Loads”, *ACI Special Publication*, Vol. 237, pp. 149-164, 2006.

56. Shirai, N., “Evaluation of Cyclic Deterioration and Post-Peak Behavior of RC Beam-Column Joint Assemblages by 3-D FE Analysis”, *ACI Special Publication*, Vol. 237, pp. 129-148, 2006.

57. Noguchi, H., T. Kashiwazaki and K. Miura, “Finite Element Analysis of Reinforced Concrete Joints Subjected to Multi-Axial Loading”, *ACI Special Publication*, Vol. 265, pp. 149-164, 2009.

58. BASF Construction Chemicals, *Product Manual-Building Systems*, Turkey, pp. 60-61, 2007.

59. ACI Committee 318, *Building Code Requirements for Structural Concrete (ACI 318-08) and Commentary*, American Concrete Institute, USA, 2008.

60. ACI T1.1-01, *Acceptance Criteria for Moment Frames Based on Structural Testing*, American Concrete Institute, 2001.

61. Bakir, P. G. and H. M. Boduroglu, "A New Design Equation for Predicting the Joint Shear Strength of Monotonically Loaded Exterior Beam-Column Joints", *Engineering Structures*, Elsevier, Vol. 24, pp. 1105-1117, 2002.

62. MSC. Marc Mentat, Version 2005 R3, MSC. Software Corporation, 2 MacArthur Place Santa Ana, 92707, CA, USA, 2005.

63. LS-DYNA, Version 9.71 R4.2 (64bit), Livermore Software Technology Corporation, Livermore, CA., USA, 2009.

64. LS-PrePost, Version 3.0, Livermore Software Technology Corporation, Livermore, CA., USA, 2009.

65. MSC. Marc, Version 2005 R3, MSC. Software Corporation, 2 MacArthur Place Santa Ana, 92707, CA, USA.

66. MSC. Marc Theory Manual, Version 2005 R3, MSC. Software Corporation, 2 MacArthur Place Santa Ana, 92707, CA, USA.

67. Crisfield, M. A., *Non-linear Finite Element Analysis of Solids and Structures, Volume 1: Essentials*", John Wiley & Sons Ltd., England, pp 368, 2001.

68. Bathe, K. J., *Finite Element Procedures*, Prentice Hall, United States of America, pp 1037, 1996.

69. Chopra, A. K., *Dynamics of Structures*, Prentice-Hall, New Jersey, 2000.

70. Belytschko, T., W. K. Liu and B. Moran, *Nonlinear Finite Elements for Continua and Structures*, John Wiley & Sons Ltd., England, pp. 668, 2001.

71. LS-DYNA Theory Manual, Livermore Software Technology Corporation, Livermore, CA., USA, 2006.

72. LS-DYNA Keyword User's Manual, Version 9.71, Livermore Software Technology Corporation, Livermore, CA., USA, 2007.

73. Broadhouse, B. J. and A. J. Neilson, "Modelling Reinforced Concrete Structures in DYNA3D", *Safety and Engineering Science Division,* AEE Winfrith, 1987.

74. Broadhouse, B. J., "The Winfrith Concrete Model in LS-Dyna3D", *AEA Technology*, 1995.

75. Ottosen, N. S., *Failure and Elasticity of Concrete*, A.E.K. RISØ National Laboratory Report, RisØ–M–1801, pp. 67, July 1975.

76. Ottosen, N. S., "A Failure Criterion for Concrete", *Journal of the Engineering Mechanics Division*, ASCE, pp. 528-535, August 1977.

77. Ottosen, N. S., "Constitutive Model for Short-Time Loading of Concrete", *Journal of the Engineering Mechanics Division*, ASCE, pp. 127-141, February 1979.

78. Ottosen, N. S., *Nonlinear Finite Element Analysis of Concrete Structures*, A.E.K. RISØ National Laboratory Report, RisØ–R–411, pp. 186, May 1980.

79. Ottosen, N. S. and M. Ristinmaa, *The Mechanics of Constitutive Modeling*, Elsevier, Great Britain, pp. 745, 2005.

80. Kupfer, H., H. K. Hilsdorf and H. Rüsh, "Behavior of Concrete under Biaxial Stresses", *Journal of the American Concrete Institute*, Vol. 66, Issue 8, pp. 656-666, August 1969.

81. Richart, F. E., A. Brandtzaeg and R. L. Brown, *A Study of the Failure of the Concrete Under Combined Compressive Stresses*, Bulletin No. 185, University of Illinois, Engineering Experiment Station, Urbana, Ill., 1928.

82. Wolfram Mathematica, Version 7.0, Wolfram Research Inc., 2008.

83. Chang, F. K. and K. Y. Chang, "A Progressive Damage Model for Laminated Composites Containing Stress Concentrations", *Journal of Composite Materials*, Vol. 21, pp. 834-855, September 1987.

84. Altay, S., A. Parvin, C. Yalcin and O. Kaya, "Evaluation of Bond-Slip Models for R/C Joints", *Proceedings of Ninth Canadian Conference on Earthquake Engineering*, Ottawa, Ontario, Canada, 26-29 June 2007.